

ISTANBUL TECHNICAL UNIVERSITY ★ INSTITUTE OF SCIENCE AND TECHNOLOGY

**EXPERIMENTAL INVESTIGATION OF
FLOW STRUCTURES AROUND AN OSCILLATING AIRFOIL
IN STEADY CURRENT**

**Ph.D. Thesis by
İdil FENERCİOĞLU**

Department : Aeronautical and Astronautical Engineering

Programme : Aeronautical and Astronautical Engineering

JUNE 2010

**EXPERIMENTAL INVESTIGATION OF
FLOW STRUCTURES AROUND AN OSCILLATING AIRFOIL
IN STEADY CURRENT**

**PhD Thesis by
İdil FENERCİOĞLU
(511022003)**

**Date of submission : 05 February 2010
Date of defence examination: 11 June 2010**

**Supervisor (Chairman) : Assoc. Prof. Dr. N. L. Okşan ÇETİNER-
YILDIRIM (ITU)**
**Members of the Examining Committee: Prof. Dr. Nafiz ALEMDAROĞLU
(METU)
Prof. Dr. Fırat O. EDİS (ITU)
Prof. Dr. Kadir KIRKKÖPRÜ (ITU)
Prof. Dr. M. Fevzi ÜNAL (ITU)**

JUNE 2010

İSTANBUL TEKNİK ÜNİVERSİTESİ ★ FEN BİLİMLERİ ENSTİTÜSÜ

**DAİMİ AKIŞ İÇİNDE SALINIM YAPAN BİR KANAT ETRAFINDAKİ
AKIŞ YAPILARININ DENEYSEL İNCELENMESİ**

**DOKTORA TEZİ
İdil FENERCİOĞLU
(511022003)**

Tezin Enstitüye Verildiği Tarih : 05 Şubat 2010

Tezin Savunulduğu Tarih : 11 Haziran 2010

**Tez Danışmanı : Doç. Dr. N. L. Okşan ÇETİNER-
YILDIRIM (İTÜ)**
**Diğer Jüri Üyeleri : Prof. Dr. Nafiz ALEMDAROĞLU
(ODTÜ)
Prof. Dr. Fırat O. EDİS (İTÜ)
Prof. Dr. Kadir KIRKKÖPRÜ (İTÜ)
Prof. Dr. M. Fevzi ÜNAL (İTÜ)**

HAZİRAN 2010

FOREWORD

The road to PhD thesis is believed to be paved with many distractions, and this present study was not an exception. I would like to express my sincere appreciations to my advisor Assoc. Prof. Dr. Okşan Çetiner-Yıldırım, for being my tutor and mentor on this road. She has been a source of knowledge, inspiration, and guidance in both my academic and everyday life crises.

For all the former and present members of the Trisonic Lab family, I feel lucky being able to meet you and it has been a real joy to work together with all of you. I would especially like to express my thanks to Asst. Prof. Dr. K. Bülent Yüceil for his support and encouragement even from far away, Asst. Prof. Dr. Duygu Erdem for her sincerest friendship, Asst. Prof. Dr. Hayri Acar for his creative helpfulness and Banu Yücel who had been a great helper on my chores during the last few months.

I would also like to thank our technicians Aliosman Tabanlı and Murat Tarhan for all their help with model manufacturing and with the problems which arose during the experiments.

I would like to express my gratefulness to Berk Zaloğlu for his kindness and eagerness to help whenever I struggled with the servo motors' motion control.

I would also like to thank Prof. Dr. Fırat O. Edis and other members of the examining committee for their valuable input on this study.

Mustafa Perçin could not be left without credit. He made my data-post-processing-life simpler and thus deserves all the cakes he asked for each and every Matlab script and CleanVec modification. Tufan Aydın was the one to modify the image stitching script for the ways of my usage. I thank them both.

Dear mother and dear li'l sis Mina, you always encouraged me on this path and it has always been a relief to feel the support of my whole family; thank you all.

And, Gökhan, my precious, thank you, not only for the proofreading but for just being there whenever I needed, always and forever.

June 2010

İdil FENERCİOĞLU

TABLE OF CONTENTS

	<u>Page</u>
ABBREVIATIONS	ix
LIST OF TABLES	xi
LIST OF FIGURES	xiii
SUMMARY	xvii
ÖZET	xix
1. INTRODUCTION	1
1.1 Purpose of the Thesis.....	2
1.2 Background.....	3
1.2.1 Flapping motion in nature and its applications	5
1.3 Summary of Significant Parameters	13
1.4 Literature Review	15
1.4.1 Plunging motion.....	15
1.4.2 Pitching motion	22
1.4.3 Combined pitching and plunging motion.....	35
1.5 Practical Applications.....	48
1.6 Overview of Unresolved Issues.....	56
1.7 Objectives of the Study.....	57
1.8 Outline of Dissertation.....	58
2. EXPERIMENTAL SYSTEMS AND TECHNIQUES	59
2.1 Flow System	59
2.2 Model and Mounting	60
2.3 Airfoil Motion.....	61
2.4 Image Acquisition.....	62
2.5 Post-Processing.....	64
2.6 Thrust Estimation from DPIV Data.....	65
3. RESULTS	71
3.1 Parameter Space	71
3.2 Categorization Based on Flow Structures	73
3.2.1 Category A1	76
3.2.2 Category A2	83
3.2.3 Category B	88
3.2.4 Category C	94
3.2.5 Category D	100
3.2.6 Category E	110
3.3 Summary of Categories Based on Flow Structures and Their Occurrence on Parameter Space.....	115
3.4 The Variation of Force Coefficients and Efficiencies	121
3.5 Three-Dimensionality	132
3.6 Phase Angle Effects.....	137
3.7 Effect of Mean Angle of Attack and Pitch Amplitude	142
3.8 Effect of Unequal Frequency.....	149

4. CONCLUDING REMARKS	157
4.1 Summary of Major Contributions.....	157
4.2 Recommendations for Further Study	158
REFERENCES	161
APPENDICES	171
APPENDIX A.1 Schematic of the Water Channel	173
APPENDIX A.2 List of Experimental Cases	175
APPENDIX A.3 Derivation of the Theoretical Efficiency	179
CURRICULUM VITAE.....	183

ABBREVIATIONS

α_{amp}	: Pitch amplitude
α_{eff}	: Effective angle of attack of the airfoil
η	: Propulsive efficiency
ν	: Kinematic viscosity
ρ	: Density
ψ	: Phase angle between pitch and plunge motions
ω	: Vorticity
A	: Wake width
c	: Airfoil chord
C_d	: Drag coefficient
C_f	: Thrust coefficient based on the planform area
C_T	: Thrust coefficient based on the area swept by the wing
f_1	: Oscillation frequency of plunging motion
f_2	: Oscillation frequency of pitching motion
h_{amp}	: Plunge amplitude
k	: Reduced frequency
Re	: Reynolds number based on the airfoil chord
s	: Airfoil span
St	: Strouhal number
T	: Period of the sinusoidal pitch and plunge motion
T	: Thrust
U_∞	: Freestream velocity

LIST OF TABLES

	<u>Page</u>
Table 1.1: Summary of recent studies on pitching and plunging foils.....	45
Table 2.1: The image sizes before and after the stitching process.....	64
Table 2.2: The thrust coefficient for selected cases	68
Table 2.3: The thrust coefficient comparison with Anderson’s (1996) study.....	69
Table 3.1: The parameter space for the base investigation cases.....	72
Table 3.2: Categorization of the investigated cases based on flow structures	77
Table 3.3: Summary of categories based on flow structures	117
Table 3.4: The Force Coefficients.....	123
Table 3.5: Velocity deficit profiles ($u-U_\infty$) in the near wake	124
Table 3.6: Force coefficients and efficiencies given on the parameter space.....	128
Table 3.7: For all categories, velocity deficit profiles ($u-U_\infty$) in the near wake for different phase angles.....	141
Table 3.8: For all categories, thrust coefficient and efficiency values for different phase angles	142
Table 3.9: For all categories, velocity deficit profiles ($u-U_\infty$) in the near wake	146
Table 3.10 : For all categories, force coefficient and efficiency values for varied mean angle of attack and pitch amplitude values.....	147
Table 3.11 : Values of pitch and plunge frequencies and corresponding Strouhal numbers for the cases shown in Figure 3.47.....	149

LIST OF FIGURES

	<u>Page</u>
Figure 1.1 : Reynolds number range for flight vehicles	7
Figure 1.2 : Wingspan versus mass for small unmanned flight vehicles.....	8
Figure 1.3 : The Great Flight Diagram.....	9
Figure 1.4 : Reynolds number corresponding to Strouhal number of observed fish and cetaceans.....	11
Figure 1.5 : Strouhal number for 42 species of fish, birds, bats and insects in cruising flight and swimming.	11
Figure 1.6 : Existing general aerodynamic knowledge database in terms of reduced frequency and Reynolds number.....	12
Figure 1.7 : Pitch and plunge displacement definitions.....	13
Figure 1.8 : Knoller-Betz effect illustrating thrust production by a plunging airfoil	15
Figure 1.9 : Karman vortex street indicative of drag	16
Figure 1.10 : Computed vortical wake due to sinusoidal plunging motion (a) $k = 0.5$, (b) $k = 1.0$	16
Figure 1.11 : Vortex street indicative of zero drag	17
Figure 1.12 : Reverse Karman vortex street indicative of thrust	17
Figure 1.13 : Deflected vortex street indicative of thrust and lift	18
Figure 1.14 : Transition from normal to reverse Karman vortex street with increasing kh	19
Figure 1.15 : Effect of laminar separation bubble on pressure distribution.....	23
Figure 1.16 : Instability and transition in a laminar separation bubble with a sketch of time averaged streamlines	23
Figure 1.17 : Dynamic stall events on a NACA-0012 airfoil	25
Figure 1.18 : Sketches of flow fields during dynamic stall; a) Light stall, b) Deep stall.....	28
Figure 1.19 : a-d) Successive body positions for swimming in thunniform mode, e) Diagram of the paths of caudal fin.	36
Figure 1.20 : Angle of attack traces through a wing-beat for a flapping animal	36
Figure 1.21 : Effective vs. geometric angle of attack	38
Figure 1.22 : The Insectothopter	48
Figure 1.23 : The MicroBat prototypes.....	49
Figure 1.24 : The Mentor	49
Figure 1.25 : The Flapper	50
Figure 1.26 : The NAV demonstrator vehicle.....	50
Figure 1.27 : The NanoSCOUT	50
Figure 1.28 : The MAV of Cornell University	51
Figure 1.29 : The Entomopter	51
Figure 1.30 : DelFly-II.....	52
Figure 1.31 : DelFly-Micro.....	52
Figure 1.32 : BITE-Wing.....	53

Figure 1.33 : NPS flapping wing MAV	54
Figure 1.34 : The Stingray	54
Figure 1.35 : The bioSTREAM.....	55
Figure 1.36 : The stroke-wing engine HFG3	55
Figure 2.1 : Experimental arrangement.....	61
Figure 2.2 : Experimental arrangement for three-dimensionality investigations.....	63
Figure 2.3 : Image areas of the cameras at two locations	64
Figure 2.4 : Control volume for momentum analysis	66
Figure 3.1 : Template for figures showing instantaneous vorticity patterns.....	75
Figure 3.2 : Instantaneous vorticity patterns around the airfoil Case-15 (Category A1).....	79
Figure 3.3 : Instantaneous vorticity patterns in the near-wake of the airfoil Case-15 (Category A1).....	80
Figure 3.4 : Time-resolved vorticity patterns around the airfoil for Case-15	82
Figure 3.5 : a) and b) Averaged velocity and averaged vorticity plots, c) airfoil in motion, d) variation of effective angle of attack for Case-15	83
Figure 3.6 : Instantaneous vorticity patterns around the airfoil Case-40 (Category A2)	84
Figure 3.7 : Instantaneous vorticity patterns in the near-wake of the airfoil Case-40 (Category A2).....	85
Figure 3.8 : Time-resolved vorticity patterns around the airfoil for Case-40	86
Figure 3.9 : a) and b) Averaged velocity and averaged vorticity plots, c) airfoil in motion, d) variation of effective angle of attack for Case-40	87
Figure 3.10 : Instantaneous vorticity patterns around the airfoil Case-43 (Category B2)	90
Figure 3.11 : Instantaneous vorticity patterns in the near-wake of the airfoil Case-43 (Category B2)	91
Figure 3.12 : a) and b) Averaged velocity and averaged vorticity plots, c) airfoil in motion, d) variation of effective angle of attack for Case-43	92
Figure 3.13 : a) and b) Averaged velocity and averaged vorticity plots, c) airfoil in motion, d) variation of effective angle of attack for Case-18	93
Figure 3.14 : Instantaneous vorticity patterns in the near-wake of the airfoil Case-18 (Category B1)	95
Figure 3.15 : Instantaneous vorticity patterns around the airfoil Case-44(Category C)	96
Figure 3.16 : Instantaneous vorticity patterns in the near-wake of the airfoil Case-44 (Category C)	98
Figure 3.17 : a) and b) Averaged velocity and averaged vorticity plots, c) airfoil in motion, d) variation of effective angle of attack for Case-44	99
Figure 3.18 : Instantaneous vorticity patterns in the near-wake of the airfoil and averaged vorticity plots for Case-37 (Category C).....	100
Figure 3.19 : Instantaneous vorticity patterns around the airfoil Case-45(Category D)	102
Figure 3.20 : Instantaneous vorticity patterns in the near-wake of the airfoil Case-45 (Category D)	103
Figure 3.21 : a) and b) Averaged velocity and averaged vorticity plots, c) airfoil in motion, d) variation of effective angle of attack for Case-45	104
Figure 3.22 : Instantaneous vorticity patterns in the near-wake of the airfoil Case-19 (Category D)	106

Figure 3.23 : a) Averaged velocity and b) averaged vorticity plots, c) airfoil in motion, d) variation of effective angle of attack for Case-19.....	107
Figure 3.24 : Instantaneous vorticity patterns around the airfoil for Case-31 (Category cD)	108
Figure 3.25 : Instantaneous vorticity patterns in the near-wake of the airfoil Case-31 (Category cD)	109
Figure 3.26 : a) and b) Averaged velocity and averaged vorticity plots, c) airfoil in motion, d) variation of effective angle of attack for Case-31.....	110
Figure 3.27 : Instantaneous vorticity patterns around the airfoil Case-14 (Category E)	112
Figure 3.28 : Instantaneous vorticity patterns in the near-wake of the airfoil Case-14 (Category E)	113
Figure 3.29 : a) and b) Averaged velocity and averaged vorticity plots, c) airfoil in motion, d)variation of effective angle of attack for Case-14 (Category E)	114
Figure 3.30 : a) and b) Averaged velocity and averaged vorticity plots, c) airfoil in motion, d)variation of effective angle of attack for Case-33(Category E)	115
Figure 3.31 : The occurrence of flow structures on St vs h_{amp}/c plot.....	116
Figure 3.32 : The occurrence of flow structures on k vs h_{amp}/c plot.....	119
Figure 3.33 : The occurrence of flow structures on Re vs h_{amp}/c plot.....	119
Figure 3.34 : The flow categories on St vs α_{eff} plot.....	120
Figure 3.35 : The parameter space for α_{eff} in terms of a) St , b) Re and c) k	121
Figure 3.36 : The variation of the thrust coefficient based on the planform area of the wing, C_T , with respect to a) St , b) Re and c) k	129
Figure 3.37 : The variation of the thrust coefficient based on the area swept by the wing, C_T , with respect to a) St , b) Re and c) k	130
Figure 3.38 : The variation of the efficiency, η , with respect to a) St , b) Re and c) k	131
Figure 3.39: For all categories, instantaneous vorticity patterns on the side and end view planes and averaged flow field on the end view plane.....	133
Figure 3.40: Instantaneous vorticity patterns on the end view plane Case-44 (Category C).....	135
Figure 3.41: Selected instantaneous vorticity patterns on the side and end view planes for category C and D.....	136
Figure 3.42: Selected instantaneous vorticity patterns on the side and end view planes for category E.....	136
Figure 3.43: For all categories, instantaneous vorticity patterns on the near wake for different phase angles.....	138
Figure 3.44: For all categories, averaged vorticity patterns for different phase angles	139
Figure 3.45: For all categories, averaged vorticity profiles for varied angle of attack and pitch amplitude values	144
Figure 3.46: The flow categories on St vs α_{eff} plot for different mean angle of attack and pitch amplitude values.....	148
Figure 3.47: For all categories, averaged vorticity patterns for unequal frequencies	150
Figure 3.48: Instantaneous vorticity patterns in the near-wake of the airfoil Case-121 (Category A1).....	154
Figure A.1: a) 3D view, b) top view, c) side view of the water channel.	173

EXPERIMENTAL INVESTIGATION OF FLOW STRUCTURES AROUND AN OSCILLATING AIRFOIL IN STEADY CURRENT

SUMMARY

Thrust generation and locomotion mechanisms of flying and swimming animals attract increasing attention due to the possible application areas of aerial and aquatic propulsion systems. Understanding how natural fliers and swimmers utilize and control the unsteady aerodynamic phenomena to enhance their capabilities may improve the design and development of engineered systems that take advantage of similar unsteady aerodynamic mechanisms. Currently, many research projects advance in air and water vehicles using flapping wing systems. Oscillating wing designs have also been considered for applications of mechanical power generators.

Biological inspiration offers a means to enhance the performance of the next generation of small-scale air vehicles over existing fixed and rotary wing systems. Micro air vehicles (MAVs) with wing spans of 15 cm or less are of interest for military and civilian applications. Employing the unsteady mechanisms of flapping and flexible wings might overcome the unfavorable aerodynamic conditions. Gaining a better understanding of the wing motions and flow conditions which initiate the leading and trailing edge vortex separations will aid in developing lighter MAVs with improved maneuvering capabilities.

The primary interest of this PhD thesis is to investigate the flow structures around and in the near wake of an oscillating airfoil at a low Reynolds number range which is typical of small birds and potential MAVs. An experimental study is conducted in steady water flow with a SD7003 airfoil profile which undergoes combined pitching and plunging oscillations with a phase difference between the two motions. The vortex formation is characterized using Digital Particle Imaging Velocimetry (DPIV) technique allowing detailed quantitative evolution at various Reynolds numbers. The role of separated vortex structures from the leading and trailing edges and their interactions with each other are explored to determine their contribution to the aerodynamic forces.

The relationships between wake structures and the various non-dimensional parameters are used to categorize the problem to determine the mechanisms of drag or thrust generation and the prediction of force coefficients from time dependent velocity profiles. The main parameters of the study are the freestream velocity, the frequency of pitch and plunge motions, the amplitude of plunging, the mean angle of attack, the amplitude of pitching and the phase in between two sinusoidal motions.

A detailed flow structure categorization has been carried out, identifying five flow structure categories and their occurrence on different two-dimensional parameter space. The vorticity patterns of the flow structure categories are related to the loading on the airfoil and the variation of thrust with respect to different non-dimensional parameters has been discussed. This study presents the independency on the Reynolds number in the range investigated.

The current study is probably the first to mention the formation of a deflected wake for combined pitch and plunge motions. As opposed to what is observed in pure plunge motion, it is found to be consistent and does not alternate between up and down modes. In accordance with previous studies on pure plunge motion, the deflection angle increases as the Strouhal number increases.

The effect of phase angle between pitch and plunge motions, effect of mean angle of attack and pitching amplitude, effect of use of unequal oscillating frequencies for pitch and plunge motions and three-dimensionality in the near-wake of the nominally two-dimensional wing are also considered in the scope of this study.

SABİT AKIMDA TİTREŞEN BİR KANAT ETRAFINDAKİ AKIM YAPILARININ DENEYSEL İNCELENMESİ

ÖZET

Uçabilen kanatlı canlıların ve yüzebilen su canlılarının hareket yetenekleri ve hareketlerini sürdürebilmek için yaratabildikleri itki kuvveti, bu tür hareket mekanizmalarının havacılıkta ve suda kullanılabilecek tahrik sistemleri uygulama olanakları açısından gittikçe artan bir ilgi çekmektedir. Doğal uçabilme veya yüzebilmeye yeteneğine sahip canlıların daimi olmayan aerodinamik olguları kullanım ve kontrol yöntemlerinin anlaşılması, benzer yöntemlerden yararlanan mühendislik uygulamalarının tasarımını ve geliştirilmesini sağlayacaktır. Çırpan kanat sistemlerini uygulanmasına yönelik hava ve su aracı tasarımı ile ilgili bir çok proje sürdürülmektedir.

Biyolojik esinlenme, kullanılmakta olan sabit ve döner kanatlı küçük-boyutlu hava araçlarının performansını arttırmada gelecek vaad etmektedir. Kanat açıklığı 15 cm veya daha az olan mikro hava araçları (MHA) askeri ve sivil uygulamalar açısından önem arz etmektedir. Çırpan ve esnek kanatlar etrafında oluşan daimi olmayan akım şartlarının kullanılması ile istenmeyen aerodinamik koşulların giderilmesinde katkı sağlanacağı düşünülmektedir. Hücum ve firar kenarlarından girdap kopmasına sebebiyet veren akım şartlarının daha iyi anlaşılması, manevra kabiliyeti iyileştirilmiş, daha hafif MHAların geliştirilmesine yardımcı olacaktır.

Bu doktora tezinin ilgi alanı, küçük kuşlar ve muhtemel MHAlar tarafından kullanılan düşük Reynolds sayısı aralığında çırpan bir kanat profili etrafında oluşan akım yapılarının incelenmesidir. Sabit su akışında, aralarında belli bir faz farkı olan yunuslama ve akıma dik yönde öteleme hareketlerini eş zamanlı olarak yapan bir SD7003 kanat profili kullanarak deneysel bir çalışma yapılmıştır. Çeşitli Reynolds sayılarında girdap oluşumlarının niteliksel gelişimleri Dijital Parçacık Görüntüleme Hızölçeri (DPIV-Digital Particle Imaging Velocimetry) yöntemi ile görüntülenmiştir. Hücum ve firar kenarlarından ayrılan girdaplar ve bunların birbirleriyle etkileşimlerinin aerodinamik kuvvetlere olan etkileri incelenmiştir. İz bölgesindeki akım yapılarının, yunuslama ve ötelenme hareketlerinin frekansları, genlikleri ve aralarındaki faz açısı gibi osilasyon parametreleri ile bağıntıları incelenerek sürüklenme veya itki yaratma mekanizmalarının belirlenmesine ve kuvvet katsayılarının zamana bağlı hız profillerinden tayin edilmesine çalışılmıştır.

Çalışmada problemi sınıflandırmak üzere kullanılan boyutsuz parametreler, serbest akım hızı, yunuslama ve ötelenme hareketlerinin frekansı, ötelenme hareketinin genliği, ortalama hücum açısı, yunuslama hareketinin genliği ve bu iki sinüsoidal hareket arasındaki faz farkıdır.

İki boyutlu akım alanlarının incelenmesi sonucu, akım yapısı şekilleri beş farklı kategoriye ayrılmış ve bu kategorilerin oluşum bölgeleri değişik iki boyutlu parametre düzlemlerinde belirlenmiştir. Akım yapıları kategorileri ile kanada etki eden kuvvetler arasındaki bağıntı kurulmuş ve itki kuvveti değişiminin çeşitli boyutsuz parametre ile değişimi incelenmiştir.

Yapılmış olan bu çalışma, eş zamanlı yunuslama ve ötelenme hareketleri ile yapılan deneysel çalışmalar arasında iz bölgesindeki akım yapılarının doğrusal eksenden saptığını muhtemelen ilk kez gösteren çalışmadır. Yalnızca ötelenme hareketi ile yapılan çalışmaların tersine, akım yapılarındaki bu eğim yukarı veya aşağı hareket esnasında değişimli olarak gerçekleşmemekte ve tutarlı bir karakter sergilemektedir. Ötelenme hareketi ile yapılan çalışmalara benzer şekilde akım yapılarının eğimi Strouhal sayısı arttıkça artmaktadır.

Akım yapıları kategorizasyonu ve itki oluşumunda yunuslama ve ötelenme hareketleri arasındaki faz açısının etkisi, ortalama hücum açısı ve yunuslama genliğinin etkisi, yunuslama ve ötelenme frekanslarının farklı olmasının etkisi ile iki-boyutlu kanadın yarattığı yakın iz bölgesindeki üç-boyutluluk da bu çalışma kapsamında incelenmiş ve değerlendirilmiştir.

1 INTRODUCTION

“Humans fly commercially or recreationally, but animals fly professionally.”

McMasters and Henderson, 1980

Despite the significant progress in technology for flight machines over the past century, it still is not possible to attain the endurance and agility of nature’s flyers, which have evolved over millions of years.

Mankind has been fascinated by the flying animals since early ages. The idea of constructing wings to imitate flight of birds dates back to ancient Greek mythology about the inventor and master craftsman Daedalus who built wings from feathers for himself and his son Icarus, attempting an escape from imprisonment by flight. Leonardo da Vinci had some of the earliest ideas on flight and was one of the first individuals interested in a practical solution. In the 15th century, he studied the flight of birds as well as their structure, designed and drew detailed plans for a large number of mechanical flight machines such as a human-powered ornithopter.

Millions of years of evolution of bird, bat and insect wings let those animals to become airborne in powered flight. The basic mechanisms of animal locomotion still continue to impress scientists and engineers and a considerable amount of advancement has been made in understanding some aspects how flapping and swimming animals produce avian and aquatic propulsion and maneuvering forces. Interest in biomimetic studies are increasing rapidly since many of the functions and details of flapping wings are yet to be explored.

The propulsive energy of flapping motion led investigations towards the study of oscillating airfoils and related unsteady flow structure interaction problems. Unsteady aerodynamics in low Reynolds number ranges is a significant research area considering the practical applications related to Micro Air Vehicles (MAVs) as well as the newly proposed wind / hydro-power generators as a possible renewable energy source option.

MAVs are small unmanned aerial vehicles with length scales similar to small birds and insects. The definition employed in the United States Defense Advanced Research Projects Agency (DARPA)'s MAV program limits the physical size to less than 15 cm , which puts this class of vehicles at least an order of magnitude smaller than any missionized UAV developed to date (McMichael and Francis, 1997). Although potential military use is one of the driving factors, MAVs can be used in reconnaissance, surveillance, scouting, targeting, biochemical sensing and remote observation of hazardous environments which are inaccessible to ground vehicles. Apart from the possible MAV applications, flapping motion is also considered for new and innovative design concepts of using wind and marine energy as a power source; jet-stream powered airborne wind turbines and tidal energy extraction are already in progress.

1.1 Purpose of the Thesis

Flying animals flap their flexible wings to improve their aerodynamic performance by effectively increasing the Reynolds number seen by the wings without increasing their forward speed. The flight characteristics and wing shape deformations of insects are different from small birds, which also differ from big birds that are able to glide and soar. The focus in this PhD study is on a pitching and plunging two-dimensional airfoil in presence of a steady flow in the low range of potential micro air vehicles, simulating the flapping wings of small birds in forward flight. The relationship between the oscillation parameters and the formation of vortical structures around and behind the airfoil profile is investigated experimentally via Digital Particle Image Velocimetry (DPIV). The main objectives of this study are to quantify and visualize the vortical structures, separation on the surface of the airfoil, and to determine the near-wake vorticity patterns and time dependent velocity profiles in order to be able to comment on the thrust or drag indication.

Although it may seem more appropriate to use the term ‘foil’ since the experiments are conducted in a water channel, the SD7003 profile model will be named as ‘airfoil’ throughout this study due to practical applications of MAVs.

1.2 Background

Humans' earliest aspiration to fly was inspired by birds, leading to the assumption that flapping wings are mandatory for propulsion and lift. In the early 1800s, Sir George Cayley thought that flapping was not a necessity for successful flight and proposed that it would be simpler to study steady, outstretched gliding wings of a soaring bird such as a gull. His experiments with various wing sections led him to develop an efficient cambered airfoil and he identified the four vector forces that influence an aircraft: thrust, lift, drag, and gravity. He realized that air flowing over the top of a curved, fixed wing will create lift, the upward force that opposes the pull of gravity. After Cayley's observations, imitation of nature has become less appealing for mechanical flight. Following Cayley's experiences, in the 1890s Otto Lilienthal became the first to construct various gliders and to make repeated successful flights. Lilienthal's work was credited as a major inspiration to Wright Brothers who successfully flew the first propeller driven plane in 1903. Ever since, the flapping wing aircraft concept is regarded as unpromising for further development and the traditional aerodynamic theory is founded on fixed wing airplanes, leaving the most consistent research in flapping wing flight among biologists and zoologists until towards the end of the twentieth century.

Recently, the idea of thrust generation of flapping wings has been revived by many researchers with the renewed interest in micro air vehicles (MAVs), the motivation being that unsteady aerodynamic features of small scale flapping wing flight may provide unique advantages over fixed wing designs. Thus the flapping wing research mainly focuses on understanding of unsteady flow aerodynamics resulting from wing motion. The primary interest is to understand and quantify how the separated flow in the form of vortices works to enhance lift, thrust and their efficiency.

In their independent studies, Knoller (1909) and Betz (1912) observed that a flapping wing generates an effective angle of attack, resulting in an aerodynamic force that includes both cross-stream (lift) and streamwise (thrust) components. Katzmayer (1922) was the first to experimentally verify the Knoller–Betz effect by placing a stationary airfoil into an oscillating flow field. He observed the average thrust and confirmed drag reduction with a slight increase in the lift by repeated measurements.

The same year, Prandtl (1922) proposed that, for incompressible flow past an oscillating airfoil, every change in lift must be accompanied by the detachment of a vortex from the airfoil's trailing edge, consistent with the Kelvin's theorem. Birnbaum (1924) developed a solution for inviscid incompressible flow past an oscillating airfoil. He identified the conditions that led to flutter or to thrust generation and suggested the use of a sinusoidally flapping wing as an alternative to the conventional propeller. Birnbaum introduced an important similarity parameter that he named the reduced frequency, which was the ratio between the flapping velocity and forward flight velocity.

Kramer (1932) used the same type of experimental arrangement with Katzmayer to create vertical gust to measure the behavior of airfoils at rapidly increased angle of attack variations. He showed that maximum lift coefficient increases proportionally with the increasing rate of change in angle of attack.

In 1935 von Kármán and Burgers presented an explanation of drag or thrust production depending on the location and orientation of the wake vortices and showed that the thrust indicative wakes are composed of alternately shed vortices with reversed rotational direction of a regular Karman vortex street, creating a velocity excess. This allowed Garrick (1936) to use this approach for the prediction of thrust and propulsive efficiency of harmonically plunging or pitching airfoils. Garrick applied Theodorsen's (1934) inviscid, incompressible, oscillatory flat-plate theory to determine the thrust force and showed that airfoils with plunging motion generate thrust at all frequencies but pure pitching motion can generate thrust only above a critical frequency and he also explained that thrust generation is a function of the pivot location.

In low Reynolds number aerodynamic studies, the phenomena of the generation and the effects of a laminar separation bubble (LSB) is examined in detail by many researchers. First documented experimental observation of LSB was reported by Jones (1938). The dynamics of a LSB depends on the value of the Reynolds number, pressure distribution, geometry, surface roughness and the freestream turbulence. For a fixed Reynolds number, varying the angle of attack changes the LSB (Shyy et al., 2008).

McCroskey et al. (1976) experimentally studied different types of stall conditions by varying the leading edge geometry and commented that dynamic stall did not originate from bursting of the laminar separation bubble but from a breakdown of the turbulent boundary layer. They also mentioned that the main difference between static and dynamic stall is the vortex shedding phenomenon on oscillating airfoils and lift is generated through dynamic stall. In his review McCroskey (1982) stated that the role of unsteady effects is an important flow problem and the studies on the subject were motivated by efforts to avoid or reduce undesirable consequences as flutter, vibrations, gust response and dynamic stall with potentially beneficial outcomes as propulsive efficiency of flapping motion, controlled periodic vortex generation, stall delay and improved performance.

Freymuth (1988) presented flow visualizations of the wakes shed by pure plunging and pure pitching airfoils for a time sequence of flapping motion to document basic propulsive vortical signatures and their generation. Koochesfahani (1989) also performed dye flow visualizations and Laser Doppler Velocimetry measurements of the wake flow characteristics for an airfoil pitching at small amplitudes and confirmed Garrick's earlier prediction of thrust generation of pitching airfoil and showed that the wake transforms into a jet-like flow above a certain critical reduced frequency which depends on the oscillation amplitude. He also showed that the structure of the wake can be controlled by adjusting the frequency, amplitude and the shape of oscillation wave form. The typical jet-like flow structures were also captured by Lai and Platzer (1999).

In the next section, recent investigations on flapping motion will be discussed.

1.2.1 Flapping motion in nature and its applications

Most animals, of the 1.4 million currently described and named species, can fly and near a million of them are flying insects. Of the living 13,000 warm-blooded vertebrate species, 9,000 types of birds and 1,000 types of bats flap their wings to generate propulsion in the skies (Shyy et al., 2008). Flapping wings for flying and oscillating fins for swimming stand out as one of the most complex yet widespread propulsion and locomotion methods found in nature.

Insects are the first species to evolve flying abilities and they stay unique in performance and maneuvering capabilities. Measurements of instantaneous lift forces

of insect wings show qualitative and quantitative differences with those calculated by conventional aerodynamic theories (Ellington et al., 1996). When insect wings are placed in a wind tunnel and tested over the range of air velocities that they encounter, the measured forces are substantially smaller than those required for active flight (Dickinson et al., 1999).

The failure of conventional steady-state theory has prompted the search for unsteady mechanisms that might explain the high forces produced by flapping wings. Different species of flying and swimming animals display different patterns of wing motion and although a general solution representing the force production does not exist, recent studies using real and scaled models of insect or bird wings and fish suggest that mechanisms of delayed stall, rotational circulation and wake capture might explain how flying animals' wings generate such large forces. For instance, for an insect at high angles of attack, a leading edge vortex (LEV) forms over the wings and transiently generates circulatory forces. On flapping wings, the LEV is stabilized by the presence of axial flow and it increases the lift throughout the downstroke. Delayed stall occurs when the wings sweep through the air with a large angle of attack. In addition to contributing to the lift required to keep an insect aloft, rotational circulation and wake capture generate aerodynamic forces during stroke reversals, when the wings rapidly rotate and change direction, providing that the animal can modulate the direction and magnitude of flight forces during steering maneuvers (Dickinson et al., 1999).

Muijres et al. (2008) showed that the use of unsteady aerodynamic mechanisms in flapping flight is not limited to insects but is also used by larger and heavier animals. Using digital particle image velocimetry (DPIV), they showed that a stable leading edge vortex (LEV) is developed on top of the wing of a nectar-feeding bat and it is able to increase lift by as much as 40% during slow forward flight.

Recent efforts to design aircraft as small as possible for special, limited duration military and civil missions has motivated researchers to adapt some of the unique aerodynamic advantages of flapping wings to manmade small scale air vehicles. These either remotely piloted or autonomous small unmanned aerial vehicles (UAVs) can perform a large variety of missions including surveillance, communication relay links, ship decoys, detection of biological, chemical, or nuclear materials and reconnaissance support in natural disasters. The flapping wing studies

depend on the expectation that they may provide greater propulsive efficiencies at low Reynolds numbers than fixed wings. Requirements for a typical low-altitude small UAV include long flight duration at speeds between 20 and 100 km/h, cruise altitudes of 3 to 300 m, light weight, and all-weather capabilities. Although the definition of small UAVs is somewhat arbitrary, vehicles with wing spans less than approximately 6 m and masses less than 25 kg are usually considered in this category. Recent availability of very small sensors, video cameras and control hardware allow flying vehicles possible for limited missions. These vehicles are referred to as micro air vehicles (MAVs) and they have wing spans as small as 15 cm with a mass of around 80 g, which is similar to the size of small birds and bats. The combination of small length scale and low velocities results in a flight regime with low Reynolds numbers (Mueller and DeLaurier, 2003). Figure 1.1 shows the relationship between total mass and wing chord Reynolds number for a few examples of flyers.

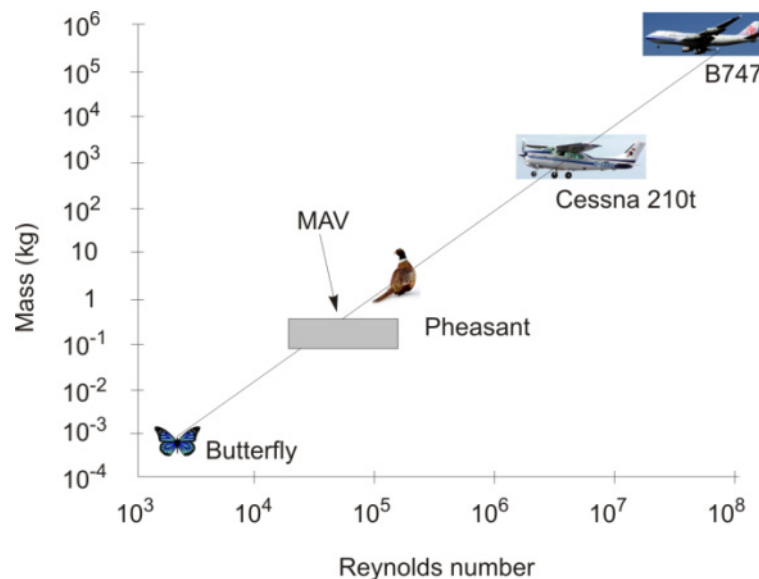


Figure 1.1 : Reynolds number range for flight vehicles (adopted from Mueller, 2001).

For a micro air vehicle, low Reynolds number flow regime of about $10^4 < Re < 10^5$ results in unfavorable aerodynamic conditions to support controlled flight and small physical dimensions results in certain favorable scaling characteristics including structural strength, reduced stall speed, and low inertia. Observations of biological flight vehicles show that wing motion and airfoil flexibility are key attributes for flight at low Reynolds numbers. The small size of MAVs corresponds in nature to small birds, which do not glide like large birds, but instead flap with considerable

change of wing shape during a single flapping cycle. By flapping their flexible wings, birds overcome the deteriorating aerodynamic performance under steady flow conditions by employing unsteady mechanisms (Shyy et al., 1999).

The small UAV regime, which also includes the MAVs, is well below conventional aircraft flight regime. These small UAVs are actually in a flow regime occupied by birds and model airplanes. The mass versus the wingspan for MAVs and UAVs, indicating the newly designed and developed vehicles, is given in Figure 1.2.

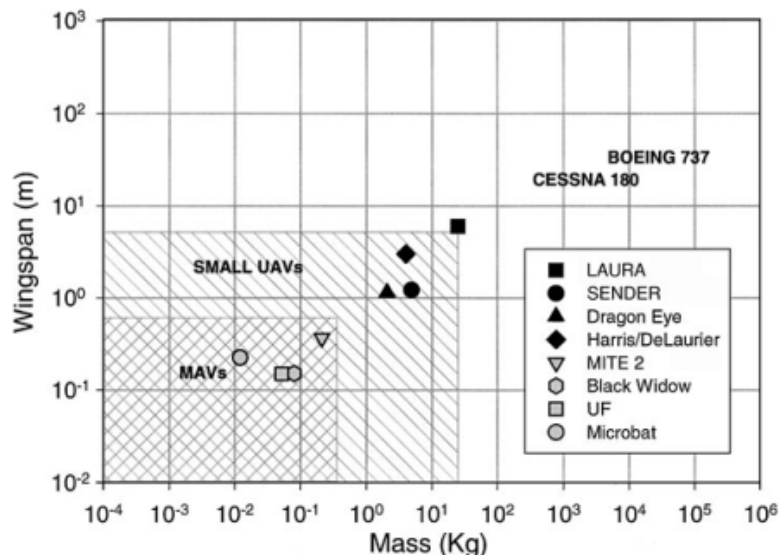


Figure 1.2 : Wingspan versus mass for small unmanned flight vehicles (adopted from Mueller and DeLaurier, 2003).

The Great Flight Diagram in Figure 1.3 gives a relation between wing loading, weight and cruising speed for flying animals and vehicles. The shaded region indicates the expanded parametric range surrounding the projected size, speed and weight for MAVs. The concept of geometric similarity can help relate different physical quantities via the dimensional argument. The assumption of geometric similarity among birds leads to insightful ways for correlating data (Shyy et al., 1999).

This vortex-dominated flow fields attract significant attention also in biohydrodynamics since there is a great need to understand the propulsion mechanisms of aquatic animals, as well as birds and insects. Hence the unsteady flows in low Reynolds number regions has been extensively investigated experimentally and numerically in recent years, with applications to flapping micro air vehicles, small unmanned aquatic vehicles and marine propulsion. The tails of

some of the fastest swimming animals closely resemble high aspect ratio foils (Triantafyllou et al., 2004).

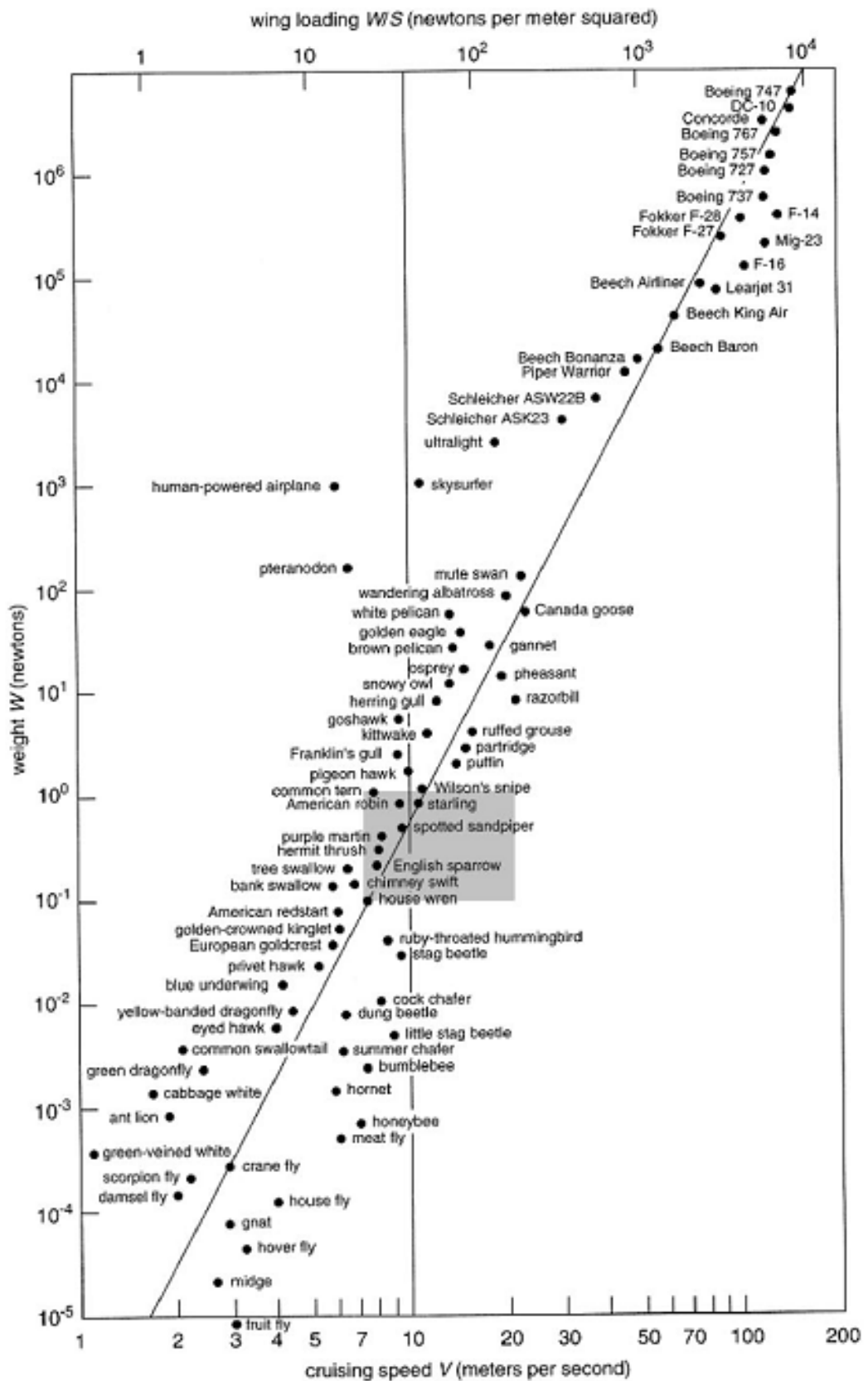


Figure 1.3 : The Great Flight Diagram (adopted from Shyy et al., 1999).

Biomimetic studies and observations from fish and cetaceans have provided some information on the kinematics of the flow, about how these animals employ their flapping tails and several fins to produce propulsive and maneuvering forces (Techet et al., 2003).

In flapping flight and swimming, one of the dimensionless parameters that govern the unsteady flow mechanisms is the Strouhal number (St) which describes the dynamic similarity characterizing the vortex dynamics and shedding behavior and the other is the reduced frequency (k) which characterizes the unsteady aerodynamics of pitching and plunging foils.

The observations of the flight and swimming of animals show that they are able to overcome the difficulties of low Reynolds number flow regimes and take advantage of the associated aerodynamic phenomena. Natural selection is likely to favor animals with high propulsive efficiency. During cruising, propulsive efficiency is more important whereas high aerodynamic force coefficient is more important in accelerations, slow locomotion or hovering. Strouhal number affects aerodynamic force coefficients and propulsive efficiency, since it defines the timescales associated with the growth and shedding of vortices, which are the sources of aerodynamic force production. In cruising flight or swimming, it is therefore predicted that animals are evolved for high efficiency over a narrow range of Strouhal number corresponding to a regime of vortex growth and shedding in which the propulsion peaks to maximum efficiency.

Figure 1.4 shows the Reynolds number corresponding to Strouhal number of observed fish and cetaceans swimming near their maximum observed speed. Birds, bats and insects also converge on the same narrow range of Strouhal number during their cruising conditions, as can be seen in Figure 1.5. Both figures confirm that most of the nature's swimmers and flyers operate at similar Strouhal number range, which seems to be a general principle of oscillatory lift based propulsion. Taylor et al. (2003) also showed that propulsive efficiency usually peaks within the interval $0.2 < St < 0.4$.

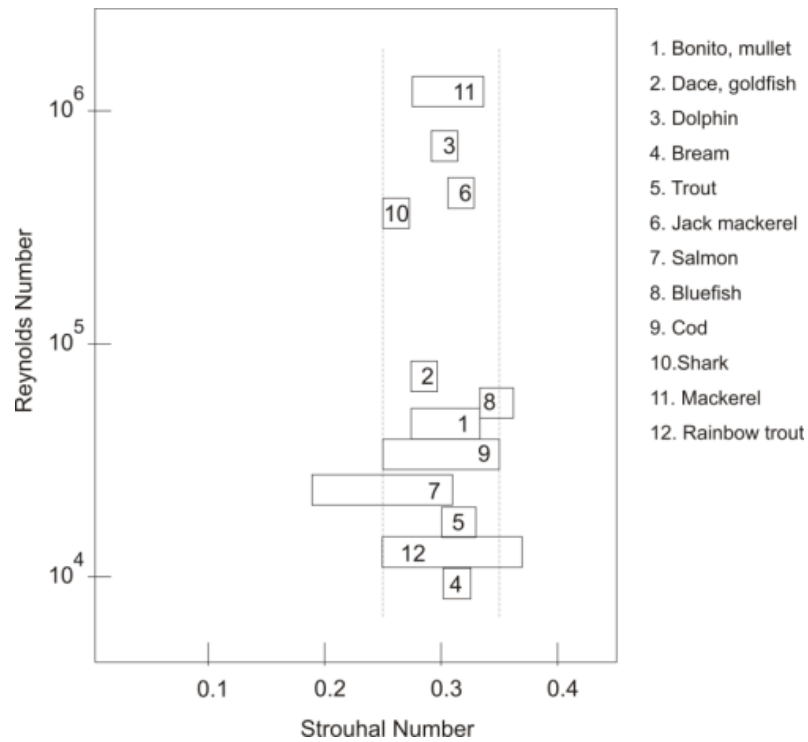


Figure 1.4 : Reynolds number corresponding to Strouhal number of observed fish and cetaceans (reproduced from Triantafyllou et al., 1992).

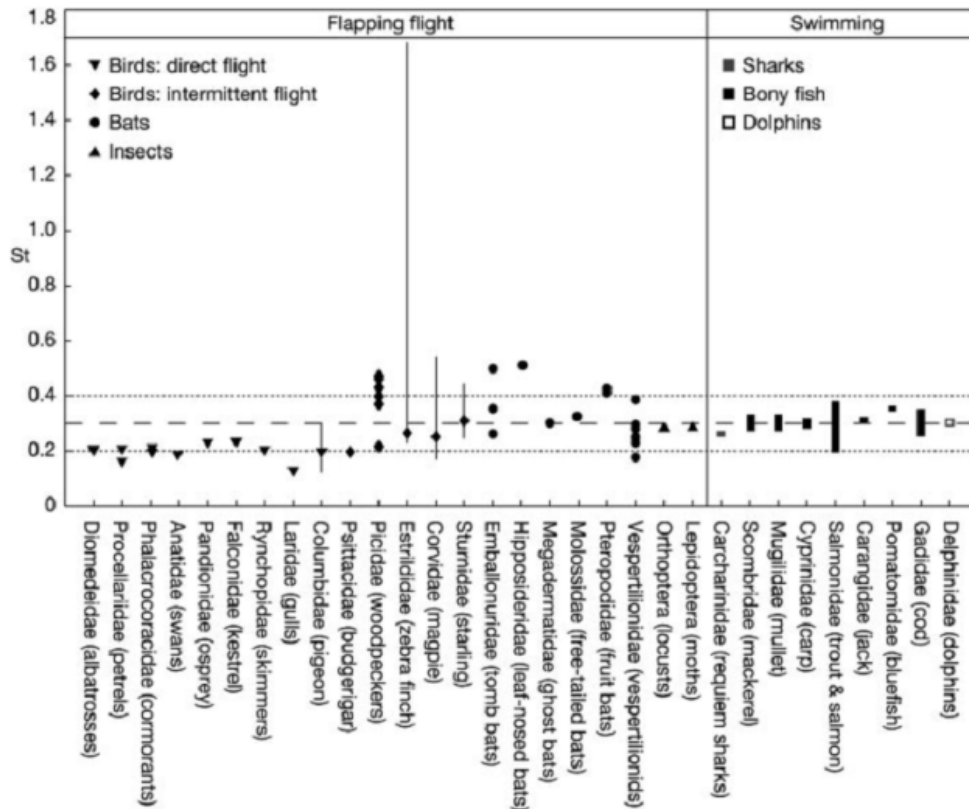


Figure 1.5 : Strouhal number for 42 species of fish, birds, bats and insects in cruising flight and swimming (adopted from Taylor et al., 2003).

Ames et al. (2001) conducted an experimental study with an objective to generate a basic experimental test case that could be used to connect and validate the results on unsteady aerodynamics over a wide range of Reynolds numbers. They state that although the aerodynamics of small-amplitude wing motion in the reduced frequency ranges $0 < k < 0.1$ is well understood for applications for large chord Reynolds numbers, many applications for autonomous flight vehicles in the atmospheres of earth and other planets occur at Reynolds number below 100,000 with some as low as 10,000. Figure 1.6 gives a graphical description of existing general aerodynamic knowledge database in terms of reduced frequency and Reynolds number.

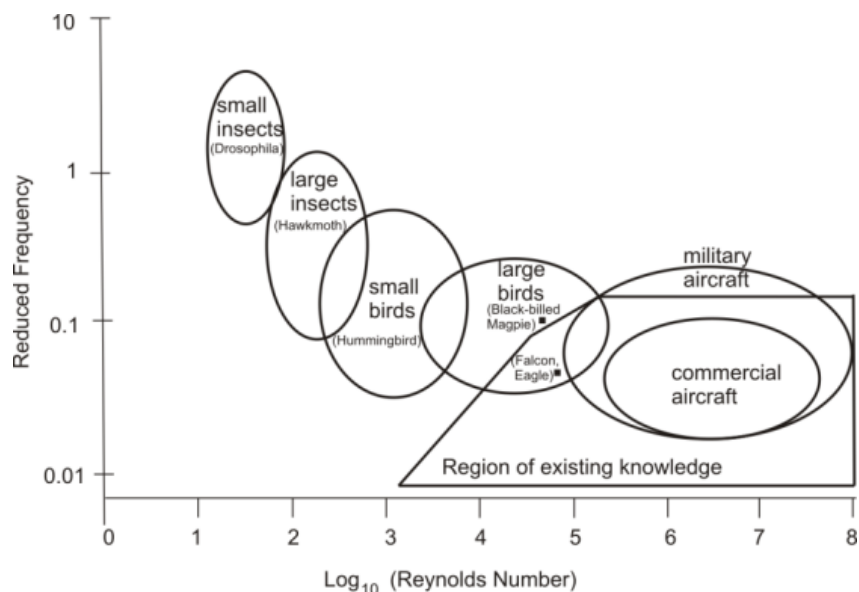


Figure 1.6 : Existing general aerodynamic knowledge database in terms of reduced frequency and Reynolds number (reproduced from Ames et al. 2001).

Several applications which require very small vehicles also require low flight speeds and high levels of unsteady motion caused by either gust or quick maneuvers. Vehicle designs in this range may benefit from the use of wings flapping with high amplitudes and frequencies. Traditional aircraft design using fixed wings attempts to ensure that flow stays attached to the airfoil at all times. In contrast, the natural mechanisms rely on vortices that separate from the trailing and leading edges, forming low pressure regions that may be used to create much higher lift and thrust than is possible with fixed wings (Young, 2005). Consequently, gaining better understanding of the relationships between flapping parameters and produced forces would aid in understanding the propulsion mechanisms of flapping and oscillating wings to design lighter, faster, durable and maneuverable micro air vehicles and more efficient renewable power sources.

1.3 Summary of Significant Parameters

The kinematic motions of the airfoil considered in the current study are sinusoidal plunging and pitching motions and they are described with the following equations:

$$h(t) = h_{amp} \cos(2\pi f_1 t + \psi) \quad (1.1)$$

$$\alpha(t) = \alpha_0 + \alpha_{amp} \cos(2\pi f_2 t) \quad (1.2)$$

where $h(t)$ is the linear plunge motion, transverse to the freestream velocity, $\alpha(t)$ is the angular pitch motion, and ψ is the phase angle between pitch and plunge. h_{amp} is the plunge amplitude, α_{amp} is the pitch amplitude and α_0 is the initial angle of attack. f_1 and f_2 are the oscillation frequencies for plunge and pitch motion respectively. Unless stated otherwise, pitching and plunging frequencies are taken as equal for most of the experimental cases in this study and represented by f .

Figure 1.7 provides an illustration of pitching and plunging motions for an airfoil with a mean angle of attack in a steady flow. The pivot point for pitching motion is at quarter-chord as depicted in the figure.

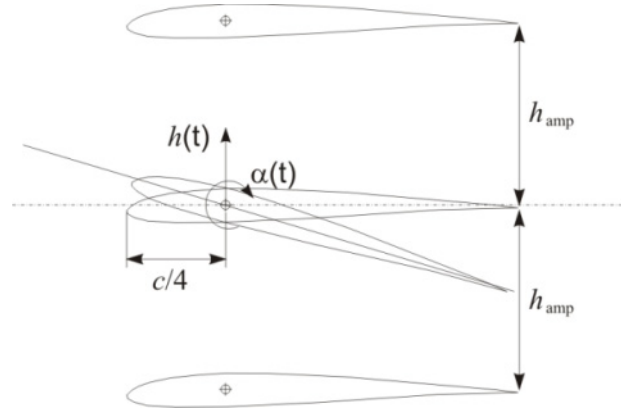


Figure 1.7 : Pitch and plunge displacement definitions.

The dimensionless parameter that characterizes the oscillation behavior was first introduced and named as the reduced frequency (k) by Birnbaum (1924). It is a measure of unsteadiness and defined as;

$$k = \frac{\omega c}{U_\infty} \quad (1.3)$$

where ω is the circular frequency, c is the chord length and U_∞ is the flow speed.

The amplitude of pitching and plunging are made dimensionless as;

$$\lambda = \frac{\alpha_{amp}}{2k \frac{h_{amp}}{c}} \quad (1.4)$$

Another important parameter characterizing the type of vortex shedding in the wake of a flapping airfoil is the Strouhal number (St). This dimensionless parameter contains both the frequency and amplitude of oscillation and defined as;

$$St = \frac{fA}{U_\infty} \quad (1.5)$$

where f is the flapping frequency, A is the peak-to-peak displacement of airfoil trailing edge (wake width). In this study, for simplicity and comparison purposes, Strouhal number values are calculated based on the displacement of the pivot point at quarter chord location.

Jones et al. (1996) has defined non-dimensional plunge velocity by the multiplication of the reduced frequency (k) and the non-dimensional plunging amplitude (h). The dimensionless plunge velocity (kh) has essentially the same meaning as Strouhal number, and it is commonly used in pure plunging airfoil studies. In studies where the airfoil undergoes combined pitching and plunging motion, Strouhal number and the reduced frequency are used sparingly.

The reduced frequency has been defined with slight differences for different studies in literature. In this study, the reduced frequency will be converted according to

$$k = \frac{\pi f c}{U_\infty} \quad (1.6)$$

During the plunging motion of an airfoil in a uniform flow, the airfoil is subjected to a resultant velocity vector which is at an angle with the chord line. This angle is known as the effective angle of attack. By using the vertical velocity of the airfoil due to the plunging motion which is calculated by taking the time derivative of Equation (1.1) as shown in Equation (1.7), the effective angle of attack, α_{eff} , for a pitching and plunging airfoil in steady current is obtained as shown in Equation (1.8).

$$\left(\dot{h}(t)\right) = -h_{amp}(2\pi f) \sin(2\pi f t + \psi) \quad (1.7)$$

$$\alpha_{\text{eff}} = \alpha(t) + \tan^{-1} \left(-\frac{\dot{h}(t)}{U_\infty}\right) \quad (1.8)$$

1.4 Literature Review

1.4.1 Plunging motion

Lewin and Haj-Hariri (2003) explained their reason to simulate the pure plunging motion of a two-dimensional airfoil by saying: “many of the phenomena of interest like thrust generation, inversion of the vortex street and leading-edge vortex separation can be captured with this simple motion”.

The earliest theories concerning flapping wing flight were related to purely heaving airfoils. Knoller (1909) and Betz (1912) were the first to observe and explain the thrust generation of plunging airfoils and their theory was experimentally confirmed by Katzmayer (1922). The Knoller-Betz effect, also known as the Katzmayer effect, states that a harmonically plunging wing in a freestream flow results in generation of an effective angle of attack, as illustrated in Figure 1.8. Neglecting viscous and three-dimensional effects, a resultant normal force vector, N , is generated containing both lift and thrust components.

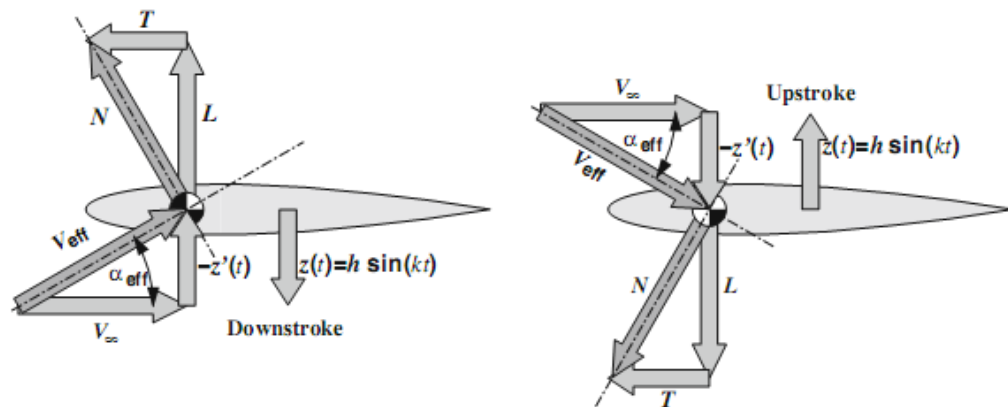


Figure 1.8 : Knoller-Betz effect illustrating thrust production by a plunging airfoil (adopted from Jones and Platzer, 2009).

Birnbaum (1924) applied Prandtl’s (1922) unsteady thin airfoil theory to quantitatively predict the thrust generation of plunging airfoils and he was able to show that an oscillating airfoil sheds vortices from its trailing edge. In 1935, von Kármán and Burgers experimentally observed that a wake consisting of two rows of counter-rotating vortices could produce a thrust force on an airfoil in an incompressible flow.

The vortical signatures of oscillating airfoils have been investigated by many researchers. The low speed flow over a stationary airfoil produces a regular Kármán vortex street as shown in Figure 1.9. In this figure, it can be seen that, for a flow from left to right, the upper row of vortices rotate clockwise and the lower row vortices rotate counterclockwise. This vortex configuration is referred as drag producing wake since time averaged velocity distribution in the wake shows a distinct momentum deficit, indicative of drag.

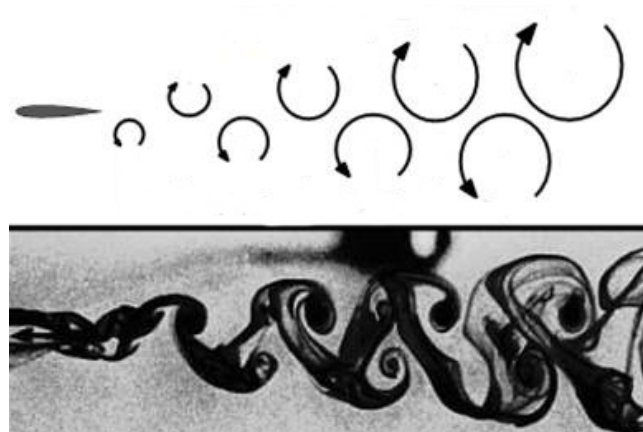


Figure 1.9 : Karman vortex street indicative of drag (adopted from Jones et al, 1996).

An oscillating airfoil sheds a vortical wake from the trailing edge with a certain wavelength, which travels the distance U_∞/ω . Increase in the reduced frequency decreases the wavelength as illustrated in Figure 1.10 (Cebeci et al., 2005).



Figure 1.10 : Computed vortical wake due to sinusoidal plunging motion (a) $k = 0.5$, (b) $k = 1.0$ (adopted from Cebeci et al., 2005).

Oscillation frequency and amplitude variations give rise to different wake formations and orientations behind a flapping airfoil. For the plunging airfoil case, as the plunge velocity is increased, the drag is decreased and eventually thrust is being produced. Between the drag indicative and thrust indicative wake formations, when the airfoil is oscillated at such amplitude and frequency, the time-averaged flow downstream

indicate zero drag. This type of vortex configuration is referred to as the neutral wake, and an example can be seen in Figure 1.11.

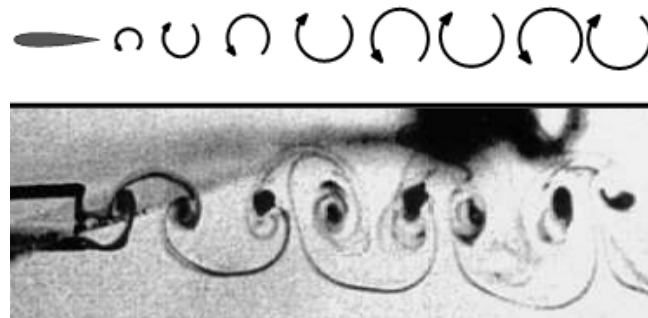


Figure 1.11 : Vortex street indicative of zero drag (adopted from Jones et al, 1996).

When the airfoil is oscillated at sufficiently high amplitude and frequency, the downstream velocity distribution becomes jet-like and thus is indicative of a net thrust on the airfoil. This vortex configuration, constituting of counterclockwise vortices in the upper row and clockwise vortices in the lower row, is shown in Figure 1.12 and referred to as the reverse Karman vortex street.

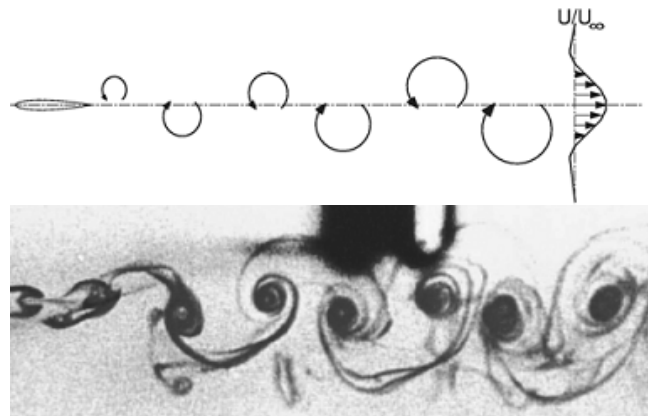


Figure 1.12 : Reverse Karman vortex street indicative of thrust (adopted from Jones and Platzer, 2009).

Mueller (2001) conducted an experimental study over swimming fish using digital particle imaging velocimetry and obtained flow patterns of a reverse Karman vortex street at maximum propulsive efficiency.

A more systematic variation of the amplitude and frequency of plunge oscillation reveal an additional flow regime as soon as the Strouhal number exceeds a certain critical value. As shown in Figure 1.13, the vortex shedding occurs with a finite deflection angle, accompanied by the shedding of additional secondary vorticity where a net lift is observed in addition to net thrust (Jones and Platzer, 2009).

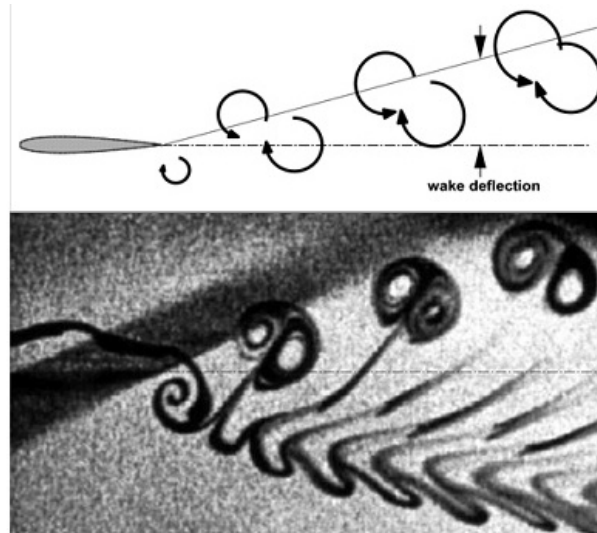


Figure 1.13 : Deflected vortex street indicative of thrust and lift (adopted from Jones and Platzer, 2009).

This type of deflected wake topology was also observed by Bratt (1950) but left without any remarks. Jones and Platzer (2009) state that the physical reason for this type of shedding seems to be the shed vortices forming too closely spaced as the frequency is increased.

Jones et al. (1996 and 1998) were able to duplicate vortex structures experimentally and numerically with a panel code and found that this type of deflected wakes is highly reproducible. However, they noted that this deflected vortex street alternate between up and down modes randomly. They named this phenomena dual-mode vortex street and suggested that relatively small disturbances might trigger the switch in the experiments. Jones and Platzer (2009) expressed that the direction of the deflected jet depends on the initial starting position of the airfoil.

Jones et al. (1996) remark that the experimental and numerical results agree well over a wide range of oscillation frequencies and plunge amplitudes indicating that the development of the vortex street over a wide range of plunge velocities is governed primarily by inviscid flow effects. At low plunge velocities, viscous effects dominate the inertial effects and experimental results show drag production rather than thrust.

Lai and Platzer (1999) conducted dye flow visualization experiments and measured the mean velocity field downstream of a plunging airfoil by a single component Laser Doppler Velocimetry system. They showed that drag producing wake turns into thrust producing jet when the non-dimensional plunge velocity (kh) exceeds

approximately 0.4, and there were transitional forms of wakes between drag-producing and jet-like vortical structures. Their results show that the wake shedding transforms from regular Karman vortex street to reverse Karman vortex street as the plunge velocity is increased, and this transition from drag producing wake to thrust indicative wake occurs via shedding of vortex pairs per half cycle of airfoil motion, as indicated in Figure 1.14.

Young and Lai (2007a) pointed out that the multiple vortex pair shedding modes observed by Lai and Platzer (1999) is caused by the interaction between the natural bluff body shedding from the trailing edge and plunging motion of the airfoil resulting in a vortex lock-in region.

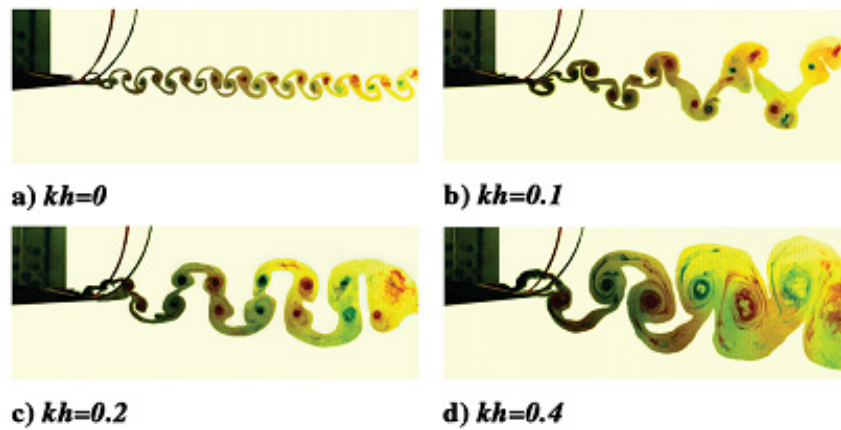


Figure 1.14 : Transition from normal to reverse Karman vortex street with increasing kh (adopted from Lai and Platzer 1999).

Heathcote and Gursul (2007a) observed experimentally that the amplitude of deflection angle of the induced jet decreases substantially with decreasing Strouhal number and changes periodically in time. The jet switching period increased with increasing airfoil stiffness and decreasing plunge frequency and plunge amplitude. The period of the switch is found to be two orders of magnitude greater than the heave period. They concluded that these large periods are challenging for numerical simulations, and might be the reason for the lack of numerical simulations that showed periodic mode switching.

Wang (2000) used an incompressible Navier-Stokes solver to study the flow over a 2D elliptic airfoil undergoing pure plunging motion to determine whether aerodynamic effects could account for flapping frequency selection in nature. She made the point that the existence of an optimum Strouhal number based on trailing

edge motion does not necessarily fix the frequency, as for a given Strouhal number, the frequency and amplitude of motion can vary. She found that there was an optimum flapping frequency for generation of maximum thrust or efficiency, which varied with Strouhal number. The flow separates from both the leading and trailing edges of the airfoil and the interaction of these vortices is important in determining thrust output. The optimum frequency is governed by two separate time scales, these being the times for formation and separation of the leading edge vortex.

Lewin and Haj-Hariri (2003) modeled the flow characteristics and power coefficients of a symmetric foil undergoing sinusoidal heaving motion. They acquired both periodic and aperiodic solutions and found out that for some cases, flow was not symmetric which meant that the flow characteristics are not mirror images of each other during the upstroke and the downstroke. They categorized the interactions between the leading and trailing edge vortices and discussed the influence of these interactions on the efficiency. For a given Strouhal number, the maximum efficiency occurs at an intermediate heaving frequency. They noted that, the reduced frequency k is the primary factor governing the topology of leading edge vortex, with kh being a secondary factor.

Lua et al. (2007) studied the formation of the large-scale wake structures around a heaving elliptic foil experimentally via DPIV method. They identified different types of interactions between the leading edge and trailing edge vortices and they stated that the generated vortical wake structures depend on how and when leading edge vortex interacts with the trailing edge vortex.

Young and Lai (2007b) indicate that for a given kh it is more beneficial to operate at a high k and a low h than at a low k and a high h to minimize the adverse effects of the leading-edge vortex.

Platzer et al. (2008) reviewed the recent developments in the field of flapping wing aerodynamics. They summarized the physics of thrust generation by an airfoil flapping in the pure plunge mode which was strongly dependent on a number of parameters. At high Reynolds numbers, efficient thrust generation is achieved by the shedding of trailing edge vortices in the form of the reverse Karman vortex street that is formed as soon as a sufficiently large Strouhal number is reached. Although leading edge vortices are detrimental to the production of thrust at high-Reynolds

numbers, their effect at low Reynolds number flows is outweighed by the increase in strength of the trailing edge vortices so that the net thrust increases with kh even in the presence of leading-edge vortices. These results indicate that the maximum thrust and optimum efficiency occur at operation near the dynamic stall boundary for a constant value of the Strouhal number. Hence, the Strouhal number is the major parameter that governs the flow behavior in this regime. However, at low-Reynolds numbers, typical for micro air vehicle flight, the flow behavior is much more complex because efficient thrust generation is achieved by shedding from both leading and trailing edges. Although the most efficient flight condition appears to occur again for a specific Strouhal number, thrust and propulsive efficiency are sensitive to the plunge frequency independent of Strouhal number due to the time for leading-edge vortex formation, separation, and convection over the airfoil surface. They also point out that the findings are largely based on computations and experiments for the NACA 0012 airfoil.

Rival et al. (2008) investigated the effect of the airfoil kinematics on the formation and development process of leading-edge vortices for sinusoidal reference case and three non-sinusoidal plunging motions. They showed that the asymmetric and peak-shifted plunge motions delayed the onset and growth of leading-edge vortex during dynamic stall and it was found that all motions exhibited vortex pinch-off, which is the process where a forming vortex ring is no longer able to entrain additional vorticity from the shear layer and eventually pinches off, within the concept of optimal vortex formation time which was suggested by Dabiri (2009) to be universal for all unsteady vortical flows. They conclude that it might be possible to stabilize the leading-edge vortex by carefully tuning the airfoil kinematics.

Cleaver et al. (2009)'s force and PIV measurements for a sinusoidally plunging airfoil showed that the upper surface leading-edge vortex-caused lift improvement is due to its convection and destructive interaction of the trailing edge vortices. Increasing the Strouhal number increases the circulation and the lifespan of the leading-edge vortex which contribute towards the lift for a longer proportion of the cycle, until its dissipation on the upper surface while the lower surface leading-edge vortex strengthens resulting in a decrease in lift.

Jones and Platzer (2009) summarized the numerical and experimental investigations that led them to develop their flapping-wing micro air vehicle which has a fixed wing

for lift and two plunging wings for thrust production. Their studies showed that using two counter-phase flapping airfoils mounted downstream from a fixed wing is a very effective flow control device which stabilizes the upstream flow and initiates the leading edge vortex downstream on the fixed main wing to reattach.

1.4.2 Pitching motion

As unsteady flow over airfoils constitute a popular investigation topic, sinusoidal pitching motions draw considerable interest which closely represent the incidence variations experienced by helicopter rotor blades, wind turbines and turbomachinery. It is necessary to understand the associated aerodynamics so that the unsteady separated flows could be eliminated or taken under control for performance enhancement.

In his review, McCroskey (1982) focused on the role of unsteady effects in two-dimensional oscillating airfoils, and on the advances that have been made towards understanding these challenging flows. He stated that the studies of unsteady airfoil flows have been motivated mostly by efforts to avoid or reduce undesirable effects such as vibrations, buffeting, gust response, flutter and dynamic stall. Some attention has also been given to potentially beneficial effects of unsteadiness, such as the propulsive efficiency of flapping motion, controlled periodic vortex generation, and stall delay, to improve the performance of rotary applications by controlling the unsteady force in some optimum way. Most of these studies and applications concern either periodic motion of an airfoil in a uniform stream or periodic fluctuations in the approaching flow.

Any airfoil with a positive angle of attack in a moving fluid will generate lift with a direction perpendicular to the flow. Prandtl's lifting line theory (1920) suggests that lift generation is linked to vortex generation and lift can only be maintained if the airplane (or an airfoil) continues to generate trailing vortices.

In general, at low Reynolds number flight regime, laminar to turbulent transition usually occurs in combination with a large laminar separation bubble. In the laminar boundary layer, the kinetic energy of the flow in the thin layer near the airfoil surface is not high enough to overcome the adverse pressure gradient so that the laminar flow tends to separate before becoming turbulent. Small disturbances present in the laminar flow are strongly amplified in the shear layer of the separated flow and rapid

transition to turbulence takes place. The turbulence, in turn, creates a large momentum transport normal to the shear layer which overcomes the adverse pressure gradient so that the flow reattaches to the surface and a closed bubble is formed in the time-averaged mean. Downstream of the reattachment point, the fresh turbulent boundary layer is capable of negotiating much higher adverse pressure gradients without separation than the laminar boundary layer (Duyvis, 1995). This laminar separation, transition to turbulent followed by reattachment enclose a region of recirculation flow called the 'Laminar Separation Bubble' (LSB) and its effect on pressure coefficient, C_p can be seen from the sketch in Figure 1.15.

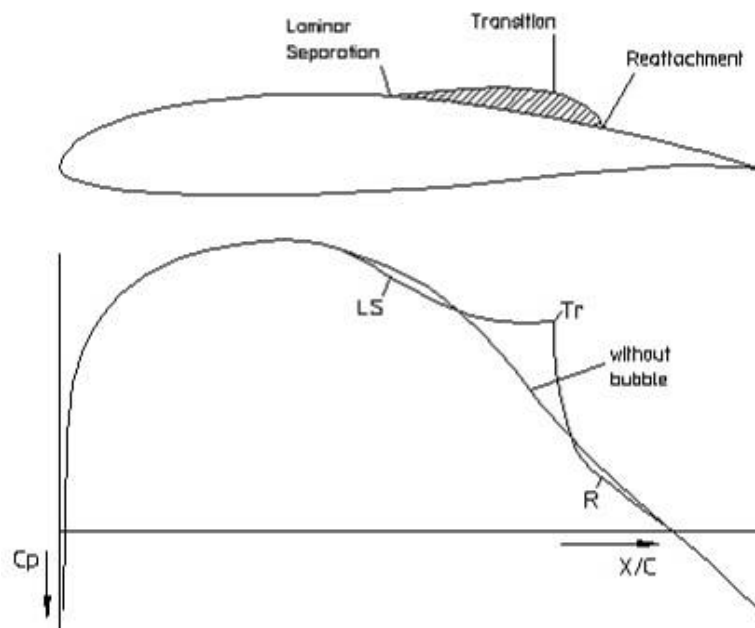


Figure 1.15 : Effect of laminar separation bubble on pressure distribution (adopted from Duyvis, 1995).

The principal flow behavior of instability and transition inside a laminar separation bubble is sketched in Figure 1.16.

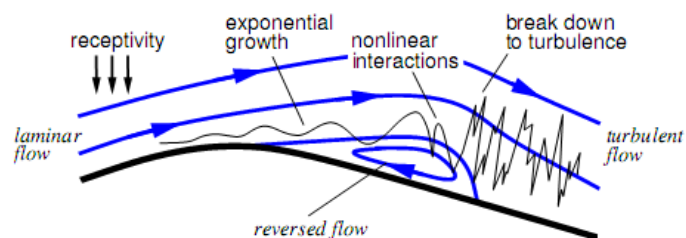


Figure 1.16 : Instability and transition in a laminar separation bubble with a sketch of time averaged streamlines (adopted from Windte et al., 2004).

The presence of LSB is the main reason for degradation in performance at low Reynolds numbers. LSBs usually create additional drag as they displace the outer

inviscid flow (Windte et al, 2006). Transition of the boundary layer while separated yields bad starting conditions of the turbulent boundary layer. This means it becomes thicker and is more sensitive to separation near the trailing edge. The bubble produces mainly pressure drag due to its effect on the pressure distribution which results in a thick wake behind the airfoil (Duyvis, 1995).

Jones (1938) was the first to document experimental observation of LSB. The dynamics of a LSB depends on the value of the Reynolds number, pressure distribution, geometry, surface roughness and the freestream turbulence. For a fixed Reynolds number, varying the angle of attack changes the LSB as well (Shyy et al., 2008).

McCroskey et al. (1976) varied the leading edge geometry of an NACA 0012 airfoil and examined three different types of stall production, where vortex shedding was a predominant feature of each. They stated that dynamic stall did not originate from bursting of the LSB but from a breakdown of the turbulent boundary layer. They also mentioned that the main difference between static and dynamic stall is the vortex shedding phenomenon on oscillating airfoils and lift is generated through dynamic stall.

A full understanding of static airfoil stall can be achieved by studying the changes in the boundary layer on the airfoil's suction surface. Leading edge stall typically is preceded by the formation of a separation bubble which starts to burst as soon as a critical incidence angle is exceeded. Trailing edge stall progresses from the trailing edge toward the leading edge. A radically different stall behavior is observed if the airfoil is subjected to rapid changes in angle of attack (Cebeci et al., 2005).

Kramer (1932) conducted experiments on a fixed wing subjected to varying incidence airflow via rotatable vanes. He demonstrated that as the angle of attack of the airfoil is suddenly increased, the maximum lift coefficient increases proportionally and the wing can experience lift coefficients above the steady-state value. Carr (1987) observed this Kramer effect which states that extra lift can be created by rapid pitching of airfoils, and he showed that this extra lift is associated with a vortex formed on the airfoil during the unsteady motion.

Dynamic stall is the term often used to describe the dynamic delay of stall on airfoils for angles beyond the static stall angle, which is usually followed by large excursions

in lift and pitching moment. The reasons for this lift overshoot for a short period of time can be understood by examining the sequence of events which is shown in Figure 1.17.

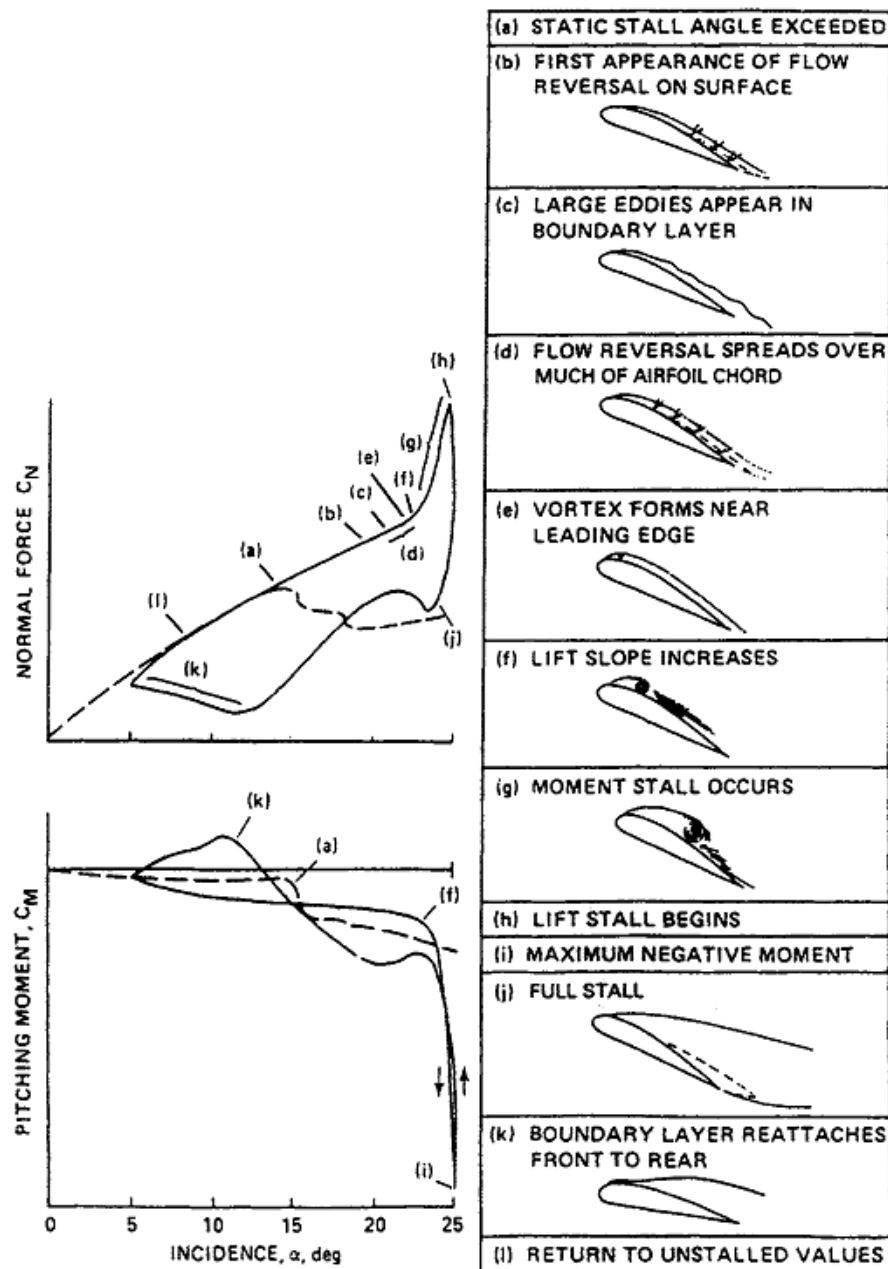


Figure 1.17 : Dynamic stall events on a NACA-0012 airfoil (adopted from Carr, 1987).

A similar but diverse type of stall which resembles dynamic stall is the stall flutter. McCroskey (1982) defines stall flutter as oscillations of an elastic body that are caused by separated flow which would be nominally steady in the absence of any motion of the body, but which is made unsteady by the flow-induced body oscillations. The term dynamic stall, on the other hand, usually refers to unsteady

separation and stall phenomena on airfoils that are forced to execute time-dependent motion, oscillatory or otherwise, or to cases where flow-field perturbations induce transitory stall. Although stall flutter and dynamic stall share many common features; the primary difference is that the amplitude of the motion is often smaller in stall flutter.

The vortex shedding process during angle of attack variations involves a series of distinct events. When the static stall angle is exceeded by rapid rotation of the airfoil, the boundary layer remains thin and shows no evidence of separation or flow reversal because of the lag time between airfoil motion and pressure response. As a consequence, for a short while the airfoil "sees" a lower angle of attack than the geometric angle of attack and therefore boundary layer separation is delayed (Cebeci et al., 2005). As the angle of attack is increased higher, the boundary layer on the rear portion of the airfoil begins to thicken rapidly and large eddies start to form. The region of highly disturbed boundary layer flow progress upstream with increasing incidence and small disturbances begin to appear in the surface pressure distribution slightly after first flow reversal is indicated. As the increment in angle of attack is increased, the boundary layer on the front of the airfoil abruptly breaks down in the turbulent flow almost to the leading edge, although the boundary flow in the immediate vicinity of the laminar leading edge bubble does not separate until slightly later. When this sudden separation occurs, the static suction begins to rise indicating an initial formation of a vortex. As this vortex begins to form and move downstream, the magnitude of the reversed velocity near the surface of the airfoil model increases. During this phase of the dynamic stall process, additional lift is produced. Due to this movement of the dynamic stall vortex, the center of pressure moves downstream causing a significant increase in nose-down pitching moment. The sudden change in the pressure distribution on the airfoil causes the aerodynamic pitching moment to change drastically, and this is called the moment stall. When the vortex is approximately at mid-chord, a maximum in lift coefficient is reached followed by a rapid loss of lift (lift stall) as soon as the dynamic stall vortex passes the trailing edge. As the vortex passes off the trailing edge, normal force coefficient continues to decrease and moment coefficient increases to values representative of static stall. The final stage then is complete flow separation, followed by flow reattachment as soon as the angle of attack is reduced below the static stall angle.

The phenomenon of dynamic stall which produces transient forces and moments that are fundamentally different than their static-stall counterparts, has been studied for many years (McCroskey et al., 1976). A certain degree of unsteadiness always accompanies the flow over an airfoil at high angle of attack, but the stall of a thin body undergoing unsteady motion is more complex than static stall (McCroskey, 1982). If the angle of attack oscillates around a mean value α_0 that is of the order of the static stall angle, large hysteresis develop in the dynamic forces and moments with respect to the instantaneous angle $\alpha(t)$. The maximum values of the lift, drag, and pitching moment coefficients can greatly exceed their static equivalents, and even the qualitative behaviors cannot be reproduced by neglecting the unsteady motion of the airfoil. The stall onset condition represents the limiting case of the maximum unsteady lift that can be obtained with no significant change in pitching moment or drag. Further increases in angle of attack produce the dynamic stall conditions which are characterized by large phase lags and hysteresis in the separation and reattachment of the viscous flow. Figure 1.18 illustrates some of the qualitative differences in light and deep dynamic stall. Moment stall occurs rather abruptly in both cases, but the deep-stall drop in lift is not evident in the light-stall case.

Figure 1.18a shows the light stall category of dynamic stall, which shares some of the general features of classical static stall, such as loss of lift and significant increases in drag and nose-down pitching moment compared with the theoretical inviscid values, when angle of attack exceeds a critical value. Another distinguishing feature of light dynamic stall is the scale of the interaction. The vertical extent of the viscous zone tends to remain of the order of the airfoil thickness, as illustrated in Figure 1.18a, and this is generally less than for static stall.

A combination of large amplitudes of the oscillation and large maximum angles is essential to the development of deep stall. Figure 1.18b shows the effects of increasing the maximum incidence to values above the static-stall angle. It can be noted that the thickness of the viscous interaction zone is on the order of the airfoil chord during the vortex-shedding process. The initial breakdown of the flow in this deep-stall regime, beginning with the formation of a strong vortex in the leading edge region which is shed from the boundary layer moving downstream over the upper surface of the airfoil has been explained previously.

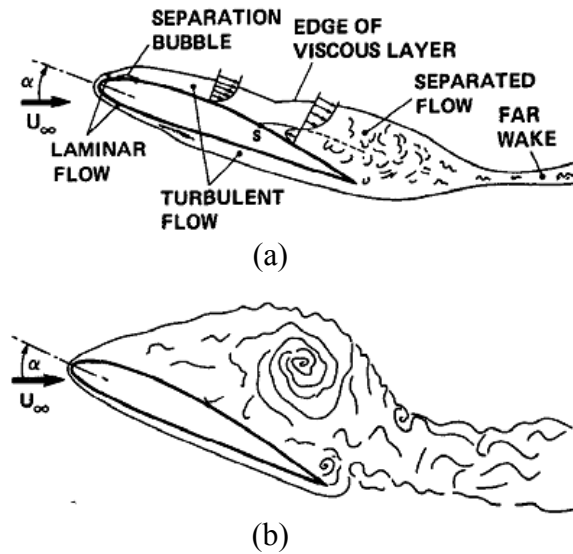


Figure 1.18 : Sketches of flow fields during dynamic stall; a) Light stall, b) Deep stall (adapted from McCroskey, 1982).

Some insects, such as the tiny wasp *Encarsaria Formosa*, use the clap and fling mechanism (Zhang et al., 2007) where the wings are clapped together and then flung open before the start of the downstroke, creating a lift-enhancing vortex around each wing. However, most insects and birds rely on a leading edge vortex (LEV) created by dynamic stall during flapping where a strong spanwise flow is generated by the pressure gradients that cause the LEV to spiral out to the wingtip. Technical applications of the fling are limited by the mechanical damage that accompanies repeated clapping of the wings, but the LEV can be used to enhance the lift production of propellers for micro-air vehicles (Ellington, 1999). The vortical structure of the LEV produces a region of low pressure near the wing surface and influences the strength of the bound circulation about the wing and it is observed to be stable for the duration of the half-stroke for flapping wing fliers (McClung, 2009). The dynamic stall and LEV phenomenon has been observed and studied extensively by many zoology and aerodynamics researchers in recent years.

Ellington et al. (1996) performed experiments on a hawkmoth, *Manduca sexta*, tethered in a wind tunnel and visualized that a vortex spirals out towards the wingtip with a spanwise velocity comparable to the flapping velocity. van den Berg and Ellington (1997) continued the flow visualization experiments with a robotic insect that mimicked the wing movements of a hovering hawkmoth. They confirmed the existence of a small, strong and stable three-dimensional LEV, increasing in size from wingbase to wingtip. The growth of this vortex with time and spanwise position

identified dynamic stall as the unsteady aerodynamic mechanism responsible for high lift production. They declared that for optimal performance, the vortex separation should be postponed as long as possible. However, their observation of the axial flow on the wing of a hawkmoth was not detected in the flow around helicopter rotors or wind turbine blades (McCroskey et al., 1976), which is an evidence that the axial flow component is reduced in high aspect ratio wings.

Kim and Park (1988) examined the chronological flow patterns around an airfoil oscillating in pitch with relatively small amplitude using a smoke wire technique. The unsteady separation was observed to be accomplished as the front of the reversed flow region reached its uppermost position. The instantaneous angle of attack at which the separation took place was seen to depend on the reduced frequency k .

Thrust generation by pure pitching has been experimentally demonstrated by Koochesfahani (1989). He performed flow visualization and quantitative laser measurements of the wake flow characteristics of a NACA 0012 airfoil pitching about its quarter chord and confirmed Garrick's (1936) earlier prediction that a pitching airfoil would generate thrust only above a certain critical pitching frequency, but at a higher value than that indicated by calculations based on the classical linear inviscid theory. He showed that the structure of the wake could be modified by control of the frequency, amplitude and the shape of the oscillation waveform. He also observed axial flow exists in the cores of the wake vortices and the magnitude of this axial flow increases linearly.

Gursul and Ho (1992) measured the aerodynamic loads acting on a stationary NACA0012 wing in a vertical water channel of a sinusoidally varying freestream. They state that, during deceleration, the downstream convection of vorticity decreases while the accumulated vorticity forms a separation vortex near the leading edge. The lift increases as long as the convex streamlines reattach on downstream of the vortex and lift drops after the vortex leaves the trailing edge, hence the lift coefficient vary with the variations of the freestream velocity variations. They explain the high lift coefficients observed when the acceleration of the freestream is zero by the high pressure gradient produced by the large separation vortex which increases the suction on the upper wing surface.

Panda and Zaman (1994) documented the cyclic variations of a pitching airfoil's near wake flowfield with flow visualization and phase-averaged vorticity measurements. They observed that a vortex originates from the trailing edge just when dynamic stall vortex is shed and they referred to this kind of opposite signed vortex pair as a "mushroom" wake since together they take a shape of the cross-section of a mushroom while convected away from airfoil. They stated that the sum of absolute values of all vorticity convected into the wake is independent from the reduced frequency and the amplitude of oscillation but dependent of the mean angle of attack and they proposed a method that estimated the time varying component of the lift from the shed vorticity flux.

Tuncer and Platzer (1996) parametrically studied thrust generation on a single flapping airfoil and a flapping / stationary airfoil combination in tandem. They found that the propulsive efficiency is a strong function of the reduced frequency and the flapping amplitude. The numerical solutions predicted thrust and a propulsive efficiency of more than 70% in flapping foils and thrust and efficiency augmentation more than 40% in tandem. They also pointed out that the augmentation of thrust due to the trailing airfoil was more significant at relatively high reduced frequencies.

Oshima and Ramaprian (1997) and Rank and Ramaprian (1998) performed instantaneous velocity field measurements of an oscillating NACA0015 airfoil with PIV technique in the same experimental facility. The former study focused on dynamic stall and the latter on light stall characteristics. Oshima and Ramaprian (1997) showed that the dynamic stall vortex consists of rolled-up shear layer along with remnants of several vortices generated by shear layer instability at low Reynolds numbers. The increase of lift at post-static stall incidences is shown to be due to the presence of vortical structures close to surface, till they are eventually ejected prior to dynamic stall. Infusion of counterclockwise vorticity from the airfoil surface due to local adverse pressure gradient forces the shear layer to lift up and thus creates the leading edge vortex. The continued influx of counterclockwise vorticity from the surface produces a secondary counterclockwise vortical structure underneath the leading edge vortex, which causes the shear layer to roll up. The rolled-up shear layer, along with the remnants of several vortices generated by the shear layer instability, forms the dynamic stall vortex. The dynamic stall vortex grows in size and is eventually ejected abruptly at a large angle with respect to the

airfoil surface leading to the dynamic stall. Early transition to turbulence at high Reynolds numbers causes the leading edge vortex to form at larger incidences, but more abruptly than at low Reynolds numbers. At high Reynolds numbers the dynamic stall vortex is more compact, has fewer remnants of vortical structures, and is ejected abruptly from the airfoil surface in a direction almost normal to the surface. The dynamic stall vortex is clearly separated from another dominant vortical structure, the shear layer vortex, which occupies the mid-to-aft region of the airfoil. Rank and Ramaprian (1998) performed a subsequent study of pitching airfoils with a rather low reduced frequency of $k=0.05$ to observe the characteristics of light dynamic stall. They observed that even as the angle of incidence is increased to 19° , which is the beginning of pitch down cycle, there was no evidence of a leading edge vortex. At this point, the flowfield is separated from the airfoil surface at the leading edge and a very thick layer of very low velocity extends over the surface of the airfoil. This flow structure was previously observed and described as the shear layer vortex by Oshima and Ramaprian (1997). It is primarily caused by the upstream advancement of the region of low and reverse velocity initially formed at the trailing edge and it seems to be a characteristic feature of the NACA 0015 airfoil geometry tested.

Sun and Sheikh (1999) numerically studied the oscillating airfoil to suppress the dynamic stall. Pitching oscillations with amplitude of 10° about a mean angle of attack of 15° and with reduced frequencies of 0.15 and 0.25 were examined. The blowing location is near the airfoil leading edge, and the unsteady tangential blowing was found more effective than the steady blowing.

Ames et al. (2001) used a closed circuit wind tunnel run at a chord Reynolds number of 20,000 with reduced frequency $k = 0.5$ for a sinusoidal flapping motion with amplitude between -13.4° and 35.2° . Their results showed that the vorticity is distributed over tip vortex, unlike what is seen in vortices at higher Reynolds number and the tip vortex cores become stretched in the direction of wing flapping during downstroke with a highly asymmetric velocity distribution across the vortex core.

Kuo and Hsieh (2001) studied the unsteady vortex structures and vorticity convection over an NACA 0012 airfoil oscillating periodically near the static stalling angle of attack at a high reduced frequency of $k=4.05$. They observed that the leading edge separation vortices are combined one by one into a vortex near the trailing edge and

then shed together downstream into the wake. They named this kind of vortex structure as the synchronized shedding type. The hysteresis characteristics of unsteady flow structure exists for low and high frequency oscillations, but the wavelength of unsteady vortex structure over the airfoil was found to be significantly different from that at low reduced frequencies. They also noted that the effect of different pivoting axis is insignificant on the unsteady flow structure at such high reduced frequency oscillations.

Ramamurti and Sandberg (2001) studied the pitching NACA0012 airfoil as well as pitching and heaving motions using a finite element flow solver. They observed the effect of the pitching amplitude variations on the force coefficient to show that the critical parameter for thrust generation is not the reduced frequency but the Strouhal number.

Birch and Lee (2005) investigated flow structures and lift-induced drag of the near field tip vortex behind a pitching NACA0015 airfoil at $Re=1.86 \times 10^5$. For light stall oscillations they observed that the tip vortex changed from a wake-like to a jet-like behavior during the oscillation cycle. The vortex strength and the lift-induced drag values increased with angle of attack, and their values were higher during pitch-down than during pitch-up motion. For deep-stall oscillations, they observed that the axial flow was always wake-like and the vortex was more organized and axisymmetric during pitch-up than during pitch-down motion. The tangential velocity, circulation and lift-induced drag had higher values during pitch-up than during pitch-down and increased with the airfoil incidence. The vortex size, however, was larger during pitch-down than during pitch-up. They concluded that the normalized circulation within the inner region of the tip vortex also was insensitive to the reduced frequency.

Jung and Park (2005) experimentally investigated the frequency characteristics of Karman vortex shedding in the near-wake of a pitching airfoil and found that the frequency variation during the cycle of oscillation diminishes as the reduced frequency of oscillation is increased.

Sarkar and Venkatraman (2006) examined the vortex patterns of a harmonically pitching airfoil using a two-dimensional discrete vortex simulation. They observed that the thrust force increases with increase in oscillation frequency and decrease in

mean angle of attack. However, in a clear deviation from inviscid theory trends, they observed only drag for pitching at high amplitudes about high mean angle of attack. They also observed that the frequency for obtaining thrust is dependent on the pitch axis location and this critical frequency increases as the pitching axis is shifted away from the leading edge.

Ringuette et al. (2007) experimentally investigated the force generated by the unsteady vortex formation of low-aspect-ratio flat plates with one end free and showed that the tip vortex produces a significant maximum in the plate force. They also demonstrated that the plate drag coefficient increases with decreasing aspect ratio.

The most recent studies focusing in pitching airfoils are summarized below.

Kim and Chang (2009) investigated the effects of Reynolds number between 2.3×10^4 to 4.8×10^4 keeping the reduced frequency fixed at $k=0.1$ for a pitching NACA0012 airfoil. The smoke-wire visualization of the boundary layers showed that the reattachment and unsteady laminar separation are delayed in downstroke and hastened in upstroke with increasing Reynolds number.

Contradicting the results of Kim and Chang (2009), Alam et al. (2009)'s comparative computational and experimental study of a pitching SD7003 airfoil model at a high reduced frequency of $k=3.93$ and high amplitude of 21.5° degrees with initial angle of attack of 4° at $Re=10000$ and 40000 showed that the flow structures are independent of variations in Reynolds number and the wake is always deflected in upwash, despite the positive camber of the airfoil.

Lian (2009a)'s simulations on a flat plate showed that the influence of the Reynolds number on the flow structure has strong dependence when the pitch rate was low and its impact weakened as the pitch rate is increased. As the pitch rate is increased, the formation of the leading edge vortex on the upper surface was delayed and the vortex became more compact and strong. He also showed that changing the position of pitch changes the effective angle of attack. Moving the pitch position further aft the quarter chord point reduced the strength of the LEV on the top surface when the plate was pitched upward and when the pitch position was moved past the middle chord, the vortex appeared at the bottom surface.

Mulleners et al. (2009) experimentally investigated the flow over an OA209 airfoil by means of time resolved particle image velocimetry (TR-PIV) and surface pressure measurements. The airfoil had a sinusoidal pitching motion under dynamic stall conditions. They classified the major features of dynamic stall with successive stages of boundary layer separation, vortex formation and convection until the stall onset, massive flow separation at stalled stage, and flow reattachment. The dynamic stall delay is defined as the delay between the time the effective angle exceeds the static stall angle and onset of dynamic stall when the dynamic stall vortex is detached from the boundary layer. The delay of dynamic stall was attributed to the formation time of the primary stall vortex and was observed to decrease with increasing unsteadiness described by the induced speed of the leading edge.

Garmann and Visbal (2009) simulated the transitional flows over a flat plate and SD7003 airfoil undergoing a pitch up motion from an initial zero incidence to 40° at a constant pitch rate, hold, and return maneuver at low Reynolds numbers of 10^4 and 4×10^4 . They showed that the angular acceleration increased the interactions of the trailing edge vortices with the dynamic stall vortex, which led to significant differences in the aerodynamic loads on the pitch down portion of the motion.

Ol (2009a) considered a similar problem of a linear pitch-ramp with large amplitude up to 40° at $Re=10000$ and high reduced frequency of 0.1 to 2.8. He observed that increasing pitch rate tends to tighten the LEV and produce a trailing edge vortex system dominated by a counter-rotating pair. He compared a SD7003 airfoil, a low aspect ratio (AR) flat plate and an $AR=2$ flat plate to show that the LEV formation for all models is qualitatively similar but the airfoil had stronger trailing edge vortices and the $AR=2$ plate had a smaller, tighter and more concentrated LEV system than does the wall-to-wall plate. He showed that the pitch pivot point location is crucial to the leading edge vortex size and formation.

Lian (2009b)'s numerical study with a pitching elliptic wing also indicated that moving the pitch position further aft makes LEV weaker on upper surface during pitch up, and once pitch axis is moved past the middle chord, the vortex appears at the bottom surface, due to effective angle of attack. His simulations show that as the pitch rate is increased the formation of a more compact and stronger LEV on the top surface is delayed.

1.4.3 Combined pitching and plunging motion

Wang's (2000) computational study results indicate that pure heaving motion is insufficient to generate thrust at low Reynolds numbers. Heaving motion is mostly employed by large animals like birds and fish operating in the low frequency regime at larger Reynolds numbers, and insects typically use the combination of heaving (plunging) and pitching motions in low Reynolds number regime.

As already mentioned in the previous chapters, operational efficiency of flying species are produced by dynamic movements of their wings. Oscillatory wing motion profiles and associated tip paths differ for each flying animal and how a particular species is set into motion is determined by the morphology, wing configuration, body structures, joints and physiology of that animal (McClung, 2009).

Some insects use a "clap and fling" mechanism to fly; the wings are clapped together at the end of the upstroke and then peeled and flung open just before the beginning of the downstroke, creating a lift-enhancing vortex around each wing. Most insects however, use a method that creates a spiraling leading edge vortex; a strong spanwise flow is generated by the pressure gradient on the flapping wing, causing the leading edge vortex created by the dynamic stall to spiral out to the wingtip (Ellington, 1999). Although the technical applications of the fling are restricted by the probable mechanical damage that may be caused by the repeated clapping of the wings, there is a possibility to use the spiral leading edge vortex to augment lift production of propellers, rotors and micro-air vehicles.

In their review of experimental biomimetic studies, Triantafyllou et al., (2004) classified the similar mechanisms of force production and flow manipulation in fish and birds, namely; the formation of leading edge vortices ("delayed stall"), influence of shed vorticity through the stable formation of Kármán streets ("wake capture") and effective angle of attack and angular velocity ("rotational circulation"), noting that the conditions of swimming is different from flying. They remark that whereas the primary goal in flying is the continuous production of steady lift to balance the large body weight within a medium with small density, the major goal in swimming is to minimize drag forces within a medium with higher density and generation of steady lift to support the small net weight is of secondary importance.

Figure 1.19 illustrates a cycle of propulsive movements of a thunniform mode swimming fish, *Euthynnus affinis* (mackerel tuna). The motion of its caudal fin is similar to the wing-stroke plane angle traces of a bird, which is illustrated in Figure 1.20.

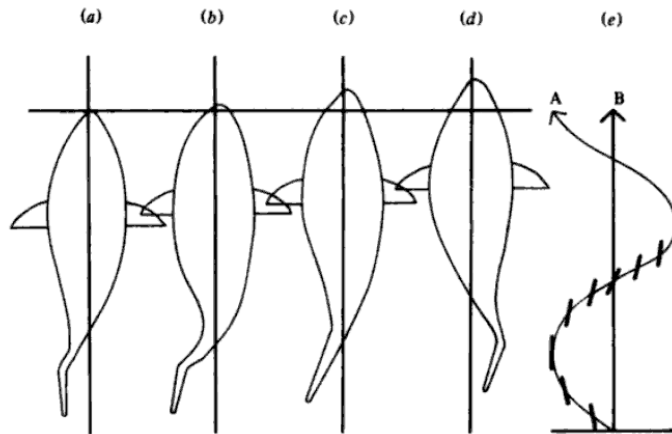


Figure 1.19 : a-d) Successive body positions for swimming in thunniform mode, e) Diagram of the paths of caudal fin (adopted from Blake, 1983).

In Figure 1.20, representative traces of angle of attack through a wing-beat for an animal flap-running (WAIR) vertical flight (red) and in horizontal flight (blue) demonstrate the similarity of behaviors.

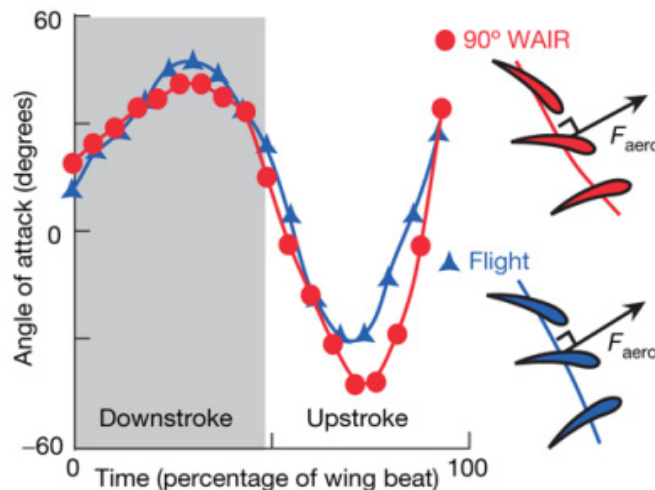


Figure 1.20 : Angle of attack traces through a wing-beat for a flapping animal (adopted from Dial et al., 2008).

Most flying animals have light-weight and flexible wing structures and the structural flexibility of the wing can also influence the unsteady flow over flapping wings in addition to variations in the wing motion. Heathcote et al. (2004) investigated the effect of airfoil stiffness on thrust generation for an airfoil plunging at zero freestream velocity, which is relevant to hovering birds and insects, and they found

that the deformation of the flexible airfoils produce a periodically varying angle of attack with a phase angle with respect to plunging motion. Flexible flapping airfoil propulsion has also been studied by Miao and Ho (2006), Heathcote and Gursul (2007b) and Heathcote et al. (2008). They state that the amplitude and phase of this combined plunging and induced-pitching motion play a major role in thrust production.

The first systematic study to analyze the propulsion of combined pitching and plunging wings was Garrick's (1936) linear approach. However, as Jones et al. (2001) put it, if flying species have evolved to initiate the combined pitch and plunge motion to be advantageous, then linear theory is a poor model of the real physics in those cases.

Ohmi et al. (1990, 1991)'s investigations in on the formation of leading edge vortices revealed that the wake patterns depend on more varied parameters than believed and neglected in many of the previous traditional dynamic stall experiments. They conducted unsteady 2-D Navier-Stokes computations and streamline visualization of the wake patterns generated by elliptic and NACA0012 airfoil profiles which have steady translation in a tow tank and a harmonic oscillation in pitch. They showed that the vortex formation of oscillating airfoils depend on the value of the reduced frequency and the variation of the wake patterns is influenced by the leading edge vortices which are shed and travel downstream to incorporate with the newly-formed trailing edge vortices. The determinant factors for various wake formation are identified as mean incidence, position of pitching axis and airfoil cross section. The formation of synchronized vortex shedding pattern is optimized by setting the mean incidence near critical static stall angle, displacing the pitching axis from half-chord to one-third-chord point for a NACA0012 foil and the effect of Reynolds number is stated to be small compared to the other parameters.

Triantafyllou et al. (1991) propose that the wake dynamics of a flapping foil is dominated by a single non-dimensional parameter, the Strouhal number (St) and the frequency of maximum spatial amplification in the wake provides optimal thrust production in the range of $0.25 < St < 0.35$.

Even though nearly all examples of flapping wing propulsions in nature combine both pitching and plunging motions, the availability of pitch and plunge does not

solely suffice for propulsion. The parameter space for combined plunging and pitching motion includes amplitudes and the phase angle, ψ , between pitch and plunge. The key parameter determining whether an airfoil creates thrust or extracts power from the flow is the effective angle of attack and the variation of effective angle of attack with the geometric angle of attack is illustrated in Figure 1.21.

In Figure 1.21a, the airfoil is just plunged, creating an induced angle of attack. If the airfoil is just pitched, then it may have an induced angle of attack at the leading edge, depending on where the pitch angle is located (Figure 1.21b). If a flapping airfoil is pitched with low amplitude, the negative effective angle of attack relative to the flight path leads to thrust generation as shown in Figure 1.21d. If the airfoil is pitched with large amplitude, greater than the induced angle of attack from the plunge motion, then power is extracted from the flow as depicted in Figure 1.21e. At some point in between, the induced angle of attack is just offset by the geometric angle of attack, and the wing is said to *feather* through the flow, essentially flapping without disturbing the flow, as illustrated in Figure 1.21c (Jones et al., 2001).

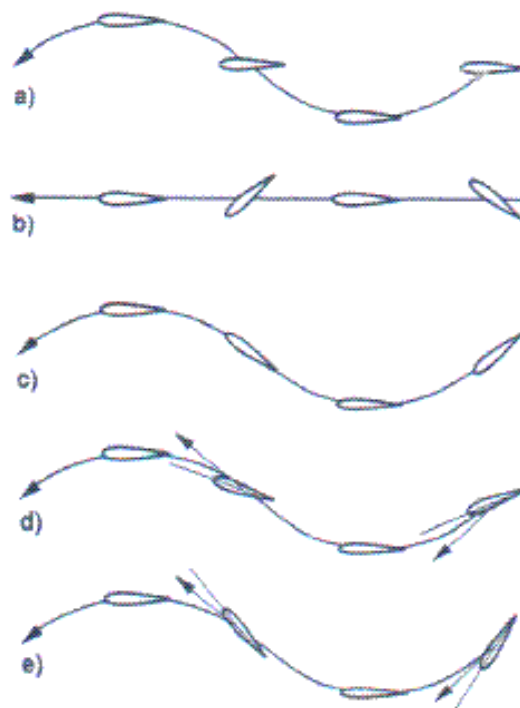


Figure 1.21 : Effective vs. geometric angle of attack (adopted from Jones et al., 2001).

Jones and Platzer (2001)'s panel code results show that for the same reduced frequency and plunging amplitude values, changing the effective angle of attack

would result in a change in propulsive efficiency. For a case where optimum efficiency occurs at around phase angle of 100° with a minimum in the thrust coefficient, if effective angle of attack is changed, keeping the other parameters constant, both the highest efficiency and maximum power extraction can be achieved for phase angles near 90° .

Anderson et al. (1998) also observed the significant role that the phase angle between pitch and heave oscillations play in maximizing the propulsive efficiency. Their experimental study is one of the extensive investigations in the field of pitching and plunging airfoils. They carried out force and power measurements in addition to flow visualizations with PIV method for a NACA0012 airfoil at Reynolds number of 40000 and 1100 respectively. They defined the conditions for optimal thrust production to be operation at $0.25 < St < 0.4$, a large maximum angle of attack of $15^\circ < \alpha_{max} < 25^\circ$ and a large amplitude of heave motion to chord ratio of order one. In their flow visualization experiments they observed high efficiency during the generation of a moderately strong LEV per half-cycle on alternating sides of the foil which is then convected downstream to interact with trailing-edge vorticity to form a reverse Karman street. They note that a mild leading edge vortex benefits the efficiency, but a large LEV leads to very a low efficiency and high drag. They state that the timing of the formation and shedding of a LEV is determined by the phase angle between heave and pitch motions and showed that high thrust values can be achieved with high propulsive efficiency if the shedding of the leading edge vortex is properly timed. The optimal value for propulsion efficiency is found at phase angle of 75° while pitch leads the heave motion for a pivot point at one-third chord position. Guglielmini and Blondeaux (2003)'s vorticity equation computations showed good agreement with Anderson et al. (1998)'s experiments and they concluded that the high efficiency and thrust coefficients are related with the formation of a jet of fluid leaving the foil from the trailing edge.

The shedding of leading edge vortices and the use of dynamic stall process is well recognized as the key to lift generation of flapping wing mechanisms (Platzer and Jones, 2006). Isogai et al. (1999) numerically examined the dynamic stall phenomena around a pitching and plunging NACA 0012 airfoil. Their calculations showed that the highest efficiency was obtained when and the pitch oscillation lead the plunge motion by about 90° and when no significant flow separation occur in spite of large-

amplitude oscillations. Efficiency was found to decrease rapidly accompanied by large scale leading separation for conditions other than this range of phase angles and reduced frequency. They observed that viscous and nonlinear effects dominate the low reduced frequency flow and amplitude values of the flapping motion results in a decrease in the average thrust and the propulsive efficiency.

Tuncer and Platzer (2000) presented the flow separation characteristics and thrust-producing wakes of a plunging and pitching as well as pure plunging NACA 0012 airfoil in terms of unsteady particle traces. Their computations showed that the maximum propulsive efficiency is obtained when the flow remains attached to the airfoil. For pure plunging cases at high frequencies, higher thrust coefficients were obtained when large leading edge vortices were present, however the propulsive efficiency dropped significantly for those cases.

Ramamurti and Sandberg (2001) used a finite element incompressible Navier-Stokes solver and obtained good agreement with the experiments of Koochesfahani (1989) for pitching airfoils and of Anderson et al. (1998) for pitching and plunging airfoils. They examined a slight loss of lift due to attached vortex on the upper surface of the airfoil and observed that the lift force begin to recover when this vortex lifts off the surface. Their computations confirmed Anderson's observation that the phase angle between the pitch and plunge oscillation was the critical parameter in maximizing thrust or propulsive efficiency and they showed that the thrust coefficient reaches a maximum value when the pitching motion lead the plunging motion by 120° and the maximum efficiency is obtained when the phase difference is 90° .

Read et al. (2003) provided systematic data experimentally for a heaving and pitching NACA0012 airfoil and they found that a phase angle of $90^\circ < \psi < 100^\circ$ provides the best thrust performance. They observed that the thrust coefficient decreases for high Strouhal numbers when the induced angle of attack is no longer a harmonic function of time. They also tested foils with superimposed pitch bias and impulsive start in still water and showed that harmonically oscillating foils are able to produce large lateral forces for maneuvering capabilities.

Hover et al. (2004) used the same kinematic arrangements of Read et al. (2003) and compared the performance of four different angle of attack profiles of a harmonically heaving and pitching foil. The highest thrust coefficients were obtained by sawtooth

wave profiles but the cosine angle of attack profiles improved the thrust values with highest efficiency.

Tuncer and Kay (2004)'s numerical optimization of an airfoil flapping in combined pitch and plunge showed that thrust generation is maximized at large plunge amplitudes as large leading edge vortices form and shed into the wake and the airfoil stays at large effective angle of attack values. They found that the propulsive efficiency is increased if plunging amplitude and effective angle of attack is reduced, and the large scale leading edge vortex formation is prevented. Their following optimization data (Tuncer and Kaya, 2005) confirmed that high thrust values could be obtained at the expense of propulsive efficiency.

Schouveiler et al. (2005) added a bias to the pitch angle and broke the symmetry of a pitching and plunging foil by changing the angle of attack and thus generated very high side forces which can be useful for the maneuverability of the propelled vehicle.

Milano and Gharib (2005) applied a genetic algorithm to their experiments in a tow tank to achieve optimal lift force for a rotating and translating rectangular flat plate. They showed that maximum lift was generated when the leading edge vortex pinch off just at the end of the half stroke. A following study was performed by Ringuette et al. (2007) using a translating low aspect ratio plate to investigate the impact of the tip vortex in the start-up process. Again the leading edge vortex was found to pinch off at around end of the half stroke.

Yang et al. (2006)'s optimization computations were in a good agreement with Isogai et. al. (1999)'s results. They showed that higher efficiency occurs at lower reduced frequency and higher thrust occurs at higher reduced frequency. They note that the pitching pivot position has minor effect on optimization and the optimal phase angle of pitching ahead of plunging lies between 70° and 90° .

Lian and Shyy (2007)'s Navier-Stokes computations using a flapping NACA0012 airfoil showed that both the reduced frequency and the Strouhal number should be considered independently to determine the flapping airfoil aerodynamics. They showed that the large freestream velocity variations could be smoothed out by the flapping wing, making it resistant to gust. They also explained that a leading edge vortex, which is formed when the airfoil starts to descent, travels downstream

creating a low pressure zone on the upper surface and increases the lift and thrust of the flapping airfoil.

The mechanisms influencing the propulsive efficiency of pitching and plunging motions were also investigated numerically by Young and Lai (2007b). Their results using the Garrick (1936) analysis predicted the peak in propulsive efficiency successfully compared with the experiments of Anderson et al. (1998) in combined pitch and plunge motions, but the peak shown in Heathcote et al. (2008)'s pure plunge motion experiments was not captured. Their simulation with the unsteady panel method and Navier-Stokes codes indicate that for low Strouhal numbers, the viscous drag causes a decrease in the propulsive efficiency. The leading edge vortex formation, convection and shedding was found to be controlled by the reduced frequency. They conclude that although the Strouhal number alone is not sufficient to characterize the efficiency of flapping-foil propulsion, the efficiency peak emerges in the range of $0.1 < St < 0.4$.

Good qualitative agreement was found by Lian et al. (2008) between a set of different computational methods and Particle Imaging Velocimetry experiments using a pitching and plunging SD7003 airfoil. They considered two cases, one of them was a pure plunging motion and the other was a pitching and plunging airfoil, where pitch led plunge by 90° , with a mean angle of attack of 8° , pitch amplitude of 8.42° and dimensionless plunge amplitude of 0.5, corresponding to a reduced frequency of 0.25 and peak effective angle of attack of 13.6° , which is beyond the static stall angle (Ol et al., 2005). This case was an example of weak dynamic stall and momentum wake profiles from the experiment results showed net drag producing wake whereas computations for time-averaged force show a slight positive drag.

Most of the viscous flow calculations of flapping airfoils assume either pure laminar or fully turbulent flow. Windte and Radespiel (2008) transitional flow simulations included laminar separation bubbles which could create additional pressure drag as they displace the outer inviscid flow. Their zero mean angle of attack flapping simulations used a phase shift of 90° as pitch led the plunge. They showed that the amount of thrust could be controlled by changing the motion amplitudes and maintaining good propulsive efficiency. The maximum propulsive efficiency was obtained when the ratio of pitch and plunge amplitude (λ) was 0.8 and the reduced

frequency k was 0.25. For pure plunge motion ($\lambda=0$) the vortex losses and hence drag losses are large, indicating that pure plunge is not suited to obtain high efficiencies.

Kang et al. (2009) studied the Reynolds number effects on the flow field of a pitching and plunging SD7003 airfoil. Their choice of experimental parameters ensured the airfoil to “*feather*”, with the geometric angle partially cancelling the plunge-induced angle of attack. They observed a leading edge vortex only for low Reynolds number flow at $Re=1\times 10^4$ in the experimental data showing reversed flow at the upper surface of the airfoil with a thicker boundary layer. With a higher Reynolds number of 3×10^4 , the agreement between experimental and numerical simulations was improved.

McGowan et al. (2009) used different numerical approaches to determine the kinematic parameters that would produce an equivalence between pure plunge or pure pitch cases with the combined pitch and plunge motion to support the validity of superposition. They found combinations of pitch and plunge motions with zero net lift coefficient. They noticed that when lift coefficient time history matched between a pure pitch and a pure plunge case, the flowfield behaviors can be quite different due to the circulatory effects that dominate at high reduced frequency flows.

Rival and Tropea (2009) investigated the dynamic stall characteristics of a pitching, plunging and combined pitching and plunging SD7003 airfoil at low Reynolds numbers using direct force measurements and smoke visualization experiments. They stated that the mean angle of attack is an important parameter since it affected the level of dynamic stall over the profile. They observed an increase in lift for the higher reduced frequency cases, accompanied by large nose-down pitching moments (moment stall) when operating at deep stall or beyond.

Shallow stall of a combined pitching and plunging and deep stall of pure plunging SD7003 airfoil are compared by Ol et al. (2009) using experimental, computational and numerical methods to validate lift coefficient prediction by the attached-flow theory even in the presence of significant separation. For combined pitching and plunging cases, the Laminar Separation Bubble (LSB) shrank with increasing Reynolds number and diminished for flow at $Re = 75000$. Their results showed good agreement between computation and experiment for the shallow-stall case, whereas although a qualitatively similar leading edge vortex size is obtained, computed flow

separation lags that of the experiment in the deep-stall case. This study was sustained by Bernal et al. (2009), where they conducted force measurements during mild and deep stall of plunging and pitching and plunging motions of an SD7003 airfoil. Their force measurements show that the pure plunge case has significantly larger lift coefficients compared to the combined pitch-plunge case. Their unsteady flow results for pure plunge oscillations with large effective angle of attack showed that the detachment of the leading edge vortex and the formation of the trailing edge vortex initiate an increase in lift coefficient, which is well above Theodorsen's unsteady linear theory prediction.

The abovementioned computational and experimental studies using NACA0012 and SD7003 airfoil profiles for combined pitching and plunging motions are summarized in Table 1.1.

Table 1.1 : Summary of recent studies on pitching and plunging foils.

Author	Type of Study	Foil cross section	pivot point	Re	$k = \frac{\pi fc}{U_\infty}$	$h = \frac{h_0}{c}$	kh	$St = \frac{2h_0 f}{U_\infty}$	α	ψ	Remarks
Triantafyllou et al. (1991)	2D Exp.	NACA0012	3/4 c	25700	0.31 0.43	1.27		0.25 0.35	19.3° 26.1°	90°	Max. $\eta_P = 0.2$ at $St=0.25$
Anderson et al. (1998)	2D Exp.	NACA0012	1/3 c	1100		0.25		0.05-0.6	0° - 60°	75°-105°	Max $C_{Tmean} = 0.77$ at $St=0.32$, $\psi = 105^\circ$, $\alpha_{max} = 20.4^\circ$, $h/c=0.75$.
				40000		0.75			5° - 30°		Max $\eta_P = 0.87$, $C_{Tmean} = 0.67$ at $St=0.3$, $\psi=75^\circ$, $\alpha_{max}=20.2^\circ$, $h/c=0.75$.
Isogai et al. (1999)	2D Compr. Navier-Stokes	NACA0012	1/2 c	10^5	0.4 - 1.0	1			20°	30°-150°	Max. $\eta_P = 0.72$ at $\psi = 90^\circ$, $k=0.5$; Max. $C_{Tmean} = 0.70$ at $\psi = 120^\circ$, $k = 1.0$
					0.15 - 0.5	2		10°	Max. $\eta_P = 0.8$ for $\psi = 90^\circ$, $k = 0.15$; Max. $C_{Tmean} = 1.0$ for $\psi = 60^\circ$, $k = 0.15$		
Tuncer and Platzer (2000)	2D Compr. Navier-Stokes (M=0.3)	NACA0012	1/2 c	10^5	0.15, 0.5	1	0.15, 0.15		10°	30°, 90°	Max. $\eta_P = 0.86$, $C_{Tmean} = 0.072$ at $\psi = 90^\circ$, $k = 0.15$; Max. $C_{Tmean} = 0.44$, $\eta_P = 0.25$ at $\psi = 90^\circ$, $k = 0.5$
				10^4	0.5, 0.67	0.75	0.375, 0.5025		7° - 20°	75°	Max $\eta_P = 0.56$, $C_{Tmean} = 0.177$ at $\alpha_0=20^\circ$, $k = 0.5$; Max $C_{Tmean} = 0.44$ $\eta_P = 0.26$ at $\alpha_0=10^\circ$, $k=0.65$
Ramamurti and Sandberg (2001)	2D Incompr. Navier-Stokes	NACA0012	1/4 c	1100	1.88				15°	90°	Max. $C_{Tmean} = 1.35$ at $St=0.6$
					2.64	1		0.6	30°	30°-140°	Max. $C_{Tmean} = 2.42$, $\eta_P = 0.24$ at $k= 2.64$, $\psi = 120^\circ$ Max. $\eta_P = 0.3$ at $k = 2.64$, $\psi = 90^\circ$

Table 1.1 : (Continued) Summary of recent studies on pitching and plunging foils.

Author	Type of Study	Foil cross section	pivot point	Re	$k = \frac{\pi fc}{U_\infty}$	$h = \frac{h_0}{c}$	kh	$St = \frac{2hf}{U_\infty}$	α	ψ	Remarks
Read et al. (2002)	2D Exp.	NACA0012	1/3 c	40000	0.125-0.94	0.75, 1	0.047 - 0.345	0.06-0.44	10° - 40°	80°-100°	Max. $\eta_P = 0.715$, $C_{Tmean} = 0.18$ at $\psi = 90^\circ$, $St=0.16$, $\alpha_{max} = 15^\circ$ $C_{Tmean} = 2.41$, $\eta_P = 0.43$ at $\psi = 100^\circ$, $St=0.6$, $\alpha_{max} = 35^\circ$
Guglielmini and Blondeaux (2003)	2D Stream fnct'n vort. eqt'n	NACA0012	1/3 c	1100				0.3, 0.35	0°, 15°, 30°	75°-105°	Max. η_P for $10^\circ < \alpha_{max} < 20^\circ$ at $St = 0.25$
Hover et al. (2004)	2D Exp.	NACA0012	1/3 c	30000		1		0.2-0.8	10°-35°	90°	Max. $\eta_P = 0.64$, $C_T = 0.624$ at $St=0.35$, $\alpha_{max} = 20^\circ$ for cosine $\alpha(t)$ profile Max. $C_T = 6.02$, $\eta_P = 0.3$ at $St=0.8$, $\alpha_{max} = 35^\circ$ for sawtooth $\alpha(t)$ profile
Tuncer and Kaya (2005)	2D Navier-Stokes (M=0.1)	NACA0012	1/2 c	10^4	0.5	0.45-1.6			5° - 36°	30°-103.4°	Max. $\eta_P = 0.68$, $C_T = 0.18$ at $\phi=86.5^\circ$, $k = 0.5$; Max. $C_T = 1.45$, $\eta_P = 0.36$ at $\phi=94.9^\circ$, $k = 0.5$
Schouveiler et al. (2005)	2D Exp.	NACA0012	1/3 c	40000		0.75		0.1-0.45	10° - 35°	90°	Max. $\eta_P = 0.73$, $C_{Tmean} = 0.32$ at $St = 0.25$, $\alpha_{max} = 15^\circ$ Max. $C_{Tmean} = 1.05$, $\eta_P = 0.42$ at $St = 0.45$, $\alpha_{max} = 30^\circ$
Yang et al. (2006)	3D Compr. Euler / N-S (M=0.1-0.3)	NACA0012	1/4 c, 1/3 c, 1/2 c		0.1-1	0.75, 1, 1.25			10°, 20°, 30°	0°-180°	Max. $\eta_P = 0.9$, $C_T = 0.236$ at $k=0.22$, $\psi = 68.5^\circ$

Table 1.1 : (Continued) Summary of recent studies on pitching and plunging foils.

Author	Type of Study	Foil cross section	pivot point	Re	$k = \frac{\pi fc}{U_\infty}$	$h = \frac{h_0}{c}$	kh	$St = \frac{2h_0 f}{U_\infty}$	α	ψ	Remarks
Young and Lai (2007b)	2D Compr. N-S	NACA0012	1/3 c	20000-40000	0 - 2.15	0.25, 0.75		0 - 0.6	-15° - 55° $\alpha_0 = 5^\circ, 15^\circ$	75°, 90°	Max. η_P at $0.1 < St < 0.4$.
Lian et al. (2008)	2D Exp.	SD7003	1/2 c	60000	0.25	0.5			8.42° $\alpha_0 = 8^\circ$	90°	No leading edge vortex visible. Net drag production.
	2D Incompr. Navier-Stokes										RANS without transition: $C_{Lmean} = 0.8$, $C_{Dmean} = 0.016$, no leading edge vortex visible.
											RANS with transition: $C_{Lmean} = 0.85$, $C_{Dmean} = 0.04$, separation bubble visible.
											DES: $C_{Lmean} = 0.88$, $C_{Dmean} = 0.07$, separation bubble visible.
Windte and Radespiel (2008)	Unsteady Re-ave. N-S	SD7003	not stated	60000	0.25, 0.5, 1.0	0.1			$\alpha_0 = 0^\circ$	90°	Max. $\eta_P = 0.84$ for $\psi = 90^\circ$, $k = 0.25$ and $\lambda = 0.8$.
Rival and Tropea (2009)	2D Exp.	SD7003	1/4 c	60000	0.05, 0.1	0.5			-10°, 2.5° $\alpha_0 = 5^\circ, 10^\circ$	90°	Max. $C_L = 1.95$ with $\alpha_{max} = 23^\circ$ at $k = 0.1$ and $\alpha_0 = 10^\circ$
Ol et al. (2009) and Bernal et al. (2009)	2D Exp./ Re-ave. N-S	SD7003	1/4 c	60000	0.25	0.5		0.08	8.42° $\alpha_0 = 8^\circ$	90°	at $\alpha_{eff} = 14.03^\circ$, max. $C_L = 1.35$ (Exp.), max. $C_L = 1.45$ (RANS)

1.5 Practical Applications

Apart from the parametrical studies on motion kinematics by aerodynamicists, the unsteady aerodynamics of biological flyers and swimmers has been the subject of many investigations by biologists and vehicle designers as well as governments' concern for development of spy drones.

The first flight of an insect-sized unmanned air vehicle (UAV) was accomplished in the 1970s by the 'Insectohtopter', developed by United States of America's Central Intelligence Agency (CIA)'s Office of Research and Development. It was the size of a dragonfly and painted to look like one, as can be seen in Figure 1.22. Although it was noted that the test flights were very successful, the project was abandoned because of the difficulty of controlling crosswinds (Url-1).



Figure 1.22 : The Insectohtopter (adopted from Url-1).

In 1992, The Defense Advanced Research Projects Agency (DARPA) of the United States Department of Defense conducted a workshop titled "Future Technology-Driven Revolutions in Military Operations" and one of the discussion topics was "mobile microrobots". The microdrone concept was released in 1994 by the RAND Corporation and engineering studies by the Lincoln Laboratories at the Massachusetts Institute of Technology and the United States Naval Research Laboratory in Washington DC demonstrated that the concept was feasible. In 1997, DARPA began a multi-year program to develop micro air vehicles (MAVs) with largest dimension no more than 15 centimeters, which would carry a day-night imager; have an endurance of about two hours; and be very low cost (Url-2).

Apart from fixed-wing and rotary-wing designs, flapping-wing concept was also designed and tested for DARPA's MAV project.

The first electrically powered palm-sized ornithopter was the ‘MicroBat’ developed at the California Institute of Technology along with AeroVironment Inc. and University of California Los Angeles in 1998. The first prototype was powered by two super capacitors and was flown for 9 seconds (Figure 1.23a). To achieve a longer flight, a rechargeable battery as a power source was used for the second prototype which had a flight performance of 22 seconds (Figure 1.23b). The latest prototype was radio-controlled and capable of turning left or right, pitching up or down, weighed 12.5 grams and the best flight duration achieved was 42 seconds (Figure 1.23c) (Url-3).

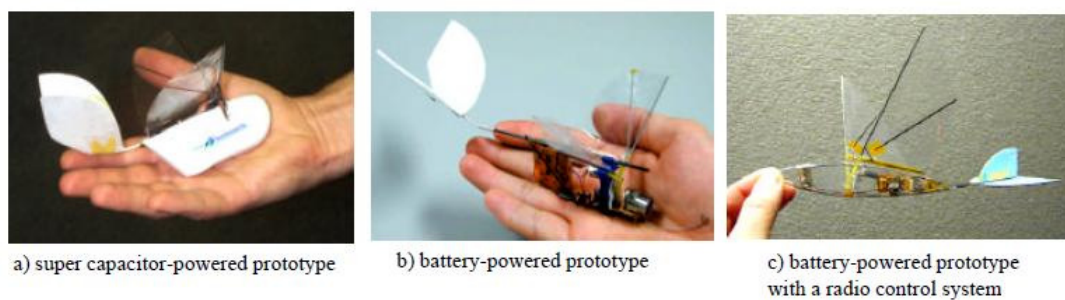


Figure 1.23 : The MicroBat prototypes (adopted from Url-3).

The world's first mechanical hummingbird, the ‘Mentor’ (Figure 1.24), was built by a research group from University of Toronto Institute for Aerospace Studies in Canada, in collaboration with Stanford Research Institute. This hovering ornithopter also holds promise of transitioning into efficient high-speed horizontal flight (Url-4).

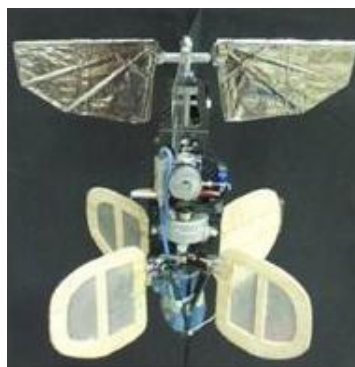


Figure 1.24 : The Mentor (adopted from Url-5).

University of Toronto Institute for Aerospace Studies research group was also able to develop a jet-engine-assisted, human-piloted ornithopter, the ‘Flapper’ in 2006 (Figure 1.25), which sustained level flight for 14 seconds covering a distance of over a third of a kilometer (Url-6).



Figure 1.25 : The Flapper (adopted from Url-6).

Development of a Nano Air Vehicle (NAV) that mimics the wing movement of a hummingbird that has 20 minutes of flight time and can withstand 2.5 m/s wind gusts is also a project supported by DARPA. AeroVironment Inc. researchers have developed a prototype (Figure 1.26) and made a successful test flight, lifting itself and its energy source. This demonstration aircraft at the end of Phase-I program was constrained on a hinged beam (Url-7).



Figure 1.26 : The NAV demonstrator vehicle (adopted from Url-7).

DARPA's NAV program continues in Phase-II where the conceptual NAV in smaller size and weight will be able to use a pair of flapping wings for both propulsion and flight control, climbing, descending and flying forwards, backwards and sideways in hover. The drone will be called 'NanoSCOUT' (Figure 1.27) and will be painted to resemble a hummingbird (Url-8).



Figure 1.27 : The NanoSCOUT (adopted from Url-9).

Another hummingbird inspired micro air vehicle is designed by a research group at Cornell University, which was 24 g including batteries and was capable of flapping-hovering flight. The design consists of independently powered four pairs of wings (Figure 1.28) and intended to operate in a similar manner to an insect, taking advantage of passive wing bending and the clap-and-fling effect (Url-10).

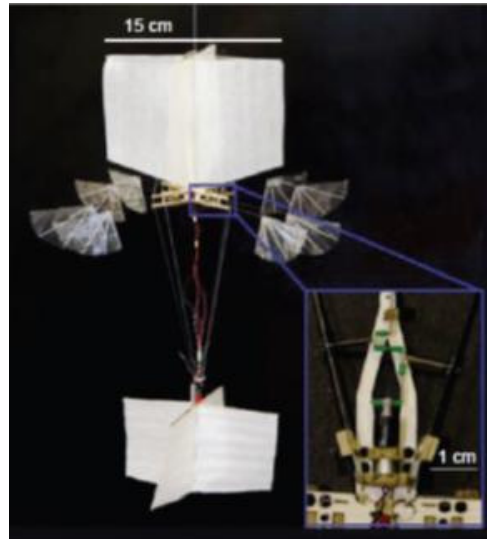


Figure 1.28 : The MAV of Cornell University (adopted from Url-10).

A design team from Georgia Tech Research Institute made another ornithopter called the ‘Entomopter’. Their aim was to closely mimic the flight of birds and eliminate the usage of gears and motors (Url-11). The Entomopter (Figure 1.29) is propelled by a pair of flapping wings driven by a Reciprocating Chemical Muscle (RCM) which is capable of generating autonomic wing beating from a chemical energy source without an ignition source, combustion, or atmospheric oxygen (Url-12).



Figure 1.29 : The Entomopter (adopted from Url-12).

Robotic flies could also be well-suited as a new generation of interplanetary explorers. In 2001, NASA Institute for Advanced Concepts (NIAC) funded the second phase of the Entomopter study to develop an autonomous Mars surveyor for

flight in the lower atmosphere of Mars (Url-13). The anaerobic RCM propulsion system would function without oxidizers in the rarefied and carbon dioxide Mars atmosphere (Url-12), making Mars Entomopter ideal for upcoming Mars micro-missions.

About 30 years after the ‘Insectothopter’, another robot-dragon fly, the ‘DelFly’, was built by the MavLab of Technical University of Delft in Netherlands in 2005 (Url-14). The original DelFly-I was a micro-aircraft measuring 50 cm and weighing 23 grams that could detect objects through image recognition. A year later DelFly-II was designed and built measuring 28 cm and weighing 16 grams and could carry a camera that could transmit the images to the ground station. It could fly horizontally for 15 minutes at a velocity of 10 m/s or hover for 8 minutes and fly backwards at a velocity of -0.5 m/s, making it the first ornithopter in the world that has such a wide flight envelope without any adjustments in its configuration (Url-15). An illustration and a photograph of DelFly-II can be seen in Figure 1.30.

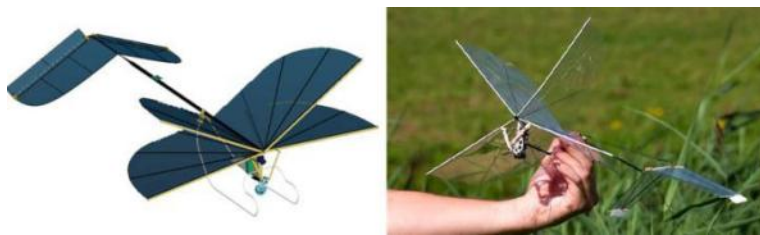


Figure 1.30 : DelFly-II (adopted from Url-15).

The DelFly-Micro is the same group’s new Micro Air Vehicle (MAV), developed in 2008, and it measures 10 cm from wingtip to wingtip, while weighing 3 grams. It can be seen in Figure 1.31.



Figure 1.31 : DelFly-Micro (adopted from Url-16).

An even smaller fly-like MAV with 3 cm in length and weighing 65 milligrams was able to fly in 2007 by a team from Harvard University, however it could only fly while attached to a rope-like tether that supplies power whereas the DelFly-Micro has a battery on board. On the other hand, unlike the DelFly-II, the DelFly-Micro

cannot hover in the air or fly backwards (Url-16). It has been noted that the DelFly-Micro is very useful for the progress of science, being an ideal platform to study the aerodynamics and autonomy of small, flying ornithopters. The research group's next aim is to manufacture DelFly-Nano with a wingspan of 5 cm and weight of 1 gram.

The United States Air Force is also funding a number of research projects in universities across the United States for MAVs about the size of a sparrow, ready to fly by year 2015 and even smaller, dragonfly-sized drones ready to fly in swarms by year 2030 (Url-17).

The 'BITE-Wing' (Biplane Insectoid Travel Engine) is a flapping-wing micro air vehicle with no fixed lifting surfaces and it has been developed by the United States Naval Research Laboratory. During a flapping cycle, the biplane-configured wing pairs clap against each other and then separate, similar to the technique observed in insect flight. The vehicle uses the same structure for flight, hover, hop takeoffs, and ground locomotion. The BITE-Wing experimental research vehicles shown in Figure 1.32 are 40 cm long and weigh 20 grams (Url-18).

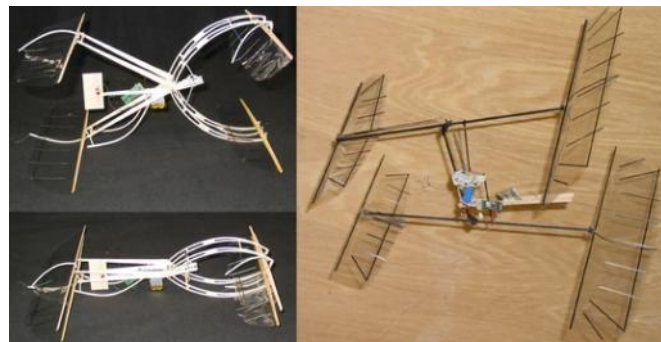


Figure 1.32: BITE-Wing (adopted from Url-18).

Researchers from United States Naval Postgraduate School (NPS) developed and flight tested a radio controlled MAV propelled with a different configuration of bi-plane flapping wing (Figure 1.33). They used a large fixed wing to develop most of the vehicle lift, followed by a bi-plane pair of wings flapping in counterphase to produce thrust, simulating a single wing flapping in ground effect (Url-19). The downstream placement of the flapping wings helps prevent flow separation over the main wing, allowing the aircraft to fly efficiently at very low speeds with high angles of attack without stall (Url-20).

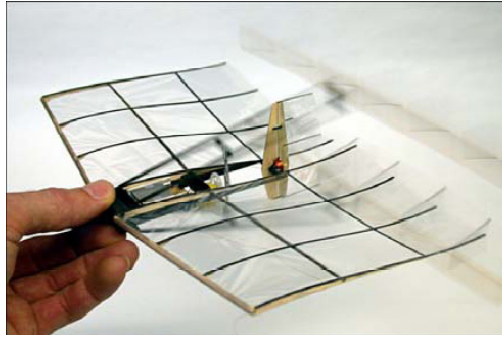


Figure 1.33 : NPS flapping wing MAV (adopted from Jones and Platzer, 2009).

Oscillating wing designs have also been considered for applications of mechanical power generators to harvest water energy.

Although not yet widely used, tidal power has potential for future electricity generation and flapping wings holds a possible future system for tidal energy. In 2003, a novel wave energy converter with oscillating hydroplane device, the ‘Stingray’, developed by Engineering Business Ltd. Scotland, was tested off the Scottish coast, Shetland (Url-21). The Stingray uses hydrofoils to create oscillation (Figure 1.34), which allows it to create hydraulic power (Url-22).



Figure 1.34: The Stingray (Url-23).

BioPower Systems. Ltd Australia is also looking to develop biomimicry technologies based on tidal energy conversion in an ocean environment. Their pilot study of the ‘bioSTREAM’(Figure 1.35) will be operating at Tasmania, Australia in 2010 (Url-24), which mimics the shape and motion characteristics of Thunniform mode swimming species (Url-25).



Figure 1.35: The bioSTREAM (Url-24).

In 2004, the stroke-wing engine ‘HFG3’ of ANIPROP GbR Germany was launched in Augsburg, Germany to extract energy from the small, fast flowing river channel Mittlerer Lech (Figure 1.36). The development pursues the goal of gaining renewable energy directly from the kinetic energy in the flow with the physical concept of a coupled pitching and plunging motion (Url-26).



Figure 1.36 : The stroke-wing engine HFG3 (Url-26).

An innovative renewable energy source concept has been proposed in belief that huge kite-like wind-power generators could be the solution to the world’s electrical requirements (Url-27). A research group from University of Technology in Sydney, Australia in collaboration with Sky WindPower California has broadened this idea and is trying to harness jet stream energy over continents (Url-28).

Moreover, it is a new initiative that using flapping wings on an Unmanned Aerial Vehicle (UAV) such as the solar powered High Altitude Long Endurance (HALE) vehicle like the Zephyr (Url-29), might turn out to be a possible option of extracting power from the potential wind energy in the jet stream with higher efficiencies (Platzer, 2009).

1.6 Overview of Unresolved Issues

Flying animals flap their wings to generate lift and thrust besides performing remarkable maneuvers with rapid accelerations and decelerations. It is apparent that a better understanding of the propulsion mechanism of birds, insects and fish is essential for the development of lighter, more efficient and more maneuverable micro air vehicles or to be used for similar applications.

In comprehension of motion kinematics of flapping wings, the aforementioned literature survey of experimental and numerical investigations provide valuable information on a range of unsteady aerodynamic problems; however, most of the studies are devoted to either pure plunge or pure pitch motions. Due to the complexity of the problem and large number of governing parameters, the combined pitch and plunge motion of the flapping wings, the effect of non-dimensional parameters, the occurrence of different flow structures and hence thrust or drag production on a parameter space are left relatively unexplored.

Besides the role of major non-dimensional parameters, unresolved issues also includes topics such as the three-dimensionality of a nominally two-dimensional flapping wing, the effect of phase angle between pitch and plunge, the use of unequal pitch and plunge frequencies.

Three-dimensional behavior of oscillating airfoils has also gained some attention in recent years. Von Ellenrieder et al. (2003) investigated the flow behind a heaving and pitching finite-span wing using dye flow visualization at a Reynolds number of 164 to model the three-dimensional vortex structures. Dong et al. (2006)'s analysis of vortex topology showed that the wake of low aspect ratio flapping foils is dominated by two sets of interconnected vortex loops that evolve into distinct vortex rings as they convect downstream. The spanwise flow over pitching and plunging airfoils was also investigated experimentally by OI (2007) and numerically by Lian (2009a).

In most of the studies of combined pitching and plunging airfoils in literature, the phase angle between pitch and plunge motions is usually kept at $\psi = 90^\circ$ where pitch leads the plunge. In experimental studies, Anderson (1996) and Anderson et al. (1998) used a NACA0012 airfoil profile and varied the phase angle between 30° and 110° . They reported highest efficiency values for the phase angle between heave and pitch of about 75° and highest thrust coefficient for $\psi = 105^\circ$, when the reference

point for heave motion is at the one-third chord length from the leading edge. Later on, Read et al. (2003)'s study revealed similar results; their range of phase angle was between 75° and 105° in their experiments and found that $\psi = 90^\circ$ provides the best thrust and efficiency, and little improvement can be made by increasing ψ .

Moreover, effects of unequal oscillating frequencies of pitching and plunging motions have received little attention. Ol (2007) briefly studied the oscillations of an SD7003 airfoil experimentally where pitch and plunge frequencies differ. He considered a motion where the plunge frequency is half of the pitch frequency with pivot point at $3/4c$. He observed that a separated leading edge vortex is formed every pitch period, unlike all prior tested pure plunge cases.

Webb et al. (2008) also considered the effects of unequal pitch and plunge motion of an SD7003 airfoil, with various pitch pivot locations, trying to model the gust response with the lower-frequency motion where the higher-frequency motion is the kinematics of the flapping MAV. They considered results based on experiments at $Re = 10000$ and computations at $Re = 1000$, stating a similar vortex shedding behavior. For the case where the pitch frequency is double the plunge frequency and the pitch pivot point is at half chord, they point out a discrepancy between experiment and computational results, experiments showing a deflected wake at quarter period position for the airfoil's second period of motion. Flow visualization with dye injection showed that placing the pivot point closer to downstream location results in the formation of a stronger leading edge vortex. They observed the reverse Karman vortex street when they switched to the standard case of equal pitch and plunge frequencies. Their study leaves many aspects unmentioned, hence the role of unequal oscillation frequencies on the formation of vortex structures and the production of lift and thrust are yet to be explored.

1.7 Objectives of the Study

Motivated with practical applications to micro air vehicles with the size of small birds that do not glide but flap wings instead, and with the aid of the aforementioned literature review, an experimental study is conducted using a pitching and plunging airfoil in steady water flow, to observe the relationships between the flapping parameters and the related leading and trailing edge vortex formation and their interaction to comment on how they contribute to lift and propulsion and how to

optimize the process. The overall objectives of this study are to determine the classes of vortex formation around and in the near-wake of a SD7003 airfoil model undergoing pitching and plunging motions in a steady current, to characterize a detailed quantitative evaluation of flow structures with instantaneous patterns of vorticity, to obtain averaged velocity profiles in the near-wake in order to comment on thrust or drag production and to relate these vorticity patterns to the loading on the airfoil. Besides changing the plunge amplitude, the freestream speed and frequency of motion to explore the occurrence of different flow structures in a two-dimensional parameter space, effect of phase angle between pitch and plunge motions, effect of mean angle of attack and pitching amplitude, effect of use of unequal oscillating frequencies for pitch and plunge motions and three-dimensionality in the near-wake of the nominally two-dimensional wing are also considered in the scope of this study.

1.8 Outline of Dissertation

In Chapter 1, an introduction to flapping wing aerodynamics has been given as well as the motivation of the current study. Significant parameters are summarized prior to the literature review. Practical applications have also been addresses and unresolved issues are pointed out. Chapter 1 finally includes the objectives of the current study.

Chapter 2 describes the experimental setup and the techniques used in this study. The results are given in Chapter 3. Chapter 4 summarizes the major contributions of this experimental study and provides recommendations for further investigations.

Appendices give details of experimental cases and derivation of the theoretical efficiency according to Prandtl (1952).

2 EXPERIMENTAL SYSTEMS AND TECHNIQUES

2.1 Flow System

Experiments were performed in the close-circuit, free-surface, large scale water channel located in the Trisonic Laboratories at the Faculty of Aeronautics and Astronautics of Istanbul Technical University. The test section is constructed of transparent plexiglas and formed of three segments with upstream and downstream PVC reservoirs. City water is filtered first to fill an external reservoir and then a second filtration system made of a series of 25 μ polypropylene sediment and 5 μ carbon filters is used parallel to the water channel closed circuit system. By means of a centrifugal pump, water in the settling chamber section is forced to flow through the flow conditioners and then through the 2:1 contraction section, where it is accelerated into the test section. After the test section, water is directed into the downstream reservoir and then is sent back to settling chamber by a 28cm-diameter pipe.

A set of honeycomb and five screens, whose locations and cell sizes are determined according to Reshotko et al. (1997), are used to condition the flow to provide low levels of turbulence in the test section. Although LDA measurements are carried out to determine the turbulence intensity, due to the limitation of the system (Park et al., 2005), it is not possible to determine a value under 1%. The water channel used in the experiments is a replica of one of two water channels located in the Fluid Mechanics Laboratories of Lehigh University with the exception of length of the test section, which is 5.85m for our channel instead of 4.5m. Hot film measurements yielded turbulence intensity of the order of 0.2% maximum for the water channel at Lehigh University so it is expected that the turbulence intensity of our channel is below 1% and anticipated that it is about 0.2% as in the original channel. The coefficient of variation equivalent to turbulence intensity is measured to be 0.029 for $U_{\infty}=0.0058$ m/s (Aydin et al., 2010).

The cross section dimensions of each of the three test section segments are 1010 mm \times 790 mm. In this study, the first segment right after the contraction section is used. The water flow velocity at the test section is adjusted via an ABB AC drive (ABB-ACS800-01) controlling the RPM of the centrifugal flow pump. The flow speed vary linearly and calibrated for a test section water depth of 713 mm according to $U_{\infty}[\text{mm/s}] = (0.091 \times \text{RPM}) + 1.047$.

Extensive DPIV measurements are carried out to determine flow uniformity in different parts of the test section and the results showed that the flow is uniform above $U_{\infty} = 4.7$ mm/s. The experiments were conducted at flow speeds ranging from 8.3 mm/s to 137.5 mm/s, corresponding to Reynolds number of 825 to 13 700 based on the airfoil chord. Additional information about water channel specifications can be seen in Aydin (2008), and summarized in Appendix A.1.

2.2 Model and Mounting

An airfoil with SD7003 profile is produced in CNC milling machine with a chord length of 10cm and span of 30cm. It is manufactured of transparent plexiglas and allows laser light to illuminate both the suction and pressure sides. This airfoil has a maximum thickness of 8.5% and camber of 1.48% (Url-30). The SD7003 airfoil is optimized for flows of low Reynolds number below 10^5 and it exhibits long, stable laminar separation bubble (LSB) over a broad range of angle of attack therefore it can be considered for applications to micro air vehicles (Ol et al., 2005, Windte et al., 2006). There is also high quality experimental Particle Image Velocimetry (PIV) data available for this airfoil in static conditions; such as the studies by Radespiel et al. (2007) and Zhang et al (2008). Aerodynamic load measurement comparisons for this stationary airfoil in three different facilities are also available from Ol et al. (2005). The selection of the airfoil profile is motivated by a NATO-RTO task group AVT-149 (Ol, 2009b).

The airfoil model is mounted in a vertical cantilevered arrangement in the water channel about its quarter chord as shown in Figure 2.1. The connection rod connects the airfoil to the servo motor to provide a sinusoidal pitching motion via a coupling system which itself is connected to a linear table. Two rectangular end plates made of plexiglas of 98cm \times 150cm with 30° outward bevel are suspended from the top of the channel about 5mm above and below the fully submerged airfoil to reduce the end

effects. The top end plate is painted mat-black to avoid background reflections and it has a 65mm slit to ensure the maximum plunging motion amplitude. The blockage ratio of the airfoil at its maximum angle of attack is 1.6%.

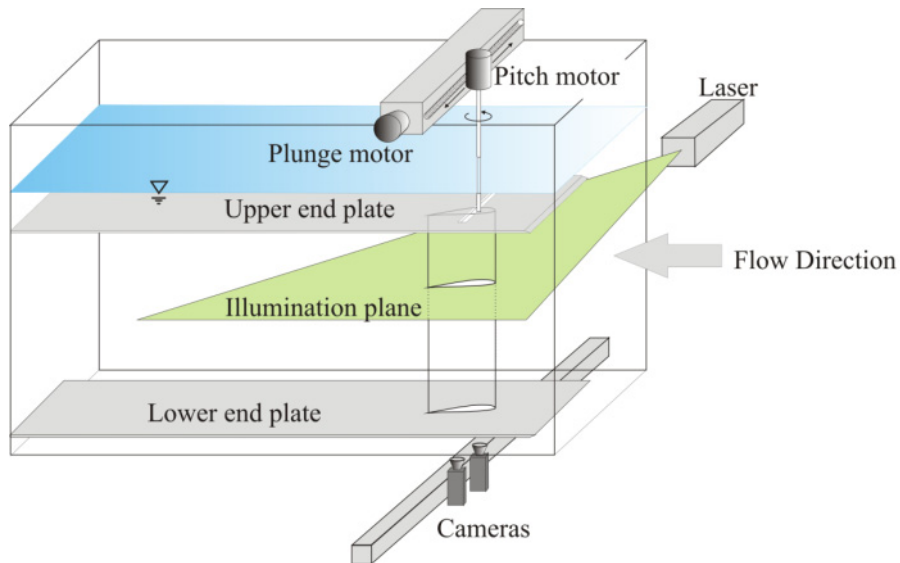


Figure 2.1 : Experimental arrangement.

2.3 Airfoil Motion

The pitching and plunging motions of the airfoil are described in Chapter 1 with Equation (1.1) and Equation (1.2).

The sinusoidal pitching and plunging motion profiles are generated by a signal generator Labview VI (Virtual Instrument) for the given frequency, amplitude and mean offset values of pitch and plunge. The data acquisition of the PIV system is triggered using a step-trigger function by the same VI at the beginning of the third motion cycle of the airfoil oscillation and the synchronization is achieved using a National Instruments PCI-6601 timer device.

The motion of the airfoil is provided by two Kollmorgen/Danaher Motion AKM33E servo motors, one for each axis. The servo motors are connected to a computer via digital servo amplifiers with different servo drivers and graphical user interfaces (GUI); ServoSTAR S300 is used for pitch and ServoSTAR S600 is used for plunge. The position signal that is generated by the VI is transmitted to servo driver control unit and transformed into velocity signal. The following error between the position command and the actual motion is less than 1mm for plunge and less than 1° for pitch motions. The smoothing coefficients are determined to adjust the position and

velocity gain parameters for each frequency and amplitude of the experimental test cases for plunge motion. The use of low and high pass filters to decrease the vibrations of the servo velocity loop control signal is sufficient for pitching motion.

Maximum rotation speed of the pitching servo motor is 5000 rpm, rated (optimum) speed is 4000 rpm and its optimum torque is 2.34Nm, and for plunging servo motor, the values are 5490 rpm, 4500 rpm and 2.34 Nm respectively.

2.4 Image Acquisition

Instantaneous quantitative flow images are captured and processed by a Digital Particle Image Velocimetry (DPIV) system. It is a non-intrusive, optical laser flow measurement technique to acquire time dependent velocity fields. First comprehensive reviews of PIV techniques are given by Adrian (1989, 1991), Rockwell et al. (1992, 1993) and recently by Raffel et al. (2007).

Very briefly, the PIV technique provides instantaneous velocity vector measurements in a cross-section of a flow. In principle, the velocity vectors are derived from subsections of the target area of the particle-seeded flow by measuring the movement of particles between two light pulses.

Prior to the experiments, the water in the channel, with a volume of approximately 14m^3 , is seeded with 25 grams of silver coated hollow glass spheres with a mean particle diameter of $10\mu\text{m}$ and density of $1.1\text{g}/\text{cm}^3$.

For this study a single plane DPIV is employed using DynamicStudio v2.21 software (Dantec Dynamics A/S) for image acquisition and interrogation. The seeded flow is illuminated by a dual cavity New Wave Solo-PIV Nd:Yag laser, with 15 Hz repetition rate for each cavity. Time between the pulses of two laser cavities is set to $2000\mu\text{s}$. The maximum output energy of the laser is 120 mJ per pulse at 532 nm wavelength with pulse duration of 3-5 ns. A beam expander is used to form and adjust the thickness of the laser sheet which horizontally illuminates the flow field and the vertically mounted airfoil from one side of the water channel.

Two 10-bit Dantec Dynamics FlowSense 2M CCD cameras with Nikkor 60mm/f 2.8D lenses are positioned underneath the water channel at two different locations for image acquisition. After a set of experiments are completed at one location focusing

on the flow around the airfoil, the cameras are shifted downstream to the other location to observe the near-wake structures.

Image pairs are recorded at two different acquisition rates per each investigated case. To allow phase averaging, the image acquisition frequency is set to record 200 images for 50 periods of the airfoil motion and then the same case is repeated for detailed analysis of the motion cycle by recording at least two periods for each individual motion frequency, giving a total of 340 sets of data. The details of the parameters for each set are given in Appendix A.2.

It should be noted that for a limited number of cases the flow structures on a cross-section parallel to the planform area of the wing have been also recorded to allow insight into the three-dimensionality of the flow. Although the image acquisition equipment is the same, a single camera is used. The experimental arrangement and the visualized flow field are sketched in Figure 2.2.

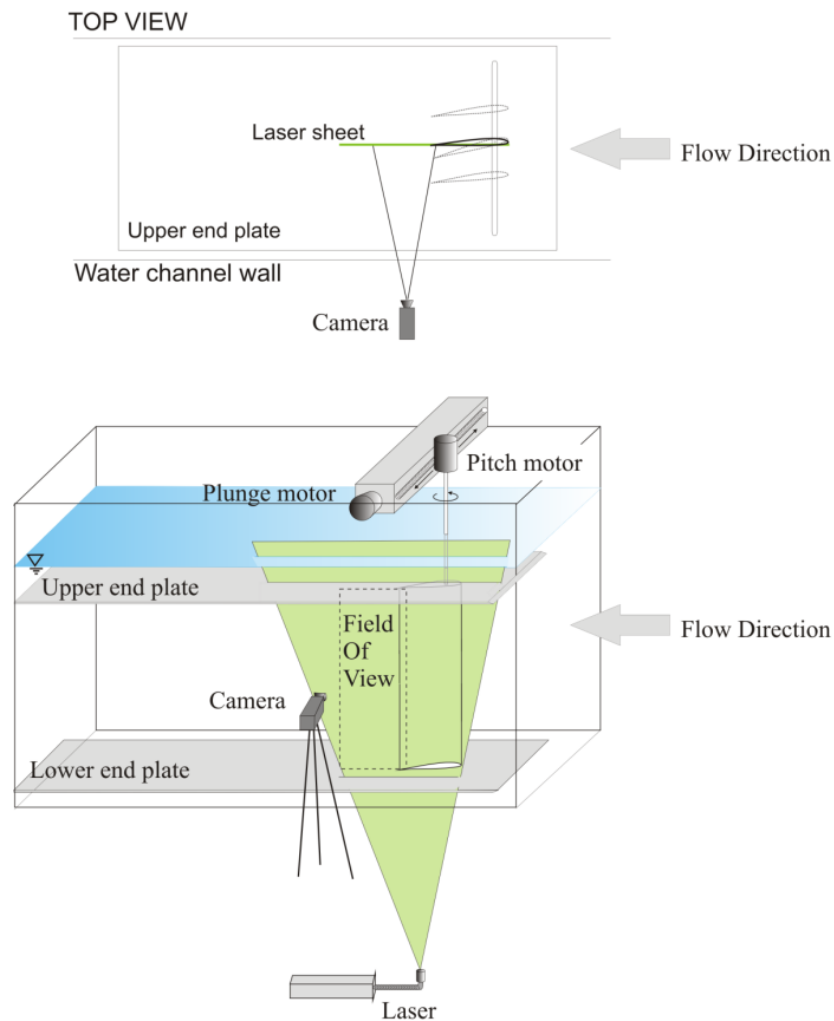


Figure 2.2 : Experimental arrangement for three-dimensionality investigations.

2.5 Post-Processing

For each location, the two images from the two cameras are stitched before interrogation by an in-house script run in the MATLAB (The MathWorks Inc., 1984) link of Dynamic Studio software. This script requires two reference points to be selected. Figure 2.3 shows field of view of the stitched images for the same case observed at two locations.

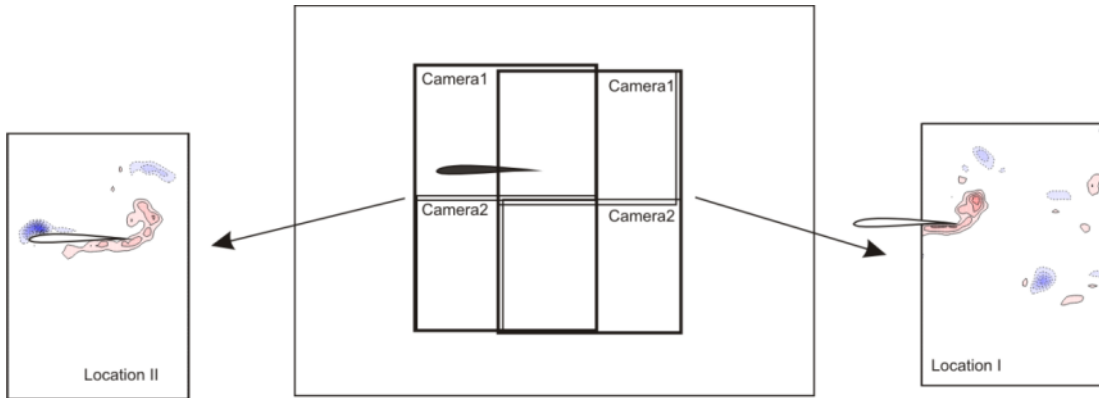


Figure 2.3 : Image areas of the cameras at two locations.

The image sizes before and after the stitching process is given in Table 2.1 for the two camera positioning locations. Their pixel resolution and corresponding image area according to the scale factors and locations used in the experiments are also given in Table 2.1.

Table 2.1: The image sizes before and after the stitching process.

		Before Stitch			After Stitch		
		Scale Factor	Image Size [pix]	Image Size [mm]	Image Size [pix]	Image Size [mm]	No. of vectors
Loc.I	Cam.1	14.76	1600×1200	174.78×131.09	1644×2357	179.5×257.4	3600 (50×72)
	Cam.2	14.91		176.57×132.43			
Loc.II	Cam.1	15.07	1600×1200	178.39×133.79	1617×2363	180.2×263.4	3528 (49×72)
	Cam.2	15.17		179.65×134.74			

Stitched images are interrogated using a double frame, cross-correlation technique with a window size of 64×64 pixels, 50% overlapping in each direction. The resulting measurement plane and number of velocity vectors are also given in Table 2.1 depending on two camera locations. The final grid resolution of velocity vectors is 3.49 mm × 3.49 mm in the plane of the flow for Location I and 3.56 mm × 3.56 mm for Location II. The image stitching and the cross correlation processes were carried out using the commercial DynamicStudio software by Dantec Dynamics A/S.

The images acquired to visualize the three-dimensionality are also interrogated using a double frame, cross-correlation technique with a window size of 64×64 pixels, 50% overlapping in each direction. The final grid resolution of velocity vectors is $7.85 \text{ mm} \times 7.85 \text{ mm}$ in the plane of the flow.

After interrogation, masking and bad vector removal and replacement procedures are applied by MATLAB scripts, the PIV vector validation software, CleanVec (Soloff and Meinhart, 1999) and the in-house code, NFILVB (Lin, 1994). Since the acquired instantaneous images show the airfoil in pitching and plunging motion, the mask has to move with the airfoil as well. An in-house MATLAB script (Percin, 2009) defines the boundary of the oscillating airfoil for each instantaneous velocity field, and creates masks in ASCII form. NFILVB is then used to blank out the vectors in the masked area. Range and magnitude difference validations are employed by CleanVec for the removal of incorrect vectors. After the areas of missing vectors were interpolated and filled with NFILVB, vector field with vorticity distribution is generated. NFILVB uses a bilinear least-square fit technique on the surrounding vectors to fill the removed vector areas. The program also employs Gaussian weighted technique based on that of Landreth and Adrian (1989) in order to smooth the resultant velocity field. A suggested smoothing parameter of 1.3 has been used for the results of this study. An ensemble-averaged velocity field for each case is obtained using the in-house program NEWNSAV (Lin, 1996). The vorticity contours and the velocity field are displayed using TecPlot software (Amtec Engineering Inc., 1988).

Error analysis is performed according to Adrian (1991) and Raffel et al. (2007). The random measurement uncertainty in PIV imaging, including uncertainty due to particle slip, uncertainty of magnification and uncertainty in locating the particle centroid, remains below 2% in total.

2.6 Thrust Estimation from DPIV Data

An average thrust force and efficiency estimate were calculated from the DPIV velocity data using the wake excess velocity and the momentum theorem expressed for a control volume bounded by a control surface, using the steps provided by Anderson et al. (1998). The control volume is sketched in Figure 2.4 where the

freestream velocity U_∞ is across the upstream boundary bc and the velocity $u(y)$ is across the downstream boundary ad .

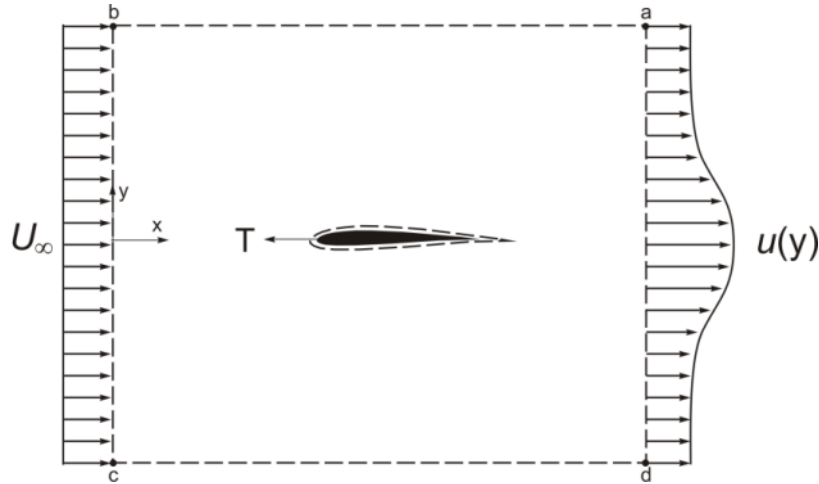


Figure 2.4 : Control volume for momentum analysis.

Assuming incompressible, steady flow with constant pressure along the control volume boundaries, the thrust on the foil T can be written in terms of the momentum flux in the x -direction as;

$$T = -F_x = \rho \int_{-\infty}^{\infty} U_\infty^2 - u(y)^2 dy \quad (2.1)$$

Applying mass conservation, Equation (2.1) simplifies to:

$$T = \rho \int_{-\infty}^{\infty} u(y)(u(y) - U_\infty) dy \quad (2.2)$$

Although full field DPIV velocity data is obtained to compute the time rate of change of momentum inside the control volume, the pressure along the control volume boundaries is not known and the assumption of steady flow is incorrect since the vortex wakes are unsteady with variable pressure. In spite of this, Anderson (1996) showed that the approximation using momentum flux calculation is a very good measure of the force, compared to actual force measurements for flapping foils and oscillating cylinders.

According to Anderson (1996), the average wake velocity excess in the streamwise direction is calculated by averaging slices of the wake spanning one path wavelength (U_∞/f) behind the trailing edge, at one instant in time. Depending on the freestream

velocity and oscillating frequency of each experimental case, the number of slices to be considered is varied. When the wavelength of the motion is larger than the experimental view, two or more instantaneous images of the wake are taken into account. The net thrust is then calculated by integrating the velocity slices from the instantaneous images of wake velocity profiles according to Equation (2.2). The integration is performed using trapezoidal rule.

On the other hand, it is possible to calculate the averaged flow field using several oscillation cycles acquired in detail at high frequency. Since there are 15 instantaneous images to take into account in certain cases according to Anderson's (1996) calculation method, the latter is adopted for a uniform evaluation of forces and efficiencies. Eight columns of velocity profiles starting approximately one-chord downstream of the airfoil have been integrated and averaged to determine the thrust coefficient. This is where the integrated value does not change considerably and is as far as possible in the wake excluding the column just at the edge of the field of view.

The thrust coefficient of the foil, C_f , is defined similar to drag coefficient as follows, using Equation (2.3).

$$C_f = \frac{T}{\frac{1}{2}\rho U_\infty^2 cs} \quad (2.3)$$

where c is the chord and s is the span of the airfoil.

In order to compare the results of the two aforementioned methods, a case, in general, representing a different category and can be assessed by a single instantaneous image is selected. Two additional cases found to be the most similar to those of Anderson (1996) in terms of investigated parameters have also been included to complete the comparison. Table 2.2 gives an overview of these results and Table 2.3 shows in detail the comparison with Anderson's both direct measurements and PIV results.

A close look at the Table 2.2 and consequently the investigation of both instantaneous and averaged images yield a major common issue. The velocity at the upper and lower edges of the field of view is not necessarily equal to the freestream velocity. This is sometimes due to the large amplitude of plunging motion, sometimes due to the inclination of the wake, etc. which will be discussed in the next

chapter. The velocities at the upper edge of the images are averaged and given in Table 2.2 for both the averaged and instantaneous images. As the Reynolds number increases the difference between the actual freestream velocity and those averaged velocities at the upper edge of the image is minimal. If the thrust coefficient is also calculated assuming the freestream velocity as the averaged velocity at the upper edge of the image, the result would differ considerably for low Reynolds numbers from the value obtained using the actual freestream velocity. A further investigation is performed in order to determine if this discrepancy causes an under or over estimation of the thrust or drag coefficient. For the time being, it should be noted that the calculation based on actual freestream value is more reliable.

Another conclusion of results presented in Table 2.2 is that the number of instantaneous images does not affect the results on thrust coefficient, or more properly, the difference in using the two methods of calculation, namely that of Anderson (1996) and the calculation based on averaged flow field.

Table 2.2: The thrust coefficient for selected cases

Flow Structure Category	Case #	# of images for a wavelength	St	k	h_{amp}/c	f	Re	U_{∞} [m/s]	Instantaneous images U_{inst} [m/s]	Averaged image U_{ave} [m/s]	C_t based on instantaneous image(s)		C_t based on averaged image
											U_{∞}	U_{ave}	
B2	28	1	0.6	3.79	0.25	0.10	825	0.0083	0.0067	0.0052	3.60	7.10	2.79
A1	15	1	0.8	2.50	0.5	0.20	2500	0.0251	0.0143	0.0136	7.49	31.30	8.22
A2	40	1	1.0	6.26	0.25	0.60	3000	0.0301	0.0289	0.0196	18.28	20.12	13.28
A1	23	2	0.6	1.88	0.5	0.30	5000	0.0502	0.0533	0.0415	3.48	2.98	3.50
B2	43	1	0.4	2.54	0.25	0.60	7400	0.0743	0.0692	0.0683	1.42	1.95	0.92
E	61	5	0.3	0.47	1	0.15	10000	0.1004	0.1321	0.0998	2.91	0.44	0.69
D	45	2	0.2	1.25	0.25	0.60	13700	0.1375	0.1330	0.1390	0.30	0.52	0.22

The most similar cases to those of Anderson (1996) in terms of investigated parameters are shaded in rose in Table 2.2. Except a slight difference in maximum effective angle of attack and a considerable difference in Reynolds number, Case 61 of this study is identical to the experiment "fa01" of Anderson's study (1996). However, the PIV experiment "fa01" lies outside the force measurement parameter space (NIS). Considering the success of force prediction via PIV in comparison with the direct force measurement in Anderson's study (1996), the thrust coefficient calculated in the current study using the averaged flow field yields a closer result. The difference may be due to the difference in Reynolds numbers and the large plunge amplitude, enough that the averaged wake width covers all the vertical extent of the PIV image. On the other hand the second similar case denoted as Case 45 in

this study have additional difference on the reduced frequency in comparison with experiment "fa11" of Anderson's study (1996). The predicted and measured force coefficients are close, however there is a relatively larger under estimation of thrust coefficient in the results of the current study in comparison to previous case.

Table 2.3: The thrust coefficient comparison with Anderson's (1996) study

Case #	# of images for a wavelength	St	k	h_{amp}/c	α_o	maximum α_{eff}	Re	C_r (Anderson, 1996 - experimental, PIV)	C_r (Anderson, 1996 - experimental, meas.)	C_r based on instantaneous image(s)		C_r based on averaged image
										U_o	$U_{ave.}$	
61	5	0.3	0.47	1	8	42.6	10000			2.91	0.44	0.69
fa01	?	0.3	0.47	1	7	36.3	1100	1.04	NIS			
45	2	0.2	1.25	0.25	8	31	13700			0.30	0.52	0.22
fa11	?	0.3	1.88	0.25	15	28	1100	0.77	0.88			

Despite all approximations and the limited extent of the field of view, the drag or thrust coefficient calculated using the averaged flow field will be assumed to be reliable and evaluated at the level of its order of magnitude.

Considering a propeller and its actuator disk, the thrust coefficient for a flapping motion can be also calculated using the area swept by the airfoil. In that case, peak to peak value of the plunge motion should be used instead of the airfoil span. Therefore, the thrust coefficient based on the area swept by the wing, C_T , will be in terms of thrust coefficient C_f based on the planform area of the wing;

$$C_T = \frac{T}{\frac{1}{2}\rho U_\infty^2 2h_o s} = \frac{C_f}{\frac{2h_o}{c}} \quad (2.4)$$

The efficiency is the ratio of the work usefully applied to the total amount of work supplied. Using Prandtl's (1952) calculations, the theoretical efficiency for a propeller is defined as;

$$\eta = \frac{2}{1 + (C_T + 1)^{\frac{1}{2}}} \quad (2.5)$$

The derivation of the theoretical efficiency is summarized in Appendix A.3.

3 RESULTS

3.1 Parameter Space

The parameters are defined in Chapter 1.3. The parameter space for the base investigation is summarized in Table 3.1. Each cell without shading corresponds to an investigated case. For these cases, mean angle of attack, the amplitude of pitching motion and the phase angle between pitch and plunge are fixed to be $\alpha_0=8^\circ$, $\alpha_{\text{amp}}=8.6^\circ$ and $\psi = \pi/2$ where pitch leads the plunge motion. The pitch and the plunge frequencies are also equal to each other.

The limits of non-dimensional parameters investigated in this study are as follows:

- $825 < Re < 13\,700$
- $0.05 < St < 1.0$
- $0.25 < h_{\text{amp}}/c < 1.0$
- $0.16 < k < 6.26$
- $0.05 < \lambda < 0.96$

In addition to the base investigation, the thick bordered cases in Table 3.1 are considered for:

- the change in the phase angle between pitch and plunge as follows:
 - $\psi = 75^\circ$, pitch leading plunge
 - $\psi = 105^\circ$, pitch leading plunge
- the change in the mean angle of attack and the pitch amplitude as follows:
 - $\alpha_0 = 0^\circ$ and $\alpha_{\text{amp}} = 8.6^\circ$
 - $\alpha_0 = 0^\circ$ and $\alpha_{\text{amp}} = 12.9^\circ$
 - $\alpha_0 = 8^\circ$ and $\alpha_{\text{amp}} = 12.9^\circ$

Table 3.1: The parameter space for the base investigation cases.

h_{amp}/c	f	Strouhal number										
		1.0	0.9	0.8	0.7	0.6	0.5	0.4	0.3	0.2	0.1	0.05
0.25	0.1					Re=825 k= 3.79 $\lambda= 0.08$		Re=1250 k= 2.5 $\lambda= 0.12$	Re=1650 k= 1.9 $\lambda= 0.16$	Re=2500 k= 1.25 $\lambda= 0.24$	Re=5000 k= 0.63 $\lambda= 0.48$	Re=10000 k= 0.31 $\lambda= 0.96$
	0.2			Re=1250 k= 5.01 $\lambda= 0.06$		Re=1650 k= 3.79 $\lambda= 0.08$		Re=2500 k= 2.5 $\lambda= 0.12$	Re=3300 k= 1.9 $\lambda= 0.16$	Re=5000 k= 1.25 $\lambda= 0.24$	Re=10000 k= 0.63 $\lambda= 0.48$	
	0.6	Re=3000 k= 6.26 $\lambda= 0.05$		Re=3750 k= 5.01 $\lambda= 0.06$		Re=5000 k= 3.75 $\lambda= 0.08$		Re=7400 k= 2.54 $\lambda= 0.12$	Re=10000 k= 1.88 $\lambda= 0.16$	Re=13700 k= 1.25 $\lambda= 0.24$		
0.5	0.05						Re=1000 k= 1.56 $\lambda= 0.1$	Re=1250 k= 1.25 $\lambda= 0.12$	Re=1650 k= 0.95 $\lambda= 0.16$	Re=2500 k= 0.63 $\lambda= 0.24$	Re=5000 k= 0.31 $\lambda= 0.48$	Re=10000 k= 0.16 $\lambda= 0.96$
	0.1	Re=1000 k= 3.13 $\lambda= 0.05$		Re=1250 k= 2.5 $\lambda= 0.06$		Re=1650 k= 1.9 $\lambda= 0.08$	Re=2000 k= 1.56 $\lambda= 0.1$	Re=2500 k= 1.25 $\lambda= 0.12$	Re=3300 k= 0.95 $\lambda= 0.16$	Re=5000 k= 0.63 $\lambda= 0.24$	Re=10000 k= 0.31 $\lambda= 0.48$	
	0.2			Re=2500 k= 2.5 $\lambda= 0.06$		Re=3300 k= 1.9 $\lambda= 0.08$	Re=4000 k= 1.56 $\lambda= 0.1$	Re=5000 k= 1.25 $\lambda= 0.12$	Re=6750 k= 0.93 $\lambda= 0.16$	Re=10000 k= 0.63 $\lambda= 0.24$		
	0.3	Re=3000 k= 3.13 $\lambda= 0.05$		Re=3750 k= 2.5 $\lambda= 0.06$		Re=5000 k= 1.88 $\lambda= 0.08$	Re=6000 k= 1.56 $\lambda= 0.1$	Re=7400 k= 1.27 $\lambda= 0.12$	Re=10000 k= 0.94 $\lambda= 0.16$	Re=13700 k= 0.63 $\lambda= 0.24$		
1.0	0.05	Re=1000 k= 1.56 $\lambda= 0.05$		Re=1250 k= 1.25 $\lambda= 0.06$		Re=1650 k= 0.95 $\lambda= 0.08$		Re=2500 k= 0.63 $\lambda= 0.12$		Re=5000 k= 0.31 $\lambda= 0.24$	Re=10000 k= 0.16 $\lambda= 0.48$	
	0.1	Re=2000 k= 1.56 $\lambda= 0.05$		Re=2500 k= 1.25 $\lambda= 0.06$		Re=3300 k= 0.95 $\lambda= 0.08$		Re=5000 k= 0.63 $\lambda= 0.12$		Re=10000 k= 0.31 $\lambda= 0.24$		
	0.15	Re=3000 k= 1.56 $\lambda= 0.05$		Re=3750 k= 1.25 $\lambda= 0.06$		Re=5000 k= 0.94 $\lambda= 0.08$		Re=7400 k= 0.63 $\lambda= 0.12$	Re=10000 k= 0.47 $\lambda= 0.16$	Re=13700 k= 0.31 $\lambda= 0.24$		

– different frequencies of motion for plunge and pitch as follows:

- f_2 (pitch) = $2 f_1$ (plunge)
- f_2 (pitch) = $1/2 f_1$ (plunge)
- f_2 (pitch) = $5 f_1$ (plunge)
- f_2 (pitch) = $1/5 f_1$ (plunge)

PIV images at a cross-section parallel to the planform area of the wing have also been acquired for the cases of base investigation to allow insight into the three-dimensionality of the flow.

3.2 Categorization Based on Flow Structures

Although there are an intensive number of studies in literature on flapping foils, a detailed categorization based on flow structures around and in the near-wake of the foils has not been done yet. The investigation of Anderson et al. (1998) is probably the only one which considers a large number of parameters and at the same time commenting on flow structures presenting five cases obtained using DPIV. Three of the cases are described as follows:

- The foil does not produce thrust and the wake is marginally at the state where all vortices are aligned.
- A strong jet and a reverse Karman street are produced which provides maximum wake spatial amplification. No leading-edge vortex is observed.
- A very strong jet results and a leading-edge vortex is formed.

The last case is actually used as a basis for comparison with the next two cases where the phase angle between pitch and plunge is changed from 90° to either 105° or 75° .

The goal of this study is to perform a classification of vorticity patterns similar to those by Ohmi et al. (1990) for a pitching and translating airfoil. Although Ohmi et al. (1990) distinguished different vorticity patterns, they did not provide the representation of their appearance on a parameter space; whereas Anderson et al. (1998) present vorticity patterns as a function of Strouhal number and the angle of attack for $h_0/c = 1$, despite their limited classification. It should be noted that although Anderson et al. (1998)'s study is based on an extensive number of

experiments, the flow visualization results are obtained only for $Re = 1100$ and represented for only 12 experiment cases.

To fulfill the lack of categorization in literature, the present study aims to establish a classification of flow structures around and in the near-wake of the flapping foil based on different independently controllable parameters. As mentioned before, in the first set of experiments defined as the base investigation, the Reynolds number, the amplitude of plunging motion and the oscillation frequency varies, when the mean angle of attack and the amplitude of pitching motion are fixed at $\alpha_0 = 8.6^\circ$ and $\alpha_{amp} = 8^\circ$, respectively. The effect of the phase angle and unequal oscillation frequency of pitch and plunge motions are separately investigated based on major classes of flow structures. Unless otherwise stated, the oscillation frequencies of pitch and plunge are taken to be equal where the pitch leads the plunge with a phase difference of $\pi/2$.

The classification of flow structures around and in the near-wake of the airfoil are based on instantaneous vorticity patterns around the airfoil, instantaneous near-wake vorticity patterns and averaged flow fields (vorticity patterns and velocity fields) obtained either using up to 100 images per cycle of oscillation depending on the frequency of motion in order to visualize time-resolved flow structures or 200 images taken only at four distinct instants of an oscillation cycle, i.e., 50 images per maximum, minimum and the middle in both directions of plunging. In addition to that, the flapping form of the airfoil, the variation of the effective angle of attack, calculated thrust coefficient and efficiency are also considered. Figure 3.1 is a template for all the following figures presenting instantaneous vorticity patterns around the airfoil or in the near-wake of the airfoil. The first image is at the right hand side of the figure where the airfoil is at its mid-plunge position. The airfoil first moves upward and then images 3 to 7 represent the downstroke. The ninth image on the left hand side represents the beginning of the following cycle of oscillation. The images are aligned on a sinusoidal curve. As the flow is from left to right in the experiments, the figure simulates the forward motion of the airfoil from right to left. However, the amplitude and period of the curve is not scaled with the actual motion due to the limitation of the page layout. The actual motion will be represented separately. The first image on the figure is the beginning of the third cycle of the oscillation from the startup of the motion for all cases unless stated otherwise.

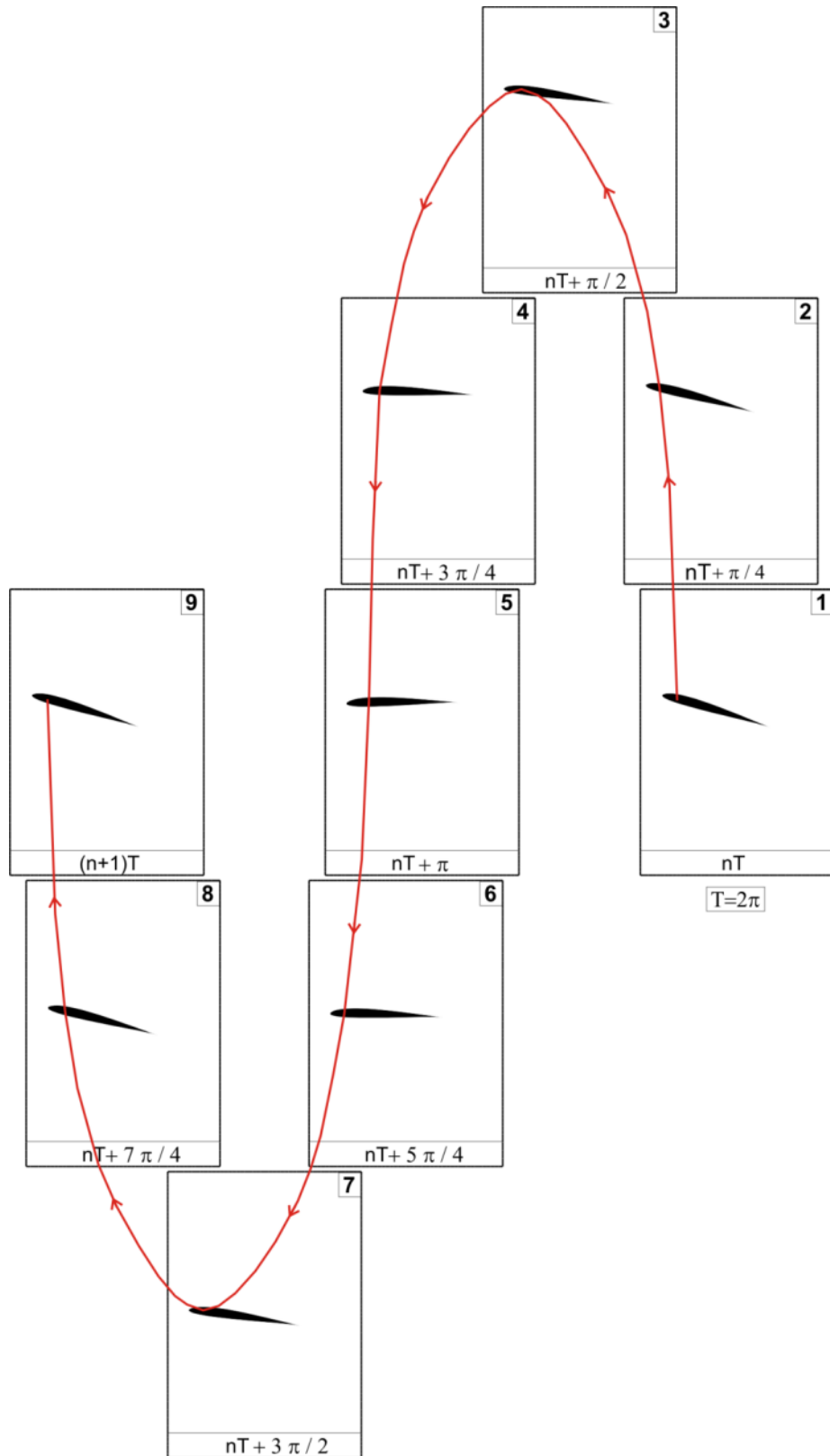


Figure 3.1: Template for figures showing instantaneous vorticity patterns.

In order to establish a guide for categorization, the investigated cases are given in Table 3.2. This table precedes the descriptions to provide a beforehand map of occurrence for each category. The denotation letters given for each category will be described subsequently in detail based on a highlighted case. 10 cases which are shown with bold case numbers in the table are selected to investigate the effect of other parameters; such as mean angle of attack, pitch amplitude, and phase angle, and will be discussed in the following subchapters. The borders of each category are also outlined with different colors.

In Table 3.2, the rows are grouped based on the plunge amplitude. For each row, the plunge amplitude and the frequency of motion, for both pitch and plunge, are the same. As we move to the right on a given row in the table, the flow speed is increasing or in other words, based on a reference frame moving with the flow, the forward speed of flapping motion is increasing. The Strouhal number is fixed for each column and decreases from left to right; however due to the difference in flapping motion frequency, the flow speed is not the same in a column.

3.2.1 Category A1 (Ex: Case-15)

Figure 3.2 and Figure 3.3 show the instantaneous flow structures for Case-15. There are two counter-rotating pairs of vortices formed during an oscillation cycle, a pair on the lower side of the airfoil during the upstroke and a pair on the upper side during the downstroke. However, the near-wake images in Figure 3.3 indicate only a pair of counter-rotating vortices shed in the wake during a cycle of oscillation.

Figure 3.4 shows the downstroke and upstroke motion in a time-resolved manner; four extra images have been included in between previously presented ones in Figure 3.2. In the first column of images, it is possible to observe how the positive vortex shed from the leading edge during the upstroke moves towards the trailing edge on the lower side of the airfoil. It interacts first with the opposite sign vortex forming from the leading edge due to the suction on the upper side of the airfoil. The interaction continues and causes some negative vorticity to appear on the lower side of the airfoil until it connects with the same sign vortex forming at the trailing edge. On the second column of images, the remaining detached positive vorticity concentration at the leading edge moves towards the upper side of the airfoil and interacting with the negative vortex therein decays considerably.

Table 3.2: Categorization of the investigated cases based on flow structures

h_{amp}/c	f	Strouhal number										
		1.0	0.9	0.8	0.7	0.6	0.5	0.4	0.3	0.2	0.1	0.05
0.25	0.1					<u>28</u> B2		<u>29</u> B2	<u>30</u> C	<u>31</u> cD	<u>32</u> E	<u>33</u> E
	0.2			<u>34</u> A2		<u>35</u> B2		<u>36</u> B2	<u>37</u> C	<u>38</u> D	<u>39</u> E	
	0.6	<u>40</u> A2		<u>41</u> A2		<u>42</u> B2		<u>43</u> B2	<u>44</u> C	<u>45</u> D		
0.5	0.05						<u>1</u> B1	<u>2</u> B1	<u>3</u> D	<u>4</u> DE	<u>5</u> E	<u>6</u> E
	0.1	<u>7</u> A1		<u>8</u> A1		<u>9</u> A1	<u>10</u> B1	<u>11</u> B1	<u>12</u> D	<u>13</u> E	<u>14</u> E	
	0.2			<u>15</u> A1		<u>16</u> A1	<u>17</u> B1	<u>18</u> B1	<u>19</u> D	<u>20</u> DE		
	0.3	<u>21</u> A1		<u>22</u> A1		<u>23</u> A1	<u>24</u> B1	<u>25</u> bD	<u>26</u> D	<u>27</u> DE		
1.0	0.05	<u>46</u> A1		<u>47</u> A1		<u>48</u> B1		<u>49</u> D		<u>50</u> E	<u>51</u> E	
	0.1	<u>52</u> A1		<u>53</u> A1		<u>54</u> B1		<u>55</u> D		<u>56</u> E		
	0.15	<u>57</u> A1		<u>58</u> A1		<u>59</u> B1		<u>60</u> D	<u>61</u> DE	<u>62</u> E		

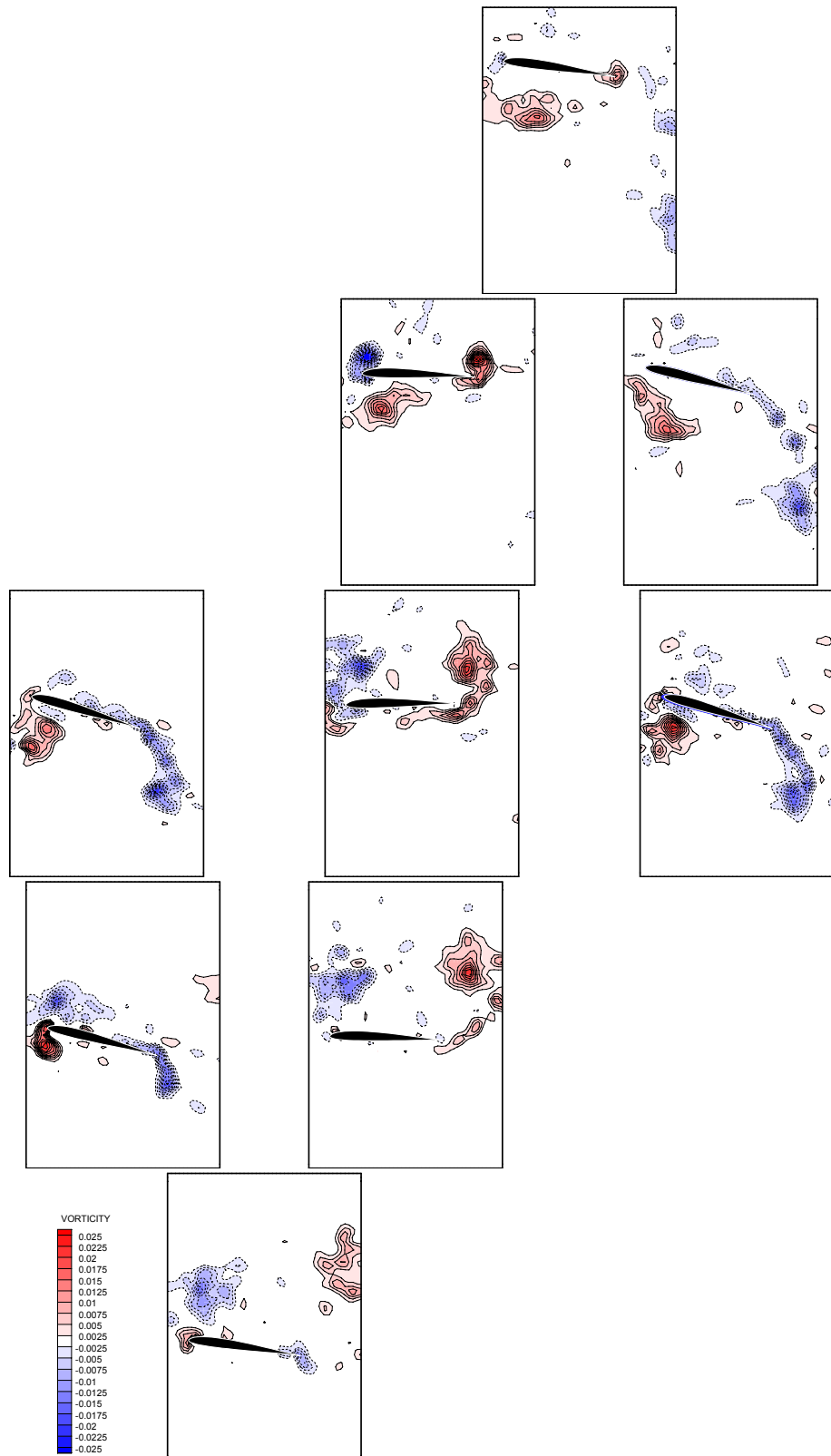


Figure 3.2: Instantaneous vorticity patterns around the airfoil Case-15 (Category A1)

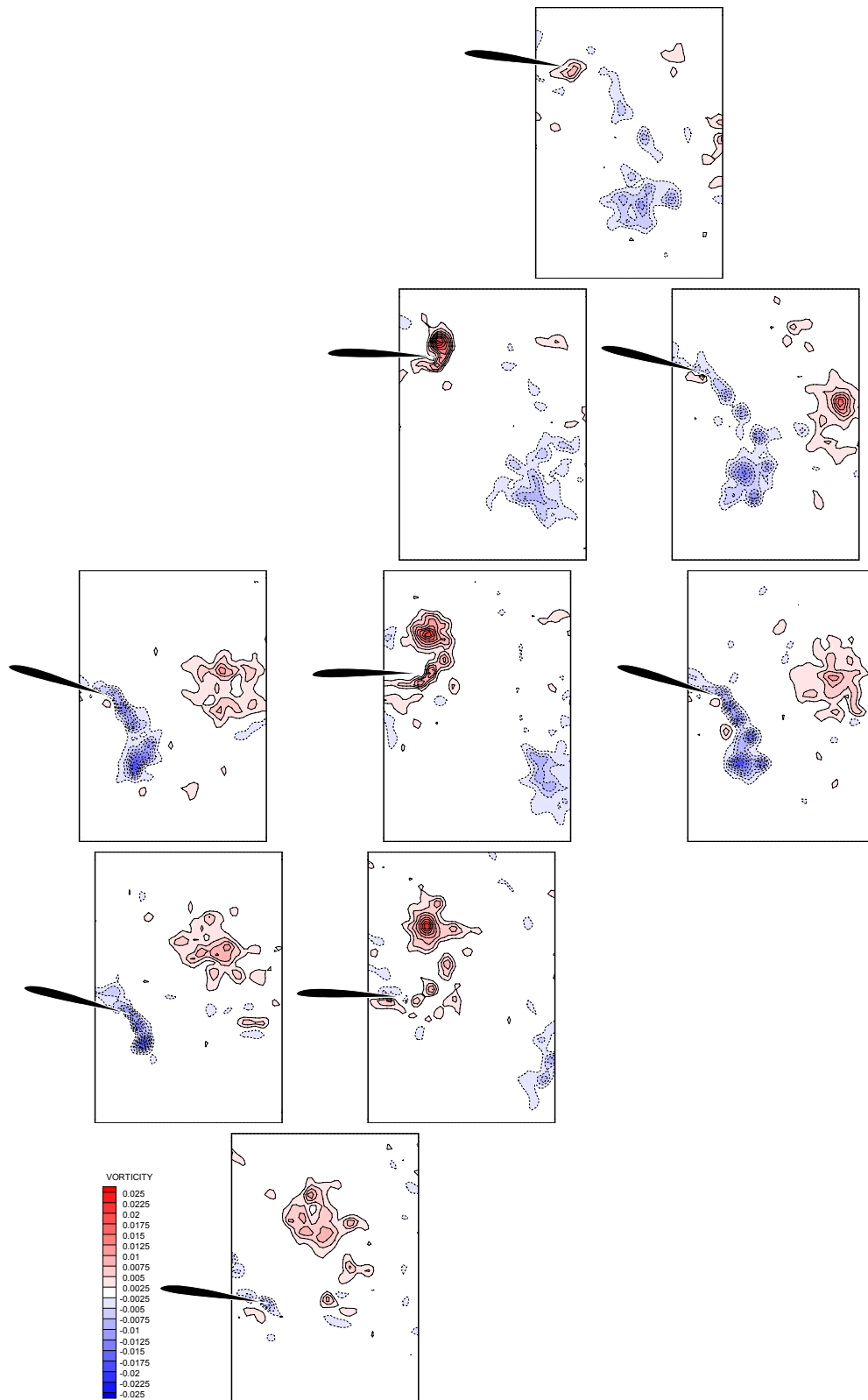


Figure 3.3: Instantaneous vorticity patterns in the near-wake of the airfoil Case-15 (Category A1)

A similar mechanism happens during the upstroke of the airfoil. The third column of images in Figure 3.4 shows how previously shed negative vortex from the leading edge on the upper side of the airfoil interacts with the opposite sign vortex forming on the lower side and connects with the same sign vortex forming at the trailing edge moving in the flow direction. In comparison with the interaction mechanisms during the downstroke, the fourth column of images indicates relatively less competition of opposite sign vortices around the leading edge. Most of the previously shed vorticity joins the same sign trailing edge vorticity and its roll-up to the other side of the airfoil around the leading edge is not evident as in the downstroke.

The trajectory of the shed vortices is inclined downward especially evident from the trajectory of the negative vortex which leaves the scene at the lower right corner of the field of view in the near-wake vorticity patterns presented in Figure 3.3. Average of several cycles of time-resolved data indicates the same inclination with approximately 35° as can be seen in Figure 3.5b. On the other hand, the average of four distinct instants of an oscillation cycle over 50 periods of motion (Figure 3.5a) reveals a mushroom like vorticity formation close to the trailing edge of the airfoil. This is a typical picture for high amplitudes of plunge motion ($h_{\text{amp}}/c \geq 0.5$) where the roll-up radius of vortex shedding from the trailing edge is large. No matter which kind of averaging is adopted, the average velocity field indicates jet like flow. This is in accordance with instantaneous vorticity patterns where the positive vortex shed in the wake remains above the airfoil chord line and the negative vortex below which result in a formation of a reversed Karman vortex street indicating thrust production. It should be noted that the jet like flow is slightly downward and a lift production to some extent should be expected too.

Figure 3.5c shows the airfoil in motion, represented by a straight line with three points, namely the leading edge, trailing edge and pitch pivot (the quarter chord from the leading edge in this study) points. The amplitude and period of the sinus is scaled with the plunge motion and flow speed, respectively. The airfoil is never tangent to its trajectory, it does not feather, however highly disturb the flow around. The effective angle of attack shown in Figure 3.5d is positive during the downstroke motion and negative during the upstroke. However, the airfoil reaches angles of attack beyond the stall limits. Those facts are related to the formation of pairs of vortices during the downstroke and upstroke.

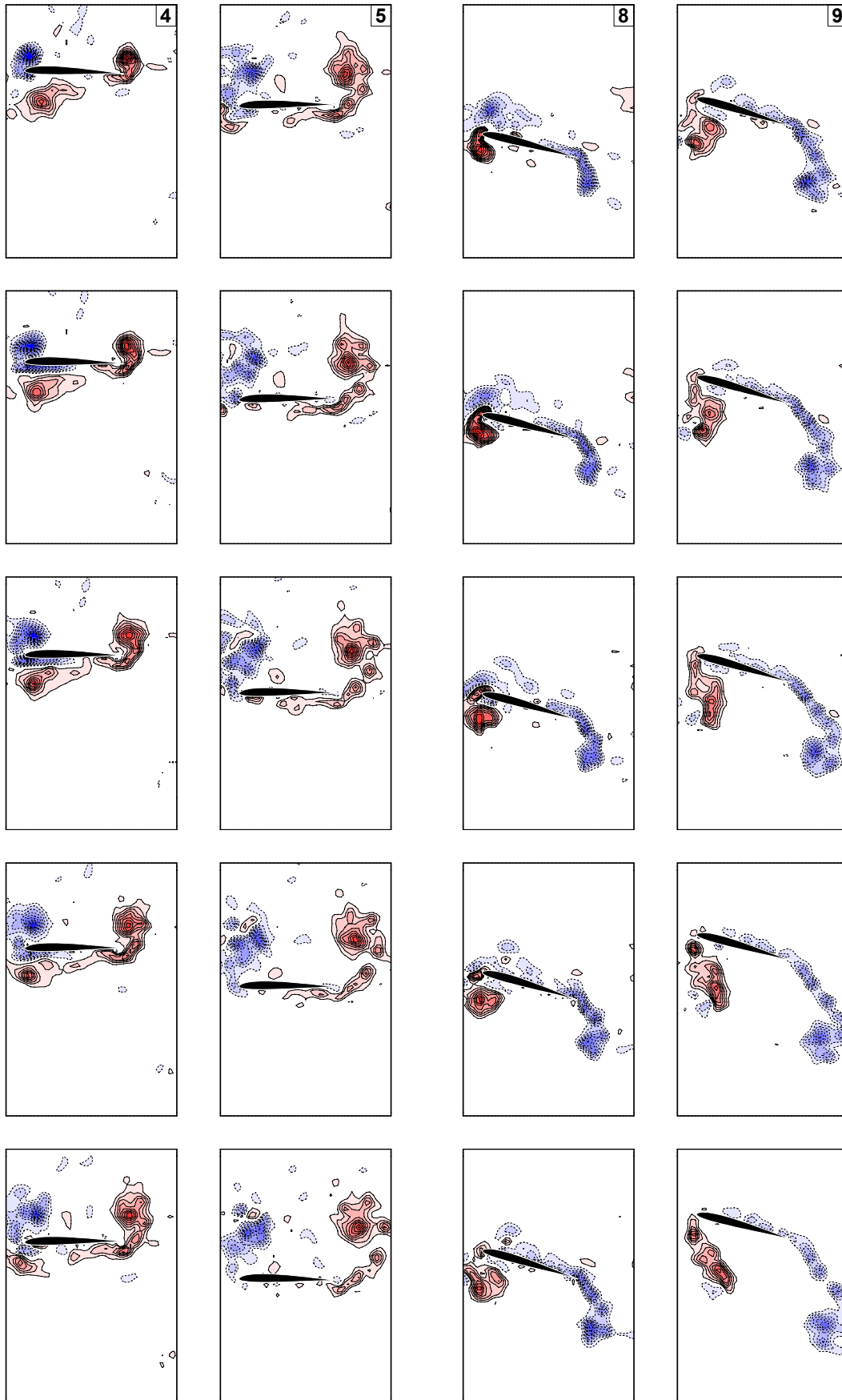


Figure 3.4: Time-resolved vorticity patterns around the airfoil for Case-15

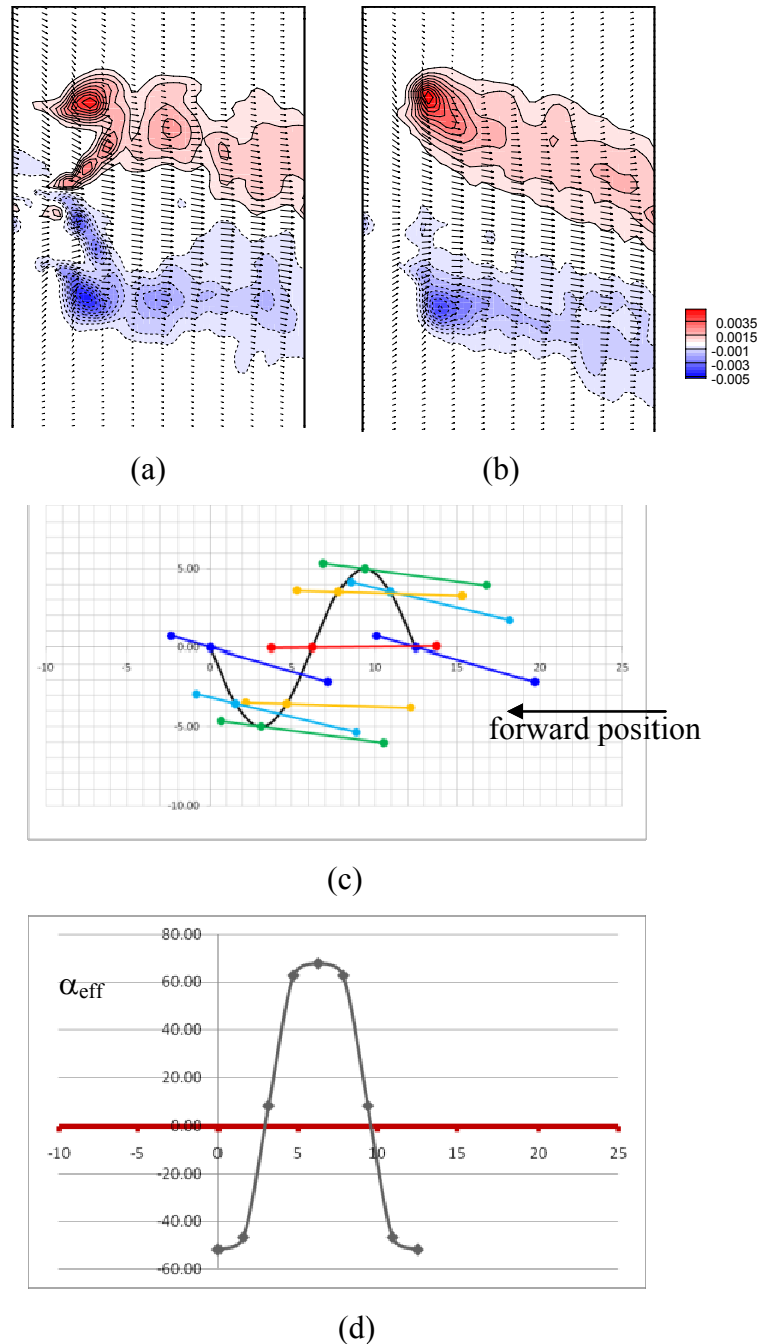


Figure 3.5 : a) and b) Averaged velocity and averaged vorticity plots, c) airfoil in motion, d) variation of effective angle of attack for Case-15

3.2.2 Category A2 (Ex: Case-40)

This category is a subset of Category A. In terms of flow structures, the case investigated is very similar to the previous one. However, due to its lower amplitude of plunging motion and higher frequency of oscillation, it differs at some points which will be emphasized herein. Figure 3.6 shows formation of two counter-rotating pair of vortices during a cycle of oscillation and it is possible to observe the pair of vortices shed together in the near-wake of the airfoil (Figure 3.7).

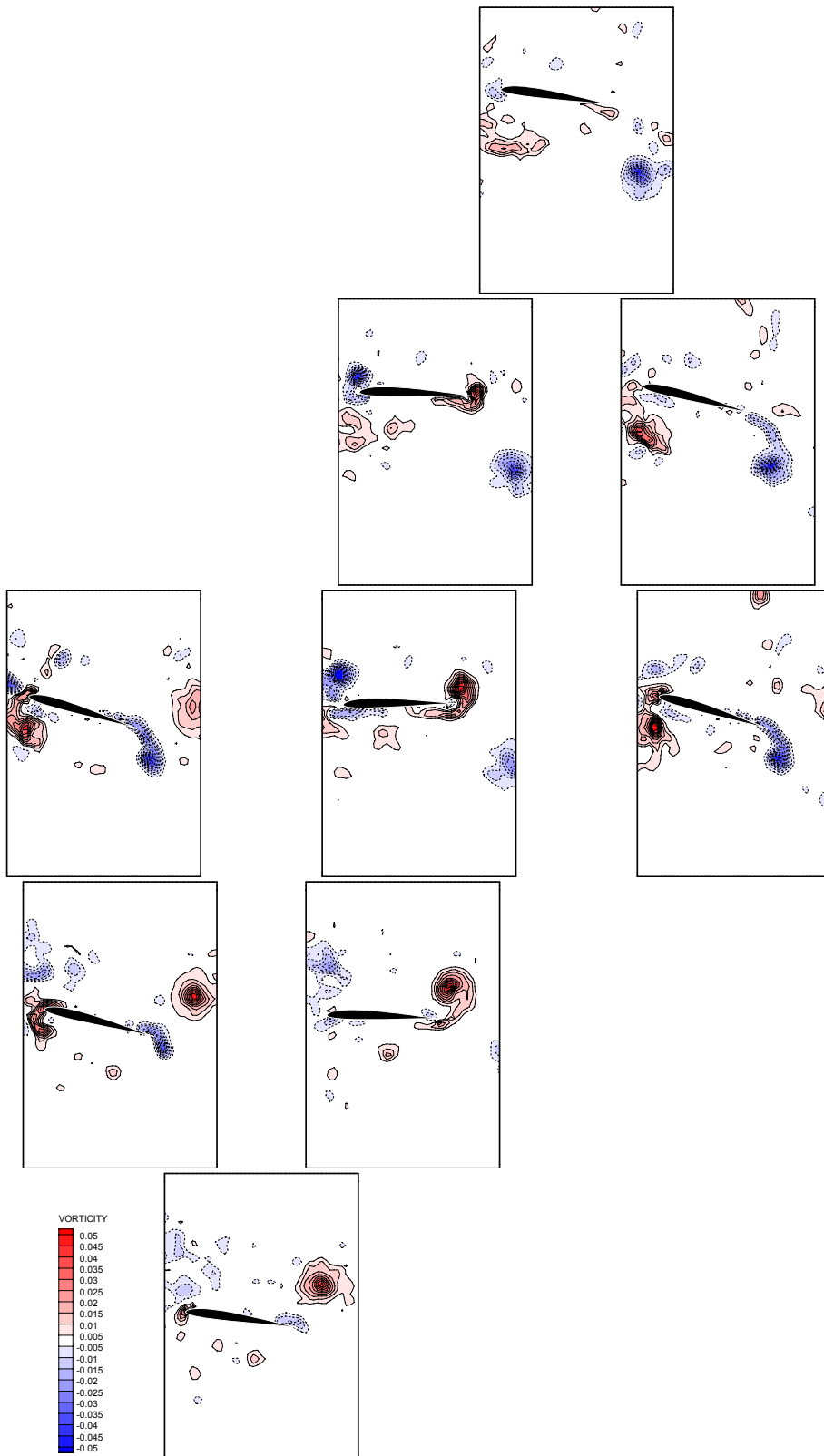


Figure 3.6 : Instantaneous vorticity patterns around the airfoil Case-40 (CategoryA2)

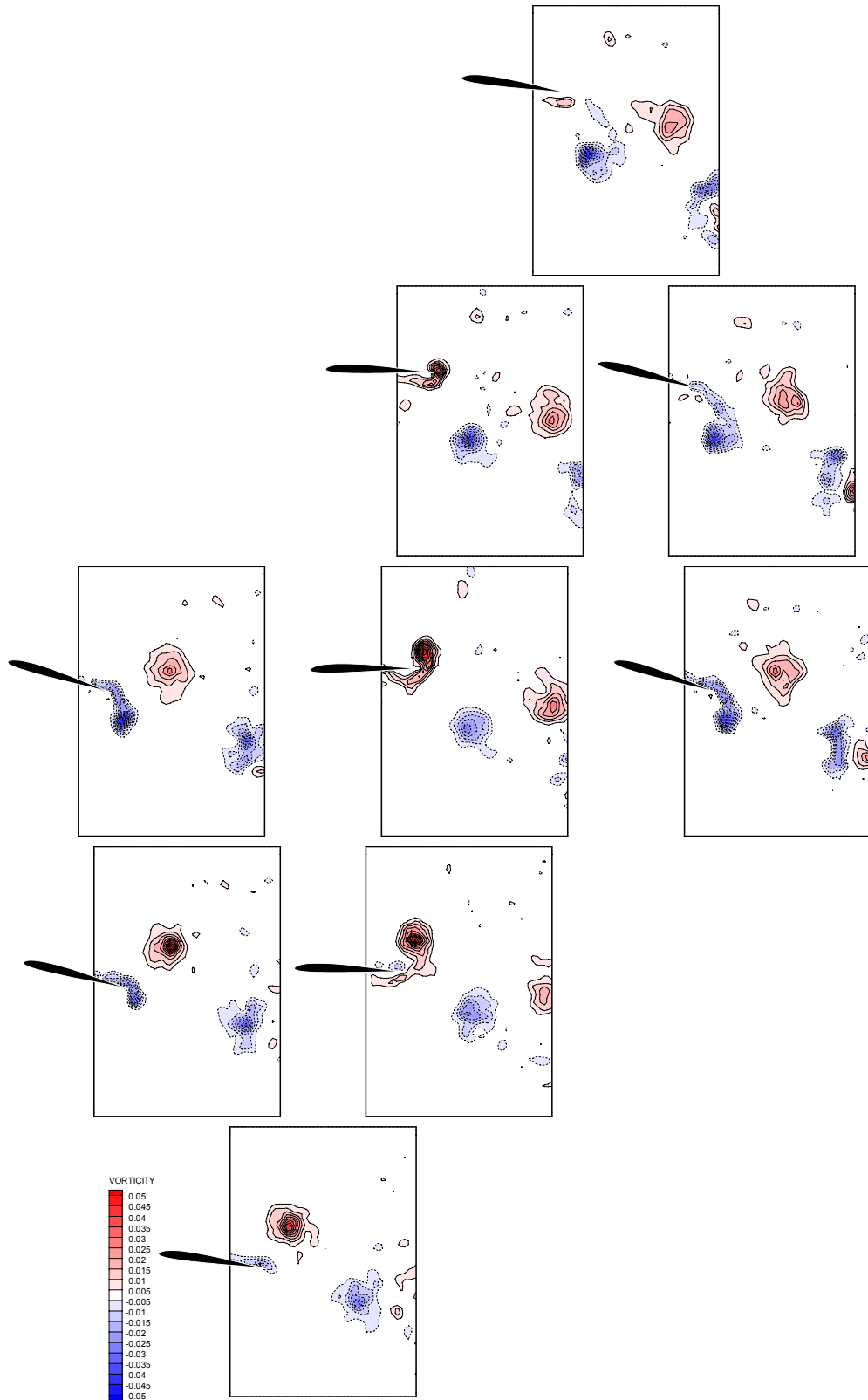


Figure 3.7 : Instantaneous vorticity patterns in the near-wake of the airfoil Case-40 (Category A2)

Due to the high frequency of motion, time-resolved patterns include only an extra image in between those previously presented in Figure 3.6 and are given in Figure 3.8. Although the positive vortex shed from the leading edge interacts during the downstroke in a similar way as in the previous category with the opposite sign vortex forming on the upper side of the airfoil, i.e. it draws a part of the negative vorticity concentration from the suction side towards the pressure side, it is not able to connect to the positive vortex forming from the trailing edge. Instead, its strength diminishes and the vortex finally breaks apart and is diffused. On the other hand, during the upstroke, the negative vortex shed from the leading edge is not able to move in the flow direction; therefore it never connects the same sign vorticity concentration forming at the trailing edge. Its diffusion seems to be faster than that with the opposite sign shed from the leading edge during the downstroke.

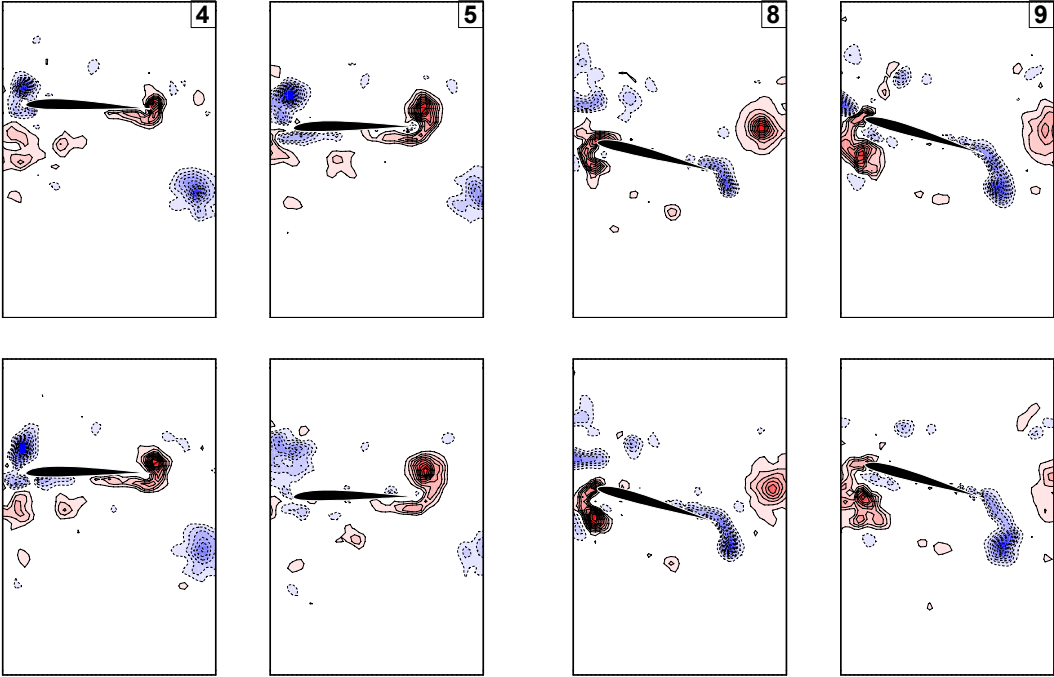


Figure 3.8 : Time-resolved vorticity patterns around the airfoil for Case-40

Observing Figure 3.7, we can easily track the counter-rotating pair of vortices in the near-wake and notice that they leave the scene close to the right lower corner of the image. Therefore, the occurrence of a jet like velocity profile inclined downward at a similar angle as in the previous category is obvious as confirmed by the averaged data shown in Figure 3.9a and b. However, the major difference in comparison with the previous category is that the mushroom like vorticity formation at the trailing edge of the airfoil is not distinguishable anymore and the wake width of the jet like

velocity profile is substantially decreased. As the amplitude of plunge motion is low, the roll-up radius of the vortex shedding is small.

The flapping characteristics (Figure 3.9c) and the variation of the effective angle of attack (Figure 3.9d) are very similar to those of the previous category; hence the categorization of the case as a subset, based on the flow structures, is in accordance with the motion characteristics. As it is stated previously, the frequency of motion is higher and the plunge amplitude is lower for this subset.

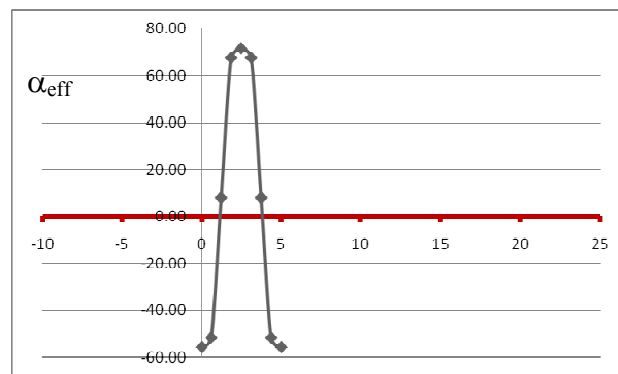
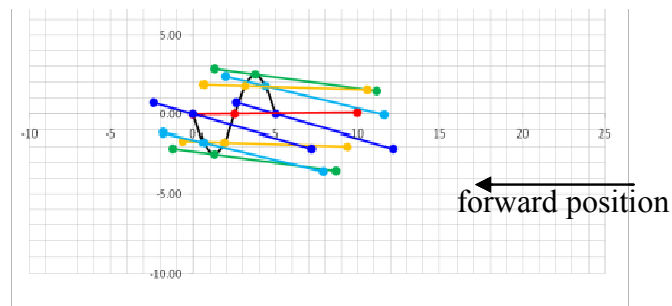
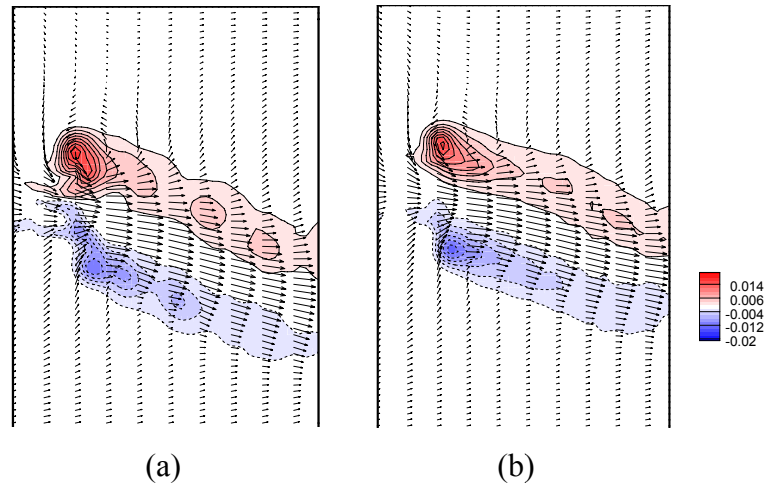


Figure 3.9 : a) and b) Averaged velocity and averaged vorticity plots, c) airfoil in motion, d) variation of effective angle of attack for Case-40

3.2.3 Category B (Ex: Case-43)

The example case for this category is selected from the same set including the previous case presented for Category A2 in terms of frequency of motion and plunge amplitude, i.e. these two cases are in the same row of

Table 3.2. As we move to the right in the table, the flow speed is increasing, therefore the Strouhal number is decreasing.

Figure 3.10 shows the instantaneous flow structures around the airfoil for Case-43. The vorticity concentrations at the leading and trailing edges do not evolve in an equivalent strength and extent as they are for Category A. At the beginning of the downstroke, a part of the positive vorticity concentration formed on the lower side of the airfoil during the previous upstroke stage remains at the leading edge. It enhances first the strength of the negative vortex forming on the upper side of the airfoil and then connects to the same sign vorticity concentration evolving at the trailing edge before the mid-plunge position is reached. While the negative vortex enlarges preserving its strength and detaches from the leading edge, the positive vortex is shed in the wake at the end of the downstroke. The process does not seem to be nearly reversed during the upstroke as it was the case for Category A. The negative vortex at the leading edge slowly decreases in strength preserving its location until the airfoil reaches the mid-plunge position. In the meantime, the negative vorticity concentration at the trailing edge evolves to be shed and the positive concentration forming at the leading edge first covers equally the upper and lower surfaces of the airfoil and then it stretches all along the lower surface when the airfoil reaches its mid-plunge position. In the second half of the upstroke, the negative vortex at the leading edge quickly stretches along the upper surface of the airfoil, connects to the same sign evolving at the trailing edge, a part of it breaking apart and diffusing. As a consequence a fast decrease in concentration level is observed. The negative vortex is shed in the wake from the trailing edge at the end of the upstroke.

The near-wake vorticity patterns are presented in Figure 3.11. In accordance with the flow structure interactions around the airfoil, only a pair of counter-rotating vortices is shed in the wake.

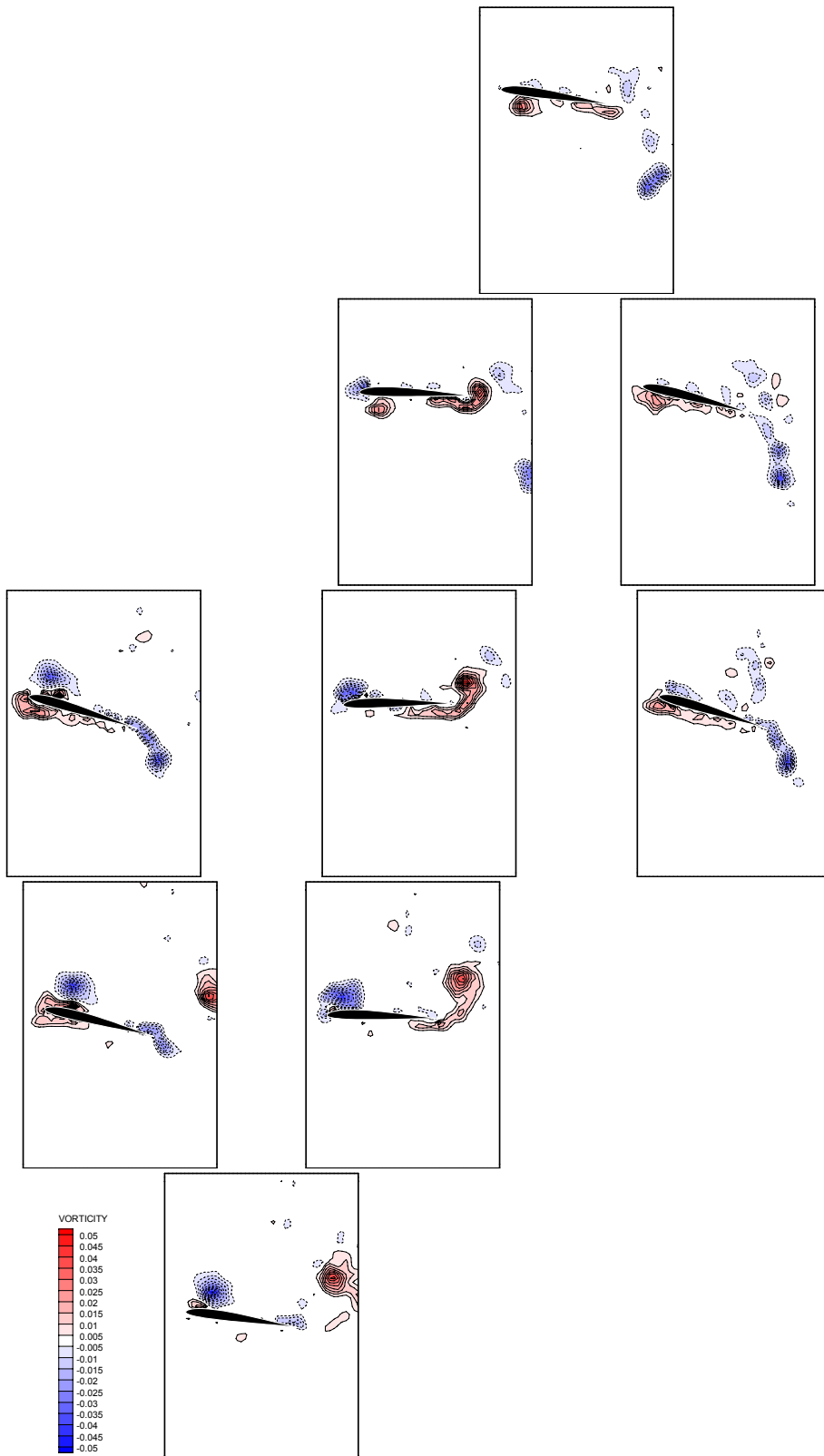


Figure 3.10 : Instantaneous vorticity patterns around the airfoil Case-43 (Category B2)

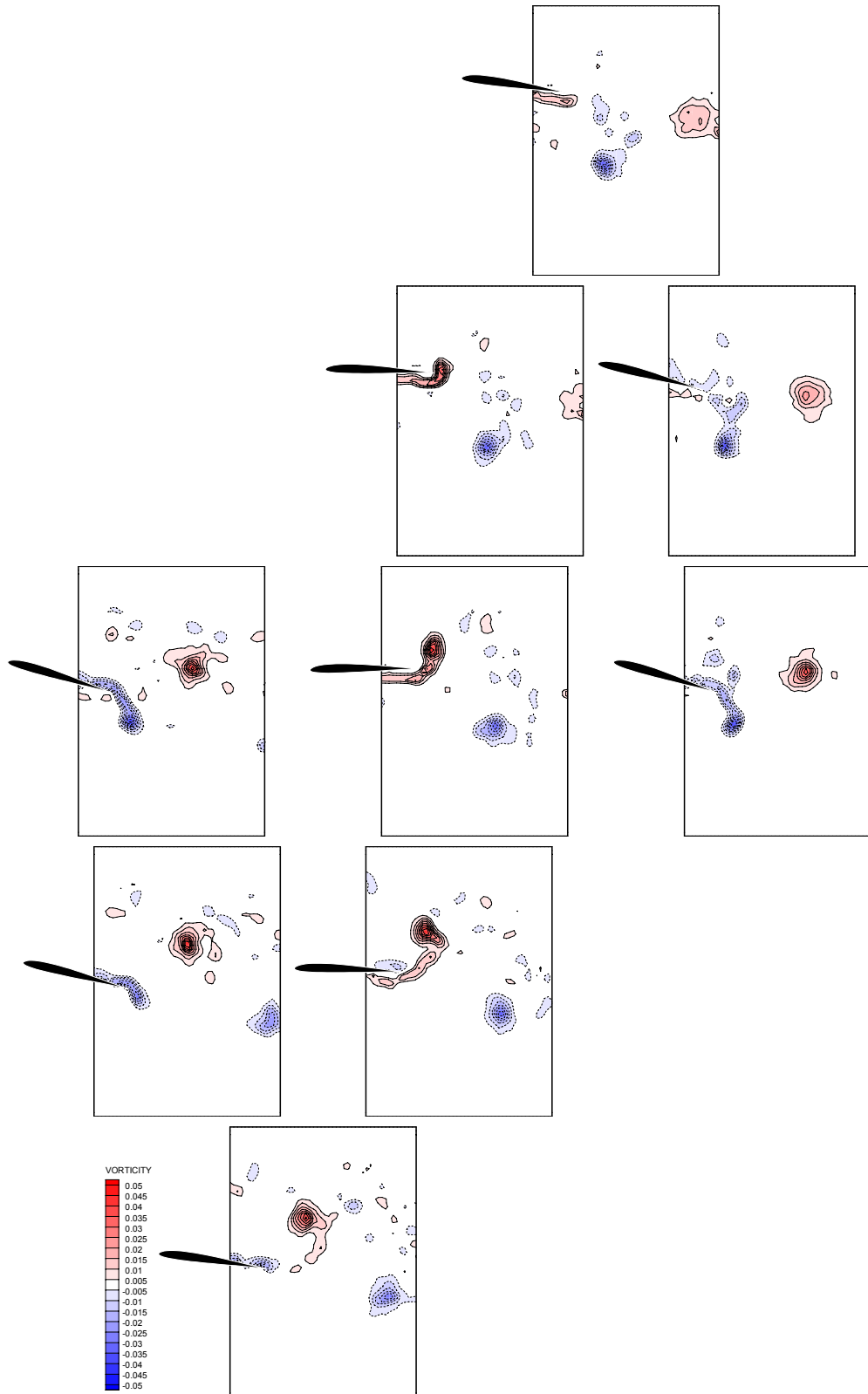
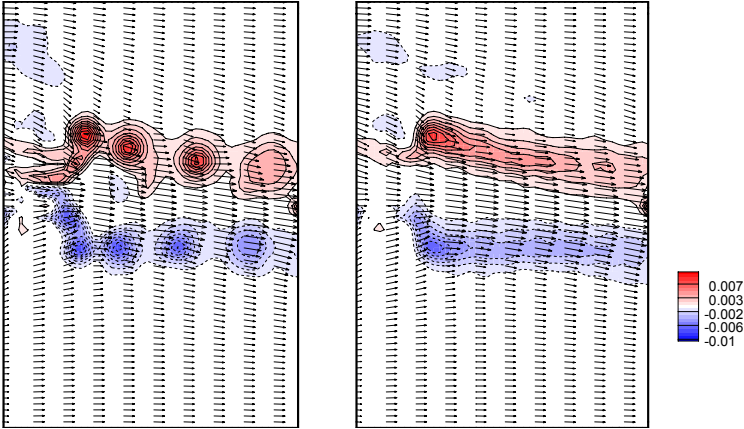
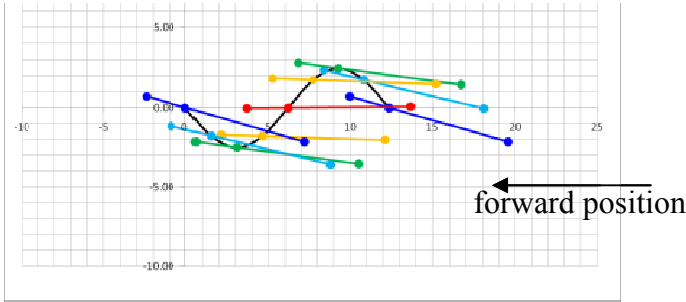


Figure 3.11 : Instantaneous vorticity patterns in the near-wake of the airfoil Case-43 (Category B2)

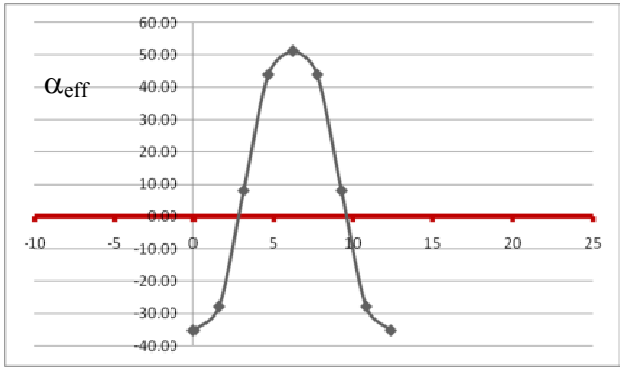
The trajectory of the shed vortices is slightly inclined downwards; the shed vortices leave the scene close to the horizontal centerline of the image. This is confirmed by the averaged vorticity fields shown in Figure 3.12a and b where the inclination angle is determined to be approximately 10°. It should be noted that the inclination is of the same order of magnitude as the mean angle of attack of the airfoil.



(a) (b)



(c)



(d)

Figure 3.12 : a) and b) Averaged velocity and averaged vorticity plots, c) airfoil in motion, d) variation of effective angle of attack for Case-43

The average of four distinct instants of an oscillation cycle over 50 periods of motion (Figure 3.12a) reveals localized cells of positive and negative vorticity

concentrations. This indicates a relatively slow decay rate and consistent positioning of vortices in the wake.

Despite the fact that the frequency of motion is the same as in Case-40 (Category A2), the flapping characteristics presented in Figure 3.12c are more like those of Case-15 (Category A1) due to increased flow speed. If this elongation in the time axis is not taken into account, in general, the variation of the effective angle of attack is similar to that of Category A. Although the maximum and minimum values are slightly lower, they are still over the stall limits.

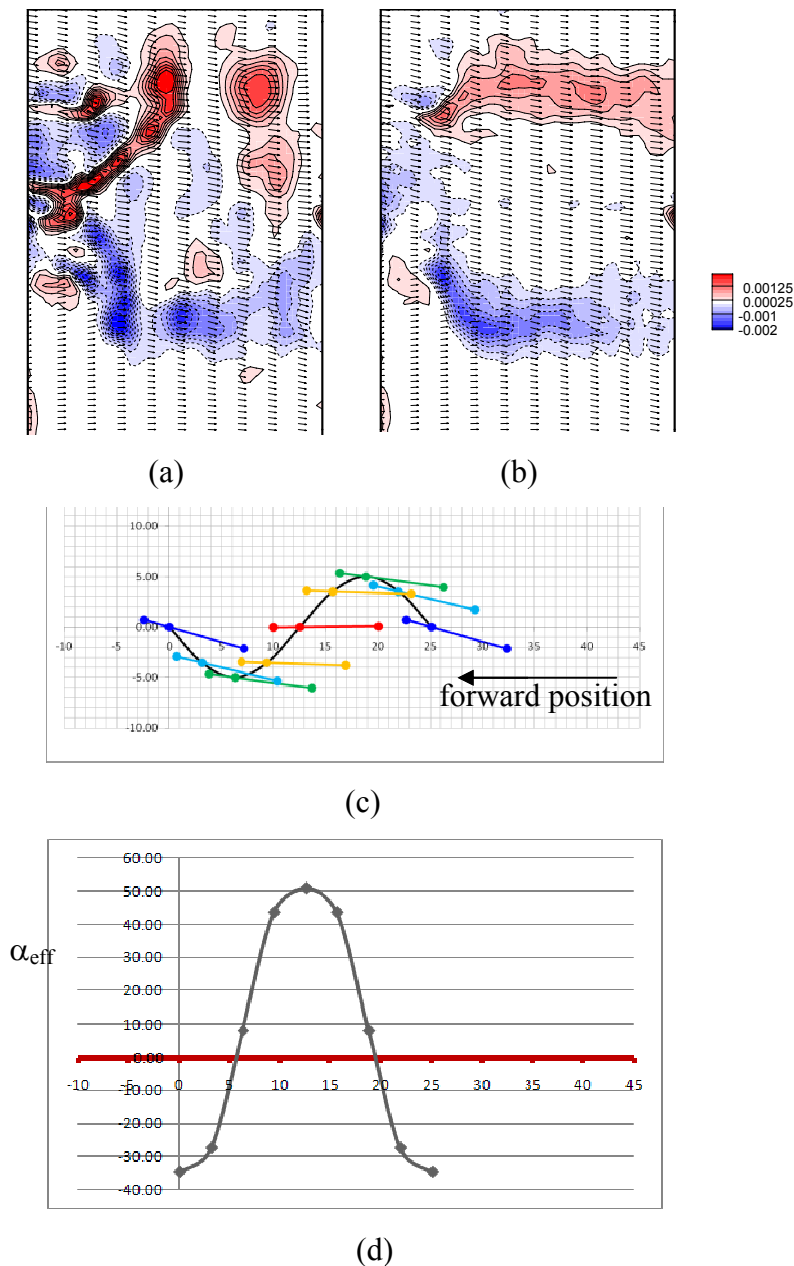


Figure 3.13 : a) and b) Averaged velocity and averaged vorticity plots, c) airfoil in motion, d) variation of effective angle of attack for Case-18

Similar to Category A, depending on the amplitude of plunge motion, Category B actually presents two subsets with the same distinguishable differences in between. As shown in Figure 3.13, when the amplitude of plunge is equal or larger than $0.5c$, in the average of four distinct instants of an oscillation cycle there is a mushroom like vorticity formation at the trailing edge of the airfoil and the wake width of the jet like velocity profile is substantially increased. It should be noted that Case-18 presented in Figure 3.13 have very similar flapping characteristics to Case-43 and although the period of motion is larger, the limits of the effective angle of attack are the same. Therefore, it is possible to categorize Case-18 as B1 and Case-43 as B2. The mushroom like vorticity formation is related to the large roll-up radius of vortex shedding; as evident by the instantaneous vorticity patterns in the near wake for Case-18 as shown in Figure 3.14. The roll-up radius of vortex shedding is so large that the vorticity layer extends to the edge of field of view and the shed positive vortex is detectable at the upper right corner of the image at the end of the downstroke.

3.2.4 Category C (Ex: Case-44)

The selection criteria for the example case in this category is similar to that in the previous category; the plunge amplitude and frequency of motion is the same as previous two examples, the flow speed is increased. The flow structures belonging to this category is present only for $h_{amp}/c=0.25$. The major characteristic is the shedding of two negative sign vortices per cycle of motion. Figure 3.15 presents the vorticity patterns around the airfoil. At the beginning of the downstroke motion, a negative vortex is present in the near-wake and another same sign vortex is about to be shed in the wake. During the downstroke a positive vortex is forming at the trailing edge and a negative vortex at the leading edge. The positive vorticity concentration which looks like an individual vortex formation at the lower surface of the airfoil close to the leading edge at the beginning of the downstroke, moves in the flow direction and connects to the same sign concentration developing at the trailing edge. At the end of the downstroke, the positive vortex is shed in the wake and a negative vortex with a considerable strength is present at the upper surface of the airfoil close to the leading edge.

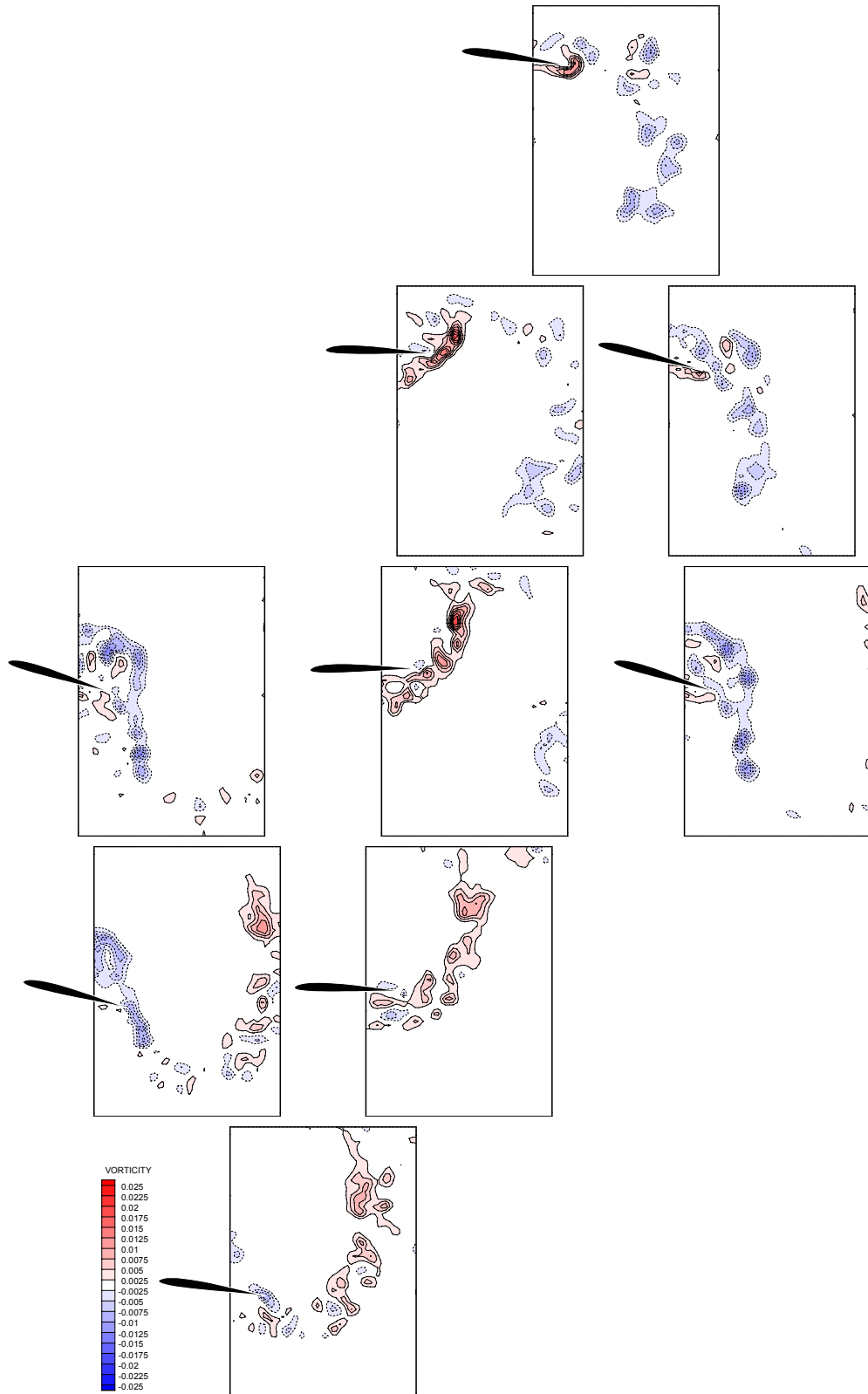


Figure 3.14 : Instantaneous vorticity patterns in the near-wake of the airfoil Case-18 (Category B1)

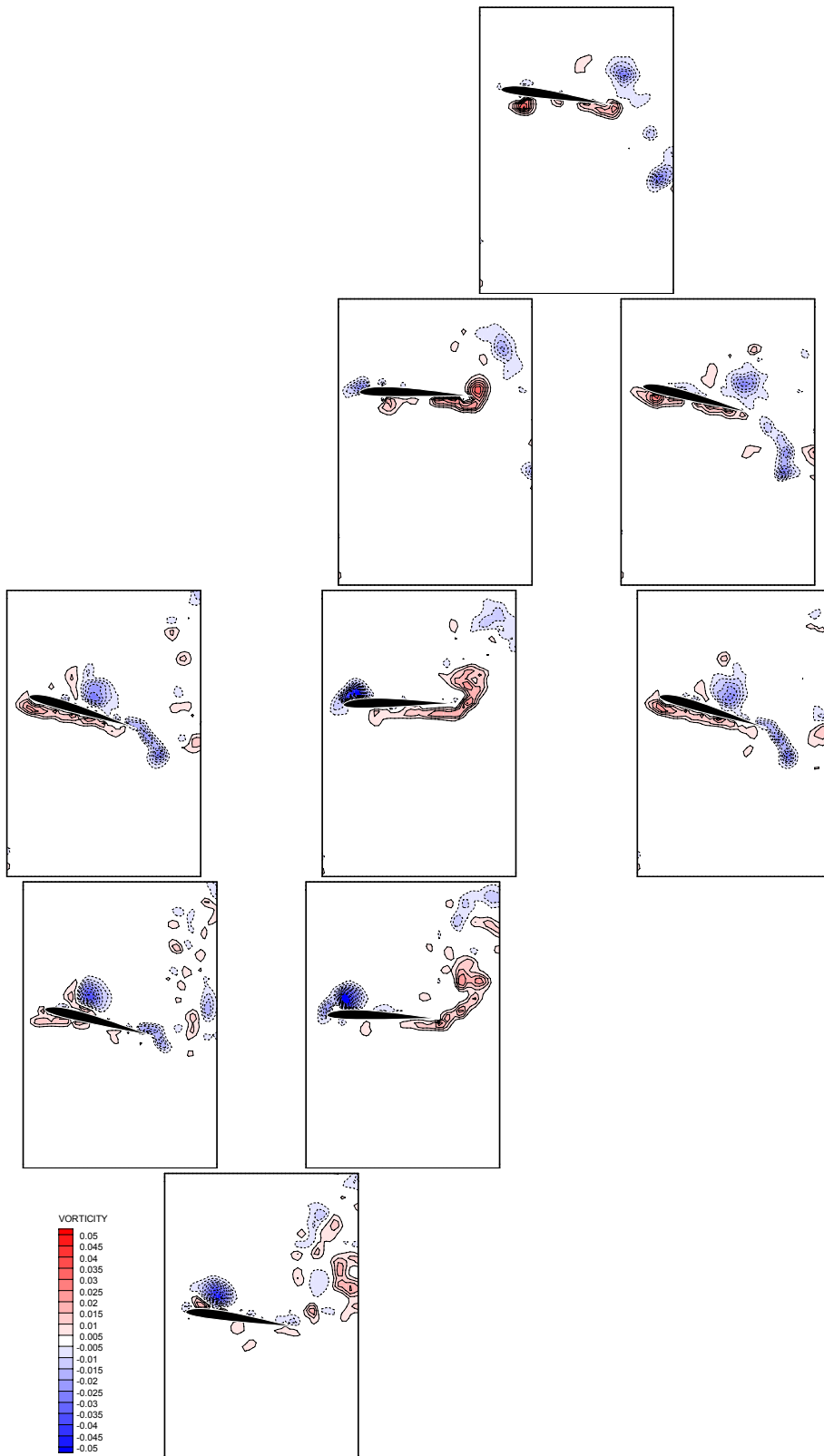


Figure 3.15 : Instantaneous vorticity patterns around the airfoil Case-44(Category C)

During the upstroke, we observe the formation of a negative vortex at the trailing edge and the movement of the same sign at the leading edge towards the trailing edge. At the mid-plunge position they are about to be connected, however this does not happen; the one formed at the trailing edge is shed right after the mid-plunge position, however the other one is shed at the end of the plunge motion. Therefore, there are two negative vortices shed consecutively and a single positive vortex shed per cycle of motion.

Figure 3.16 visualizes those vortices in the near-wake of the airfoil. The vortices are circled and labeled as N1, N2 and P1. The positive vortex P1 and the first negative vortex shed during the upstroke, N1, moves straight in streamwise direction; however the negative vortex N2 shed later in the cycle follows a trajectory upward. The strength of N1 is slightly larger than that of N2. Therefore, although the Karman-like shedding is modified, it is expected to see a jet like velocity profile aligned approximately with the chord line at mid-plunge position. This is somewhat confirmed by the averaged data presented in Figure 3.17. A third layer of negative vorticity concentration, inclined upward, is especially evident in Figure 3.17b. The two opposite sign vorticity layers, responsible for the formation of jet like velocity profile are approximately horizontal. Similar to the previous category, this one also presents localized cells of positive and negative vorticity concentrations in the average of four distinct instants of an oscillation cycle (Figure 3.17a), which is assumed to be an indication of relatively slow decay rate and consistent positioning of vortices in the wake.

The flapping characteristics presented in Figure 3.17c are very similar compared to those of the previous category's example case. In accordance with the increase in the flow speed, the period of flapping motion is slightly increased and the peak values of the effective angle of attack are decreased (Figure 3.17d).

Case-37 belongs to the same category although the frequency of motion is reduced to one third. The flapping characteristics and therefore the variation of the effective angle of attack is exactly the same as those of Case-44. Figure 3.18 highlights the major typical patterns. Instantaneous vorticity contours in the near wake show the presence of a single positive and two negative vortices shed per cycle of oscillation. In accordance, the average vorticity patterns clearly indicate the upward trajectory of additional negative vortex shed in the wake.

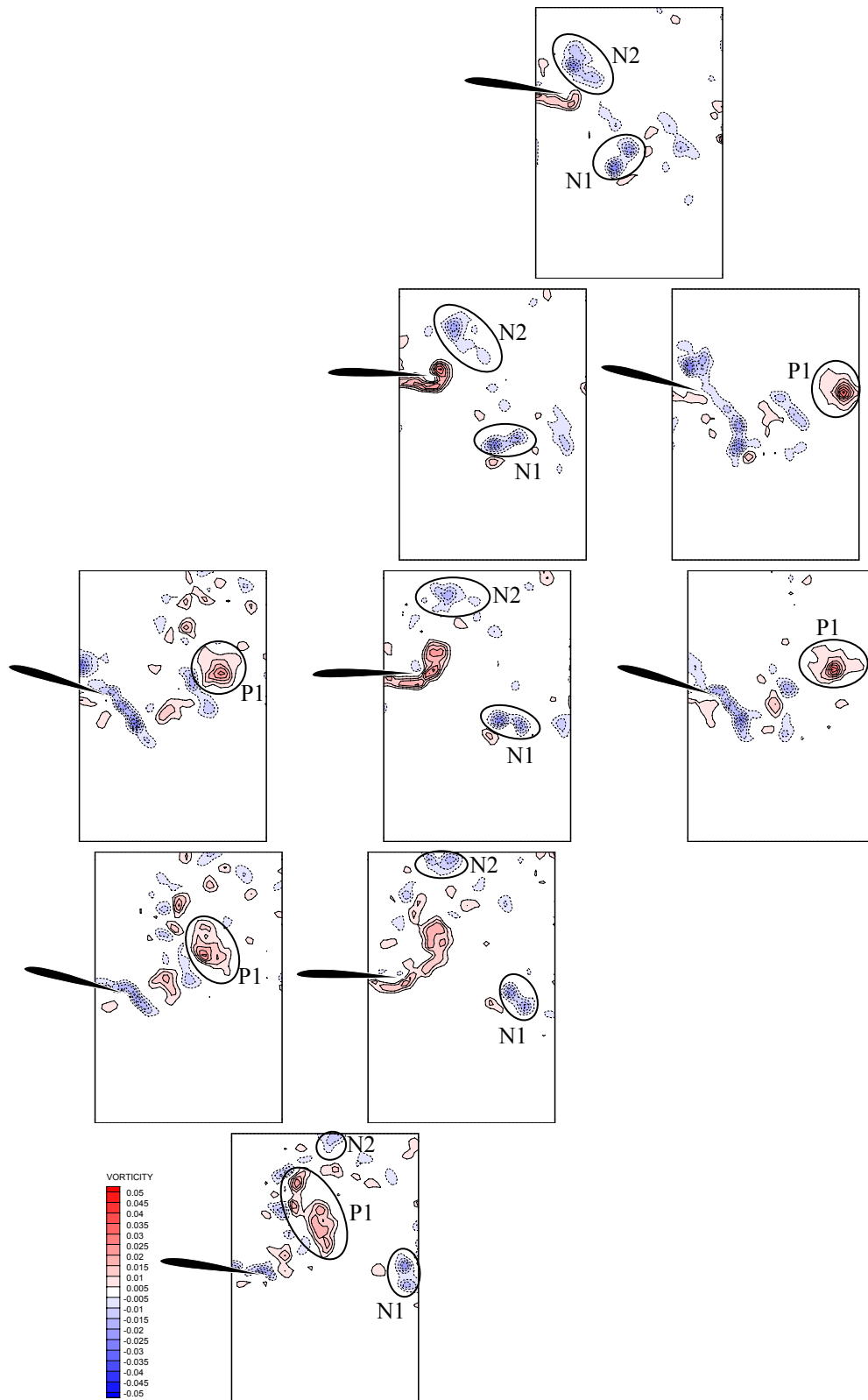
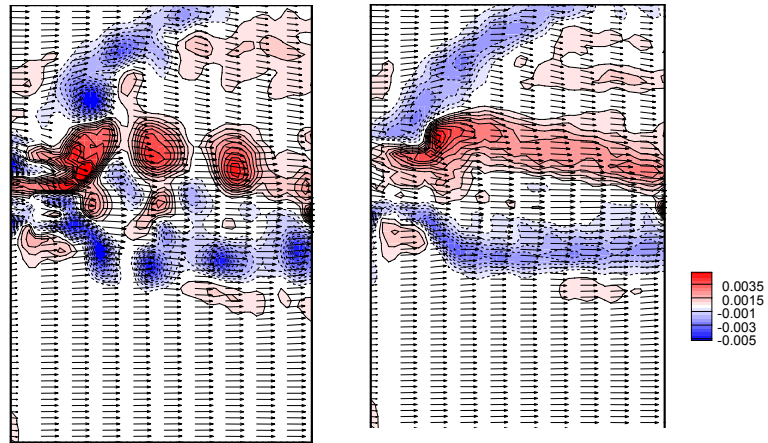
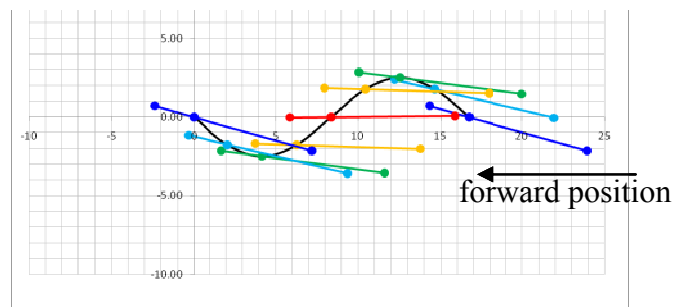


Figure 3.16 : Instantaneous vorticity patterns in the near-wake of the airfoil Case-44 (Category C)

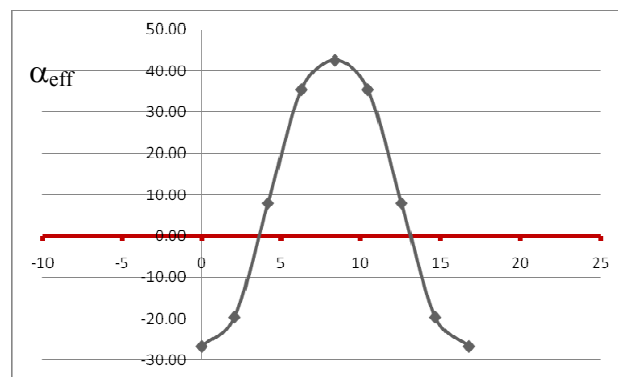


(a)

(b)



(c)



(d)

Figure 3.17 : a) and b) Averaged velocity and averaged vorticity plots, c) airfoil in motion, d) variation of effective angle of attack for Case-44

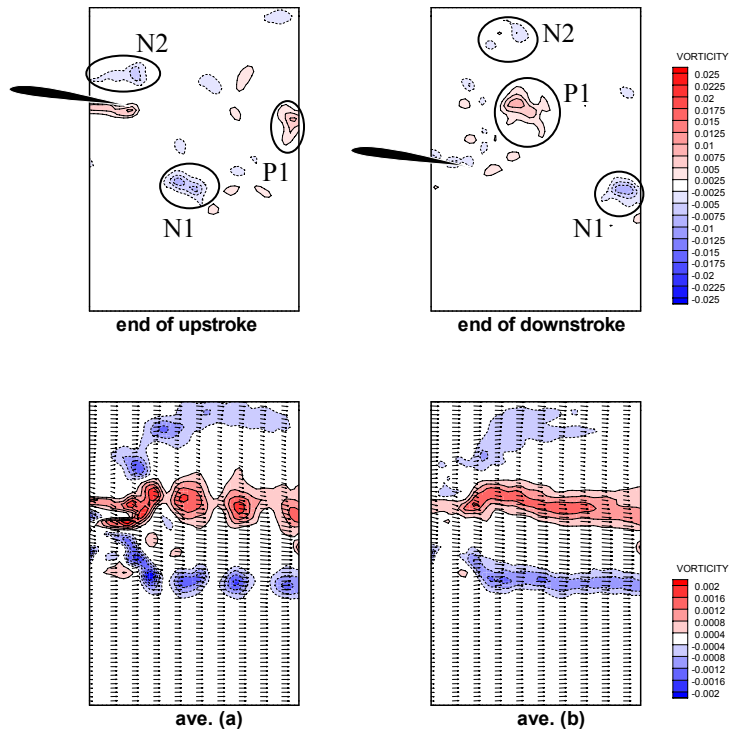


Figure 3.18 : Instantaneous vorticity patterns in the near-wake of the airfoil and averaged vorticity plots for Case-37 (Category C) (left: average of four distinct instants over 50 periods of motion; right: average of time-resolved data)

3.2.5 Category D (Ex: Case-45)

The example case for this category is selected from the same row in

Table 3.2 having the same plunge amplitude and frequency of motion as in the examples of previous two categories. Figure 3.19 shows the flow structures around the airfoil. Although the formation of the leading edge vortex during the downstroke and its separation and shedding during the upstroke are evident in the images, the roll-up of positive vortex at the trailing edge is considerably reduced. As seen in the high Strouhal number cases of previous categories, the formation of counter-rotating pair of vortices during the upstroke is no longer evident. Instead, there is a layer of positive vorticity concentration lying on the lower surface of the airfoil. This layer is generally present during all the stages of the motion except when the leading edge vortex is at its maximum strength around the minimum plunge position. The near-wake vorticity patterns presented in Figure 3.20 show the negative vortex shed in the wake, broken apart and following a downward arc trajectory. On the other hand, the positive vorticity layer at the trailing edge stretches in the wake and a trail of positive vortices lie along an upward arc.

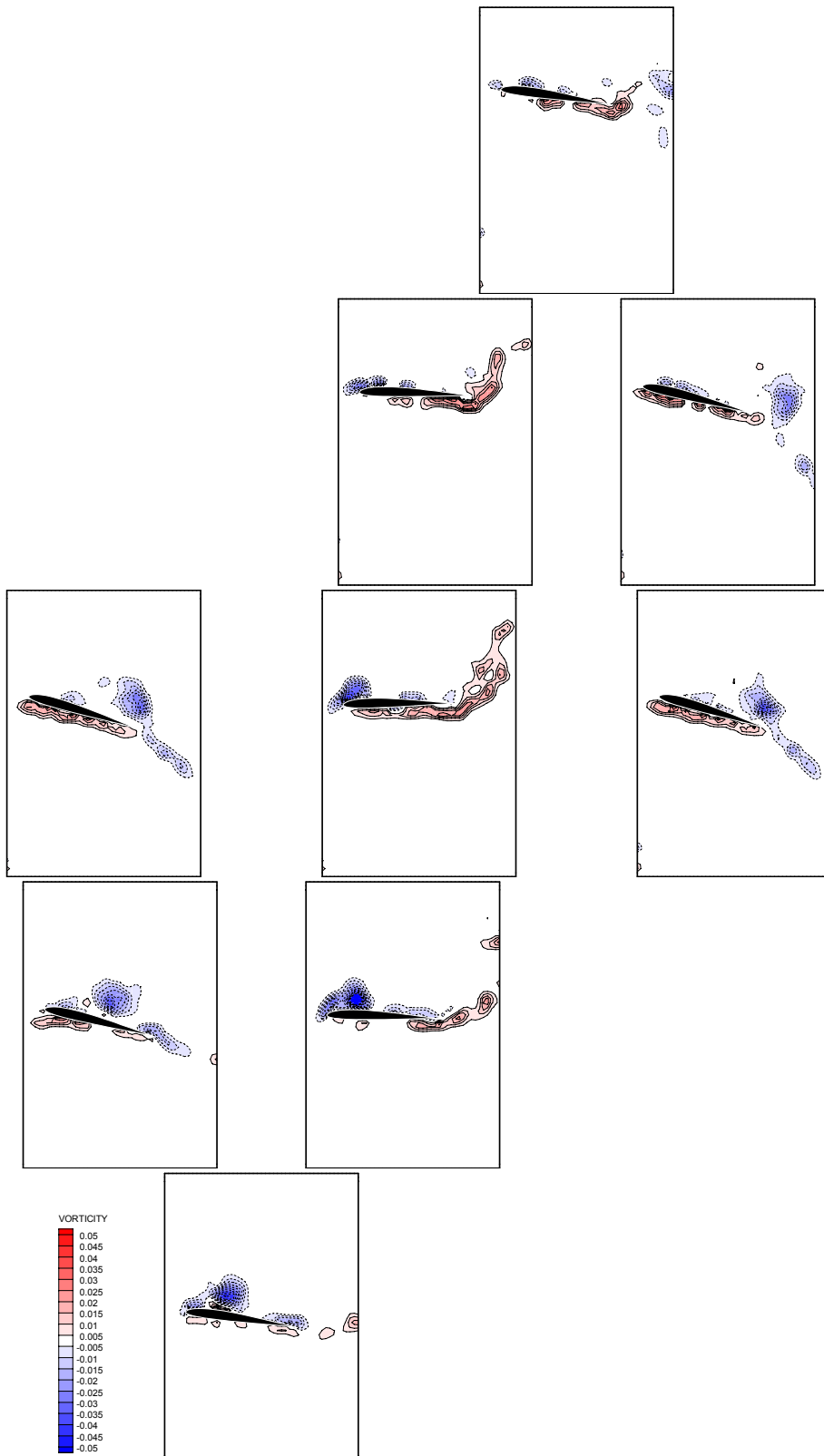


Figure 3.19 : Instantaneous vorticity patterns around the airfoil Case-45(Category D)

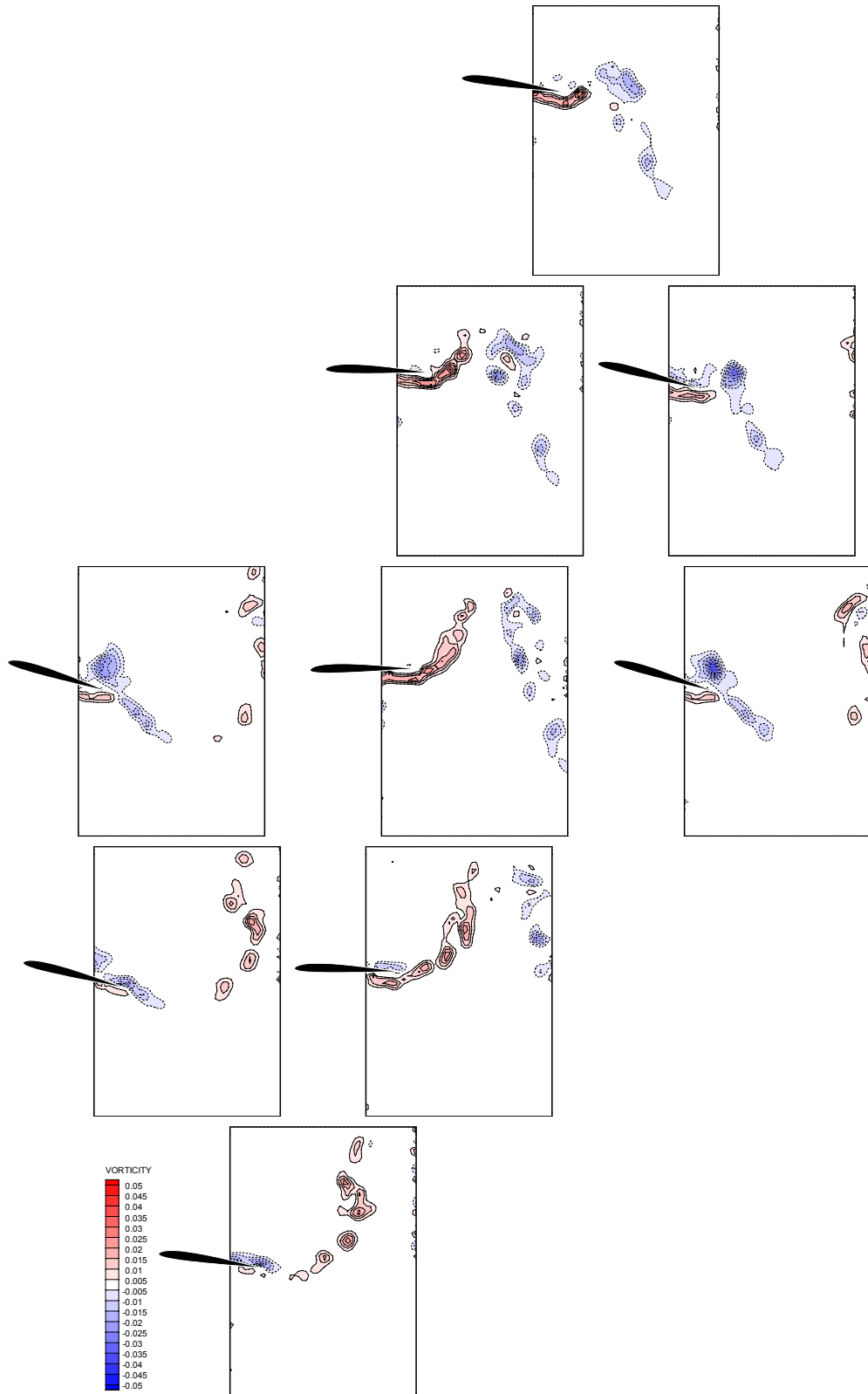


Figure 3.20 : Instantaneous vorticity patterns in the near-wake of the airfoil Case-45 (Category D)

These near-wake patterns indicate that the flapping motion will still induce a jet like velocity profile at this low Strouhal number regime. In accordance to that, the

averaged vorticity pattern plot shown in Figure 3.21b exhibits positive vorticity layer above and negative vorticity layer below the centerline of plunging motion. Vorticity patterns in the average of four distinct instants of an oscillation cycle (Figure 3.21a) are not as organized as those of previous categories. The variation of the effective angle of attack is similar to those of previous categories, however it should be noted that the maximum value is reduced and the time axis is elongated further (Figure 3.21d).

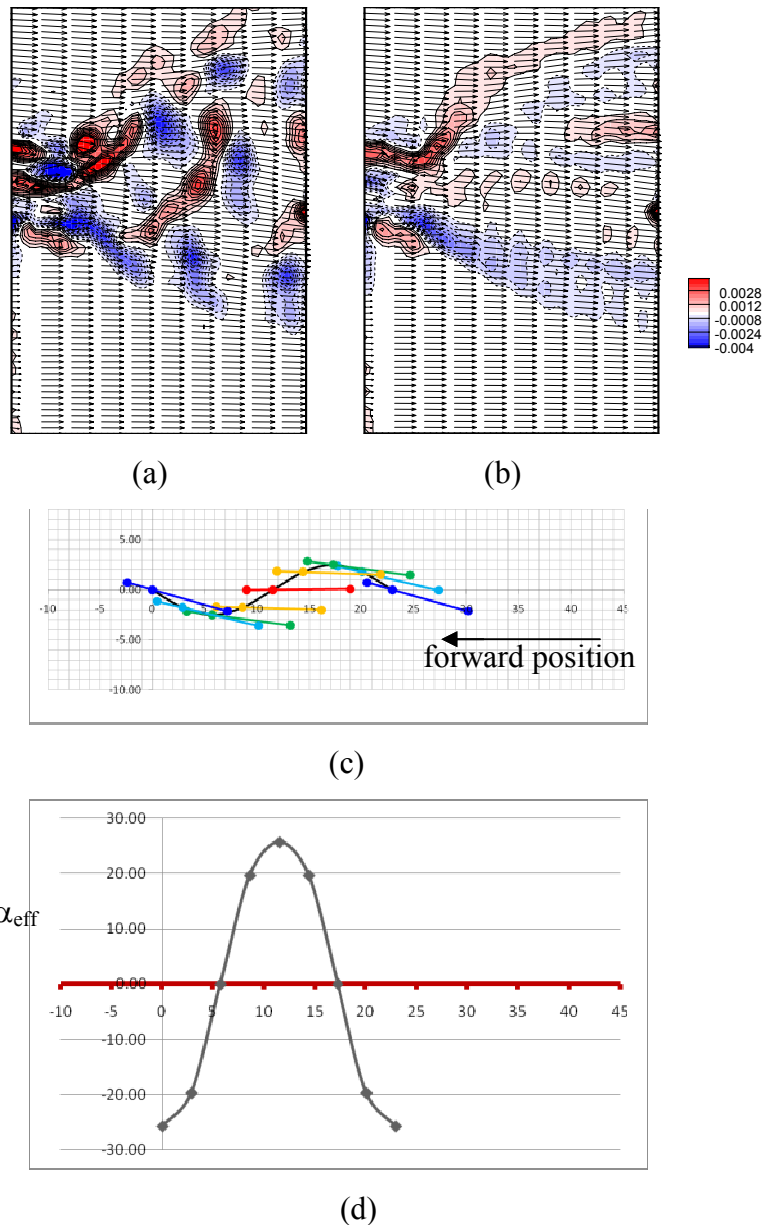


Figure 3.21 : a) and b) Averaged velocity and averaged vorticity plots, c) airfoil in motion, d) variation of effective angle of attack for Case-45

The flapping characteristics is more like a feathering wing, especially during the upstroke the airfoil chord line is close to be tangent to its sinusoidal trajectory as can be seen in Figure 3.21c.

The existence of a possible subset at higher plunge amplitudes has been checked and the absence is confirmed on an example case, namely Case-19, which exhibits the same category flow structures. The near-wake vorticity patterns shown in Figure 3.22 comply with the same story, i.e. the shedding of the leading edge vortex, its breaking apart, the positive trailing edge vorticity layer being unable to roll-up and stretching along an upward arc. The averaged vorticity patterns presented in both Figure 3.23a and 3.23b confirm this similarity. Not surprisingly, the flapping characteristics are similar; the airfoil is close to feather in the upstroke motion. Nevertheless, in comparison with Case-45, there are slight increases in both the amplitude and period of the effective angle of attack.

In Table 3.2, there are cases identified as a transition from one category to the next. These are denoted with two letters, the one with larger font size corresponds to the category with the dominant flow structure. To exemplify this fact, Case-31 is selected as a transition from Category C to Category D and called Category cD. The vorticity patterns around the airfoil shown in Figure 3.24 more likely belong to Category D. More specifically, one of the characteristics is that the trailing edge vorticity layer does not roll-up and extends to form an upward arc. On the other hand, the near-wake vorticity patterns shown in Figure 3.25 exhibit single, stronger positive vortex traceable in the wake until it leaves the field of view. Although the positive vorticity layer detaching from the trailing edge forms an extended arc, the near-wake patterns show that the end is actually rolled-up unlike it is observed in Category D.

The averaged vorticity patterns confirm the coexisting characteristics of the two categories. Vorticity patterns in the average of four distinct instants of an oscillation cycle (Figure 3.26a) are not as organized as in the case of Category D. On the other hand, averaged vorticity patterns presented in Figure 3.26b include positive and negative vorticity layers diverging above and below the mid-plunge position along with secondary horizontal positive and negative layers of vorticity at the center.

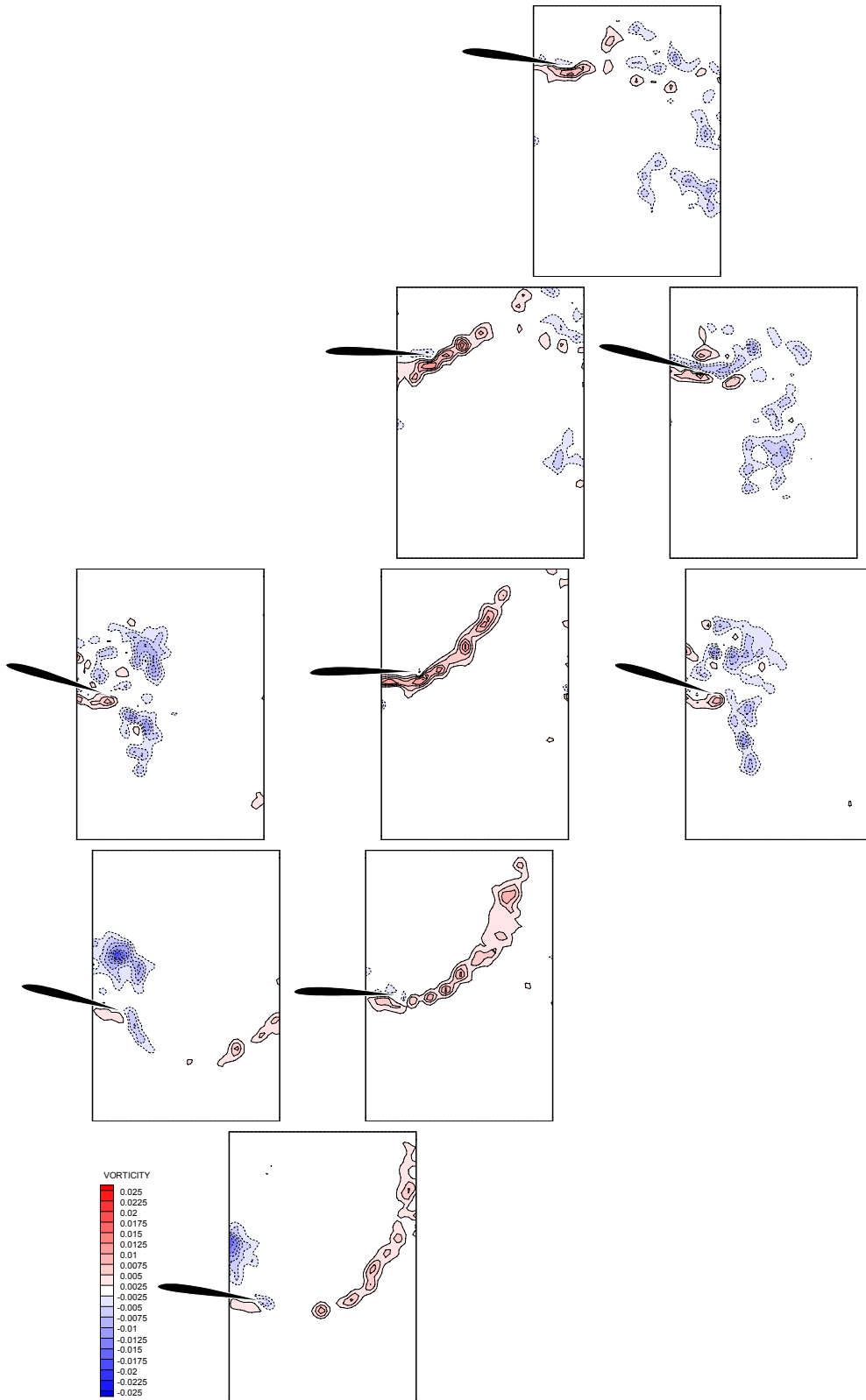
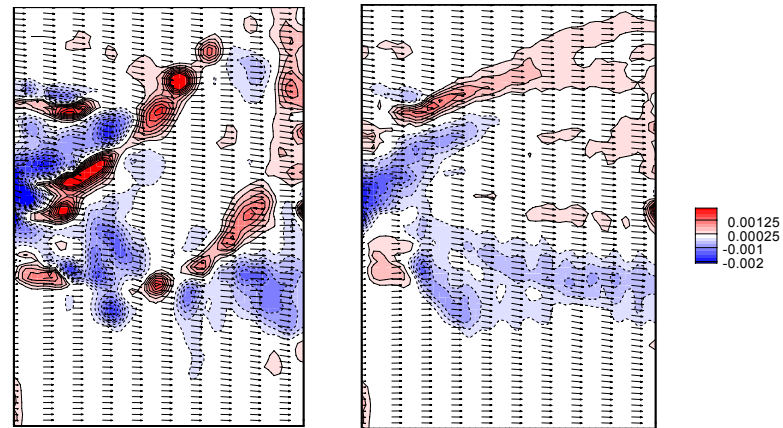
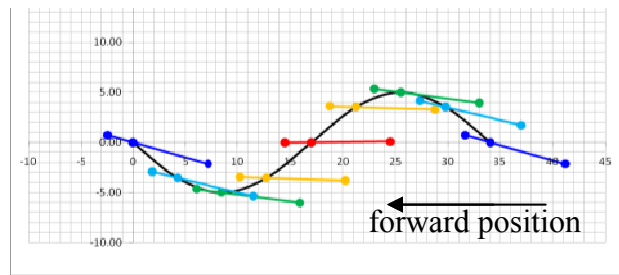


Figure 3.22 : Instantaneous vorticity patterns in the near-wake of the airfoil Case-19 (Category D)

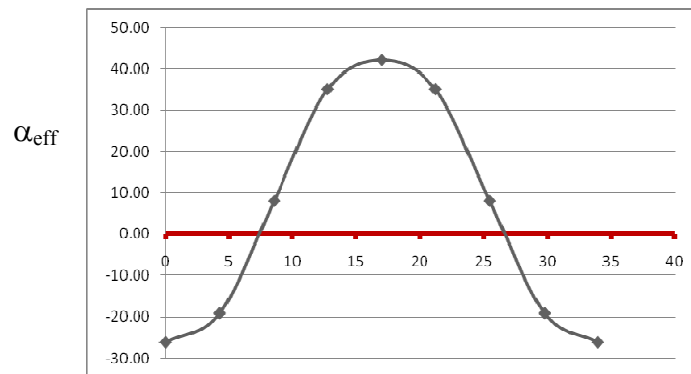


(a)

(b)



(c)



(d)

Figure 3.23 : a) Averaged velocity and b) averaged vorticity plots, c) airfoil in motion, d) variation of effective angle of attack for Case-19

Those are related to strong vortices detached from the layers forming upward and downward arcs and leaving the field of view approximately at the center of the right edge of the image frame. The origin of those layers is indicated on the near-wake patterns in Figure 3.25. Finally, since the flapping characteristics and the variation of the effective angle of attack resemble more of those of Category D, the dominance is decided to be given to this category.

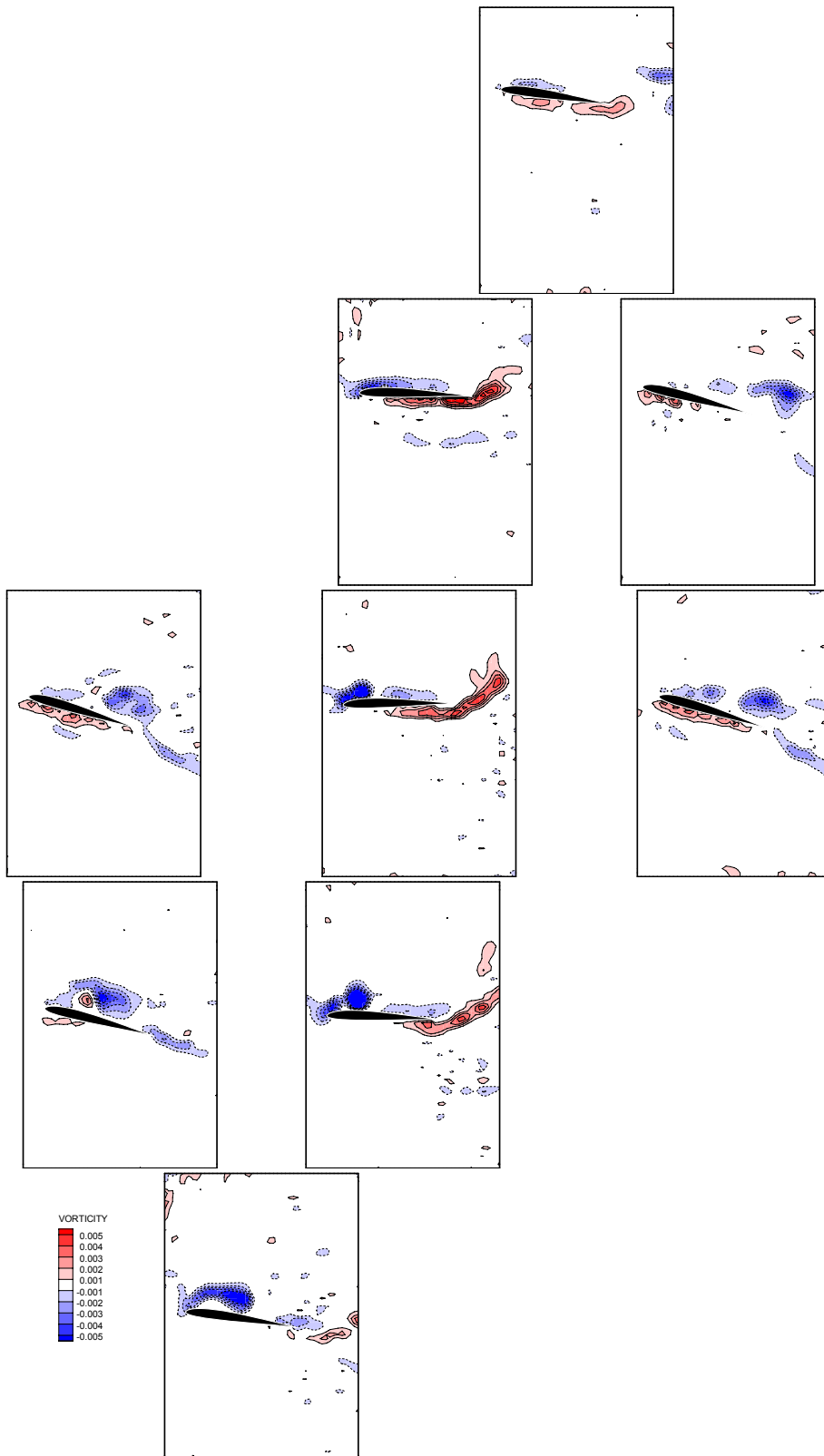


Figure 3.24 : Instantaneous vorticity patterns around the airfoil for Case-31 (Category cD)

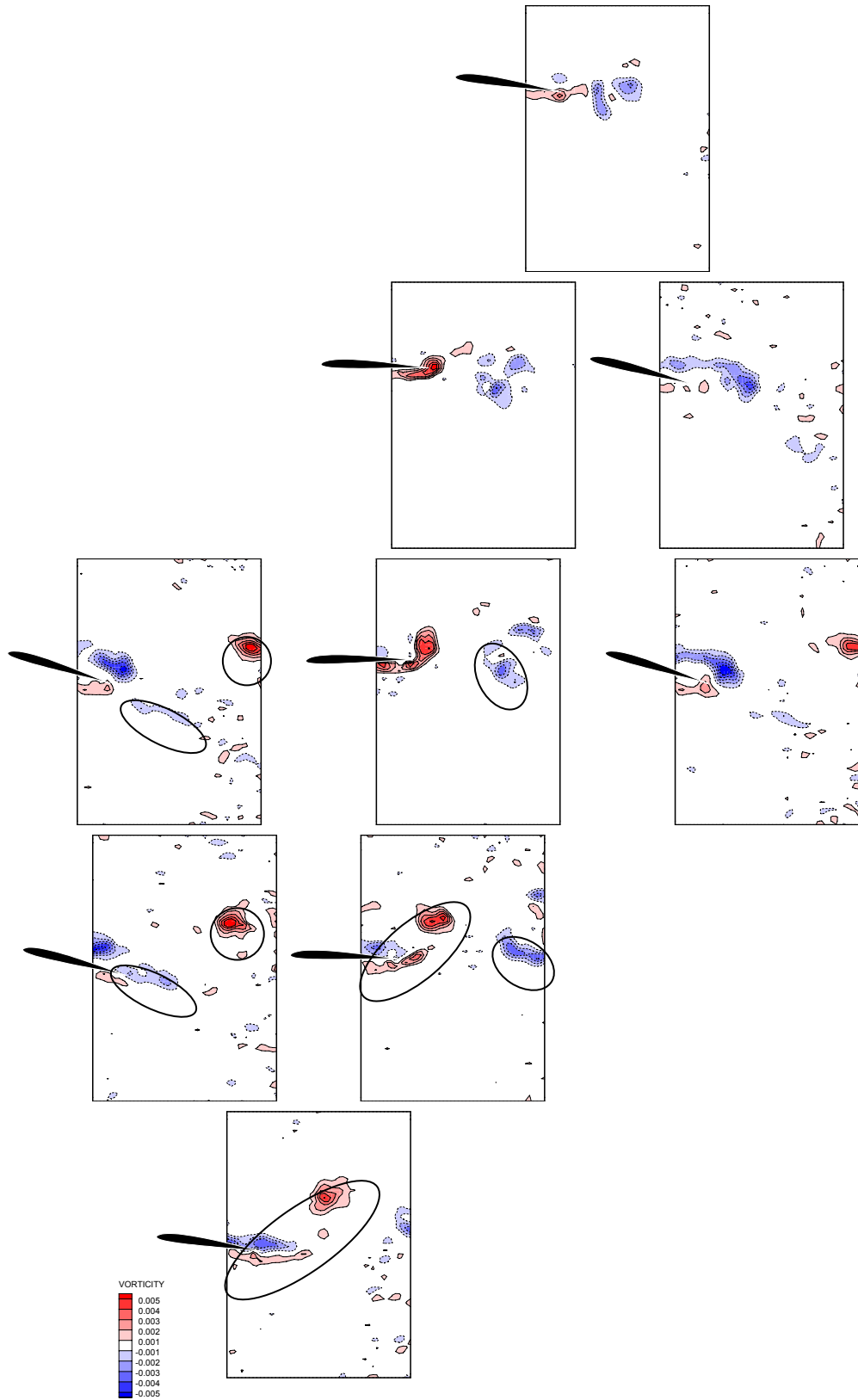


Figure 3.25 : Instantaneous vorticity patterns in the near-wake of the airfoil Case-31 (Category cD)

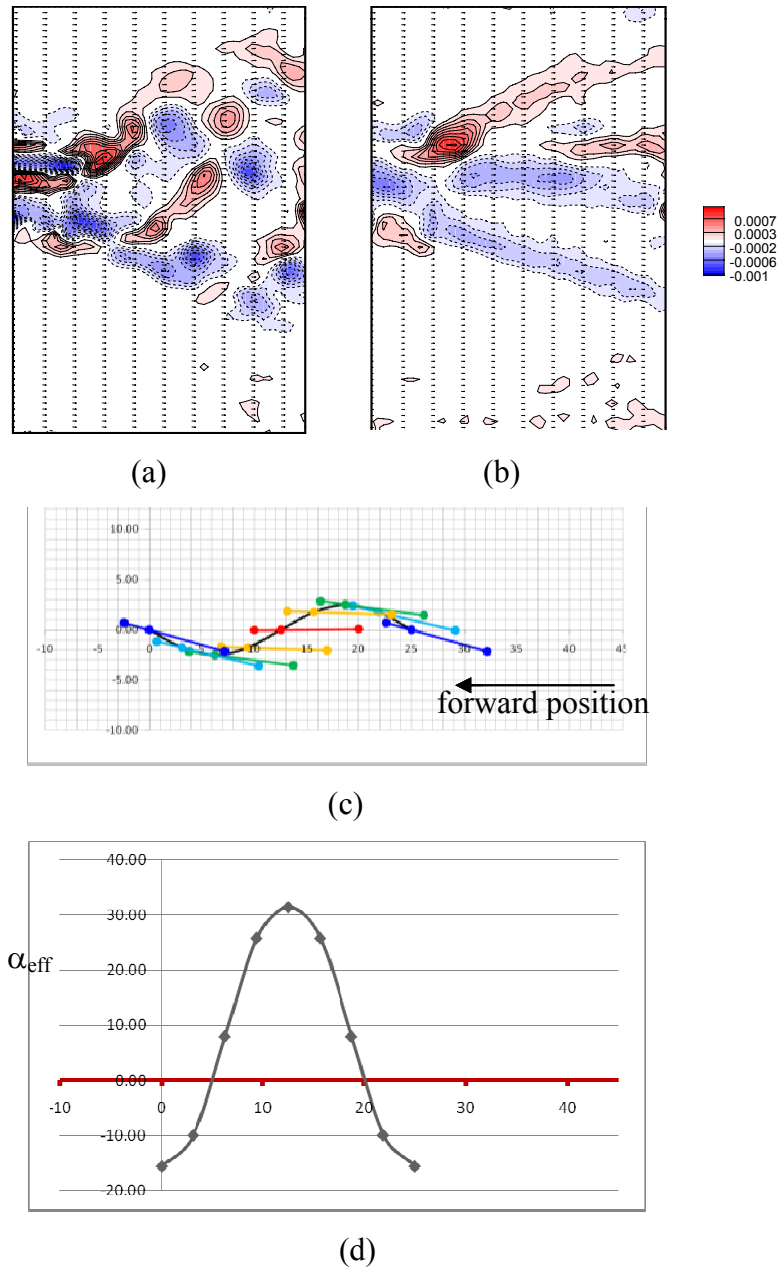


Figure 3.26 : a) and b) Averaged velocity and averaged vorticity plots, c) airfoil in motion, d) variation of effective angle of attack for Case-31

3.2.6 Category E (Ex: Case-14)

The example case of the previous category was obtained at the freestream velocity limit of the water channel. Therefore at the same plunge amplitude and frequency of motion, the last category of flow structures observed was Category D. However, for lower frequencies of motion either at the same or higher plunge amplitudes, it is possible to observe another category. Figure 3.27 shows the vorticity patterns for Case-14 which exemplifies this category. There are no apparent single and strong

leading edge or trailing edge vortices. A negative vorticity layer on the upper surface and a positive vorticity layer on the lower surface of the airfoil are present during all the stages of the motion. During the upstroke these vorticity layers are thin and attached to the surface; however, the negative vorticity layer detaches from the surface during the downstroke and exhibits localized cells of vorticity concentration. The parameters governing the airfoil motion are very close to the investigations made earlier in the context of AVT-149 experiments. Not surprisingly, the flow structures studied in detail in Fenercioglu and Cetiner (2008) are also very similar to those observed in Figure 3.27. A closer look at the upper surface of the airfoil indicates localized separations and reattachments especially close to the mid-plunge position during the downstroke (Fenercioglu and Cetiner, 2008). In parallel, the near-wake vorticity patterns shown in Figure 3.28 exhibit similar formations, i.e., Karman-like vortices at the beginning of the downstroke. The near-wake announces a velocity deficit; in the wavy layers of vorticity the negative is above and positive is below the centerline which also oscillates up and down with the airfoil motion.

The averaged vorticity patterns presented in Figure 3.29a show four layers of negative and positive vorticity aligned horizontally in that order, in accordance with the oscillations of the wake captured at four distinct instants of a motion cycle. On the other hand, the averaged vorticity field shown in Figure 3.29b exhibit only two of those negative and positive layers, characteristic of Category E cases. Although this is the single category where we can predict a definite drag producing wake, the drag coefficient is expected to be respectively low since the flapping characteristics is the best presentation of feathering among all the cases investigated in this study. The period of the trajectory is large and the effective angle of attack is almost always positive, the maximum value is not surpassing the stall limits. Just to show and prove the consistent characteristic of Category E, i.e., the formation of two negative and positive vorticity layers on the averaged flow field, Case-33 is presented in Figure 3.30. The case has lower plunge amplitude with respect to Case-14, same as Case-45 exemplifying Category D and same frequency of motion as Case-14, however lower than that of Case-45. The vorticity patterns around the airfoil and in the near-wake are similar to those of Case-14 and are not shown for the sake of brevity.

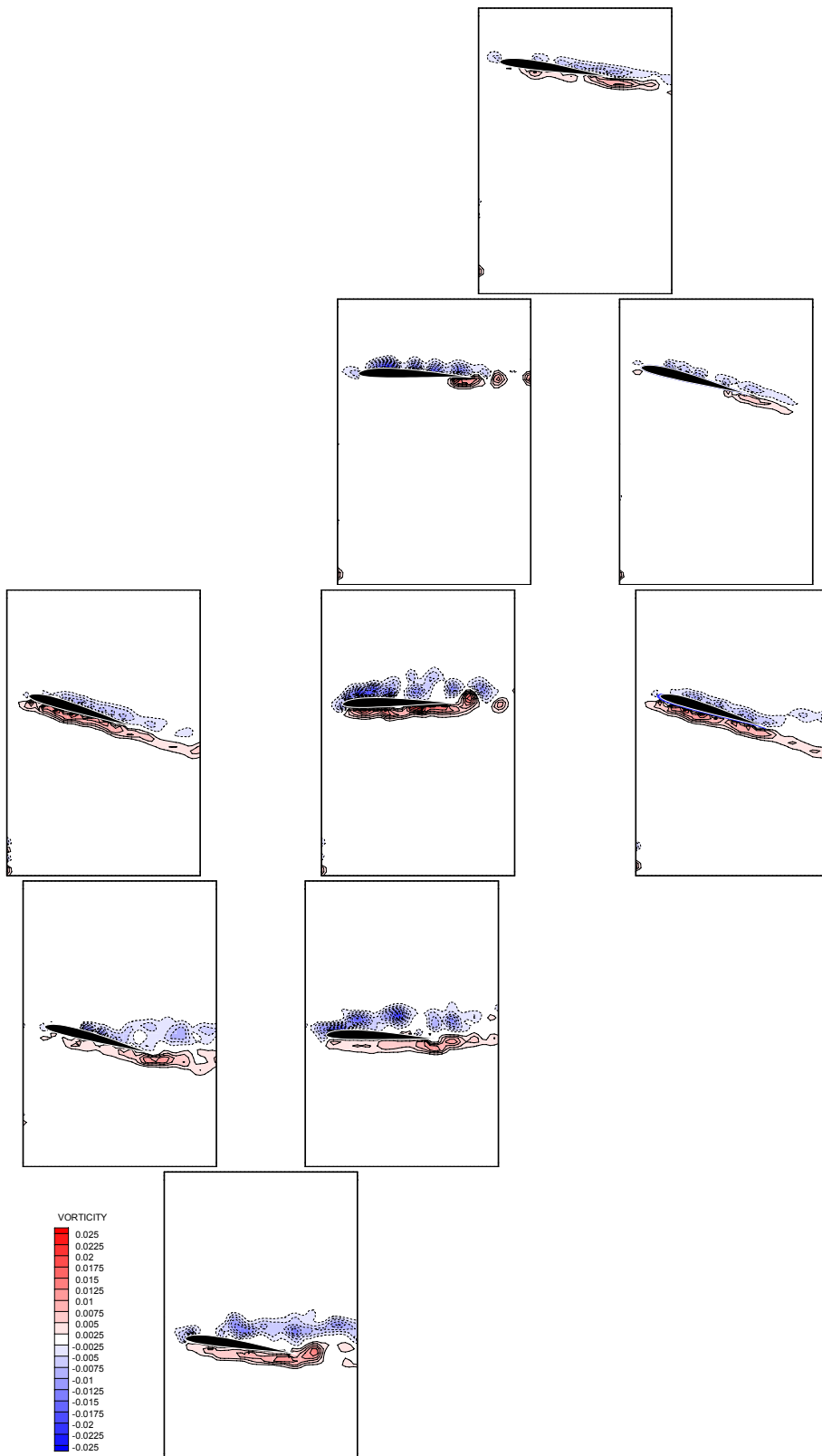


Figure 3.27 : Instantaneous vorticity patterns around the airfoil Case-14(Category E)

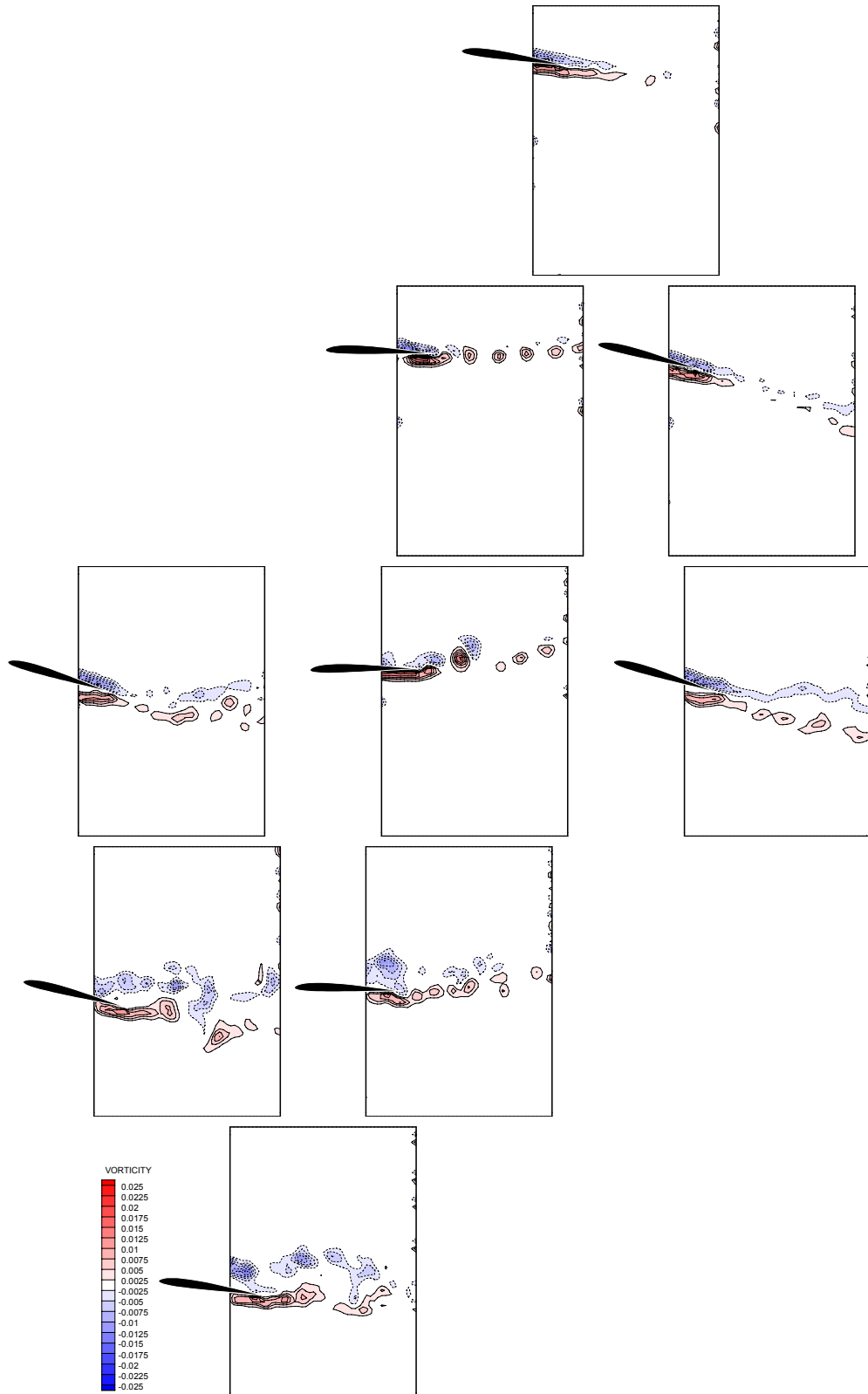
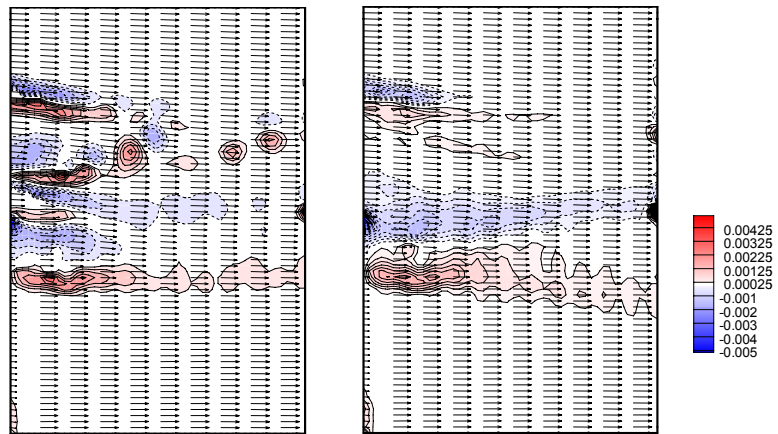
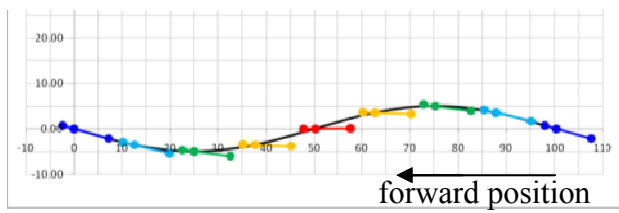


Figure 3.28 : Instantaneous vorticity patterns in the near-wake of the airfoil Case-14 (Category E)

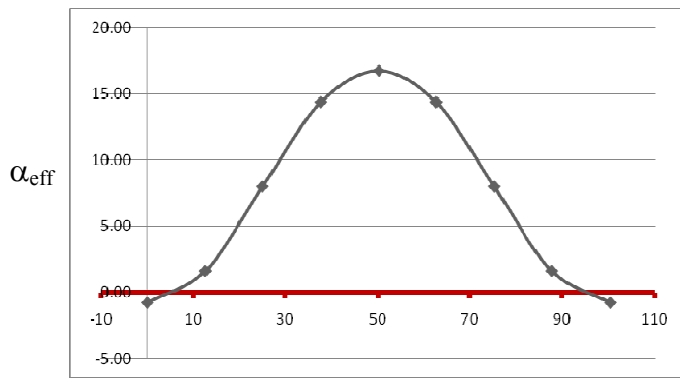


(a)

(b)



(c)



(d)

Figure 3.29 : a) and b) Averaged velocity and averaged vorticity plots, c) airfoil in motion, d)variation of effective angle of attack for Case-14(Category E)

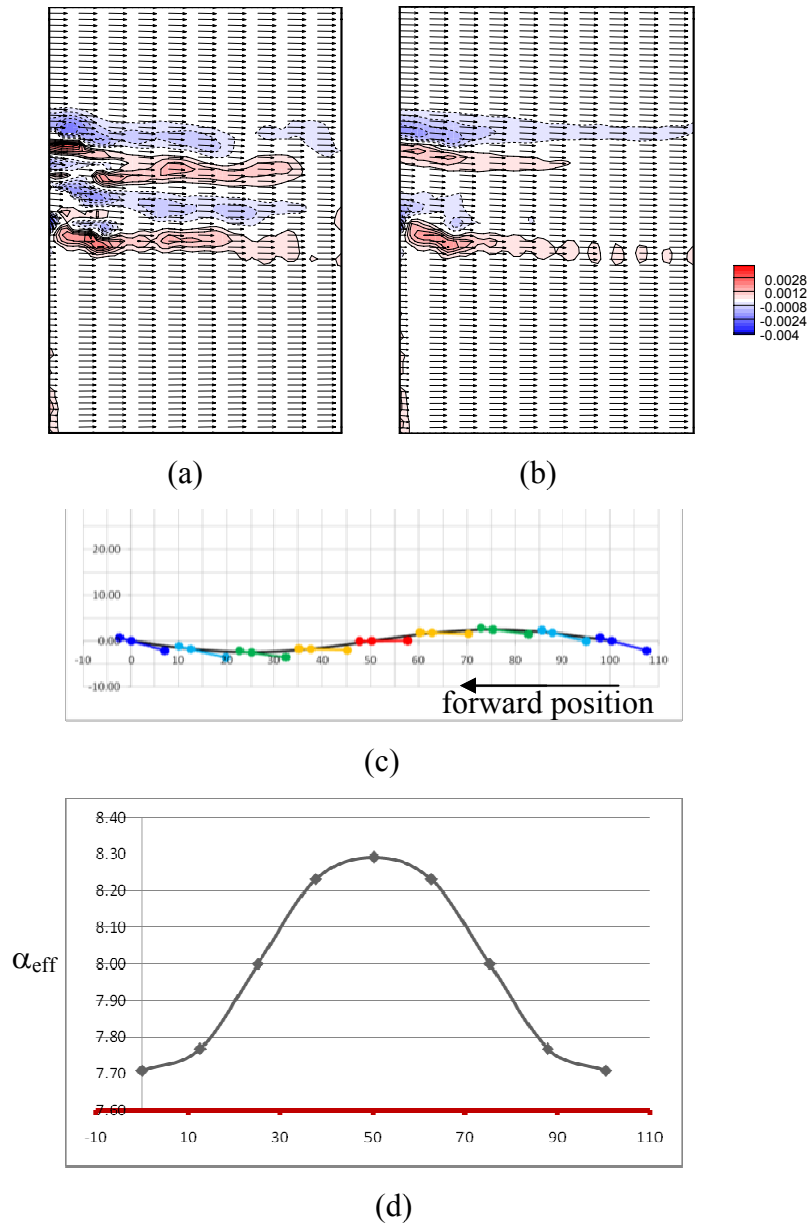


Figure 3.30 : a) and b) Averaged velocity and averaged vorticity plots, c) airfoil in motion, d) variation of effective angle of attack for Case-33(Category E)

3.3 Summary of Categories Based on Flow Structures and Their Occurrence on Parameter Space

Flow structure categorization described in detail in previous subchapters is summarized in the Table 3.3. It should be noted that there is a pair of counter rotating vortices formed at the leading and trailing edges of the airfoil for Category A. On the other hand, for Category C and D, the roll-up radius of the trailing edge vortex is large and its timing of shedding is not same as or close to that of the leading edge vortex; therefore these two categories exhibit more likely a LEV (Leading Edge Vortex). Although the counter rotating vortices are not shed together for Category B,

the presence of a pair is still observed. A negative vortex likely to be the LEV is still detectable at the leading edge and covers nearly half of the airfoil's upper surface during the upstroke in Categories A1 and B2. For Category B1, that vortex is not able to evolve as a LEV and dissipates during the upstroke. Finally for Category E, instead of a large scale LEV, there are small scale vortex rolls along the upper surface of the airfoil.

As given in Table 3.2, the first approach is to study the occurrence of the flow structure categories based on Strouhal number. Figure 3.31 presents the regions where it is possible to observe a flow structure category on a St vs h_{amp}/c plot. The same regions are also distinguishable in Table 3.2. As mentioned before, there is a threshold for Category C to appear, i.e. $h_{amp}/c < 0.25$. The remaining categories are in order; Category A appears at large Strouhal numbers and Category E at low Strouhal numbers.

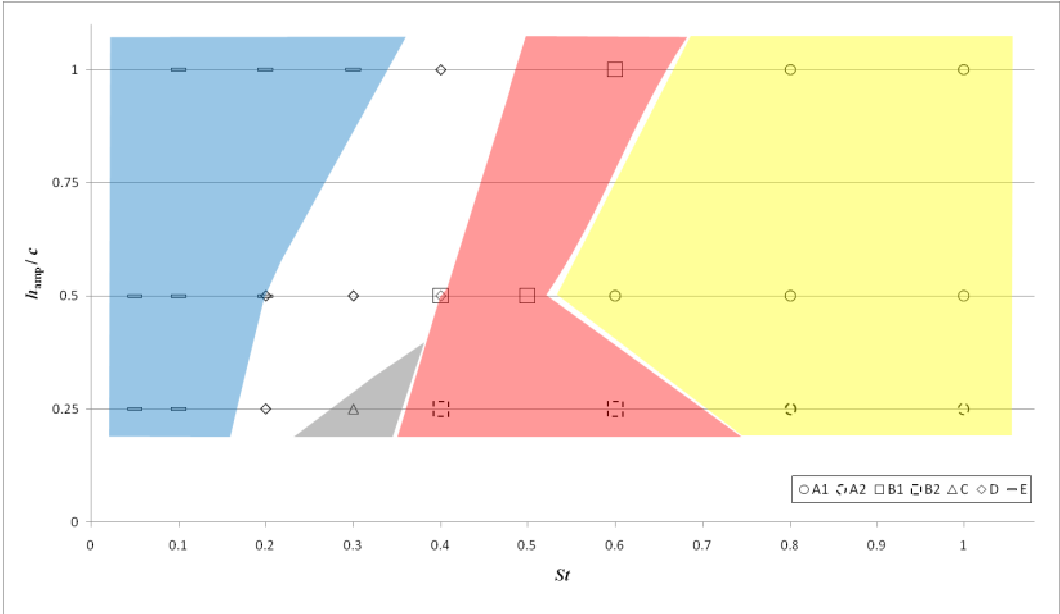


Figure 3.31 : The occurrence of flow structures on St vs h_{amp}/c plot

Figure 3.32 presents the categories on a parameter space of k vs h_{amp}/c . Although the order of occurrence of the flow structure categories is the same as in the previous plot, the category bands which are shown by regions of different color are extending from low k and high h_{amp}/c values to large k and low h_{amp}/c values.

Table 3.3: Summary of categories based on flow structures

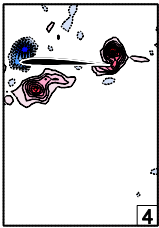
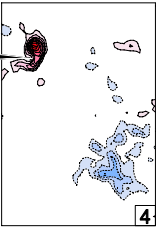
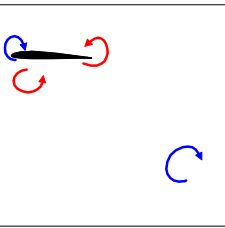
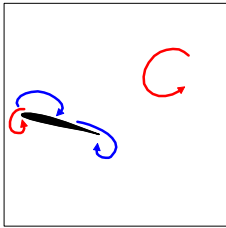
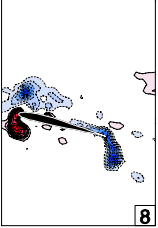
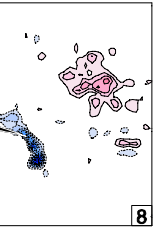
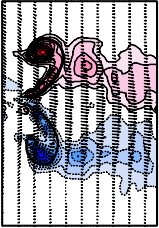
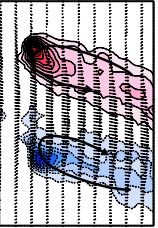
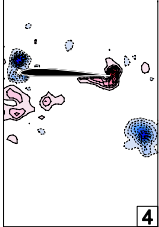
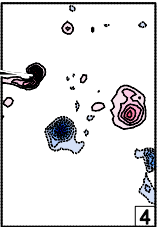
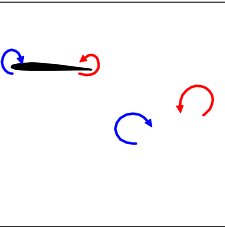
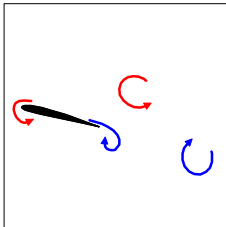
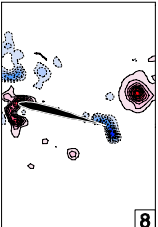
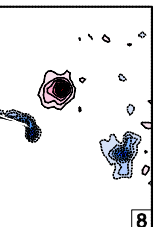
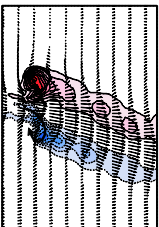
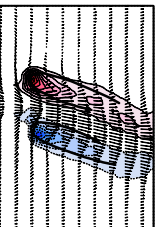
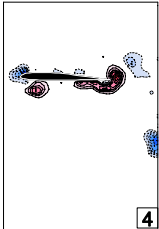
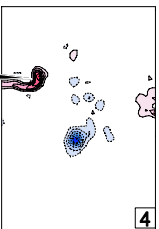
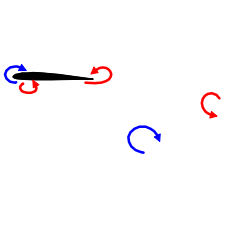
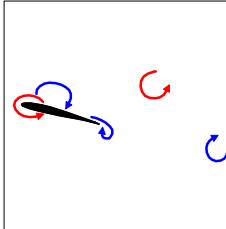
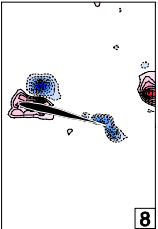
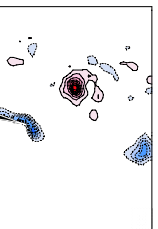
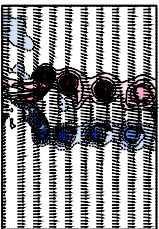
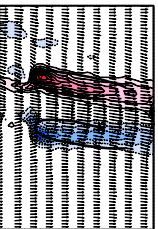


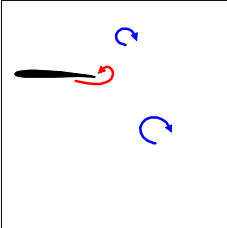
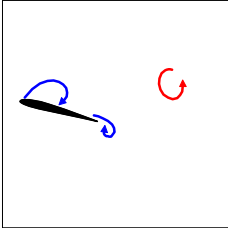


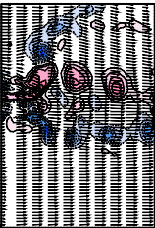
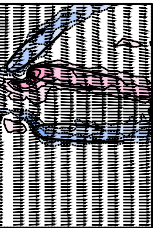
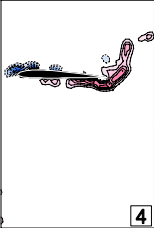
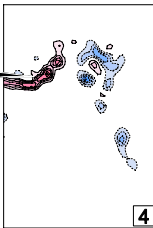
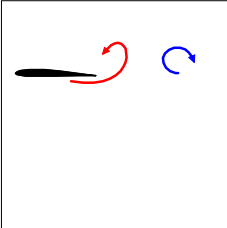
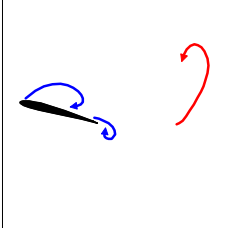
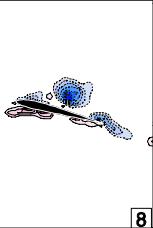
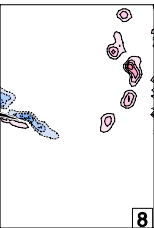
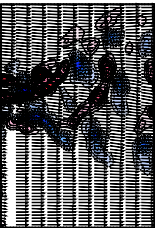
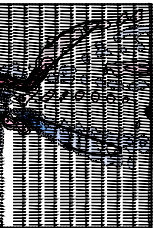
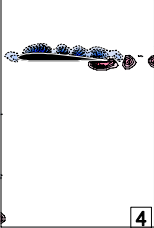
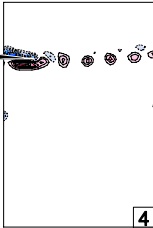
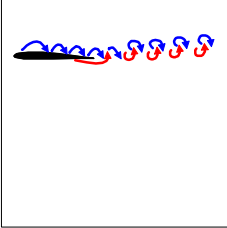
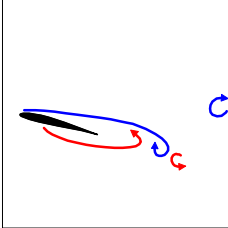
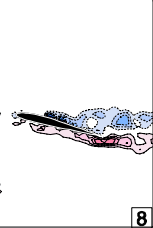
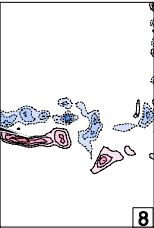
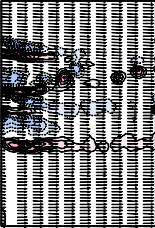
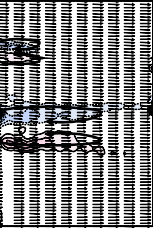
Category	Instantaneous vorticity		Downstroke	Upstroke	Instantaneous vorticity		Averaged vorticity	
A1								
A2								
B2								

Table 3.3: (Continued) Summary of categories based on flow structures

Category	Instantaneous vorticity		Downstroke	Upstroke	Instantaneous vorticity		Averaged vorticity	
C								
D								
E								

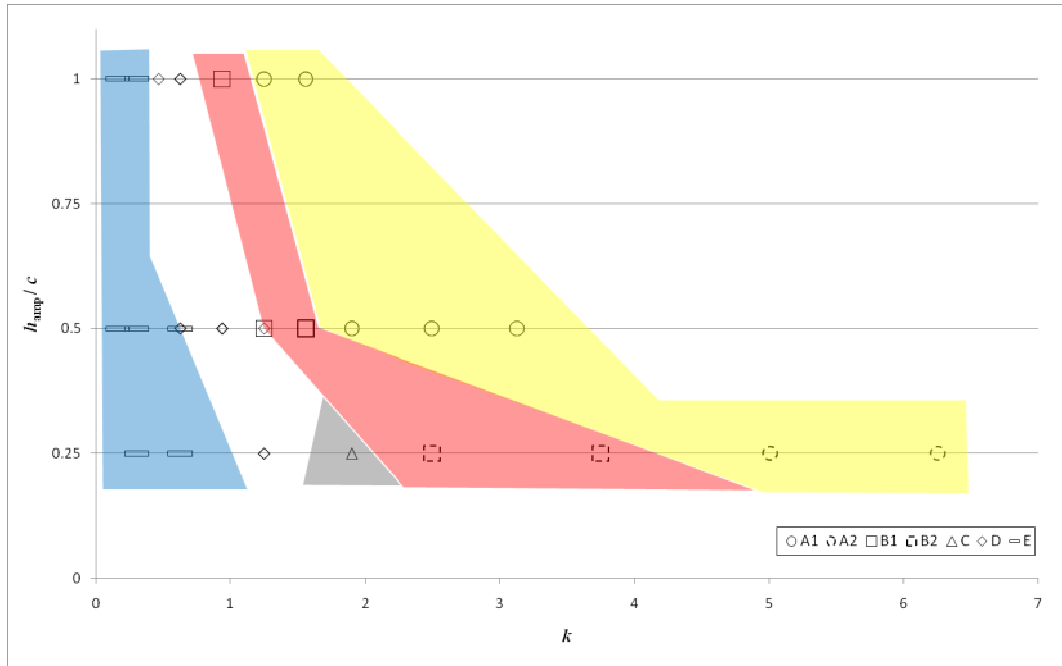


Figure 3.32 : The occurrence of flow structures on k vs h_{amp}/c plot

The Reynolds number dependency of the flow structure categories is shown in Figure 3.33. The regions are overlapping and it is impossible to predict a definite range of or an arrangement according to Reynolds number. Therefore, the results of the current study show that, in a range of $800 < Re < 14\ 000$, the flow structure categories are independent of Reynolds number.

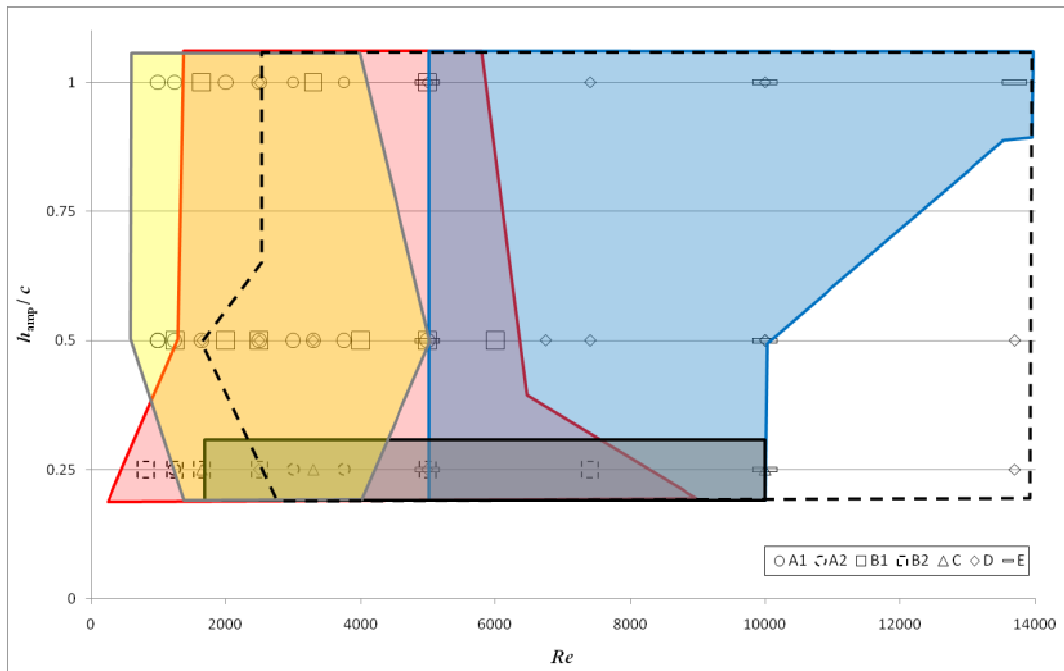


Figure 3.33 : The occurrence of flow structures on Re vs h_{amp}/c plot

In order to establish a comparison with the results of Anderson (1996), the flow categories are also presented on a St vs α_{eff} plot as shown in Figure 3.34. It should be noted that in the 62 base cases presented so far, the mean angle of attack and the amplitude of pitching motion are the same. Therefore, the effective angle of attack depends only on Strouhal number.

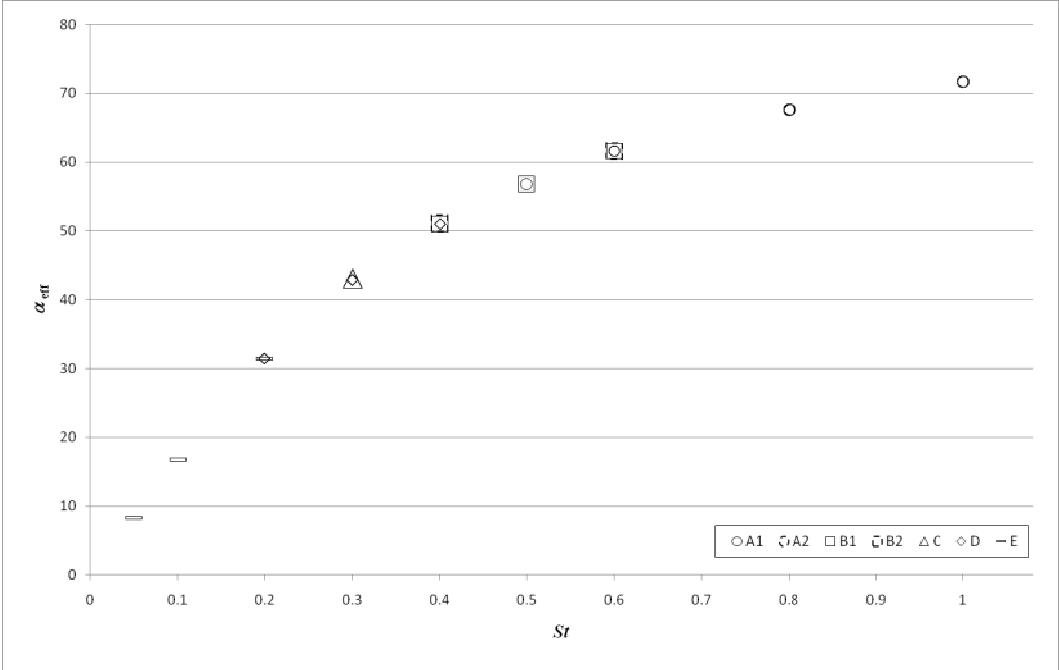


Figure 3.34 : The flow categories on St vs α_{eff} plot

The parameter space in a point of view of the effective angle of attack is presented in Figure 3.35.

On the investigation of flow structures as function of the Strouhal number and the effective angle of attack, the cases studied are aligned on an opposite curve in comparison with those of Anderson (1996). Figure 3.34 shows the categories in order from A to E for decreasing Strouhal numbers. There are some overlaps for different plunge amplitudes or frequency of motion. A common region of investigation with the study of Anderson (1996) is for low Strouhal numbers and low effective angles of attack where there is an agreement in the flow structure descriptions.

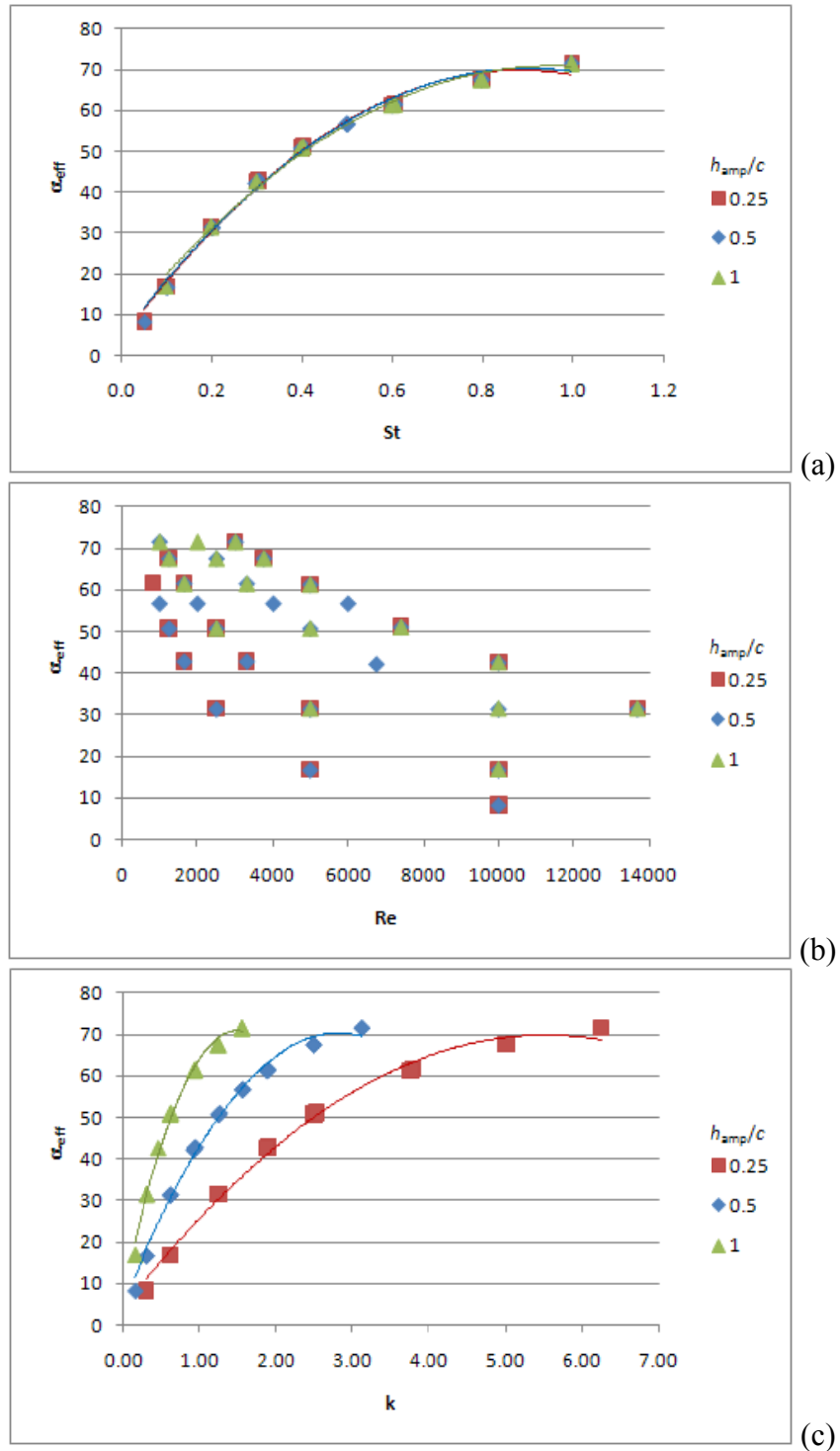


Figure 3.35 : The parameter space for α_{eff} in terms of a) St , b) Re and c) k

3.4 The Variation of Force Coefficients and Efficiencies

Although the calculations of drag/thrust coefficients and efficiencies require a considerable amount of assumptions which are mostly violated in the experiments, the results are not very far from direct measurements and valuable to show the trends.

Table 3.4 gives in detail the results of drag/thrust coefficient for each case as well as other details including the value of major parameters and the deviation from the freestream velocity at the upper edge of the field of view of PIV images. Table 3.4 should be considered together with Table 3.5 which presents freestream velocity subtracted velocity profiles of the 62 base cases obtained at 1.1 chord away from the trailing edge. As the freestream velocity increases in each row of Table 3.5, the velocity deficit or jet-like profile decreases in size. Therefore, three color scales are used for the vector lengths; the purple vectors are enlarged 2.5 times with respect to the dark blue vectors and 5 times with respect to the light blue vectors.

As there are very large variations of velocity at the upper edge of the field of view in some cases, the validity of calculated drag / thrust coefficient is questioned. The velocity deficit profiles presented in Table 3.5 establish a decision tool for the calculated force coefficients. As a result Table 3.4 includes a column showing the considered values of force coefficient. In general, we do not expect to under or over estimate the force when the average velocity at the upper edge of the image differs less than 10% with respect to the freestream velocity. These values are highlighted in rose at the 9th column of the table. When the difference is larger, but less than 25%, it is highlighted in yellow. The calculated values are checked with the profile plots. Very low values are approximated to zero and cases presenting a constant or increasing deficit at the upper and/or lower edges of the image are either multiplied by two or divided by two. Therefore, although the low divergence from the freestream at the limits of the field of view is a sign to accept the calculated force coefficient as it is, there are exceptions and the decision should be made based on the shape of the profile.

Table 3.6 gives the same layout as Table 3.4, however the cells include force coefficients and efficiencies.

An overall look at the Table 3.5 together with Table 3.6 and Figures 3.30 and 3.31 yields the following remarks:

- Except low frequencies of motion, in general, high Strouhal number cases present a well defined high speed jet-like flow and yield high values for thrust coefficient. However, as Equation (2.5) dictates, the efficiencies are lower compared to low Strouhal cases whose thrust coefficients are also low.

Table 3.4: The Force Coefficients

case no	Re	St	k	f	k_{amp}/c	U_{∞} [m/s]	U_{amp} img	$\frac{ U_{\infty} - U_{amp} }{U_{\infty}}$	Calculated C_f	Considered C_f
1	1000	0.5	1.56	0.05	0.5	0.0100	0.0052	0.4821	-0.56	x 2
2	1250	0.4	1.25	0.05	0.5	0.0126	0.0067	0.4661	-0.81	x 2
3	1650	0.3	0.95	0.05	0.5	0.0166	0.0102	0.3843	-0.87	x 2
4	2500	0.2	0.63	0.05	0.5	0.0251	0.0229	0.0876	-0.41	same
5	5000	0.1	0.31	0.05	0.5	0.0502	0.0522	0.0398	0.13	0
6	10000	0.0	0.16	0.05	0.5	0.1004	0.1053	0.0488	0.18	0
7	1000	1.0	3.13	0.1	0.5	0.0100	0.0027	0.7311	16.47	same
8	1250	0.8	2.50	0.1	0.5	0.0126	0.0049	0.6120	11.41	same
9	1650	0.6	1.90	0.1	0.5	0.0166	0.0076	0.5412	5.79	same
10	2000	0.5	1.56	0.1	0.5	0.0201	0.0131	0.3476	3.04	same
11	2500	0.4	1.25	0.1	0.5	0.0251	0.0220	0.1235	1.96	/ 2
12	3300	0.3	0.95	0.1	0.5	0.0331	0.0350	0.0564	1.16	same
13	5000	0.2	0.63	0.1	0.5	0.0502	0.0517	0.0299	0.06	0
14	10000	0.1	0.31	0.1	0.5	0.1004	0.1048	0.0438	0.15	0
15	2500	0.8	2.50	0.2	0.5	0.0251	0.0136	0.4582	8.79	same
16	3300	0.6	1.90	0.2	0.5	0.0331	0.0256	0.2273	4.11	same
17	4000	0.5	1.56	0.2	0.5	0.0402	0.0364	0.0936	2.16	same
18	5000	0.4	1.25	0.2	0.5	0.0502	0.0468	0.0677	1.00	same
19	6750	0.3	0.93	0.2	0.5	0.0678	0.0655	0.0335	0.41	/ 2
20	10000	0.2	0.63	0.2	0.5	0.1004	0.1039	0.0349	0.05	0
21	3000	1.0	3.13	0.3	0.5	0.0301	0.0161	0.4655	13.10	same
22	3750	0.8	2.50	0.3	0.5	0.0377	0.0240	0.3625	8.15	same
23	5000	0.6	1.88	0.3	0.5	0.0502	0.0415	0.1733	4.27	same
24	6000	0.5	1.56	0.3	0.5	0.0602	0.0534	0.1135	2.36	same
25	7400	0.4	1.27	0.3	0.5	0.0743	0.0751	0.0108	1.33	same
26	10000	0.3	0.94	0.3	0.5	0.1004	0.1024	0.0199	0.55	same
27	13700	0.2	0.63	0.3	0.5	0.1375	0.1420	0.0324	0.13	same
28	825	0.6	3.79	0.1	0.25	0.0083	0.0052	0.3722	2.89	same
29	1250	0.4	2.50	0.1	0.25	0.0126	0.0064	0.4900	-0.40	x 2
30	1650	0.3	1.90	0.1	0.25	0.0166	0.0089	0.4628	-0.63	x 2
31	2500	0.2	1.25	0.1	0.25	0.0251	0.0195	0.2231	-0.83	same
32	5000	0.1	0.63	0.1	0.25	0.0502	0.0521	0.0378	0.12	0
33	10000	0.0	0.31	0.1	0.25	0.1004	0.1047	0.0428	0.09	0
34	1250	0.8	5.01	0.2	0.25	0.0126	0.0046	0.6335	12.02	same
35	1650	0.6	3.79	0.2	0.25	0.0166	0.0081	0.5110	5.75	same
36	2500	0.4	2.50	0.2	0.25	0.0251	0.0204	0.1873	0.94	same
37	3300	0.3	1.90	0.2	0.25	0.0331	0.0355	0.0715	0.49	same
38	5000	0.2	1.25	0.2	0.25	0.0502	0.0514	0.0239	0.21	same
39	10000	0.1	0.63	0.2	0.25	0.1004	0.1040	0.0359	0.08	0
40	3000	1.0	6.26	0.6	0.25	0.0301	0.0196	0.3493	13.28	same
41	3750	0.8	5.01	0.6	0.25	0.0377	0.0300	0.2032	9.09	same
42	5000	0.6	3.75	0.6	0.25	0.0502	0.0475	0.0538	4.68	same
43	7400	0.4	2.54	0.6	0.25	0.0743	0.0683	0.0812	0.92	same
44	10000	0.3	1.88	0.6	0.25	0.1004	0.0890	0.1135	0.33	same
45	13700	0.2	1.25	0.6	0.25	0.1375	0.1390	0.0106	0.22	same
46	1000	1.0	1.56	0.05	1	0.0100	0.0015	0.8556	10.04	same
47	1250	0.8	1.25	0.05	1	0.0126	0.0060	0.5251	5.65	same
48	1650	0.6	0.95	0.05	1	0.0166	0.0111	0.3300	3.13	same
49	2500	0.4	0.63	0.05	1	0.0251	0.0254	0.0120	1.59	same
50	5000	0.2	0.31	0.05	1	0.0502	0.0504	0.0040	-0.04	0
51	10000	0.1	0.16	0.05	1	0.1004	0.1024	0.0199	0.10	0
52	2000	1.0	1.56	0.1	1	0.0201	0.0137	0.3177	13.59	same
53	2500	0.8	1.25	0.1	1	0.0251	0.0207	0.1753	7.12	same
54	3300	0.6	0.95	0.1	1	0.0331	0.0342	0.0322	3.56	same
55	5000	0.4	0.63	0.1	1	0.0502	0.0517	0.0299	1.03	same
56	10000	0.2	0.31	0.1	1	0.1004	0.1007	0.0030	0.01	0
57	3000	1.0	1.56	0.15	1	0.0301	0.0208	0.3094	14.19	same
58	3750	0.8	1.25	0.15	1	0.0377	0.0323	0.1421	7.15	same
59	5000	0.6	0.94	0.15	1	0.0502	0.0471	0.0618	3.82	same
60	7400	0.4	0.63	0.15	1	0.0743	0.0812	0.0923	1.50	same
61	10000	0.3	0.47	0.15	1	0.1004	0.0998	0.0060	0.69	same
62	13700	0.2	0.31	0.15	1	0.1375	0.1400	0.0178	0.12	0

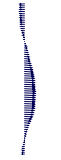
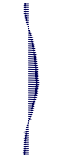
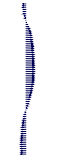














Table 3.5: Velocity deficit profiles ($u-U_\infty$) in the near wake

h_{amp}/c	f	Strouhal number										
		1.0	0.9	0.8	0.7	0.6	0.5	0.4	0.3	0.2	0.1	0.05
0.25	0.1					28		29	30	31	32	33
	0.2			34		35		36	37	38	39	
	0.6		40		41		42		43	44	45	

Table 3.5: (continued) Velocity deficit profiles ($u-U_\infty$) in the near wake

h_{amp}/c	f	Strouhal number													
		1.0	0.9	0.8	0.7	0.6	0.5	0.4	0.3	0.2	0.1	0.05			
0.5	0.05						1	2	3	4	5	6			
							10	11	12	13	14				
	0.1	7			8			9	10	11	12	13	14		
						15			16	17	18	19	20		
	0.2					15			16	17	18	19	20		
						15			16	17	18	19	20		
	0.3	21			22			23	24	25	26	27			
						22			23	24	25	26	27		

Table 3.5: (continued) Velocity deficit profiles ($u-U_\infty$) in the near wake

h_{amp}/c	f	Strouhal number										
		1.0	0.9	0.8	0.7	0.6	0.5	0.4	0.3	0.2	0.1	0.05
1.0	0.05	46		47		48		49		50	51	
												
	0.1	52		53		54		55		56		
												
	0.15	57		58		59		60	61	62		
												

- In general, very low velocity deficits or force coefficient values close to zero are observed for low Strouhal numbers, i.e. $St < 0.2$. The exception to that is for $h_{amp}/c = 0.25$ and $f = 0.1\text{Hz}$, and $h_{amp}/c = 0.5$ and $f = 0.05\text{Hz}$. The parameter common to those two rows of data is the product of the oscillation frequency and plunging amplitude to chord ratio, which is equal to 0.025. Therefore, $St = 0.2$ constitutes a boundary for thrust production for $f h_{amp}/c > 0.025$. This conclusion agrees well with previous studies of MIT group (Triantafyllou et al., 1991 and 2004). On the other hand, all of those cases presenting velocity deficits or force coefficient values close to zero exhibit flow structures in Category E. The occurrence of Category E on k vs h_{amp}/c plot resembles the plots presented in Jones et al. (1996 and 1998) for the threshold of thrust production in pure plunge motion. The threshold value is approximately the same as that presented in Jones et al. (1996), i.e. $k = 1$ based on the definition of the current study. On the other hand, a similar plot presented in Jones et al. (1998) along with the Strouhal numbers investigated shows the dependency of the threshold curve on Strouhal number which also agrees well with Figure 3.31 of the current study.
- Although Table 3.4 and Table 3.5 consider only the u component of the velocity, the jet-like flow is inclined in the cases designated with Category A. Therefore, as aforementioned, a lift production along with thrust is expected. The band of occurrence of Category A on k vs h_{amp}/c plot also agrees well with wake classification types for pure plunge motion presented in Jones et al. (1998). As the pitch amplitude and mean angle of attack are kept constant for the base investigation cases, it is expected to have similar conclusions with pure plunge motion.
- In accordance with Equation (2.5), high efficiencies are observed in general for low Strouhal numbers about $St \geq 0.2$, just before a $C_d \geq 0$ value is observed. These cases are in general designated as Category D.

Table 3.6: Force coefficients and efficiencies given on the parameter space

h_{amp}/c	f	Strouhal number										
		1.0	0.9	0.8	0.7	0.6	0.5	0.4	0.3	0.2	0.1	0.05
0.25	0.1					$C_f = 2.89$ $C_T = 5.78$ $\eta = 0.55$		$C_d = 0.80$	$C_d = 1.26$	$C_d = 0.83$	$C_d = 0$	$C_d = 0$
	0.2			$C_f = 12.02$ $C_T = 24.04$ $\eta = 0.33$		$C_f = 5.75$ $C_T = 11.50$ $\eta = 0.44$		$C_f = 0.94$ $C_T = 1.87$ $\eta = 0.74$	$C_f = 0.49$ $C_T = 0.98$ $\eta = 0.83$	$C_f = 0.21$ $C_T = 0.41$ $\eta = 0.91$	$C_d = 0$	
	0.6	$C_f = 13.28$ $C_T = 26.56$ $\eta = 0.32$		$C_f = 9.09$ $C_T = 18.18$ $\eta = 0.37$		$C_f = 4.68$ $C_T = 9.35$ $\eta = 0.47$		$C_f = 0.92$ $C_T = 1.84$ $\eta = 0.74$	$C_f = 0.33$ $C_T = 0.66$ $\eta = 0.87$	$C_f = 0.22$ $C_T = 0.44$ $\eta = 0.91$		
0.5	0.05						$C_d = 1.12$	$C_d = 1.16$	$C_d = 1.74$	$C_d = 0.41$	$C_d = 0$	$C_d = 0$
	0.1	$C_f = 16.47$ $C_T = 16.47$ $\eta = 0.39$		$C_f = 11.41$ $C_T = 11.41$ $\eta = 0.44$		$C_f = 5.79$ $C_T = 5.79$ $\eta = 0.55$	$C_f = 3.04$ $C_T = 3.04$ $\eta = 0.66$	$C_f = 0.98$ $C_T = 0.98$ $\eta = 0.83$	$C_f = 1.16$ $C_T = 1.16$ $\eta = 0.81$	$C_d = 0$	$C_d = 0$	
	0.2			$C_f = 8.79$ $C_T = 8.79$ $\eta = 0.48$		$C_f = 4.11$ $C_T = 4.11$ $\eta = 0.61$	$C_f = 2.16$ $C_T = 2.16$ $\eta = 0.72$	$C_f = 1.0$ $C_T = 1.0$ $\eta = 0.83$	$C_f = 0.21$ $C_T = 0.21$ $\eta = 0.95$	$C_d = 0$		
	0.3	$C_f = 13.1$ $C_T = 13.1$ $\eta = 0.42$		$C_f = 8.15$ $C_T = 8.15$ $\eta = 0.50$		$C_f = 4.27$ $C_T = 4.27$ $\eta = 0.61$	$C_f = 2.36$ $C_T = 2.36$ $\eta = 0.71$	$C_f = 1.33$ $C_T = 1.33$ $\eta = 0.79$	$C_f = 0.55$ $C_T = 0.55$ $\eta = 0.89$	$C_f = 0.13$ $C_T = 0.13$ $\eta = 0.97$		
1.0	0.05	$C_f = 10.04$ $C_T = 5.02$ $\eta = 0.58$		$C_f = 5.65$ $C_T = 2.83$ $\eta = 0.68$		$C_f = 3.13$ $C_T = 1.57$ $\eta = 0.77$		$C_f = 1.59$ $C_T = 0.80$ $\eta = 0.85$		$C_d = 0$	$C_d = 0$	
	0.1	$C_f = 13.59$ $C_T = 6.80$ $\eta = 0.53$		$C_f = 7.12$ $C_T = 3.56$ $\eta = 0.64$		$C_f = 3.56$ $C_T = 1.78$ $\eta = 0.75$		$C_f = 1.03$ $C_T = 0.52$ $\eta = 0.90$		$C_d = 0$		
	0.15	$C_f = 14.19$ $C_T = 7.10$ $\eta = 0.52$		$C_f = 7.15$ $C_T = 3.58$ $\eta = 0.64$		$C_f = 3.82$ $C_T = 1.91$ $\eta = 0.74$		$C_f = 1.50$ $C_T = 0.75$ $\eta = 0.86$	$C_f = 0.69$ $C_T = 0.35$ $\eta = 0.93$	$C_d = 0$		

Figures 3.36, 3.37 and 3.38 show how the thrust coefficients based on the planform area of the wing and the area swept by the wing, and the efficiency respectively vary with respect to Strouhal number, Reynolds number and reduced frequency.

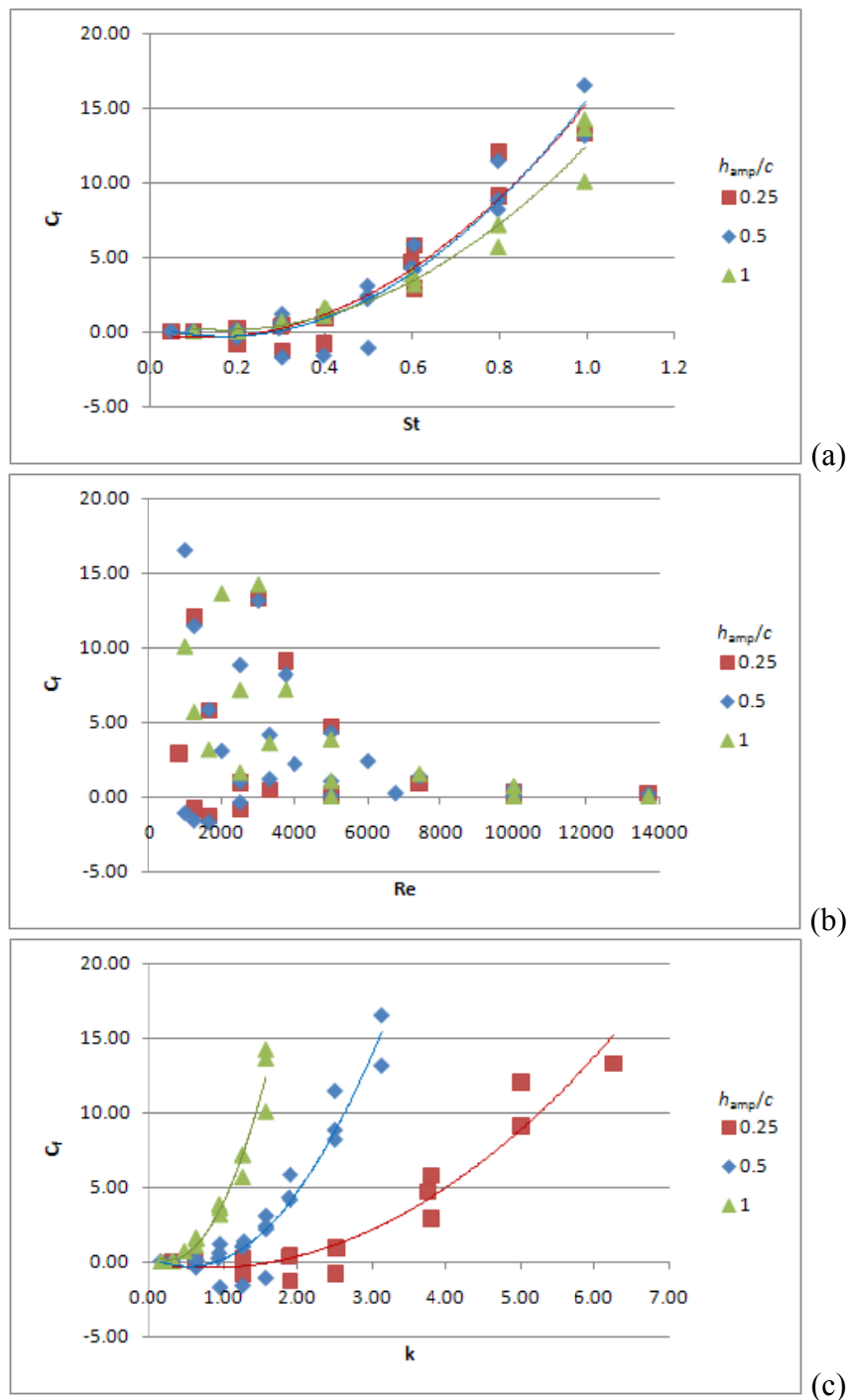


Figure 3.36 : The variation of the thrust coefficient based on the planform area of the wing, C_T , with respect to a) St , b) Re and c) k

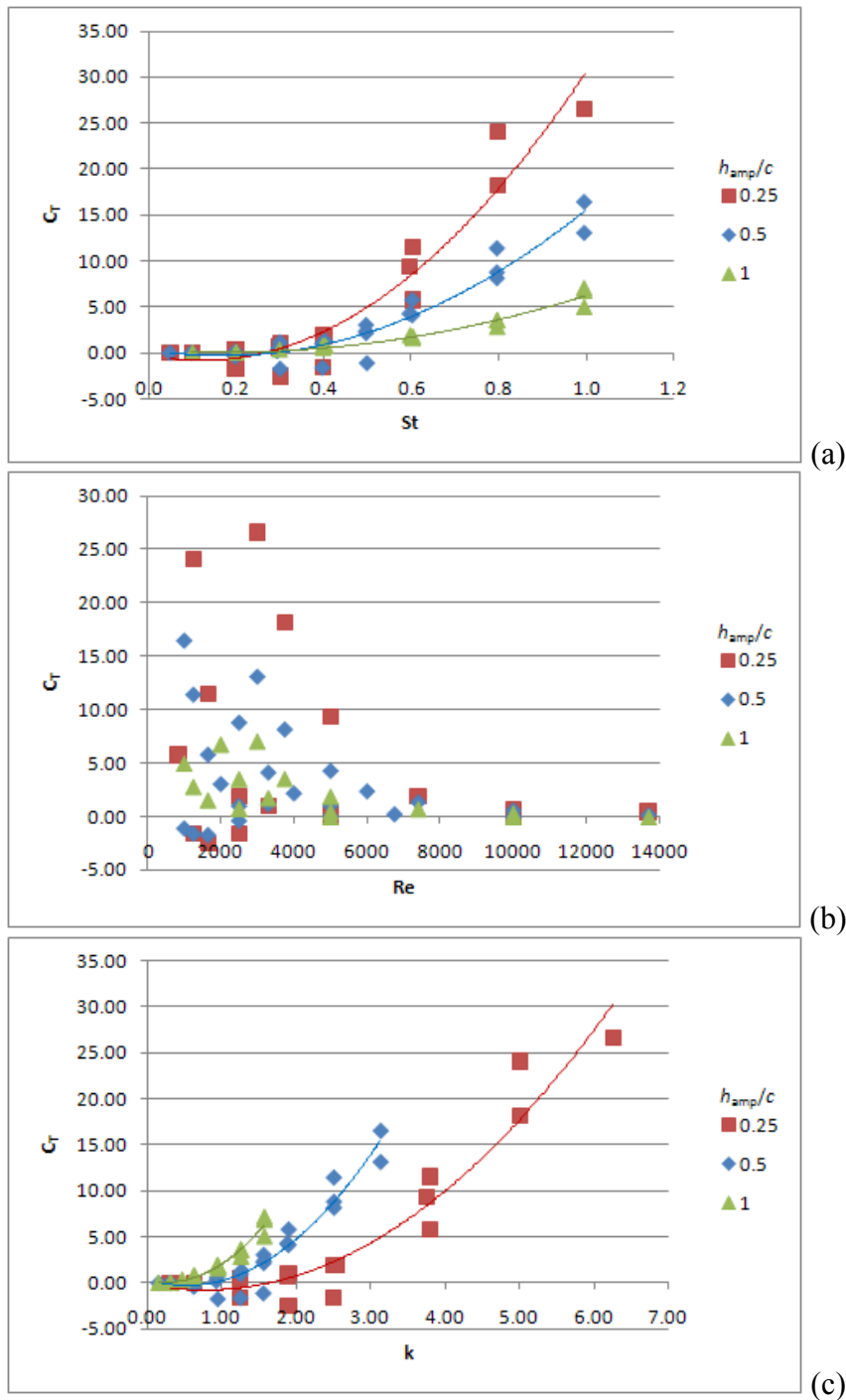


Figure 3.37 : The variation of the thrust coefficient based on the area swept by the wing, C_T , with respect to a) St , b) Re and c) k

In common to all values on the y-axis and accordance with previous comments, the variations are not sensitive to Reynolds number (Figures 3.36b, 3.37b and 3.38b). Due to the inverse dependency of the efficiency on the trust coefficient based on the area swept by the wing, the plots presented in Figures 3.37 and 3.38 are in accordance; therefore for the sake of brevity, only the variation of efficiency will be mentioned herein.

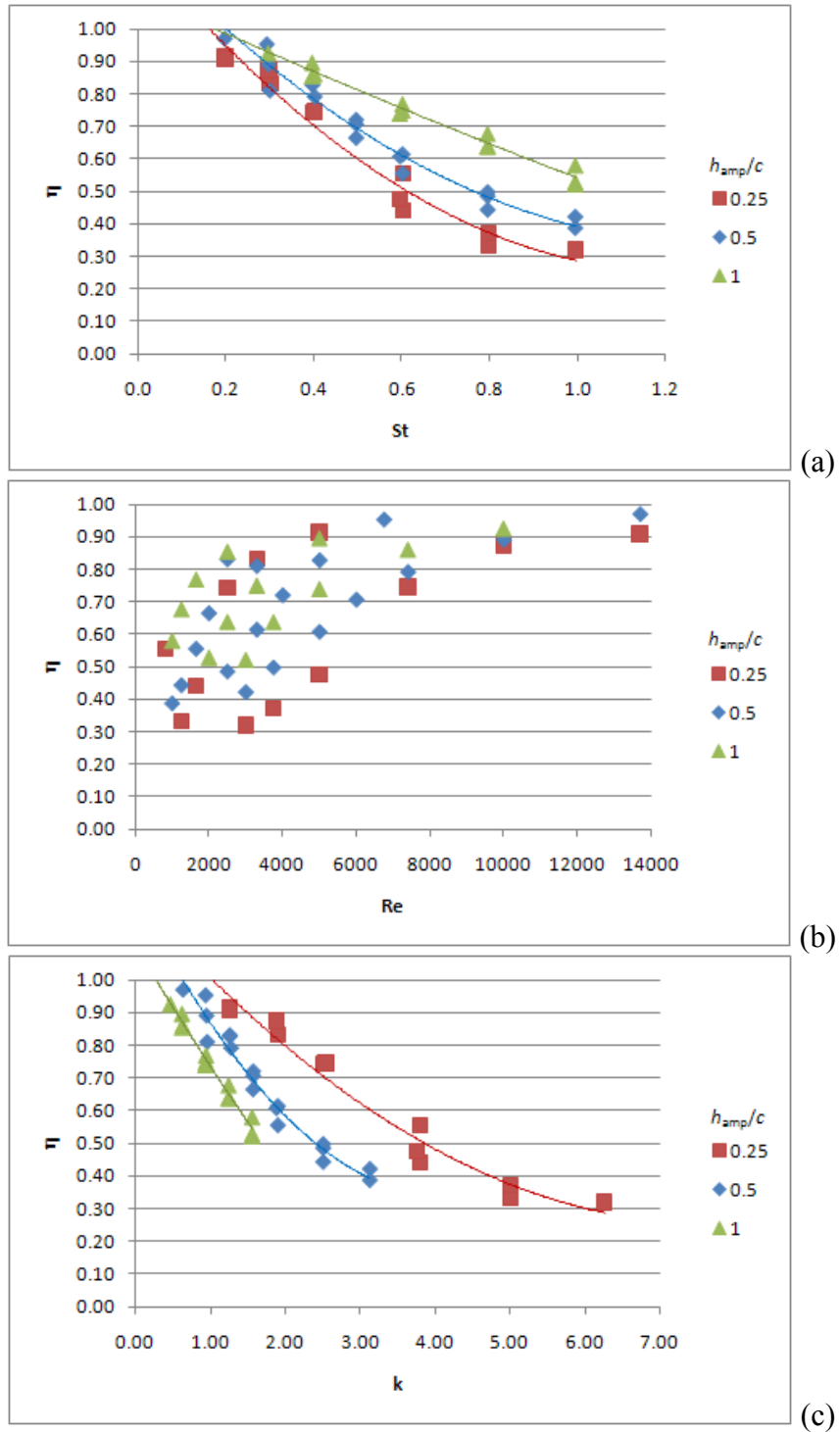


Figure 3.38 : The variation of the efficiency, η , with respect to a) St , b) Re and c) k

The trust coefficient based on the planform area of the wing is increasing with the Strouhal number and the values are aligned on a single curve without differentiation of the plunge amplitude (Figure 3.36a). On the other hand, efficiencies are decreasing with increasing Strouhal number (Figure 3.38a). The decrease slope is larger for lower plunge amplitudes.

The trust coefficient based on the plan form area of the wing is also increasing with the reduced frequency (Figure 3.36c). The increase slope is larger for larger plunge amplitudes. On the other hand, the efficiencies are also decreasing with increasing reduced frequency (Figure 3.38c). However, the decrease slope is larger this time for higher plunge amplitudes.

3.5 Three-Dimensionality

As mentioned before, 10 cases which are shown with bold case numbers in Table 3.2 are chosen to investigate the three-dimensionality of the flow around the airfoil. Figure 3.39 shows, for each flow structure category, two instantaneous images taken at the same instant during the upstroke motion in both side and end view planes along with the averaged flow field in end view plane. The green line shows the intersection of the two planes.

In general, the instantaneous images indicate that the flow is three-dimensional to some extent, however symmetric about the mid-plane of the wing. Depending on the location of the vortices the three-dimensional activity is enhanced on a different plane far from the trailing edge in the near-wake. For the selected instant in the cycle of motion, Category A1 presents a relatively low strength band of vortices close to the trailing edge since the visualized plane is cutting across the shear layer connecting the negative vortex which is about to shed from the upper surface. However, at the same instant for Category A2, the end view plane is cutting across a positive vortex in the near-wake and consequently the band of three-dimensional activity is located further downstream. The location of the band of vortices on the end view is not the same as the center of the vortex on the side view. The difference in between the two views also varies from case to case, i.e., the center of the positive vortex is approximately 140mm downstream of the trailing edge and the band of vortices is located at approximately 190mm for Case-43 (Category B2), on the other hand the center of the positive vortex is approximately 140mm downstream of the trailing edge and the band of vortices is located at approximately 190mm for Case-44 (Category C). The difference in the near-wake location of the vortex on the side view and the band of vortices on the end view is the indication of the roll-up radius of the vortex filament in the spanwise direction and this difference changes from one case to another.

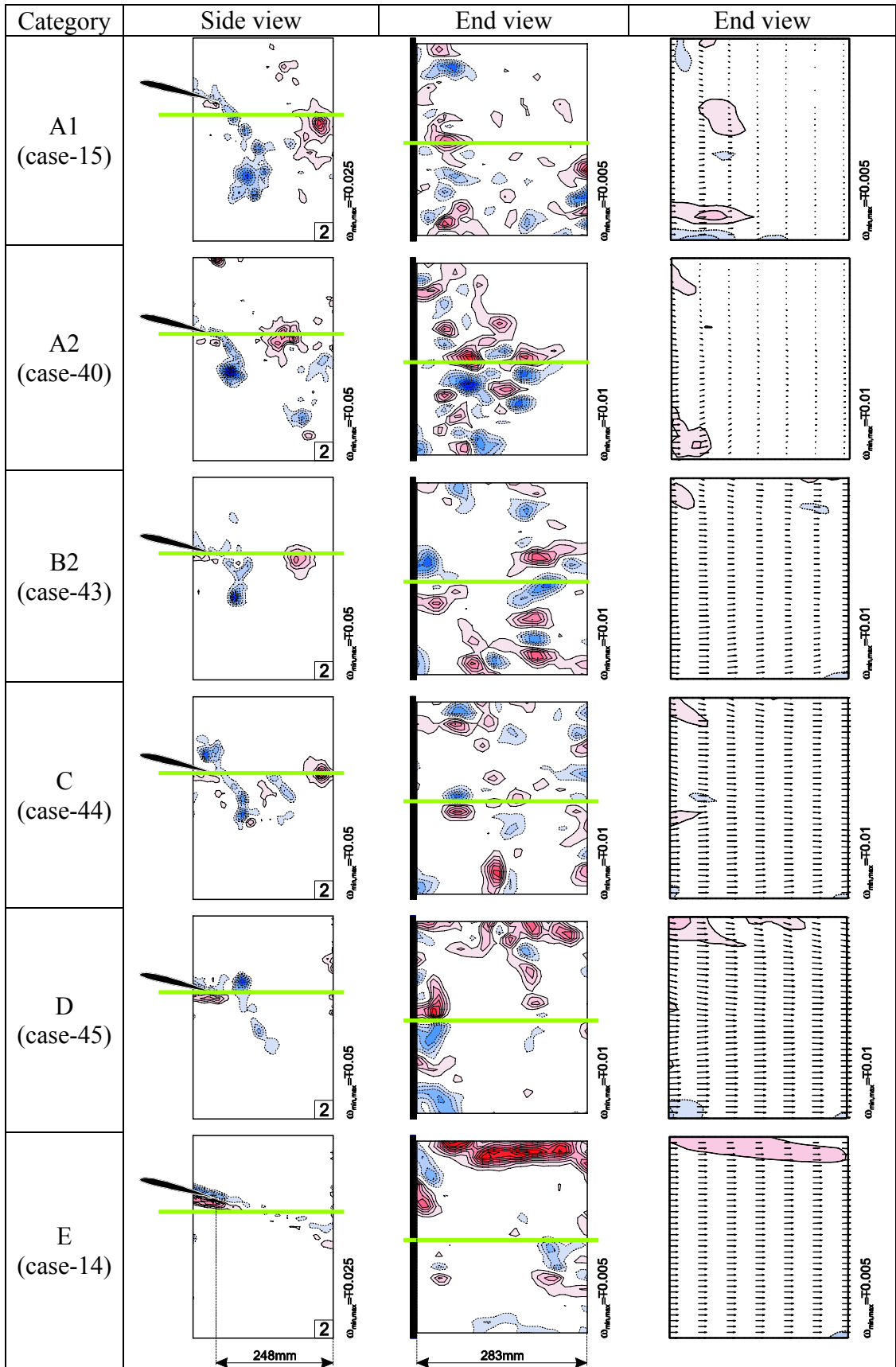


Figure 3.39: For all categories, instantaneous vorticity patterns on the side and end view planes and averaged flow field on the end view plane.

The instantaneous end view image belonging to Case 14 (Category E) exhibits strong vorticity concentrations close to the end plates. It should be noted that due to manufacturing and motion control problems, the clearance between the wing and the end plates is larger than what is usually adopted and aimed for. Except the enhanced end effect in some cases, the average flow fields on the end view plane do not exhibit considerable vorticity concentrations. It should be noted that the maximum and minimum level of contours used for an instantaneous side view image is five times larger than that used for instantaneous and averaged end view images.

Figure 3.40 presents in detail how the flow field in the end view plane evolves during a motion cycle for Case-44 of Category C. Nearly a perfect symmetry about the mid-plane of the wing is preserved during the upstroke and downstroke. Figure 3.41 exemplifies two other cases, namely Case 43 of Category B2 and Case-45 of Category D, in terms of the location of vortex formation close to the trailing edge and consequent three-dimensionality observed on the end view plane.

It should be noted that the instants in the cycle are selected as presenting the airfoil just before reaching its maximum and minimum plunge positions. As there is not a strong and detectable vorticity concentration cutting across the end view plane for Case-14 of Category E (Figure 3.42), a three-dimensional activity could not be observed except strong vorticity patterns at the upper and lower edge of the image indicating considerable end effects.

The end effects cannot infuse to the mid-span region and the vortical structures on the side view are symmetric about the mid-span, much more stronger than the end view three-dimensional activities.

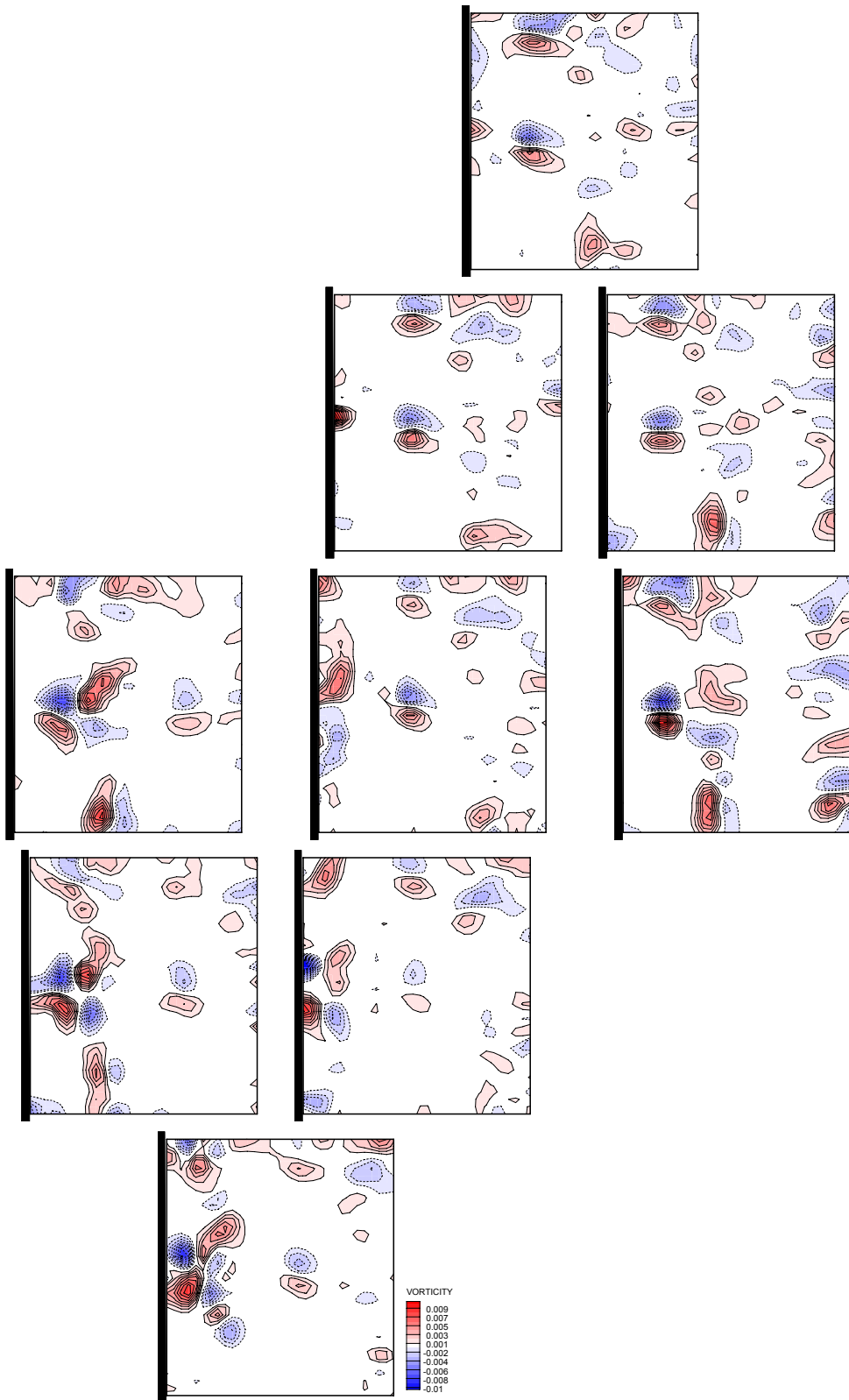


Figure 3.40: Instantaneous vorticity patterns on the end view plane Case-44 (Category C)

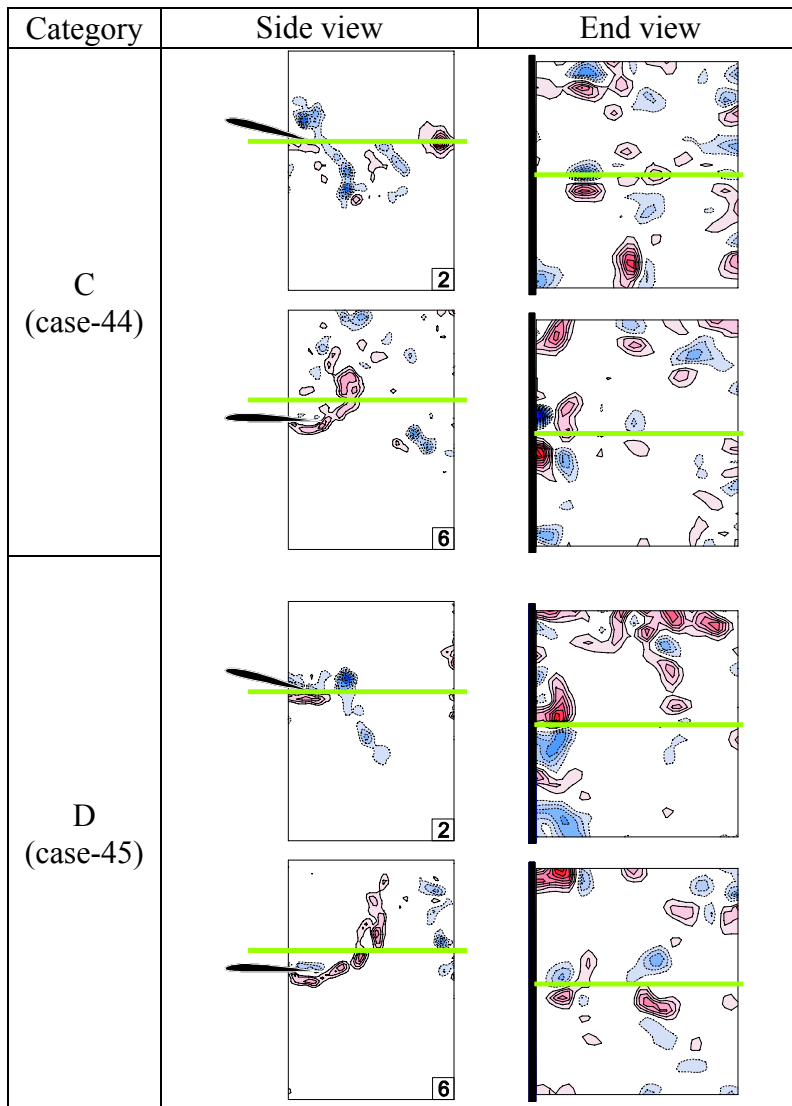


Figure 3.41: Selected instantaneous vorticity patterns on the side and end view planes for category C and D

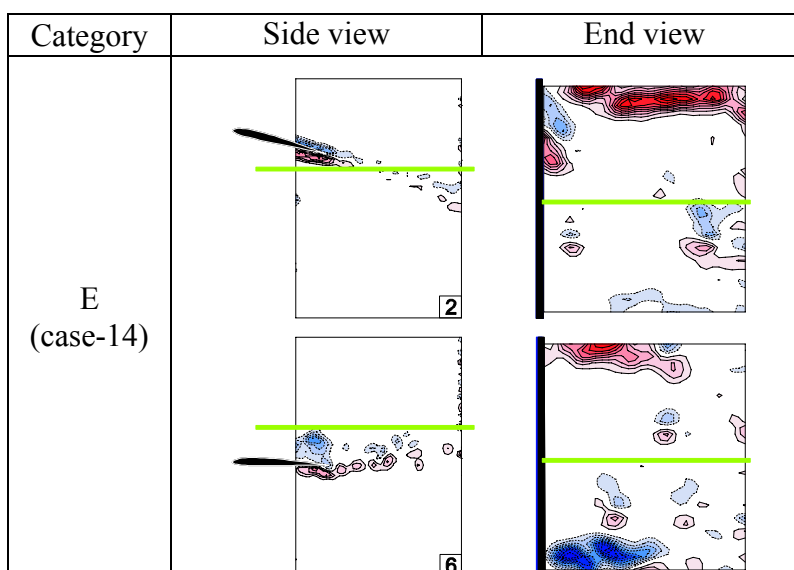


Figure 3.42: Selected instantaneous vorticity patterns on the side and end view planes for category E

3.6 Phase Angle Effects

For the base cases explained in previous sections, the phase angle defined in Equation (1.1) was set to be $\psi = 90^\circ$ where pitch led the plunge motion. The effects due to phase angle variation of $\psi = 75^\circ$ and $\psi = 105^\circ$ between the pitching and plunging motions are investigated for the same 10 cases shown with bold case numbers in the Table 3.2.

Figure 3.43 shows the instantaneous vorticity patterns at the same instant during the upstroke motion for the base cases at different phase angles between pitch and plunge. It is observed that the vorticity patterns are very similar for each flow structure category. Only a slight distance variation between the counter-rotating pair of vortices and difference of the location of the shed vortex in the near-wake are noticeable.

Figure 3.44 reveals a similar trend in averaged vorticity patterns. For each phase angle group, the figure in the left hand side column is the average of four distinct instants of an oscillation cycle over 50 periods of motion and the figure in the right hand side column is the average of several cycles of time-resolved data. In accordance with the instantaneous patterns, averaged vorticity contours do not reveal any significant change with respect to the phase angle. Although a slight flattening in the inclination angle and a decrease in the numbers of cells or contour levels of the vorticity patterns from case to case are observed, it is not possible to put forward a pronounced tendency with the phase angle variation.

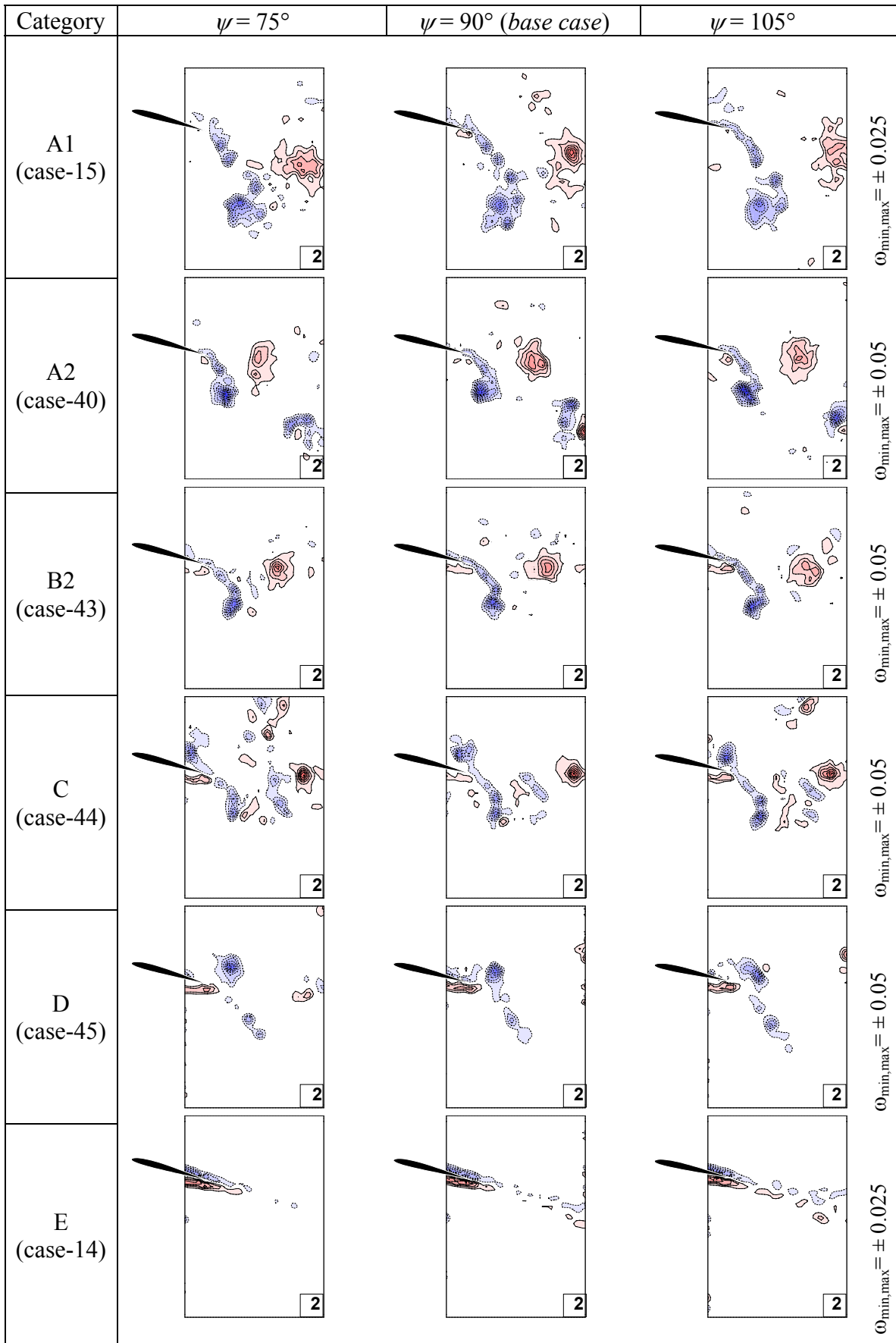


Figure 3.43: For all categories, instantaneous vorticity patterns on the near wake for different phase angles

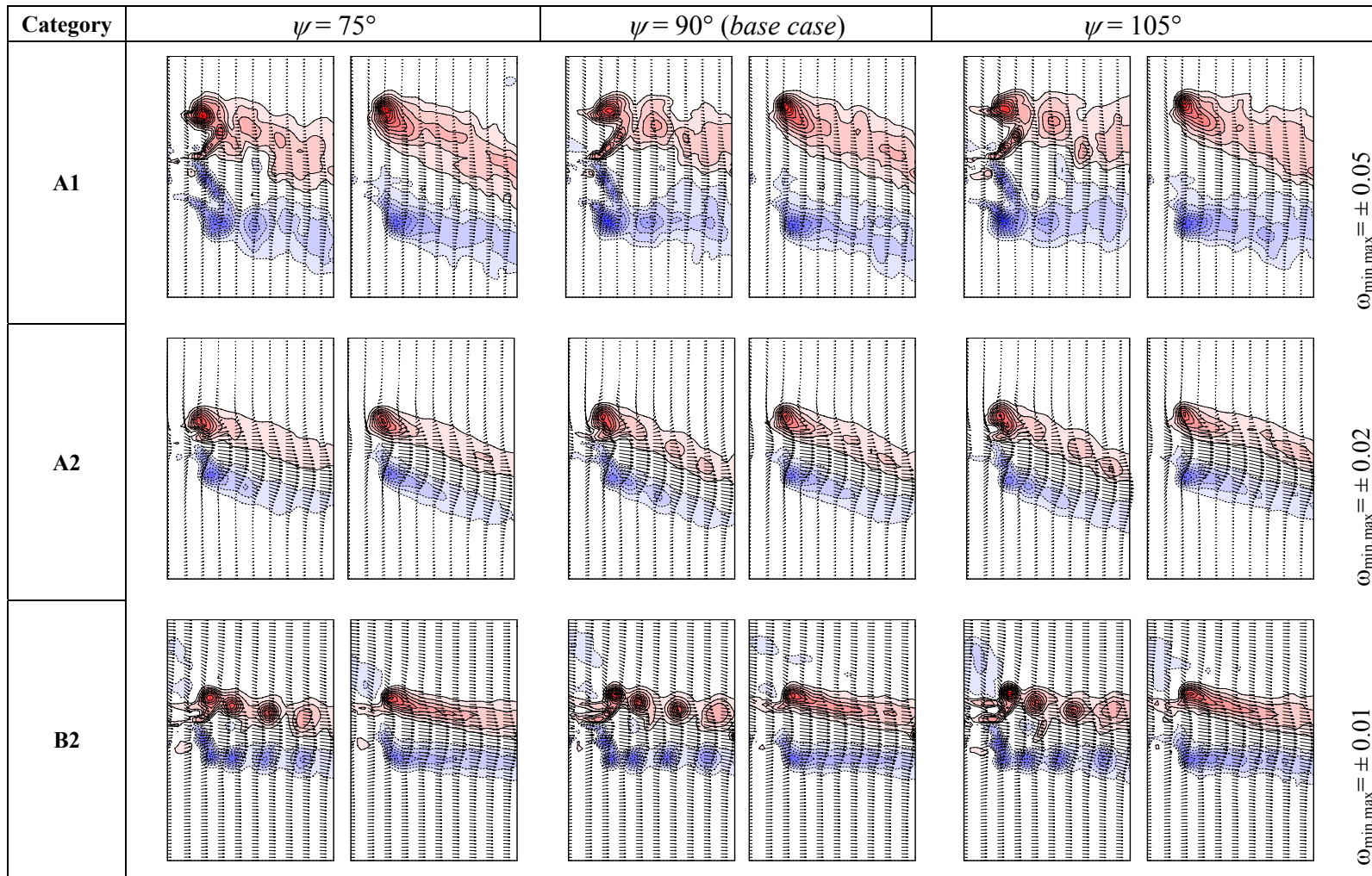


Figure 3.44: For all categories, averaged vorticity patterns for different phase angles

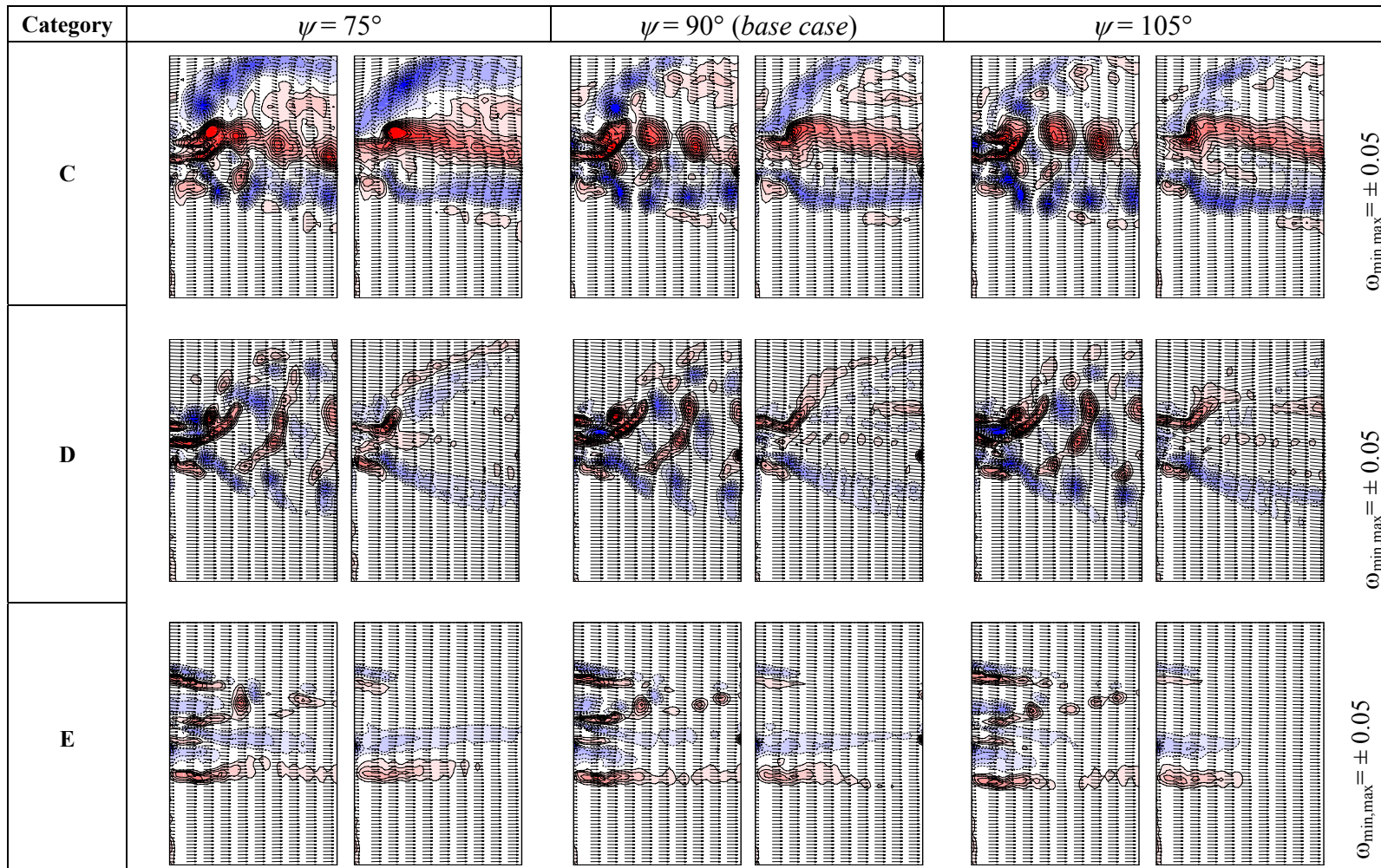
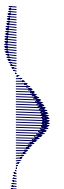













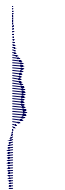





Figure 3.44: (Continued) For all categories, averaged vorticity patterns for different phase angles

The velocity deficit profiles in the near wake for different phase angles are shown in Table 3.7 and the corresponding thrust coefficient (C_f) and efficiency (η) values are given in Table 3.8.

Table 3.7: For all categories, velocity deficit profiles ($u-U_\infty$) in the near wake for different phase angles

Category	$\psi = 75^\circ$	$\psi = 90^\circ$ (base case)	$\psi = 105^\circ$
A1			
A2			
B2			
C			
D			
E			

It can be pointed out that, as a general trend, as the phase angle between the oscillating motions is increased, C_f increases while η decreases. However, compared to the base case

where $\psi = 90^\circ$, it can be noted that although the velocity deficit profiles show no significant dissimilarity, the thrust coefficient decreases to zero for category C and D in addition to category E when $\psi = 75^\circ$.

Table 3.8: For all categories, thrust coefficient and efficiency values for different phase angles

Category	$\psi = 75^\circ$	$\psi = 90^\circ$ (base case)	$\psi = 105^\circ$
A1	$C_f = 7.33$ $\eta = 0.51$	$C_f = 8.79$ $\eta = 0.48$	$C_f = 9.30$ $\eta = 0.48$
A2	$C_f = 11.0$ $\eta = 0.35$	$C_f = 13.28$ $\eta = 0.32$	$C_f = 16.09$ $\eta = 0.30$
B2	$C_f = 0.83$ $\eta = 0.76$	$C_f = 0.92$ $\eta = 0.74$	$C_f = 1.03$ $\eta = 0.73$
C	$C_d = 0$	$C_f = 0.33$ $\eta = 0.87$	$C_f = 0.44$ $\eta = 0.84$
D	$C_d = 0$	$C_f = 0.22$ $\eta = 0.91$	$C_f = 0.19$ $\eta = 0.92$
E	$C_d = 0$	$C_d = 0$	$C_d = 0$

3.7 Effect of Mean Angle of Attack and Pitch Amplitude

The effects of mean angle of attack and the variation of the amplitude of pitching motion are investigated for the same 10 cases shown with bold case numbers in the Table 3.2 and the results are presented for the six distinctive flow structure categories.

Figure 3.45 shows the averaged vorticity contours and velocity profiles for various values of angle of attack and pitch amplitude for all categories. Similarly with the previous tables showing the averaged vorticity patterns, the figure in the left hand side column is the average of four distinct instants of an oscillation cycle over 50 periods of motion and the figure in the right hand side column is the average of several cycles of time-resolved data for each category.

Since the averaged vorticity patterns for the base case where the mean angle of attack is $\alpha_0 = 8^\circ$, the pitch amplitude is $\alpha_{amp} = 8.6^\circ$ and the phase angle between pitch and plunge is $\psi = 90^\circ$ are already given previously in Figure 3.44, it is not repeated here in this figure for the sake of brevity.

It can be observed from Figure 3.45 that as long as the mean angle of attack is kept the same, changing the pitch amplitude does not make a detectable difference in the average vorticity patterns. However, as the mean angle of attack is decreased from $\alpha_0=8^\circ$ to $\alpha_0=0^\circ$, for Categories A1 and A2, the inclination of the wake vorticity is turned slightly upwards, which in turn affects the direction of the lift force. For Category A, the occurrence of the mushroom-like character of the vorticity pattern has not been affected with the change of both mean angle of attack and pitch amplitude.

Changing the values of α_0 and α_{amp} does not have any detectable difference in general in the vorticity patterns of Category B, except the enhancement of the negative vorticity pattern is evident on the upper surface of the airfoil for the case where $\alpha_0=8^\circ$ and $\alpha_{amp}=12.9^\circ$.

For Category C, the variation of vorticity patterns is caused by the change in the mean angle of attack, not the pitch amplitude. Decreasing mean angle of attack from $\alpha_0=8^\circ$ to $\alpha_0=0^\circ$ results in a change of category. The vortical patterns are categorized as Category C for the base case, which is also very similar for higher pitch amplitude with the same mean angle of attack. However, it is very apparent that decreasing α_0 influences the vorticity patterns; the additional negative upward vortex shed from the upper surface of the airfoil in a motion cycle disappears and thus results in a shift of the category from C to B. For this case, the distance between the negative and positive vorticity layers has an elliptic curvature rather than being parallel which is a characteristic of Category B2.

For Category D, the vorticity layers have nearly identical patterns when the mean angle of attack is the same. On the other hand, the vertical distance between the negative and positive vorticity layers tends to increase with increasing pitch amplitude.

Analogous to the other categories, vorticity patterns of Category E look almost the same with minor variations when the pitch amplitude changes and the mean angle of attack remains the same.

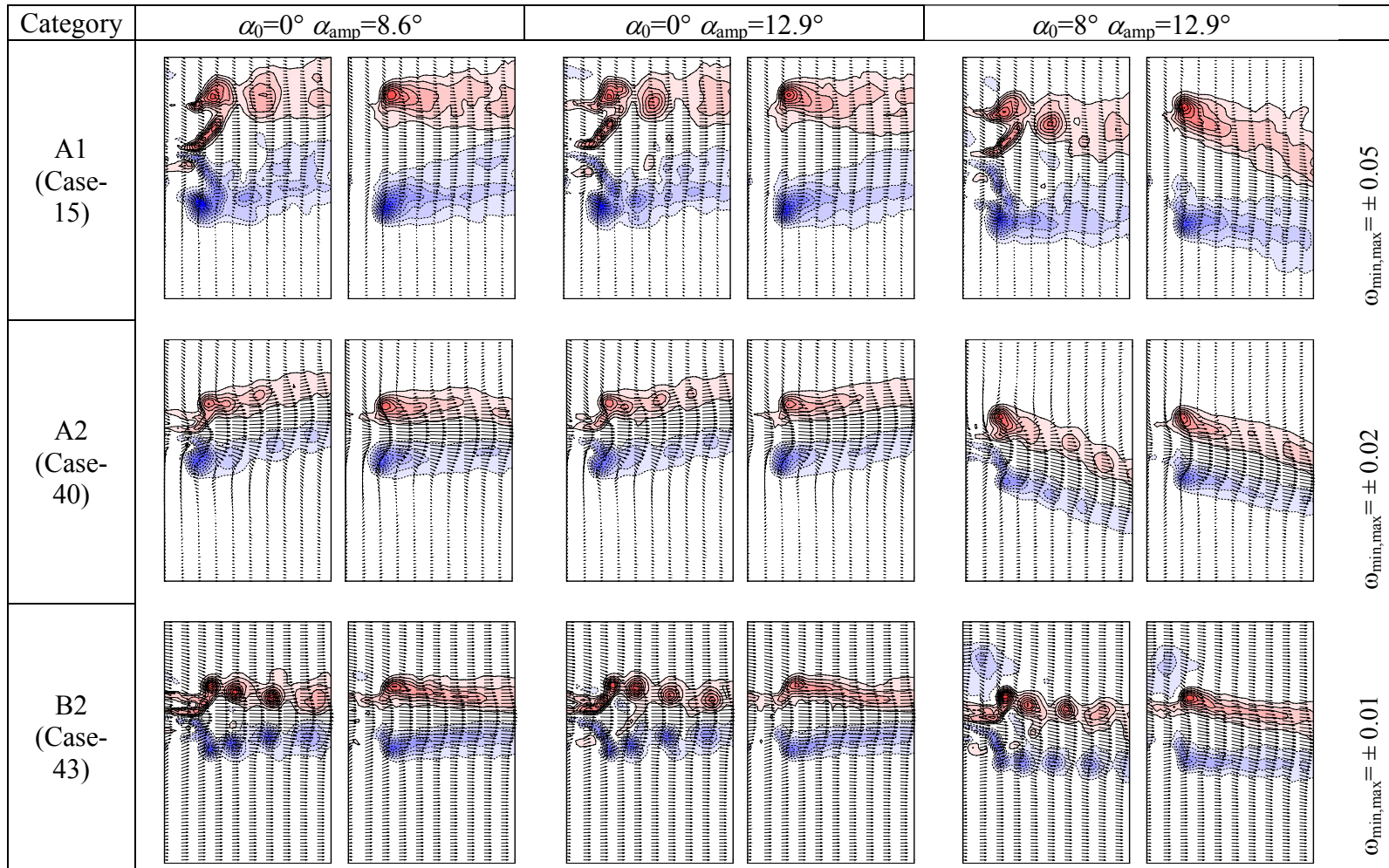


Figure 3.45: For all categories, averaged vorticity profiles for varied angle of attack and pitch amplitude values

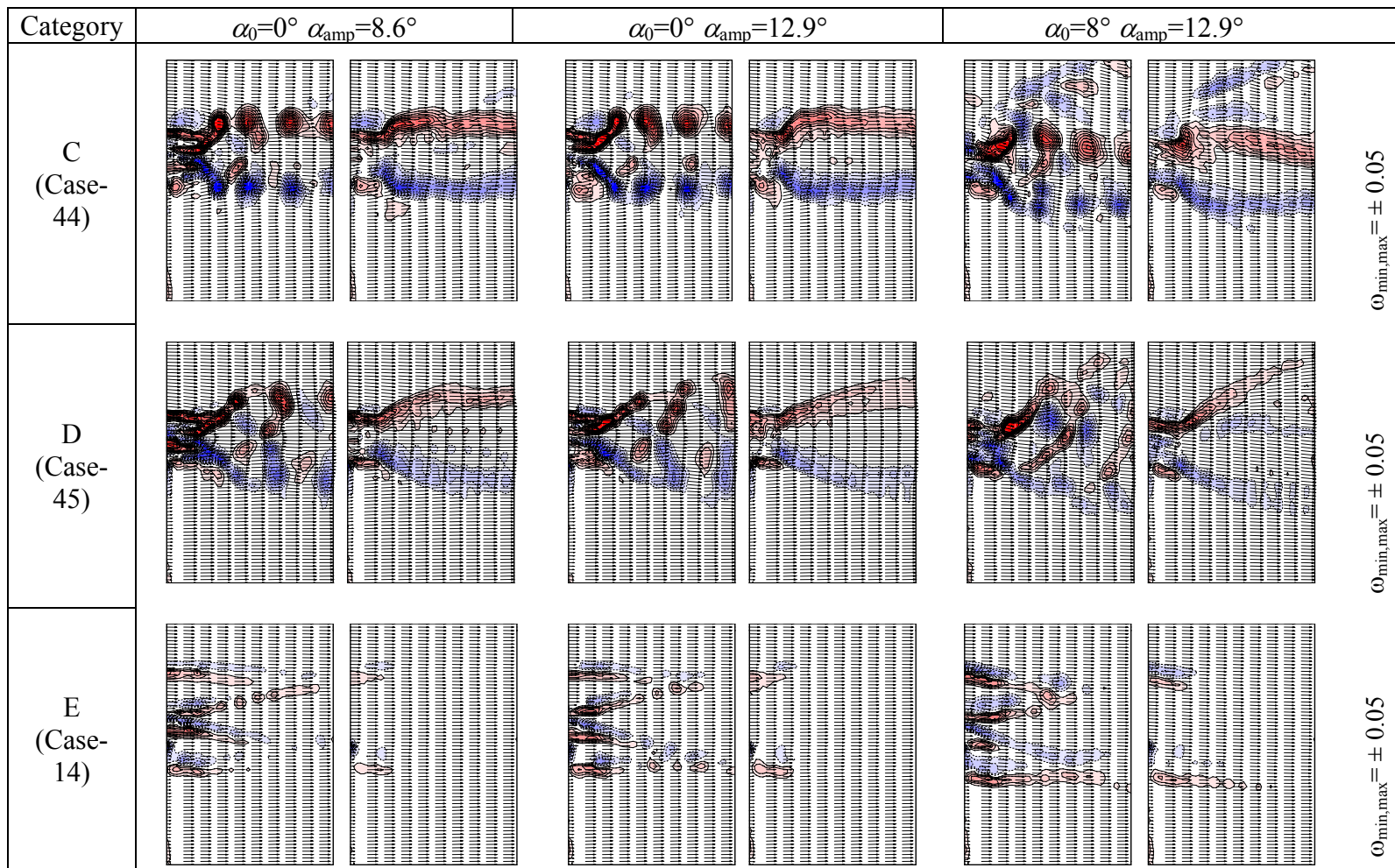


Figure 3.45: (Continued) For all categories, averaged vorticity profiles for varied angle of attack and pitch amplitude values

In accordance with the observations based on the averaged vorticity patterns, the velocity deficit profiles in the near-wake of the airfoil for all categories are given in Table 3.9. The

Table 3.9: For all categories, velocity deficit profiles ($u-U_\infty$) in the near wake

Category	$\alpha_0=0^\circ$ $\alpha_{amp}=8.6^\circ$	$\alpha_0=0^\circ$ $\alpha_{amp}=12.9^\circ$	$\alpha_0=8^\circ$ $\alpha_{amp}=8.6^\circ$ (base case)	$\alpha_0=8^\circ$ $\alpha_{amp}=12.9^\circ$
A1 (Case-15)				
A2 (Case-40)				
B2 (Case-43)				
C (Case-44)				
D (Case-45)				
E (Case-14)				

wake profiles look similar to each other when the mean angle of attack is kept the same and pitch amplitude is varied. It should be noted that the inclination of the vorticity layers cannot be seen within the wake profiles since the plots are obtained for streamwise velocity components, $(u-U_\infty)$.

For Category C, the average vorticity levels are in accordance with each other at the two pitch amplitudes with the same mean angle of attack of 8° . However it can be observed from the velocity profiles that the velocity deficit region is pronounced for $\alpha_0=8^\circ$, which is a clear indication of the additional negative vorticity layer.

The vector lengths of light blue velocity vectors in Category E are one fifth of those of the other categories. Although the freestream velocity for the cases in this category is quite high, the $(u-U_\infty)$ values are extremely small. The momentum deficit or excess for this category is therefore considered to be zero.

The force coefficient and efficiency values are given seen in Table 3.10. The general trend of force coefficient and efficiency values are in accordance with the outcome of vorticity patterns and wake profiles; the values of C_f and η fluctuate slightly within the same mean angle of attack cases. In addition to Category E where no thrust could be obtained regardless of the mean angle of attack and pitch amplitude values, the calculated thrust coefficient for Category D is minimal for the case where $\alpha_0=8^\circ$ and $\alpha_{amp}=12.9^\circ$, and therefore considered to be $C_d = 0$. This is in accordance with the velocity profile observed in Table 3.9.

Table 3.10 : For all categories, force coefficient and efficiency values for varied mean angle of attack and pitch amplitude values

Category	$\alpha_0=0^\circ$ $\alpha_{amp}=8.6^\circ$	$\alpha_0=0^\circ$ $\alpha_{amp}=12.9^\circ$	$\alpha_0=8^\circ$ $\alpha_{amp}=8.6^\circ$ (base case)	$\alpha_0=8^\circ$ $\alpha_{amp}=12.9^\circ$
A1 (Case-15)	$C_f = 8.55$ $\eta = 0.49$	$C_f = 8.31$ $\eta = 0.49$	$C_f = 8.79$ $\eta = 0.48$	$C_f = 8.54$ $\eta = 0.49$
A2 (Case-40)	$C_f = 16.51$ $\eta = 0.29$	$C_f = 15.57$ $\eta = 0.30$	$C_f = 13.28$ $\eta = 0.32$	$C_f = 15.49$ $\eta = 0.3$
B2 (Case-43)	$C_f = 1.39$ $\eta = 0.68$	$C_f = 1.137$ $\eta = 0.712$	$C_f = 0.92$ $\eta = 0.74$	$C_f = 0.61$ $\eta = 0.81$
C (Case-44)	$C_f = 0.42$ $\eta = 0.85$	$C_f = 0.54$ $\eta = 0.82$	$C_f = 0.33$ $\eta = 0.87$	$C_f = 0.27$ $\eta = 0.89$
D (Case-45)	$C_f = 0.29$ $\eta = 0.89$	$C_f = 0.22$ $\eta = 0.91$	$C_f = 0.22$ $\eta = 0.91$	$C_d = 0$
E (Case-14)	$C_d = 0$	$C_d = 0$	$C_d = 0$	$C_d = 0$

Although the variation of the effective angle of attack and flapping characteristics are not plotted herein, varying the pitching amplitude while keeping the mean angle of attack constant results in a 4.3° change in effective angle of attack values both in upstroke and downstroke motions of the airfoil.

The variation of effective angle of attack with respect to Strouhal number for all flow categories is given in Figure 3.46. As can be inspected, changing mean angle of attack and pitch amplitude values does not result in a case outside the trend of the base case. Hence, as opposed to the study of Anderson (1996), we do not include small St and large α_{eff} values or vice versa. In the region of $0.2 \leq St \leq 0.4$, a slight transition of characteristics is observed where the cases' category shifts to the next or previous one; however this change in vortex structure characteristics ceases to exist outside this band.

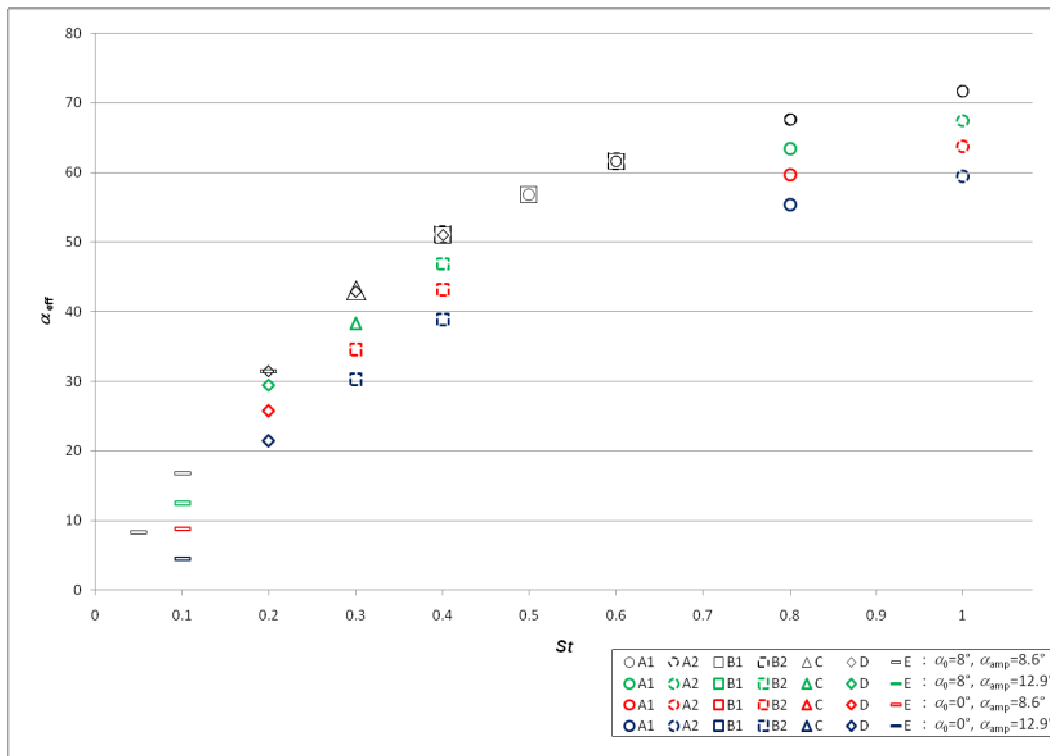


Figure 3.46: The flow categories on St vs α_{eff} plot for different mean angle of attack and pitch amplitude values

3.8 Effect of Unequal Frequency

In all of the cases considered in this study so far, the frequency of plunging motion, f_1 , was kept the same as the frequency of pitching motion, f_2 . Except a few studies, the effect of unequal frequency in flapping motion has not been addressed in the literature and those unique investigations do not reach to a conclusion as the problem becomes much more complex.

Table 3.11 summarizes the cases where unequal frequencies are adopted for flapping motion along with the six base cases representing each flow structure category. Vorticity patterns corresponding to the cases in Table 3.11 are shown in Figure 3.47 using the same order and layout of the table. In each pair, left-hand figure is the average of four distinct instants over 50 periods and the right-hand is the average of a several cycles of time resolved data.

Table 3.11 : Values of pitch and plunge frequencies and corresponding Strouhal numbers for the cases shown in Figure 3.47

A1	15		119		120	
	$f_1=0.2$	$St_1=0.8$	$f_1=0.1$	$St_1=0.4$	$f_1=0.4$	$St_1=1.6$
	$f_2=0.2$	$St_2=0.8$	$f_2=0.2$	$St_2=0.8$	$f_2=0.2$	$St_2=0.8$
		122		121		
		$f_1=0.2$	$St_1=0.8$	$f_1=0.2$	$St_1=0.8$	
		$f_2=0.4$	$St_2=1.6$	$f_2=0.1$	$St_2=0.4$	
A2	40		143		144	
	$f_1=0.6$	$St_1=1.0$	$f_1=0.3$	$St_1=0.5$	$f_1=0.6$	$St_1=1.0$
	$f_2=0.6$	$St_2=1.0$	$f_2=0.6$	$St_2=1.0$	$f_2=0.3$	$St_2=0.5$
B2	43		145		146	
	$f_1=0.6$	$St_1=0.4$	$f_1=0.3$	$St_1=0.2$	$f_1=0.6$	$St_1=0.4$
	$f_2=0.6$	$St_2=0.4$	$f_2=0.6$	$St_2=0.4$	$f_2=0.3$	$St_2=0.2$
C	44		147		148	
	$f_1=0.6$	$St_1=0.3$	$f_1=0.3$	$St_1=0.1$	$f_1=0.6$	$St_1=0.3$
	$f_2=0.6$	$St_2=0.3$	$f_2=0.6$	$St_2=0.3$	$f_2=0.3$	$St_2=0.1$
D	45		149		150	
	$f_1=0.6$	$St_1=0.2$	$f_1=0.3$	$St_1=0.1$	$f_1=0.6$	$St_1=0.2$
	$f_2=0.6$	$St_2=0.2$	$f_2=0.6$	$St_2=0.2$	$f_2=0.3$	$St_2=0.1$
E	14		113		114	
	$f_1=0.1$	$St_1=0.1$	$f_1=0.05$	$St_1=0.05$	$f_1=0.2$	$St_1=0.2$
	$f_2=0.1$	$St_2=0.1$	$f_2=0.1$	$St_2=0.1$	$f_2=0.1$	$St_2=0.1$
			116		115	
			$f_1=0.1$	$St_1=0.1$	$f_1=0.1$	$St_1=0.1$
			$f_2=0.2$	$St_2=0.2$	$f_2=0.05$	$St_2=0.05$
		118		117		
		$f_1=0.1$	$St_1=0.1$	$f_1=0.5$	$St_1=0.5$	
		$f_2=0.5$	$St_2=0.5$	$f_2=0.1$	$St_2=0.1$	

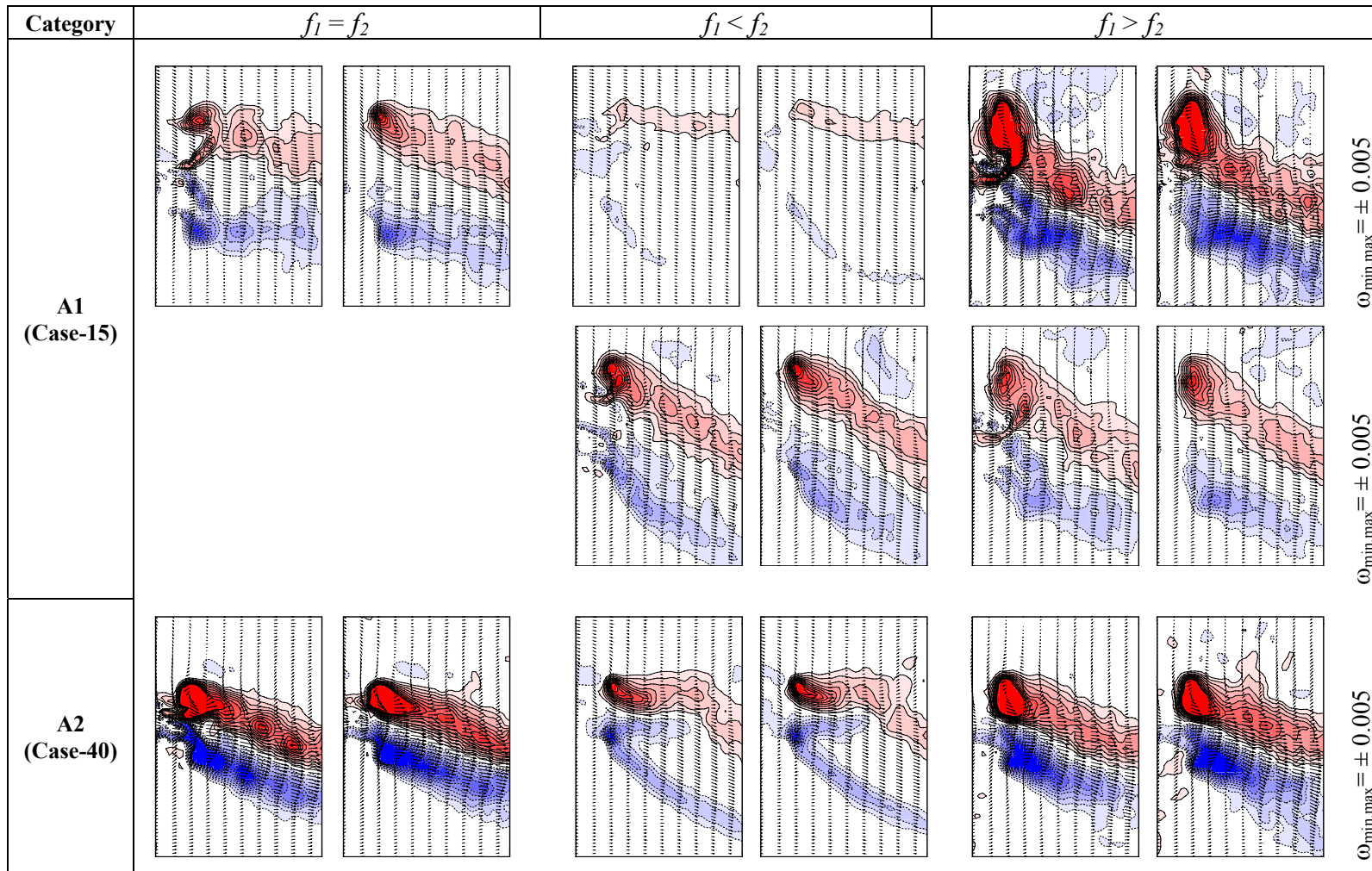


Figure 3.47: For all categories, averaged vorticity patterns for unequal frequencies

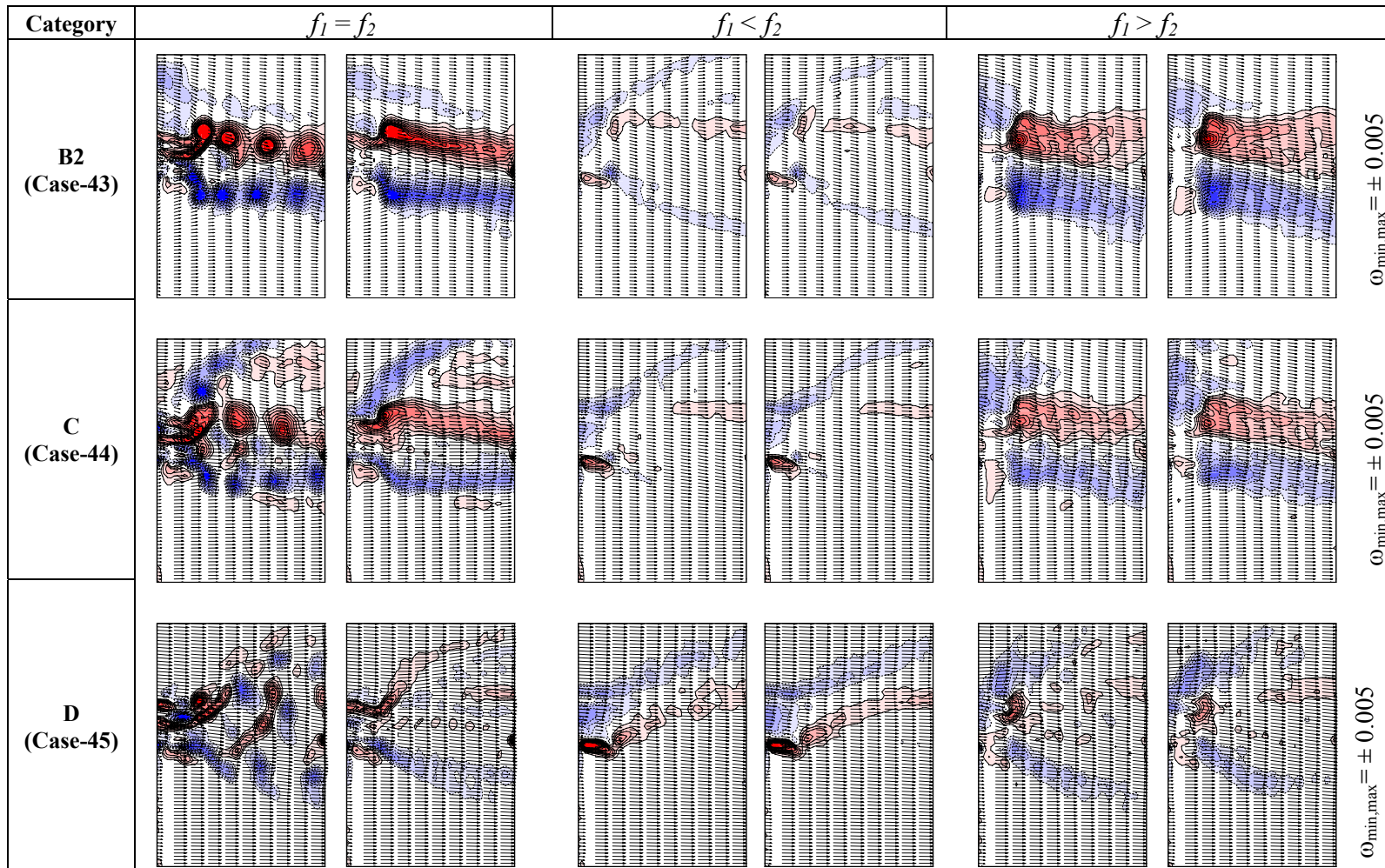


Figure 3.47: (Continued) For all categories, averaged vorticity patterns for unequal frequencies

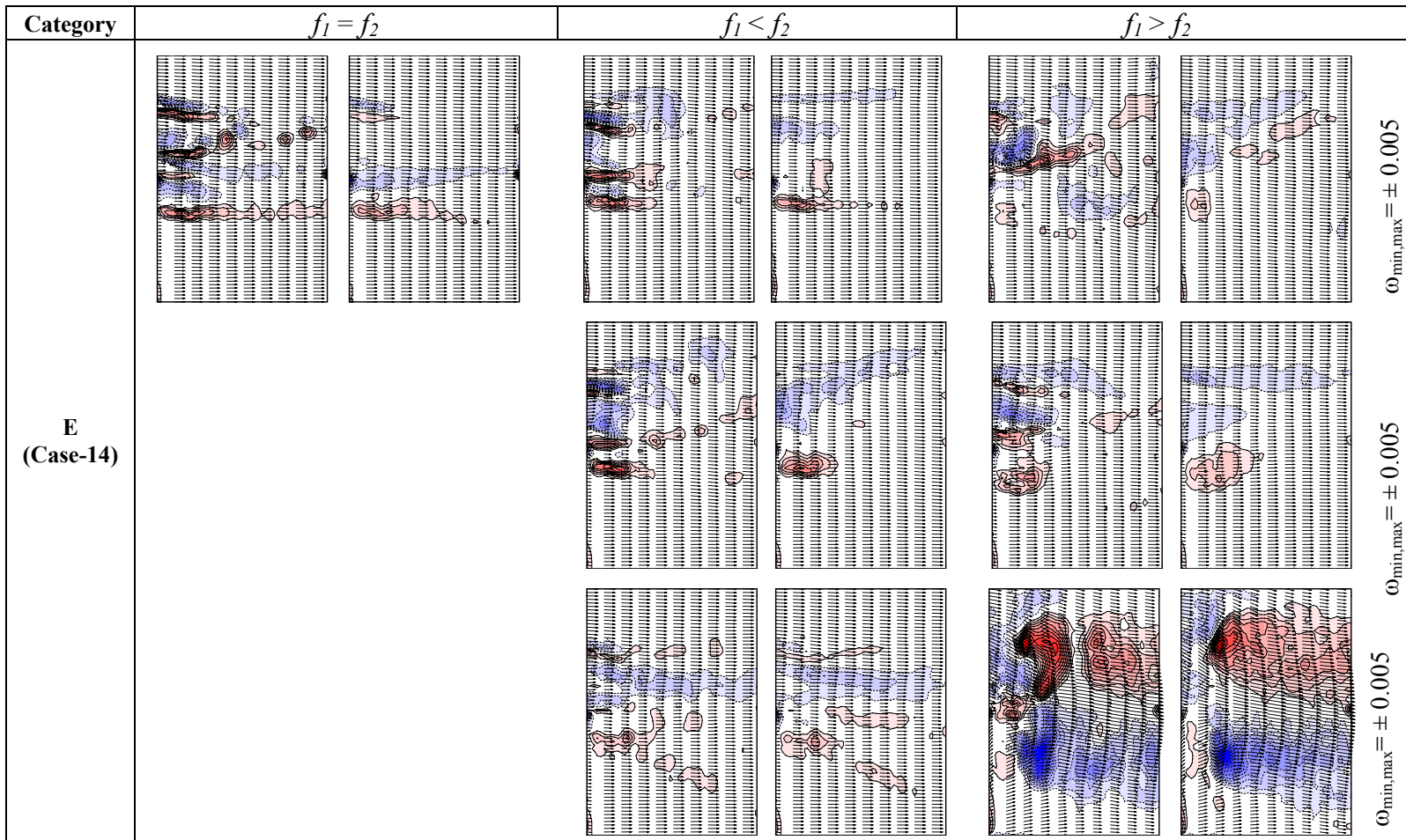


Figure 3.47: (Continued) For all categories, averaged vorticity patterns for unequal frequencies

Except for Case-121 which is a variation of the example case representing Category A1 when $f_1 > f_2$, instantaneous vorticity patterns will not be presented herein. This case exemplifies how the timing of vortex shedding changes when unequal pitch and plunge frequencies are used in a flapping motion. Figure 3.47 shows that the averaged vorticity patterns are in general mostly affected by the variation in plunge frequency. The vorticity patterns for the cases where $f_1 < f_2$ differ largely from those for the cases where $f_1 > f_2$ and the base cases. On the other hand major characteristics are similar when $f_1 < f_2$. However, the similarity in the averaged patterns does not impose a similarity in the timing of vortex shedding, and vice versa for dissimilar averaged vorticity patterns, the timing may resemble. Figure 3.48 shows the instantaneous vorticity patterns in a cycle of motion considering the large frequency for Case-121. The vorticity patterns at the mid-plunge positions within the cycle are identical regardless of the direction of the plunge motion. However, for the base cases, the vorticity patterns at the mid-plunge positions are different depending on upstroke or downstroke motion (Figure 3.3). In comparison, the vorticity patterns at the mid-plunge position during the downstroke motion for the base case are nearly identical to those obtained at the maximum plunge position when $f_1 < f_2$. It should be noted that although $f_1 < f_2$, the plunging frequencies, f_1 , are the same in both cases.

For all Categories A through D, the use of a different plunge motion frequency results generally in a decrease in the averaged vorticity levels and in a change of topology of the averaged vorticity patterns. The single exception to this argument is the Case-120 where the plunging frequency is doubled and the pitching frequency is kept the same with respect to the base case of Category A1, namely Case-15. The vorticity patterns are similar to those of the base case although a different plunge motion frequency is adopted. On the other hand, all similar topologies of averaged vorticity patterns obtained at unequal pitch and plunge frequencies actually present a reduction in the mushroom-like formation on the part of the negative vorticity layer as compared to the base case. Instantaneous images shown in Figure 3.48 explains the origin; while the positive vortex shed from the trailing edge preserves the dimension of its roll-up radius, the negative leading edge vortex is stretched before it is shed from the trailing edge. The averaged vorticity patterns that are different from the base case obtained at different plunge frequencies ($f_1 < f_2$) for Categories A1 and

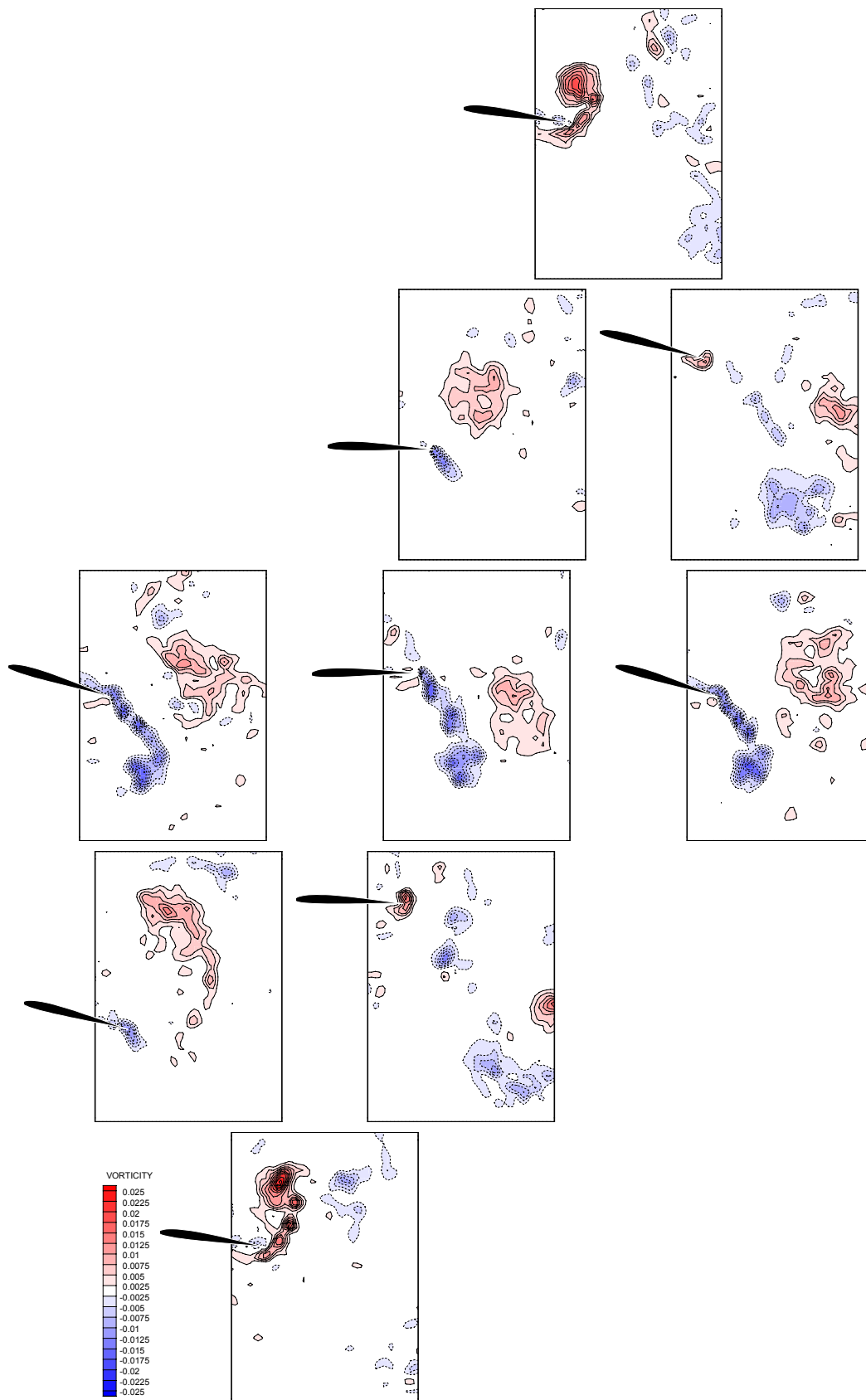


Figure 3.48: Instantaneous vorticity patterns in the near-wake of the airfoil Case-121 (Category A1)

A2 actually show how the vortex trajectories in the near-wake are affected by the use of unequal frequency. The positive vortex shed from the trailing edge follows nearly a straight line; however the negative vortex first separates from the positive and then swept away in the freestream direction.

A similar, however pronounced trajectory change occurs for Category D. The negative vortex is shed upward parallel to the positive vortex when $f_1 < f_2$.

Interesting effects of having unequal frequencies are observed for Category E. First of all using plunge frequency which is five times the pitch frequency results in a flow structure category change; i.e. Case-117 belongs to Category B rather than Category E. On the other hand, for all other cases investigated in relation to Category E, the averaged vorticity patterns exhibit an enhancement of the first negative vorticity layer at the top. When the instantaneous images are also considered, this enhancement is found to be related to the shedding of a very large leading edge vortex during the second half of the downstroke motion.

The brief overlook at the effect of unequal frequencies shows that the flapping motion becomes much more complicated and the physics underlying the effect of unequal frequencies deserves a more detailed investigation. On the other hand, the absence of reported use of unequal frequencies in nature will remain as a question mark for the practical applications of the future work.

4 CONCLUDING REMARKS

4.1 Summary of Major Contributions

Maneuvering capabilities and characteristics of biological flyers are not easy to mimic by manmade machines. Therefore, the research on flapping wings mainly focuses on the understanding of aerodynamic mechanisms resulting from the unsteady wing motions.

Traditional fixed wing design attempts to ensure that flow stays attached at all times in contrast to natural mechanisms of flapping wings which rely on vortices that separate from leading and trailing edges.

The current investigation considers a SD7003 airfoil undergoing combined pitch and plunge motions in a steady current. The flow structures are obtained around and in the near-wake of the airfoil in motion using Digital Particle Image Velocimetry (DPIV) and the thrust estimation has been done based on the averaged velocity profiles in the near-wake.

The major contributions of this study are summarized as follows:

- A thorough flow structure categorization has been accomplished. Although a similar categorization was conducted by Anderson (1996), the present study discusses in detail, covering the ranges of Strouhal number she did not observe. It should be pointed out that Anderson's (1996) categorization is based on flow visualization at a single low Reynolds number. The current study also puts forward the independency on the Reynolds number in the range investigated. The occurrence of flow structure categories on different two-dimensional parameter spaces has also been obtained.
- Depending on the interactions between airfoil movement and wake flow structures, either thrust or drag can be observed. Although the application of the momentum theory to the problem involves many violated assumptions, the results are promising and in accordance with qualitative observations and previously computed or measured data, force estimation results are then

paired with flow structure categories and the variation of thrust with respect to different non-dimensional parameters has been discussed.

- The current study is probably the first to mention the formation of a deflected wake for combined pitch and plunge motions. As opposed to what is observed in pure plunge motion, it is found to be consistent and does not alternate between up and down modes. However, in accordance with previous studies on pure plunge motion, the deflection angle increases as the Strouhal number increases.
- Isolated effects of the mean angle of attack, pitch amplitude, and the phase angle between pitch and plunge motions have also been included in the research as complementary issues of the flow structure categorization.
- As a final comment, for Micro Air Vehicle applications, it is recommended to choose Strouhal number to be equal or greater than 0.2 in order to obtain high efficiencies, except for the cases where $f h_{\text{amp}}/c = 0.025$. In general, flow structure categories A to D shows thrust production where Category A type flow structures has high thrust coefficients with low efficiencies and Category D type flow structures has low thrust coefficients with high efficiencies just before a $C_d \geq 0$ value is observed. One should keep in mind that force and therefore efficiency calculations are not validated by direct measurements and includes major assumptions.

4.2 Recommendations for Further Study

The cases investigated in this study are to some extent influenced by the limitations of the flow or motion systems used in the experiments. Therefore, it could not be possible to cover all possible or desired range of parameters, e.g., it would be instructive to study higher Reynolds number ranges if the water channel were capable of providing flow speeds up to 1m/s.

On the other hand, thrust or drag estimation results would be complemented by conducting direct force measurements. Although it is not possible to select a single load cell to be able to measure forces for a flapping airfoil in such a large range of parameters and to extract the aerodynamic forces in high accuracy from a considerable amount added mass component, direct force measurement would provide a basis for comparison and/or validation to force estimations and

computational studies. In this perspective, it is recommended to conduct sectional pressure measurements along with the acquisition of total loading on the body in order to determine the degree of the three-dimensionality on a nominally two-dimensional wing.

Considering a large number of investigations in this area performed using computational tools, it would also be insightful to perform a computational research at the same flow conditions as in this experimental study.

The flapping motion in nature regardless of being in air or in water considers a finite wing, totally three-dimensional and with small surface protrusions. The general trend of research in recent years focuses on the role of feathers or furs and flexible wings for controlling the flow around.

The current investigation covered all phases of an experimental setup from scratch for a two-axis motion control of a wing and its quantitative visualization via Digital Particle Image Velocimetry (DPIV). Due to time limitations and considering major focus of the study, a Stereo DPIV image acquisition is not undertaken to visualize the three-dimensionality of the flow. The future work, especially focusing on finite wings, will definitely require the use of such systems.

REFERENCES

- Adrian, R. J.**, 1986. Image Shifting Technique to Resolve Directional Ambiguity in Double-Pulsed Laser Velocimetry, *Applied Optics*, Vol.25, p.3855-35858.
- Adrian, R. J.**, 1991. Particle-Imaging Techniques for Experimental Fluid Mechanics, *Annual Review of Fluid Mechanics*, Vol.23, p.261-304.
- Alam, M. F., Suzen, Y. B. and Ol, M. V.**, 2009. Numerical Simulations of Pitching Airfoil Flowfields for MAV Applications. *39th AIAA Fluid Dynamics Conference*, AIAA 2009-4029.
- Ames, R., Wong, O. and Komerath, N.**, 2001. On the Flowfield and Forces Generated by a Flapping Rectangular Wing at Low Reynolds Number, Fixed and Flapping Wing Aerodynamics for Micro Air Vehicle Applications, ed. Mueller, T.J., *Progress in Astronautics and Aeronautics*, vol. 195.
- Anderson, J. M.**, 1996. Vorticity Control for Efficient Propulsion, *PhD Thesis*, Joint Program, Massachusetts Institute of Technology & Woods Hole Oceanographic Institution.
- Anderson, J. M., Streitlien, K., Barrett, D. S., and Triantafyllou, M. S.**, 1998. Oscillating Foils of High Propulsive Efficiency, *Journal of Fluid Mechanics*, Vol. 360, pp. 41-72.
- Aydin, B.T.**, 2008. Effect of self-issuing jets along the span on the near wake of a square cylinder, *MSc Thesis*, ITU, Istanbul.
- Aydin, B.T. Cetiner, O., Unal, M. F.**, 2010. Effect of self-issuing jets along the span on the near- wake of a square cylinder, *Experiments in Fluids*, Vol. 48, No. 6, pp. 1081-1094.
- Bernal, L. P., Ol, M. V., Szczublewski, D. P. and Cox, A. C.**, 2009. Unsteady Force Measurements in Pitching-Plunging Airfoils. *39th AIAA Fluid Dynamics Conference*, AIAA 2009-4031.
- Betz, A.**, 1912. Ein Beitrag zur Erklärung des Segelfluges, *Zeitschrift für Flugtechnik und Motorluftschiffahrt*, Vol. 3, pp. 269-272.
- Birch, D. and Lee, T.**, 2005. Investigation of the near-tip vortex behind an oscillating wing, *Journal of Fluid Mechanics*, Vol. 544, pp.201-241.
- Birnbaum, W.**, 1924. Das ebene Problem des schlagenden Fliigels, *Zeitschrift für angewandte Mathematik und Mechanik (ZAMM)*, Vol. 4, pp. 277-292.
- Blake, R. W.**, 1983. *Fish Locomotion*. Cambridge University Press, New York.
- Bratt, B.**, 1950. Flow patterns in the wake of an oscillating airfoil. *Aeronautical Research Council*, **R&M 2773**.

- Carr, L. W.**, 1987. Progress in analysis and prediction of dynamic stall. *Journal of Aircraft*, Vol. **25**, no.1, pp. 6-17.
- Cebeci, T., Platzer, M., Chen, H., Chang, K. C., and Shao, J. P.**, 2005. *Analysis of Low-Speed Unsteady Airfoil Flows*, Horizons Publishing, Long Beach, California.
- Cleaver, D. J., Wang, Z. and Gursul, I.**, 2009. Lift Enhancement on Oscillating Airfoils, *39th AIAA Fluid Dynamics Conference*, AIAA 2009-4028.
- Dabiri, J. O.**, 2009. Optimal Vortex Formation as a Unifying Principle in Biological Propulsion, *Annual Review of Fluid Mechanics*, Vol. **41**, pp.17–33.
- Dantec Dynamics**, 2000. *FlowManager Software and Introduction to PIV Instrumentation*, 5th Edition.
- Dial, K. P., Jackson, B. E. and Segre, P.**, 2008. A fundamental avian wing-stroke provides a new perspective on the evolution of flight. *Nature*, Vol. **451**, pp. 985-989.
- Dickinson, M. H., Lehmann, F. O. and Sane1, S.**, 1999. Wing Rotation and the Aerodynamic Basis of Insect Flight. *Science*, Vol. **284**, pp. 1954-1960.
- Dong, H., Mittal, R. and Najjar, F. M.**, 2006. Wake topology and hydrodynamic performance of low-aspect-ratio flapping foils. *Journal of Fluid Mechanics*, Vol. **566**, pp.309-343.
- Duyvis, F. D.**, 1995. An F3B high performance model sailplane design study, *Quiet Flight International*, vol 14.
- Ellington, C. P.**, 1999, The Novel Aerodynamics of Insect Flight: Applications to Micro-Air Vehicles, *The Journal of Experimental Biology*, Vol. **202**, pp. 3439-3448.
- Ellington, C. P., van den Berg, C., Willmott, A. P. and Thomas, A. L. R.**, 1996. Leading-Edge Vortices in Insect Flight, *Letters to Nature*, Vol. **19/26**, pp.626-630.
- Freytmuth, P.**, 1988. Propulsive Vortical Signature of Plunging and Pitching Airfoils, *AIAA Journal*, Vol. **26**, No. 7.
- Garmann, D. J. and Visbal, M. R.**, 2009. High-Fidelity Simulations of Transitional Flow Over Pitching Airfoils. *39th AIAA Fluid Dynamics Conference*, AIAA 2009-3693.
- Garrick, I. E.**, 1936. Propulsion of a flapping and oscillating air-foil, *NACA TR 567*.
- Guglielmini, L. and Blondeaux, P.**, 2003. Propulsive Efficiency of Oscillating Foils. *European Journal of Mechanics, B/Fluids*. Vol. **23**, pp. 255-278.
- Gursul, I. and Ho, C. M.**, 1992. High Aerodynamic Loads on an Airfoil Submerged in an Unsteady Stream. *AIAA Journal*, vol.**30**, no.4, pp.1117-1119.
- Heathcote, S. and Gursul, I.**, 2007a. Jet Switching Phenomenon for a Periodically Plunging Airfoil, *Physics of Fluids*, Vol. **19**, 027104.
- Heathcote, S. and Gursul, I.**, 2007b. Flexible Flapping Airfoil Propulsion at Low Reynolds Numbers, *AIAA Journal*, vol.**5**, no.5, pp.1066-1078.

- Heathcote, S., Martin D. and Gursul, I.**, 2004. Flexible Flapping Airfoil Propulsion at Zero Freestream Velocity. *AIAA Journal*, vol.42, no. no.11, pp.2196-2204.
- Heathcote, S., Wang, Z. and Gursul, I.**, 2008. Effect of spanwise flexibility on flapping wing propulsion, *Journal of Fluids and Structures*, Vol. 24 pp.183-199.
- Hover, F. S., Haugsdal, O. and Triantafyllou, M. S.**, 2004. Effect of Angle of Attack Profiles in Flapping Foil Propulsion. *Journal of Fluids and Structures* Vol. 19, pp. 37-47.
- Isogai, K., Shinmoto, Y. and Watanabe, Y.**, 1999. Effects of Dynamic stall on Propulsive Efficiency and Thrust of Flapping Airfoil. *AIAA Journal*, Vol. 37 n.10, pp. 1145-1151.
- Jones, B. M.**, 1938. Stalling, *Journal of Royal Aeronautical Society*. Vol.38, pp.747-770.
- Jones, K. D., and Platzer, M. F.**, 2001. On the Use of Vortex Flows for the Propulsion of Micro-Air and Sea Vehicles. *RTO AVT Symposium on "Advanced Flow Management: Part A-Vortex Flows and High Angle of Attack for Military Vehicles"* (Loen, Norway).
- Jones, K. D., and Platzer, M. F.**, 2009. Design and development considerations for biologically inspired flapping-wing micro air vehicles. *Experiments in Fluids*, Vol. 46/5, pp.799-810.
- Jones, K. D., Dohring, C. M., and Platzer, M.F.**, 1996. Wake Structures Behind Plunging Airfoils: A comparison of Numerical and Experimental Results, *AIAA 96-007 (Reno, USA)*.
- Jones, K. D., Dohring, C. M., and Platzer, M. F.**, 1998. Experimental and Computational Investigation of the Knoller-Betz Effect, *AIAA Journal*, Vol. 36, No. 7.
- Jones, K. D., Lund, T. C. and Platzer, M. F.**, 2001. Experimental and Computational Investigation of Flapping Wing Propulsion for Micro Air Vehicles, Fixed and Flapping Wing Aerodynamics for Micro Air Vehicle Applications, ed. Mueller, T.J., *Progress in Astronautics and Aeronautics*, vol. 195.
- Jung, Y.W. and Park, S.O.**, 2005. Vortex-shedding characteristics in the wake of an oscillating airfoil at low Reynolds number. *Journal of Fluids and Structures*, Vol. 20, pp.451-464.
- Kang, C., Baik, Y. S., Bernal, L., Ol, M. V., Shyy, W.**, 2009. Fluid Dynamics of Pitching and Plunging Airfoils of Reynolds Number between 1×10^4 and 6×10^4 . *47th AIAA Aerospace Sciences Meeting Including The New Horizons Forum and Aerospace Exposition*, AIAA-2009-536
- Katzmayr, R.**, 1922. Effect of Periodic Changes of Angle of Attack on Behavior of Airfoils, *NACA TM 147*.
- Kim, J. S., and Park S. O.**, 1988. Smoke Wire Visualization of Unsteady Separation Over an Oscillating Airfoil. *AIAA Journal*. Vol. 26, no. 11, pp. 1408-1410.

- Kim D. H. and Chang, J.W.**, 2009. Reynolds Number Effects on Unsteady Boundary Layer for an Oscillating Airfoil. *27th AIAA Applied Aerodynamics Conference*. AIAA 2009-3501.
- Knoller, R.**, 1909. Die Gesetze des Luftwiderstandes, *Flug- und Motortechnik (Wien)*, Vol. **3**, No. 21, pp. 1-7.
- Koochesfahani, M. M.**, 1989. Vortical Patterns in the Wake of an Oscillating Airfoil. *AIAA Journal*. Vol. **27**, no. 9, pp. 1200-1205.
- Kramer, M.**, 1932. Increase in the maximum lift of an airplane wing due to a sudden increase in its effective angle of attack resulting from a gust, *Technical Memorandum, No. 632, National Advisory Committee for Aeronautics (N.A.C.A.)*.
- Kuo, C-H. and Hsieh, J. K.**, 2001. Unsteady flow structure and vorticity convection over the airfoil oscillating at high reduced frequency. *Experimental Thermal and Fluid Science*, Vol. **24**, pp.117-129.
- Lai, J. C. S., and Platzer, M. F.**, 1999. Jet Characteristics of a Plunging Airfoil, *AIAA Journal*, Vol. **37**, No. 12.
- Landreth, C. C., and Adrian, R. J.**, 1989. Measurement and Refinement of Velocity Data Using High Image Density Analysis in Particle Image Velocimetry, *Applications of Laser Anemometry: Proceedings of 4th International Symposium*, Springer Verlag, Berlin, pp. 484-497.
- Lewin, G. C., and Haj-Hariri, H.**, 2003. Modelling Thrust Generation of a Two-Dimensional Heaving Hydrofoil in a Viscous Flow, *Journal of Fluid Mechanics*, Vol. **492**, pp. 339-362.
- Lian, Y.**, 2009a. Numerical Investigation of Boundary Effects on Flapping Wing Study. *47th AIAA Aerospace Sciences Meeting Including The New Horizons Forum and Aerospace Exposition*, AIAA 2009-539.
- Lian, Y.**, 2009b. Parametric Study of a Pitching Flat Plate at Low Reynolds Numbers. *39th AIAA Fluid Dynamics Conference*, AIAA 2009-3688.
- Lian, Y., and Shyy, W.**, 2007. Aerodynamics of Low Reynolds Number Plunging Airfoil in Steady and Gusty Environments. *45th AIAA Aerospace Sciences Meeting and Exhibit*, AIAA 2007-71.
- Lian, Y., Ol, M. V. and Shyy, W.**, 2008. Comparative Study of Pitch-Plunge Airfoil Aerodynamics at Translational Reynolds Number. *46th AIAA Aerospace Sciences Meeting and Exhibit*, AIAA 2008-652.
- Lin, J. -C.**, 1994. "NFILVB" software, Fluid Mechanics Lab., Lehigh University.
- Lin, J. -C.**, 1996. "NEWENSAV" software, Fluid Mechanics Lab., Lehigh University.
- Lua, K. B., Lim, T. T., Yeo, K. S. and Oo, G.Y.**, 2007. Wake-Structure Formation of a Heaving Two-Dimensional Elliptic Airfoil *AIAA Journal*, vol.45, no.7, pp.1571-1583.
- McClung, A. M.**, 2009. Influence of Structural Flexibility on Flapping Wing Propulsion. *PhD thesis*, Department of the Air Force Air University Air Force Institute of Technology Wright-Patterson Air Force Base, Ohio.

- McCroskey, W. J.**, 1982. Unsteady Airfoils. *Annual Review of Fluid Mechanics*. Vol. **14**, pp. 285-311.
- McCroskey, W. J., Carr, L. W. and McAlister, K. W.**, 1976. Dynamic Stall Experiments on Oscillating Airfoils, *AIAA Journal*. Vol. **14**, no. 1, pp. 57-63.
- McGowan, G. Z., Gopalarathnam, A.**, 2009 Analytical, Computational, and Experimental Investigations of Equivalence Between Pitch and Plunge Motions for Airfoils at Low Reynolds Numbers. *47th AIAA Aerospace Sciences Meeting Including The New Horizons Forum and Aerospace Exposition*, AIAA 2009-535
- McMasters, J. H., Henderson, M. L.**, 1980. Low speed single element airfoil synthesis. *Technical Soaring*, vol.6, no.2, pp.1-21.
- McMichael, J. M., and Francis M. S.**, 1997. Micro Air Vehicles – Toward a New Dimension in Flight, *Defense Advanced Research Project Agency (DARPA) Report*, Arlington, Virginia, USA.
- Miao, J-M. and Ho, M-H.**, 2006. Effect of flexure on aerodynamic propulsive efficiency of flapping flexible airfoil. *Journal of Fluids and Structures*, Vol. **22**, pp. 401–419.
- Milano, M. and Gharib, M.**, 2005. Uncovering the physics of flapping flat plates with artificial evolution. *Journal of Fluid Mechanics*, Vol. **534**, pp. 403-409.
- Mueller, T. J.**, 2001. Fixed and Flapping Wing Aerodynamics for Micro Air Vehicle Applications, *Progress in Astronautics and Aerodynamics*, vol.**195**.
- Mueller, T. J., and DeLaurier, J. D.**, 2003. Aerodynamics of Small Vehicles. *Annual Review of Fluid Mechanics*, Vol. **35**, pp.89–111.
- Muijres, F. T., Johansson, L. C., Barfield, R., Wolf, M., Spedding, G. R. and Hedenström, A.**, 2008. Leading-Edge Vortex Improves Lift in Slow-Flying Bats. *Science*, Vol. **319**, pp. 1250-1253.
- Ohmi, K., Coutanceau, M., Loc, T. P. and Duliou, A.**, 1990. Vortex Formation Around an Oscillating and Translating Airfoil at Large Incidences. *Journal of Fluid Mechanics*, Vol. **211**, pp. 37-60.
- Ohmi, K., Coutanceau, M., Daube, O. and Loc, T. P.**, 1991. Further Experiments on Vortex Formation Around an Oscillating and Translating Airfoil at Large Incidences. *Journal of Fluid Mechanics*, Vol. **225**, pp. 607-630.
- Oi, M. V.**, 2007. Vortical Structures in High Frequency Pitch and Plunge at Low Reynolds Number. *37th AIAA Fluid Dynamics Conference and Exhibit*, AIAA 2007-4233.
- Oi, M. V.**, 2009a. The High-Frequency, High-Amplitude Pitch Problem: Airfoils, Plates and Wings. *39th AIAA Fluid Dynamics Conference*, AIAA 2009-4030.
- Oi, M. V.**, 2009b. AVT-149, Micro Air Vehicle Unsteady Aerodynamics. *Final report*; publication pending.
- Oi, M. V., McAuliffe, B. R., Hanff, E. S., Scholz, U., and Kaehler, C.**, 2005. Comparison of Laminar Separation Bubble Measurements on a Low

- Reynolds Number Airfoil in Three Facilities. *35th AIAA Fluid Dynamics Conference and Exhibit*, AIAA 2005-5149.
- Ol, M. V., Bernal, L., Kang, C-K., Shyy, W.**, 2009. Shallow and deep dynamic stall for flapping low Reynolds number airfoils. *Experiments in Fluids*, Vol. **46**, no. 5, pp. 883-901.
- Oshima, H., and Ramaprian, B. R.**, 1997. Velocity Measurements over a Pitching Airfoil. *AIAA Journal*. Vol. **35**, no. 1, pp. 119-126.
- Panda, J. and Zaman, K. B. M. Q.**, 1994. Experimental investigation of the flowfield of an oscillating airfoil and estimation of lift from wake surveys. *Journal of Fluid Mechanics*, Vol. **265**, pp. 65-95.
- Park, J. T., Cutbirth, J. M. and Brewer, W. H.**, 2005. Experimental methods for hydrodynamics characterization of a very large water tunnel. *Transactions of the ASME, Journal of Fluids Engineering*, Vol. **127**, pp.1210-1214.
- Percin, M.**, 2009. Flow Around a Plunging Airfoil in a Uniform Flow, *MSc Thesis*, ITU, Istanbul.
- Platzer, M. F.**, 2009. Lecture Series: Flapping-wing Aero/hydronechanics in Nature and Engineering, Experimental and Computational Investigations of Flapping Wing Propulsion for Micro Air Vehicles. *ITU, Faculty of Aeronautics and Astronautics*. October 19-23, 2009.
- Platzer, M. F. and Jones, K. D.**, 2006. Flapping-Wing Aerodynamics: Progress and Challenges, *44th AIAA Aerospace Sciences Meeting*, AIAA 2006-500.
- Platzer, M. F., Jones, K. D., Young, J., and Lai J. C. S.**, 2008. Flapping-Wing Aerodynamics: Progress and Challenges, *AIAA Journal*, Vol. **46**, No 9
- Prandtl, L.**, 1920. Theory of Lifting Surfaces, *NACA Technical Reports*, NACA-TN-9 & NACA-TN-10-Pt-2.
- Prandtl, L.**, 1922. Über die Entstehung von Wirbeln in der idealen Flüssigkeit, mit Anwendung auf die Tragflügeltheorie und andere Aufgaben, *Hydro- und Aerodynamik*, Berlin, Julius Springer Verlag, pp. 18-33.
- Prandtl, L.**, 1952. *Essentials of Fluid Dynamics*. Great Britain, Blackie and Son Ltd.
- Radespiel, R., Windte, J. and Scholz, U.**, 2007. Numerical and Experimental Flow Analysis of Moving Airfoils with Laminar Separation Bubbles. *AIAA Journal*. Vol. **45**, no.6, pp. 1346-1356.
- Raffel, M., Willert, C., Wereley, S. T., and Kompenhans, J.**, 2007. Particle Image Velocimetry, Springer.
- Ramamurti, R. and Sandberg, W.**, 2001. Simulation of Flow about Flapping Airfoils Using Finite Element Incompressible Flow Solver. *AIAA Journal*. Vol. **39**, no. 2, pp. 253-260.
- Rank, M., and Ramaprian, B. R.**, 1998: Instantaneous Velocity Measurements Around an Oscillating Airfoil. *AIAA Journal*. Vol. **37**, no. 3: Technical Notes, pp. 401-403.

- Read, D.A., Hover, F. S. and Triantafyllou M. S.,** 2003. Forces on oscillating foils for propulsion and maneuvering. *Journal of Fluids and Structures* Vol. 17 pp. 163–183.
- Reshotko, E., Saric, W. S. and Nagib, H. M.,** 1997. Flow quality issues for large wind tunnels, *35th Aerospace Sciences Meeting & Exhibit*, AIAA 97-0225.
- Ringuette, M. J., Milano, M. and Gharib, M.,** 2007. Role of the tip vortex in the force generation of low-aspect-ratio normal flat plates. *Journal of Fluid Mechanics*, Vol. 581, pp. 453–468.
- Rival D., Prangemeier, T. and Tropea, C.,** 2008. The influence of airfoil kinematics on the formation of leading-edge vortices in bio-inspired flight. *Experiments in Fluids*, Vol. 46/5, pp.823-833.
- Rival D., and Tropea, C.,** 2009. Characteristics of Pitching and Plunging Airfoils under Dynamic-Stall Conditions. *47th AIAA Aerospace Sciences Meeting Including The New Horizons Forum and Aerospace Exposition*, AIAA 2009-537.
- Rockwell, D., Magness, C., Robinson, O., Towfighi, J., Akin O., Gu, W. and Corcoran, T.,** 1992. Structure of Unsteady Separated Flows via Particle Image Velocimetry. *Report PI-1, Fluid Mechanics Lab, Lehigh University*.
- Rockwell, D., Magness, C., Towfighi, J., Akin O. and Corcoran, T.,** 1993. High-Image Density Particle Image Velocimetry Using Scanning Techniques. *Experiments in Fluids*. Vol. 14, pp.181-192.
- Sarkar, S. and Venkatraman, K.,** 2006. Numerical Simulation of Thrust Generating Flow Past a Pitching Airfoil. *Computers & Fluids*. 35. pp. 16-42.
- Schouveiler, L., Hover, F. S. and Triantafyllou, M. S.,** 2005. Performance of Flapping Foil Propulsion. *Journal of Fluids and Structures*. Vol. 20, pp.949-959.
- Shyy, W., Berg, M. and Ljungqvist, D.,** 1999. Flapping and Flexible Wings for Biological and Micro Air Vehicles. *Progress in Aerospace Sciences*, Vol. 35, pp.455-505.
- Shyy, W., Lian, Y., Tang, J., Viieru, D. and Liu, H.,** 2008. *Aerodynamics of Low Reynolds Number Flyers*, Cambridge University Press, New York.
- Soloff, M. S. and Meinhart, C. D.,** 1999. “CleanVec” PIV Validation Software, Laboratory for Turbulence and Complex Flow, University of Illinois at Urbana-Campaign.
- Sun, M. and Sheikh, S. R.,** 1999. Dynamic stall suppression on an oscillating airfoil by steady and unsteady tangential blowing. *Aerospace Science and Technology*, no.6, pp.355-366.
- Taylor, G. K., Nudds, R. L. and Thomas, A. L. R.,** 2003. Flying and Swimming Animals Cruise at a Strouhal Number Tuned for High Power Efficiency, *Nature (London)*, Vol. 425, pp.707-711.

- Techet, A. H., Hover, F. S. and Triantafyllou, M. S.,** 2003. Separation and Turbulence Control in Biomimetic Flows. *Flow, Turbulence and Combustion*, Vol. **71**, pp.105–118.
- Theodorsen, T.,** 1934. General Theory of Aerodynamic Instability and the Mechanism of Flutter, *NACA Report 496*.
- Triantafyllou, M.S., Techet, A.H. and Hover, F. S.,** 2004. Review of Experimental Work in Biomimetic Foils, *IEEE Journal of Oceanic Engineering*, vol.29, no.3, pp.585-594.
- Triantafyllou, M. S., Triantafyllou, G. S. and Gopalkrishnan, R.,** 1991. Wake Mechanics for Thrust Generation in Oscillating Foils. *Letters, Physics of Fluids A*, Vol. **3**, n. 12, pp. 2835-2837.
- Triantafyllou, G. S., Triantafyllou, M. S. and Grosenbaugh, M. A.,** 1992. Optimal Thrust Development in Oscillating Foils with Application to Fish Propulsion. *Journal of Fluids and structures*, Vol. **73**, n. 2, pp. 205-224.
- Tuncer, I. H. and Kay, M.,** 2004. Optimization of Flapping Airfoils for Maximum Thrust and Propulsive Efficiency. *Acta Polytechnica*, Vol. **44** n.1, pp.31-37.
- Tuncer, I. H. and Kaya, M.,** 2005. Optimization of Flapping Airfoils for Maximum Thrust and Propulsive Efficiency. *AIAA Journal*, Vol. **43** n.11, pp.2329-2336.
- Tuncer, I. H. and Platzer, M. F.,** 1996. Thrust generation due to airfoil flapping. *AIAA Journal*, Vol.**34**, no.2, pp.324-331.
- Tuncer, I. H. and Platzer, M. F.,** 2000. Computational Study of Flapping Airfoil Aerodynamics. *Journal of Aircraft*. Vol. **37**, no.3, pp.514-520.
- Url-1:** <<https://www.cia.gov/about-cia/cia-museum/cia-museum-tour/index.html>>, accessed at 05.11.2009.
- Url-2:** <http://www.absoluteastronomy.com/topics/Miniature_UAVs>, accessed at 06.11.2009.
- Url-3:** <http://ho.seas.ucla.edu/publications/conference/2001/jpl10_2001.pdf>, accessed at 06.11.2009.
- Url-4:** <http://news.nationalgeographic.com/news/2003/03/0313_030313_secret_weapons2.html>, accessed at 06.11.2009.
- Url-5:** <http://www.livescience.com/technology/041210_project_ornithopter.html>, accessed at 06.11.2009.
- Url-6:** <<http://www.kennethmolsonfoundation.ca/index.php?page=recent-projects>>, accessed at 07.11.2009.
- Url-7:** <<http://nextbigfuture.com/2009/07/darpa-funds-phase-2-of-nano-uav.html>>, accessed at 06.11.2009.
- Url-8:** <http://www.avinc.com/downloads/NAVfactsheetfinal30May_1.pdf>, accessed at 06.11.2009.
- Url-9:** <http://www.avinc.com/media_gallery/images/uas/> accessed at 06.11.2009.

- Url-10:** <http://ccsl.mae.cornell.edu/papers/RAM08_vanBreugel.pdf>, accessed at 06.11.2009.
- Url-11:** <<http://onionesquereality.wordpress.com/2009/01/04/butterfly-ornithopter/>>, accessed at 06.11.2009.
- Url-12:** <<http://en.wikipedia.org/wiki/Entomopter>>, accessed at 06.11.2009.
- Url-13:** <<http://angel-strike.com/rcmbio/RCM/MICHELSON.bio.html>>, accessed at 06.11.2009.
- Url-14:** <<http://www.delta.tudelft.nl/en/archive/article/from-insectothopter-to-delfly/18456>>, accessed at 03.11.2009.
- Url-15:** <<http://www.tudelft.nl/live/pagina.jsp?id=c7b23265-5e68-4332-8f8604deb5ce4bfl&lang=en>>, accessed at 02.11.2009.
- Url-16:** <<http://www.delfly.nl/>>, accessed at 04.11.2009.
- Url-17:** <<http://www.forbes.com/2009/06/26/spy-drones-darpa-technology-break-throughs-ravens.html?partner=yahootix>>, accessed at 07.11.2009.
- Url-18:** <<http://www.nrl.navy.mil/vrs/factsheets/index.php>>, accessed at 07.11.2009.
- Url-19:** <<http://aa.nps.edu/programs/aero/propulsion/>>, accessed at 07.11.2009.
- Url-20:** <http://fir.epfl.ch/docs/FIR_proceedings_online.pdf>, accessed at 7.11.2009.
- Url-21:** <http://www.engb.com/downloads/Current_Times_Spring_05.pdf>, accessed at 07.11.2009.
- Url-22:** <http://en.wikipedia.org/wiki/Tidal_power>, accessed at 06.11.2009.
- Url-23:** <http://www.esru.strath.ac.uk/EandE/Web_sites/01-02/RE_info/tidal1.htm>, accessed at 06.11.2009.
- Url-24:** <<http://www.biopowersystems.com/biostream.php>>, accessed at 06.11.2009.
- Url-25:** <<http://www.global-greenhouse-warming.com/biomimicry.html>>, accessed at 06.11.2009.
- Url-26:** <<http://www.aniprop.de/dlrhp/index.html>>, accessed at 06.11.2009.
- Url-27:** <<http://magenn.com/>>, accessed at 10.11.2009.
- Url-28:** <<http://www.skywindpower.com/ww/index.htm>>, accessed at 10.11.2009.
- Url-29:** <http://www.qinetiq.com/home/newsroom/news_releases_homepage/2006/1st_quarter/First_flight_trial_for_Zephyr_Unmanned_Aerial_Vehicle.html>, accessed at 10.11.2009.
- Url-30:** <http://www.ae.uiuc.edu/m-selig/ads/coord_database.html>, accessed at 03.11.2009.

- van den Berg, C., and Ellington, C. P.,** 1997. The three-dimensional leading-edge vortex of a 'hovering' model hawkmoth. *Philosophical Transactions of the Royal Society B: Biological Science*, Vol. **352**, pp.329-340.
- von Ellenrieder, K. D., Parker, K. and Soria, J.,** 2003. Flow Structures Behind a Heaving and Pitching Finite-span Wing. *Journal of Fluid Mechanics*, Vol. **490**, pp. 129-138.
- von Kármán, T., and Burgers, J. M.,** 1935. General Aerodynamic Theory - Perfect Fluids, *Aerodynamic Theory*, Vol. **2**, pp. 308.
- Wang, Z. J.,** 2000: Vortex Shedding and Frequency Selection in Flapping Flight, *Journal of Fluid Mechanics*, Vol. **410** , pp. 323-341.
- Webb, C., Dong, H. and Ol, M.,** 2008. Effects of Unequal Pitch and Plunge Airfoil Motion Frequency on Aerodynamic Response. *46th AIAA Aerospace Sciences Meeting and Exhibit*, AIAA 2008-582.
- Windte, J., Radespiel, R. Scholz, U. and Eisfeld, B.,** 2004. RANS Simulation of the Transitional Flow Around Airfoils at Low Reynolds Numbers for Steady and Unsteady Onset Conditions, *RTO-MP-AVT III, RTO AVT Specialists Meeting of Enhancement of NATO Military Flight Vehicle Performance by Management of Interacting Boundary Layer Transition and Separation*.
- Windte, J., Scholz, U and Radespiel, R.,** 2006. Validation of the RANS-simulation of laminar separation bubbles on airfoils. *Aerospace Science and Technology*. Vol. **10**, pp.484–494.
- Windte, J. and Radespiel, R.,** 2008. Propulsive Efficiency of a Moving Airfoil at Transitional Low Reynolds Numbers. *AIAA Journal*, Vol. **46**, no.9, pp.2165-2177.
- Yang, S., Luo, S., Liu, F. and Tsai, H. M.,** 2006. Optimization of Unstalled Pitching and Plunging Motion of an Airfoil. *44th AIAA Aerospace Sciences Meeting and Exhibit*. AIAA 2006-1055.
- Young, J.,** 2005. Numerical Simulation of the Unsteady Aerodynamics of Flapping Airfoils, *PhD Thesis*, The University of New South Wales, Sydney.
- Young, J. and Lai, J. C. S.,** 2007a. Vortex Lock-In Phenomenon in the Wake of a Plunging Airfoil, *AIAA Journal*, Vol. **45**, No. 2.
- Young, J. and Lai, J. C. S.,** 2007b. Mechanisms Influencing the Efficiency of Oscillating Airfoil Propulsion, *AIAA Journal*, Vol. **45**, No. 7.
- Zhang, L. P., Chang, X. H., Duan, X. P. and Zhang, H. X.,** 2007. Numerical Simulations for Insect 'Clap and Fling' with Unsteady Incompressible Solver on Dynamic Hybrid Grids. *New Trends in Fluid Mechanics Research, Proceedings of the Fifth International Conference on Fluid Mechanics*.
- Zhang, W., Hain, R. and Kaehler, C. J.,** 2008. Scanning PIV investigation of the laminar separation bubble on a SD7003 airfoil, *Experiments in Fluids*, Vol. **45**, pp.725-743.

APPENDICES

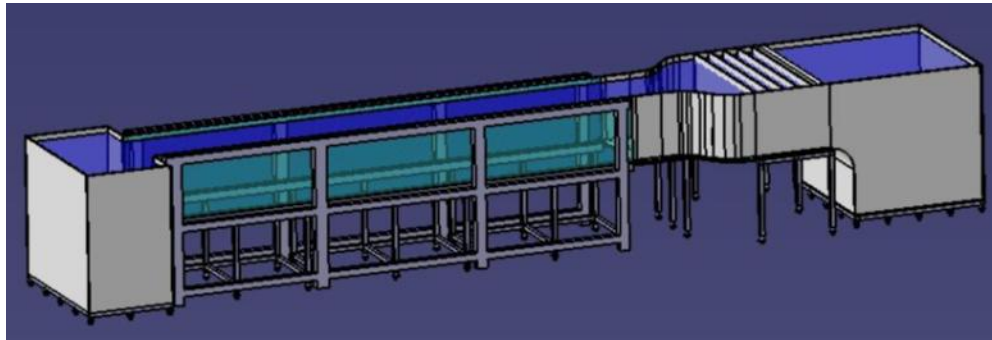
Appendix A.1 Schematic of the Water Channel

Appendix A.2 List of experimental cases

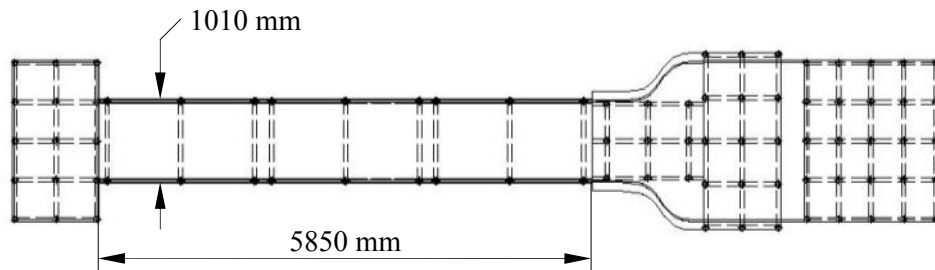
Appendix A.3 Derivation of the theoretical efficiency

APPENDIX A.1 Schematic of the Water Channel

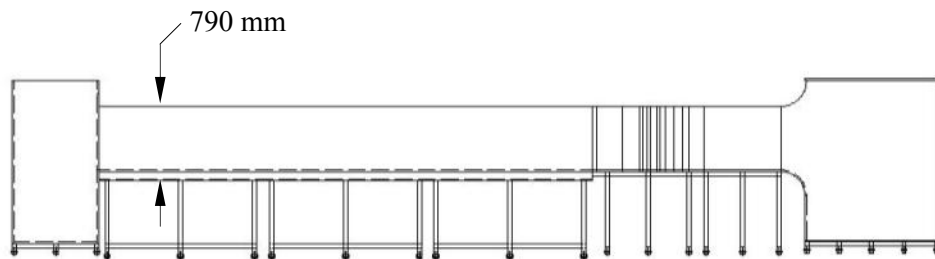
The schematic of Trisonic Research Laboratory Large Scale Free Surface Water Channel is given in Figure A.1.



(a)



(b)



(c)

Figure A.1: a) 3D view, b) top view, c) side view of the water channel.

Maximum attainable velocity = 0.138 m/s

Minimum velocity for uniform flow = 0.0047 m/s

Coefficient of variation based on DPIV data for the channel without model is 0.029 for $Re = 600$ based on the airfoil chord.

APPENDIX A.2 List of Experimental Cases

The experiments are conducted for the cases shown in Table A.2.

Table A.2: List of experimental cases

Case no.	Base case	Re	U_∞ [m/s]	h_{amp}/c	α_o [°]	α_{ampl} [°]	ψ [°]	f_{pitch}	f_{plunge}	k	λ	St
1		1000	0.010	0.5	8	8.6	90	0.05		1.56	0.10	0.5
2		1250	0.013	0.5						1.25	0.12	0.4
3		1650	0.017	0.5						0.95	0.16	0.3
4		2500	0.025	0.5						0.63	0.24	0.2
5		5000	0.050	0.5						0.31	0.48	0.1
6		10000	0.100	0.5						0.16	0.96	0.0
7		1000	0.010	0.5	8	8.6	90	0.1		3.13	0.05	1.0
8		1250	0.013	0.5						2.50	0.06	0.8
9		1650	0.017	0.5						1.90	0.08	0.6
10		2000	0.020	0.5						1.56	0.10	0.5
11		2500	0.025	0.5						1.25	0.12	0.4
12		3300	0.033	0.5						0.95	0.16	0.3
13		5000	0.050	0.5	0.63	0.24	0.2					
14		10000	0.100	0.5	0.31	0.48	0.1					
15		2500	0.025	0.5	8	8.6	90	0.2		2.50	0.06	0.8
16		3300	0.033	0.5						1.90	0.08	0.6
17		4000	0.040	0.5						1.56	0.10	0.5
18		5000	0.050	0.5						1.25	0.12	0.4
19		6750	0.068	0.5						0.93	0.16	0.3
20		10000	0.100	0.5						0.63	0.24	0.2
21		3000	0.030	0.5	8	8.6	90	0.3		3.13	0.05	1.0
22		3750	0.038	0.5						2.50	0.06	0.8
23		5000	0.050	0.5						1.88	0.08	0.6
24		6000	0.060	0.5						1.56	0.10	0.5
25		7400	0.074	0.5						1.27	0.12	0.4
26		10000	0.100	0.5						0.94	0.16	0.3
27		13700	0.138	0.5	0.63	0.24	0.2					
28		825	0.008	0.25	8	8.6	90	0.1		3.79	0.08	0.6
29		1250	0.013	0.25						2.50	0.12	0.4
30		1650	0.017	0.25						1.90	0.16	0.3
31		2500	0.025	0.25						1.25	0.24	0.2
32		5000	0.050	0.25						0.63	0.48	0.1
33		10000	0.100	0.25						0.31	0.96	0.0
34		1250	0.013	0.25	8	8.6	90	0.2		5.01	0.06	0.8
35		1650	0.017	0.25						3.79	0.08	0.6
36		2500	0.025	0.25						2.50	0.12	0.4
37		3300	0.033	0.25						1.90	0.16	0.3
38		5000	0.050	0.25						1.25	0.24	0.2
39		10000	0.100	0.25						0.63	0.48	0.1
40		3000	0.030	0.25	8	8.6	90	0.6		6.26	0.05	1.0
41		3750	0.038	0.25						5.01	0.06	0.8
42		5000	0.050	0.25						3.75	0.08	0.6
43		7400	0.074	0.25						2.54	0.12	0.4
44		10000	0.100	0.25						1.88	0.16	0.3
45		13700	0.138	0.25						1.25	0.24	0.2

Table A.2 : (Continued) Experimental cases

Case no.	Base case	Re	U_∞ [m/s]	h_{amp}/c	α_0 [°]	α_{ampl} [°]	ψ [°]	f_{pitch}	f_{plunge}	k	λ	St						
46		1000	0.010	1	8	8.6	90	0.05		1.56	0.05	1.0						
47		1250	0.013	1						1.25	0.06	0.8						
48		1650	0.017	1						0.95	0.08	0.6						
49		2500	0.025	1						0.63	0.12	0.4						
50		5000	0.050	1						0.31	0.24	0.2						
51		10000	0.100	1						0.16	0.48	0.1						
52		2000	0.020	1	8	8.6	90	0.1		1.56	0.05	1.0						
53		2500	0.025	1						1.25	0.06	0.8						
54		3300	0.033	1						0.95	0.08	0.6						
55		5000	0.050	1						0.63	0.12	0.4						
56		10000	0.100	1						0.31	0.24	0.2						
57		3000	0.030	1						8	8.6	90	0.15		1.56	0.05	1.0	
58		3750	0.038	1	1.25	0.06	0.8											
59		5000	0.050	1	0.94	0.08	0.6											
60		7400	0.074	1	0.63	0.12	0.4											
61		10000	0.100	1	0.47	0.16	0.3											
62		13700	0.138	1	0.31	0.24	0.2											
63	14	10000	0.1004	0.5	0	8.6	90	0.1		0.31	0.48	0.1						
64	15	2500	0.0251					0.2		2.50	0.06	0.8						
65	19	6750	0.0678					0.93		0.16	0.3							
66	31	2500	0.0251	0.25				0	8.6	90	0.1		1.25	0.24	0.2			
67	33	10000	0.1004								0.31		0.96	0.0				
108	37	3300	0.0331								0.2		1.90	0.16	0.3			
68	40	3000	0.0301								0.6		6.26	0.05	1.0			
69	43	7400	0.0743													2.54	0.12	0.4
70	44	10000	0.1004															
71	45	13700	0.138	1.25				0.24	0.2									
72	14	10000	0.1004	0.5				0	12.9	90	0.1		0.31	0.48	0.1			
73	15	2500	0.0251								0.2		2.50	0.06	0.8			
74	19	6750	0.0678		0.93	0.16	0.3											
75	31	2500	0.0251	0.25	0	12.9	90				0.1		1.25	0.24	0.2			
76	33	10000	0.1004								0.31		0.96	0.0				
109	37	3300	0.0331								0.2		1.90	0.16	0.3			
77	40	3000	0.0301								0.6		6.26	0.05	1.0			
78	43	7400	0.0743													2.54	0.12	0.4
79	44	10000	0.1004															
80	45	13700	0.138	1.25	0.24	0.2												
81	14	10000	0.1004	0.5	8	12.9	90				0.1		0.31	0.48	0.1			
82	15	2500	0.0251								0.2		2.50	0.06	0.8			
83	19	6750	0.0678					0.93	0.16	0.3								
84	31	2500	0.0251	0.25				8	12.9	90	0.1		1.25	0.24	0.2			
85	33	10000	0.1004								0.31		0.96	0.0				
110	37	3300	0.0331								0.2		1.90	0.16	0.3			
86	40	3000	0.0301								0.6		6.26	0.05	1.0			
87	43	7400	0.0743													2.54	0.12	0.4
88	44	10000	0.1004															
89	45	13700	0.138	1.25				0.24	0.2									

Table A.2 : (Continued) Experimental cases

Case no.	Base case	Re	U_∞ [m/s]	h_{amp}/c	α_0 [°]	α_{ampl} [°]	ψ [°]	f_{pitch}	f_{plunge}	k	λ	St
90	14	10000	0.1004	0.5	8	8.6	75	0.1		0.31	0.48	0.1
91	15	2500	0.0251					0.2		2.50	0.06	0.8
92	19	6750	0.0678	0.1				0.93	0.16	0.3		
93	31	2500	0.0251	0.1				1.25	0.24	0.2		
94	33	10000	0.1004	0.31				0.96	0.0			
111	37	3300	0.0331	0.25				0.2		1.90	0.16	0.3
95	40	3000	0.0301					0.6		6.26	0.05	1.0
96	43	7400	0.0743					2.54		0.12	0.4	
97	44	10000	0.1004					1.88		0.16	0.3	
98	45	13700	0.138					1.25		0.24	0.2	
99	14	10000	0.1004		0.5	8	8.6	105	0.1		0.31	0.48
100	15	2500	0.0251	0.2					2.50	0.06	0.8	
101	19	6750	0.0678	0.1					0.93	0.16	0.3	
102	31	2500	0.0251	0.1					1.25	0.24	0.2	
103	33	10000	0.1004	0.31					0.96	0.0		
112	37	3300	0.0331	0.25	0.2				1.90	0.16	0.3	
104	40	3000	0.0301		0.6				6.26	0.05	1.0	
105	43	7400	0.0743		2.54				0.12	0.4		
106	44	10000	0.1004		1.88				0.16	0.3		
107	45	13700	0.138		1.25				0.24	0.2		
113	14	10000	0.1004		0.50	8	8.6	90	0.1	0.05	0.31	0.48
114				0.1					0.2			
115				0.05					0.1			
116				0.2					0.1			
117				0.1					0.5			
118				0.5					0.1			
119	15	2500	0.0251	0.50	8	8.6	90	0.2	0.1	2.50	0.06	0.80
120								0.2	0.4			
121								0.1	0.2			
122								0.4	0.2			
123	19	6750	0.0677	0.50	8	8.6	90	0.2	0.1	0.93	0.16	0.30
124								0.2	0.4			
125								0.1	0.2			
126								0.4	0.2			
127	31	2500	0.0251	0.25	8	8.6	90	0.1	0.05	1.25	0.24	0.20
128								0.1	0.2			
129								0.05	0.1			
130								0.2	0.1			
131								0.1	0.5			
132								0.5	0.1			
133	33	10000	0.1004	0.25	8	8.6	90	0.1	0.05	0.31	0.96	0.05
134								0.1	0.2			
135								0.05	0.1			
136								0.2	0.1			
137								0.1	0.5			
138								0.5	0.1			
139	37	3300	0.0331	0.25	8	8.6	90	0.2	0.1	1.90	0.16	0.30
140								0.2	0.4			
141								0.1	0.2			
142								0.4	0.2			
143	40	3000	0.0301	0.25	8	8.6	90	0.6	0.3	6.26	0.05	1.00
144								0.3	0.6			

Table A.2 : (Continued) Experimental cases

Case no.	Base case	Re	U_∞ [m/s]	h_{amp}/c	α_0 [°]	α_{ampl} [°]	ψ [°]	f_{pitch}	f_{plunge}	k	λ	St		
145	43	7400	0.0743	0.25	8	8.6	90	0.6	0.3	2.54	0.12	0.40		
146								0.3	0.6					
147	44	10000	0.1004	0.25	8	8.6	90	0.6	0.3	1.88	0.16	0.30		
148								0.3	0.6					
149	45	13700	0.138	0.25	8	8.6	90	0.6	0.3	1.25	0.24	0.20		
150								0.3	0.6					
151	14	10000	0.1004	0.5	8	8.6	90	0.1		0.31	0.48	0.1		
152	15	2500	0.0251					0.2		2.50	0.06	0.8		
153	19	6750	0.0678	0.1				1.25	0.24	0.2				
154	31	2500	0.0251	0.31				0.96	0.0					
155	33	10000	0.1004	0.2				1.90	0.16	0.3				
156	37	3300	0.0331	0.25				6.26	0.05	1.0				
157	40	3000	0.0301	0.6							2.54	0.12	0.4	
158	43	7400	0.0743	1.88							0.16	0.3		
159	44	10000	0.1004	1.25							0.24	0.2		
160	45	13700	0.138	0.1							0.31	0.48	0.1	
161	14	10000	0.1004	0.5	8	8.6	90	0.1		0.31	0.48	0.1		
162	15	2500	0.0251					0.2		2.50	0.06	0.8		
163	19	6750	0.0678	0.1				1.25	0.24	0.2				
164	31	2500	0.0251	0.31				0.96	0.0					
165	33	10000	0.1004	0.2				1.90	0.16	0.3				
166	37	3300	0.0331	0.25				6.26		0.05		1.0		
167	40	3000	0.0301					2.54		0.12		0.4		
168	43	7400	0.0743					1.88		0.16		0.3		
169	44	10000	0.1004					1.25		0.24		0.2		
170	45	13700	0.138					0.1		0.31		0.48		0.1

APPENDIX A.3 Derivation of the Theoretical Efficiency

The derivation of the theoretical efficiency is summarized in this section based on Prandtl (1952)'s definitions and calculations.

Considering a propeller, defining the force in the direction of motion as the propeller thrust, T , the work usefully applied per second is,

$$E_0 = Tv \quad (\text{A2.1})$$

where v is the velocity relative to the medium.

According to the momentum theorem, a propeller works by continually setting fresh masses of fluid into motion. If the mass moved per second is M and the velocity imparted to it is q , the propeller thrust is equal to the momentum;

$$T = Mq \quad (\text{A2.2})$$

The setting of masses of fluid into motion requires kinetic energy transfer, E' ;

$$E' = \frac{1}{2}Mq^2 \quad (\text{A2.3})$$

The efficiency is the ratio of the work usefully applied to the total amount of work supplied. Omitting the work used up in friction and eddy formation, the theoretical efficiency is defined by;

$$\eta = \frac{E_0}{E_0 + E'} \quad (\text{A2.4})$$

and by using Equations (A2.1) and (A2.3) with Equation (A2.2);

$$\eta = \frac{Tv}{Tv + \frac{1}{2}Mq^2} = \frac{Mqv}{Mqv + \frac{1}{2}Mq^2} = \frac{v}{v + \frac{q}{2}} \quad (\text{A2.5})$$

Considering a screw propeller and neglecting the rotational motion imparted to the fluid by the screw, and where the pressure has its undisturbed value of p_0 , the fluid

approaching the screw has velocity v equal to the rate of advance of the screw, and the velocity of the fluid moving away from the screw is $v + q$.

Applying continuity and Bernoulli's theorem to the conditions in front of and behind the screw, the rise of pressure is;

$$\Delta p = \rho q \left(v + \frac{1}{2} q \right) \quad (\text{A2.6})$$

Using momentum theorem, the rise of pressure Δp causes a pressure equal to T , so that the thrust of the screw on area a is;

$$T = a \Delta p = \rho a q \left(v + \frac{1}{2} q \right) \quad (\text{A2.7})$$

Solving this quadratic equation for q ;

$$\frac{1}{2} q^2 + (\rho a v) q - T = 0 \quad (\text{A2.8})$$

$$\Rightarrow q = -v + \sqrt{\left(v^2 + \frac{2T}{\rho a} \right)} \quad (\text{A2.9})$$

Prandtl (1952) denoted the thrust coefficient with T_c , and introduced it to be;

$$T_c = \frac{T}{\frac{4}{\pi} \rho a v^2} \Rightarrow \frac{4T_c}{\pi} = \frac{T}{\rho a v^2} \quad (\text{A2.10})$$

Substituting this value in Equation (A2.9) gives

$$\frac{q}{v} = -1 + \sqrt{\left(1 + \frac{2T}{\rho a v^2} \right)} \Rightarrow \frac{q}{v} = -1 + \sqrt{\left(1 + \frac{8T_c}{\pi} \right)} \quad (\text{A2.11})$$

and thus, the efficiency can be written as;

$$\eta = \frac{v}{v + \frac{q}{2}} = \frac{2}{2 + \frac{q}{v}} = \frac{2}{1 + \sqrt{\left(1 + \frac{8T_c}{\pi} \right)}} \quad (\text{A2.12})$$

Using Anderson (1996)'s definitions, the thrust coefficient based on the planform area of a foil in incompressible steady flow was defined by C_f and the thrust coefficient based on the area swept by the wing was denoted by C_T in Chapter 2. The definition of C_T was formerly given as Equation (2.4) by;

$$C_T = \frac{T}{\frac{1}{2}\rho A_0 U_\infty^2} \quad \Rightarrow \quad \frac{C_T}{2} = \frac{T}{\rho A_0 U_\infty^2} \quad (\text{A2.13})$$

where T is the thrust force, A_0 is the area swept by the airfoil and U_∞ is the freestream velocity.

Substituting Prandtl's definition from Equation (A2. 10);

$$\frac{C_T}{2} = \frac{4T_c}{\pi} \quad (\text{A2.14})$$

which gives the equation for the calculations of the theoretical efficiency which was previously defined in Chapter 2 with Equation (2.5);

$$\eta = \frac{2}{1 + \sqrt{(C_T + 1)}} \quad (\text{A2.15})$$

CURRICULUM VITAE



Candidate's full name: İdil FENERCİOĞLU
Place and date of birth: Istanbul, 02 / 11 / 1977
Permanent Address: Harman Sok. No: 15/1, Florya, Istanbul
Universities and Colleges attended: Istanbul Technical University, M.Sc., 2001
Istanbul Technical University, B.Sc., 1999
Beyoglu Anatolian Highschool, 1995

Publications:

- Ozbilen A. C., **Fenercioglu I.**, Zaloglu B., and Cetiner O., 2009: The Effect of a Flexible Extension on a Pitching SD7003 Foil in Steady Current. *5th Ankara International Aerospace Conference*, August 17-19, 2009 METU, Ankara, Turkey.
- **Fenercioglu I.**, and Cetiner O., 2008: Flow Structures around an Oscillating Airfoil in Steady Current. *14th International Symposium on Applications of Laser Techniques to Fluid Mechanics*, July 06-11, 2008 Lisbon, Portugal.
- Luo X., Olivier H., and **Fenercioglu I.**, 2008: The Generation of High Particle Velocities by Shock Tunnel Technology for Coating Application. *26th International Symposium on Shock Waves*, July 15-20, 2007 German Aerospace Center (DLR), Göttingen, Germany.
- **Fenercioglu I.**, and Yuceil K. B., 2006: Determination of Shock Oscillation Character by Instantaneous Imaging of Bow Shock Wave Caused by a Projectile. *12th International Symposium on Flow Visualization*, September 10-14, 2006 German Aerospace Center (DLR), Göttingen, Germany.
- Gunes H., **Fenercioglu I.**, and Yuceil K. B., 2004: Instantaneous Imaging of Highly Unstable Bow Shock Wave Caused by a Hypervelocity Projectile with a Streamwise Nose Cavity. *11th International Symposium on Flow Visualization*, August 9 - 12, 2004 University of Notre Dame, Notre Dame, Indiana, USA.
- **Fenercioglu I.**, Balkan T., Yuceil K. B. and Edis F. O., 2002: An Experimental and Computational Investigation of a Blunt Body with a Forward Facing Nose Cavity in Supersonic Flows (in Turkish). *4th National Aviation Symposium*, May 13-15, 2002 Erciyes University, Kayseri, Turkey.